

Electronic Thesis and Dissertation Repository

---

4-24-2020 10:30 AM

# Intelligent and Efficient Ultra-Dense Heterogeneous Networks for 5G and Beyond

Yanan Liu, *The University of Western Ontario*

Supervisor: Wang, Xianbin, *The University of Western Ontario*

A thesis submitted in partial fulfillment of the requirements for the Doctor of Philosophy degree in Electrical and Computer Engineering

© Yanan Liu 2020

Follow this and additional works at: <https://ir.lib.uwo.ca/etd>

---

## Recommended Citation

Liu, Yanan, "Intelligent and Efficient Ultra-Dense Heterogeneous Networks for 5G and Beyond" (2020). *Electronic Thesis and Dissertation Repository*. 6959.  
<https://ir.lib.uwo.ca/etd/6959>

This Dissertation/Thesis is brought to you for free and open access by Scholarship@Western. It has been accepted for inclusion in Electronic Thesis and Dissertation Repository by an authorized administrator of Scholarship@Western. For more information, please contact [wlsadmin@uwo.ca](mailto:wlsadmin@uwo.ca).

# Abstract

Ultra-dense heterogeneous network (HetNet), in which densified small cells overlaying the conventional macro-cells, is a promising technique for the fifth-generation (5G) mobile network. The dense and multi-tier network architecture is able to support the extensive data traffic and diverse quality of service (QoS) but meanwhile arises several challenges especially on the interference coordination and resource management. In this thesis, three novel network schemes are proposed to achieve intelligent and efficient operation based on the deep learning-enabled network awareness. Both optimization and deep learning methods are developed to achieve intelligent and efficient resource allocation in these proposed network schemes.

To improve the cost and energy efficiency of ultra-dense HetNets, a hotspot prediction based virtual small cell (VSC) network is proposed. A VSC is formed only when the traffic volume and user density are extremely high. We leverage the feature extraction capabilities of deep learning techniques and exploit a long-short term memory (LSTM) neural network to predict potential hotspots and form VSC. Large-scale antenna array enabled hybrid beamforming is also adaptively adjusted for highly directional transmission to cover these VSCs. Within each VSC, one user equipment (UE) is selected as a cell head (CH), which collects the intra-cell traffic using the unlicensed band and relays the aggregated traffic to the macro-cell base station (MBS) in the licensed band. The inter-cell interference can thus be reduced, and the spectrum efficiency can be improved. Numerical results show that proposed VSCs can reduce 55% power consumption in comparison with traditional small cells.

In addition to the smart VSCs deployment, a novel multi-dimensional intelligent multiple access (MD-IMA) scheme is also proposed to achieve stringent and diverse QoS of emerging 5G applications with disparate resource constraints. Multiple access (MA) schemes in multi-dimensional resources are adaptively scheduled to accommodate dynamic QoS requirements and network states. The MD-IMA learns the integrated-quality-of-system-experience (I-QoSE) by monitoring and predicting QoS through LSTM neural network. The resource allocation in the MD-IMA scheme is formulated as an optimization problem to maximize the I-QoSE as well as minimize the non-orthogonality (NO) in view of implementation constraints. In order to solve this problem, both model-based optimization algorithms and model-free deep reinforcement learning (DRL) approaches are utilized. Simulation results demonstrate that the

achievable I-QoSE gain of MD-IMA over traditional MA is 15% - 18%.

In the final part of the thesis, a Software-Defined Networking (SDN) enabled 5G-vehicle ad hoc networks (VANET) is designed to support the growing vehicle-generated data traffic. In this integrated architecture, to reduce the signaling overhead, vehicles are clustered under the coordination of SDN and one vehicle in each cluster is selected as a gateway to aggregate intra-cluster traffic. To ensure the capacity of the trunk-link between the gateway and macro base station, a Non-orthogonal Multiplexed Modulation (NOMM) scheme is proposed to split aggregated data stream into multi-layers and use sparse spreading code to partially superpose the modulated symbols on several resource blocks. The simulation results show that the energy efficiency performance of proposed NOMM is around 1.5-2 times than that of the typical orthogonal transmission scheme.

**Keywords:** Ultra-Dense Network, Heterogeneous Network, Machine Learning, Resource Allocation, Virtual Small Cell, VANET

# Lay Summary

5G network becomes ultra-densified and heterogeneous to support the explosive data traffic and diverse QoS requirements. However, the densified and multi-tier architectures bring new challenges, especially on the interference coordination and resource management. In order to address these challenges in 5G ultra-dense HetNets, three novel network schemes are proposed to achieve intelligent and efficient operation based on the deep learning-enabled network awareness and multi-dimensional resource allocation.

First of all, to improve the energy efficiency of ultra-dense HetNets, a hotspot prediction based virtual small cell (VSC) operation scheme is proposed. The VSCs are formed only when the areas are hotspots, which can be predicted through deep learning technology. Then, a large-scale antenna array enabled highly directional beamforming scheme is adaptively designed to cover these VSCs. Within each VSC, one user equipment is selected as a cell head to collect the intra-cell information and relays the aggregated traffic to the macro-cell base station.

Moreover, in order to fully utilize the resource available in 5G ultra-dense networks, a novel multi-dimensional intelligent multiple access (MD-IMA) technique is developed to adaptively select the multiple access (MA) schemes. The proposed MD-IMA technique learns the overall system requirements and then adaptively multiplexes co-existing devices in multi-dimensional resources to meet the real-time QoS requirements. The resource allocation problem of the MD-IMA system is formulated as an optimization problem to maximize the overall network performance as well as to minimize receiver complexity. Both model-based optimization algorithms and model-free deep reinforcement learning-enabled approaches are proposed to solve this optimization problem.

Finally, to support growing vehicle-generated data traffic in 5G-vehicle ad hoc networks (VANET), a Software-Defined Networking (SDN) enabled 5G-VANET is presented. In this integrated architecture, SDN can provide a global view to adaptively cluster vehicles only when needed. In order to reduce the signaling overhead, one vehicle in each cluster is selected as a cell head to support the aggregated traffic. To ensure the capacity of the trunk link between the gateway and base station, a new modulation scheme is also proposed to effectively aggregate the trunk link traffic.

# **Dedication**

To my parents and husband

## Acknowledgments

I would like to express my deepest appreciation to my supervisor, Dr. Xianbin Wang, for his guidance, patience and encouragement in developing my research. It was his enlightening supervisions that inspired me to explore novel research areas and broadened my views in the research area.

Sincere thanks to Dr. Ravedra Rao, Dr. Jagath Samarabandu, Dr. Charles Ling and Dr. Wei Song for being my examination committee. I highly appreciate their precious time and constructive suggestions on my thesis and research.

Thanks to all members of our research group for the time that we spent both at work and after work. I would give my best regards to their success in both study and life. I would like to extend my thanks to all my friends at UWO. The last four years have been full of fun and warmth because of your accompany and friendship. As always, I wish to thank my husband and my parents for their love, support and encouragement throughout these years.

# Contents

<b>Abstract</b>	<b>ii</b>
<b>Lay Summary</b>	<b>iv</b>
<b>Dedication</b>	<b>v</b>
<b>Acknowledgments</b>	<b>vi</b>
<b>List of Figures</b>	<b>xi</b>
<b>List of Tables</b>	<b>xiv</b>
<b>List of Abbreviations</b>	<b>xv</b>
<b>1 Introduction</b>	<b>1</b>
1.1 Ultra-Dense Heterogeneous Networks in 5G . . . . .	1
1.1.1 5th Generation Mobile Networks (5G) . . . . .	1
1.1.2 Ultra-Dense Heterogeneous Networks (HetNet) . . . . .	2
1.2 Challenges of Ultra-dense Heterogeneous Networks . . . . .	4
1.2.1 High Management Complexity . . . . .	4
1.2.2 Severe Interference . . . . .	5
1.2.3 High Power Consumption . . . . .	5
1.2.4 Diverse and New QoS Requirements . . . . .	6
1.2.5 Spatio-Temporal Dynamics . . . . .	6
1.3 Research Objectives and Topics . . . . .	7
1.4 Technical Contributions of the Thesis . . . . .	10
1.5 Thesis Outline . . . . .	13
<b>2 Background on Enabling Technologies of Ultra-Dense HetNets</b>	<b>16</b>
2.1 Key Technologies of 5G . . . . .	16
2.1.1 Massive MIMO . . . . .	17
2.1.2 NOMA . . . . .	17
2.1.3 Massive MIMO-NOMA . . . . .	20
2.2 Deep Learning enabled Network Prediction and Control . . . . .	22
2.2.1 Deep Learning based Network Prediction . . . . .	22
2.2.2 Deep Learning based Network Control . . . . .	23
2.3 Chapter Summary . . . . .	25

<b>3</b>	<b>Cost-Effective Virtual Small Cell for Ultra Dense HetNet</b>	<b>26</b>
3.1	Introduction . . . . .	27
3.2	System Model . . . . .	30
3.2.1	Network Architecture . . . . .	30
3.2.2	Information Collection Procedure . . . . .	31
3.2.3	Channel Model for Beamformed Fronthaul . . . . .	33
3.3	VSC Formation and Protocol Conversion . . . . .	34
3.3.1	K-means based VSC formation . . . . .	34
3.3.2	Protocol Conversion for Traffic Aggregation . . . . .	35
3.4	Adaptive Beamforming Design for VSC . . . . .	38
3.4.1	Hybrid Beamforming Scheme . . . . .	38
3.4.2	Problem Formulation of Digital Beamforming . . . . .	39
3.4.3	Semi-definite Relaxation . . . . .	41
3.4.4	Low Complexity Optimization Algorithm . . . . .	43
3.5	Performance Evaluation . . . . .	46
3.5.1	Simulation Parameters . . . . .	46
3.5.2	K-means based VSC Formation . . . . .	46
3.5.3	Power Consumption Performance of the Proposed VSC . . . . .	47
3.6	Chapter Summary . . . . .	50
<b>4</b>	<b>Deep Learning Based Hotspot Prediction for VSC in Ultra Dense HetNet</b>	<b>51</b>
4.1	Introduction . . . . .	51
4.2	Overall Network Architecture . . . . .	55
4.3	Problem Formulation of Hotspot Prediction . . . . .	56
4.4	LSTM based User Distribution Prediction . . . . .	57
4.4.1	Memory Cell Structure of LSTM . . . . .	58
4.4.2	User Distribution Prediction based on One LSTM . . . . .	60
4.5	Data Set . . . . .	61
4.6	Performance Evaluation . . . . .	62
4.6.1	Baseline Algorithms of Hotspot Prediction . . . . .	63
4.6.2	Simulation Conditions . . . . .	64
4.6.3	Data Preprocessing . . . . .	66
4.6.4	CDR Numbers Forecasting Comparison . . . . .	66
4.6.4.1	Compare one LSTM with ARIMA and several LSTM . . . . .	66
4.6.4.2	Compare one LSTM with ConvLSTM . . . . .	68
4.6.5	Accuracy Evaluation of Hotspot Prediction . . . . .	69
4.6.6	Performance of Hotspot Prediction based VSC . . . . .	71
4.7	Chapter Summary . . . . .	72
<b>5</b>	<b>Multi-Dimensional Intelligent Multiple Access for 5G Beyond Networks</b>	<b>73</b>
5.1	Introduction . . . . .	74
5.2	System Model . . . . .	78
5.3	Problem Formulation . . . . .	80
5.3.1	Achievable Rate . . . . .	81
5.3.2	Weighted Energy Efficiency . . . . .	82



5.3.3	Non-orthogonality Calculation . . . . .	83
5.3.3.1	The Non-orthogonality in Space Domain . . . . .	83
5.3.3.2	The Non-orthogonality in Power Domain . . . . .	83
5.3.4	Problem Formulation . . . . .	84
5.4	Sub-optimal Solution . . . . .	84
5.4.1	User Clustering in Spatial Domain by Using K-means . . . . .	85
5.4.2	Subchannel Assignment . . . . .	86
5.4.3	Dynamic Power Allocation . . . . .	89
5.4.4	Joint Resource Allocation . . . . .	91
5.4.5	Complexity Analysis . . . . .	92
5.5	Simulation Results . . . . .	93
5.5.1	The Deployment of the MD-IMA . . . . .	93
5.5.2	Convergence and Optimality of the Proposed Algorithms . . . . .	93
5.5.3	Impact of the Weight Values on the WEE . . . . .	97
5.5.4	Impact of the Cluster Number on the Total Non-orthogonality . . . . .	98
5.5.5	Comparison of the WEE Performance for Different MA Modes . . . . .	99
5.6	Chapter Summary . . . . .	100
<b>6</b>	<b>Deep Reinforcement Learning Based Power Allocation for MD-IMA Networks</b>	<b>101</b>
6.1	Introduction . . . . .	102
6.2	Network Architecture . . . . .	104
6.3	Communication Model of MD-IMA Network . . . . .	105
6.3.1	Channel Model . . . . .	106
6.3.2	Achievable Rate . . . . .	107
6.3.3	Weighted energy efficiency . . . . .	108
6.4	Problem Formulation . . . . .	109
6.5	I-QoSE Prediction based on One LSTM . . . . .	110
6.6	Power Allocation based on DRL . . . . .	112
6.6.1	Basic Model of Reinforcement Learning . . . . .	113
6.6.2	Q-Learning . . . . .	114
6.6.3	Value-based DRL: DQN . . . . .	116
6.6.4	Actor-Critic based DRL: DDPG . . . . .	117
6.7	Simulation Results . . . . .	118
6.7.1	Environment . . . . .	118
6.7.2	LSTM Parameters Setting . . . . .	119
6.7.3	DQN Parameters Setting . . . . .	121
6.7.4	DDPG Parameters Setting . . . . .	124
6.7.5	Simulation Results . . . . .	127
6.7.5.1	Accuracy of LSTM based WEE Prediction . . . . .	127
6.7.5.2	WEE Performance of DQN with different States . . . . .	129
6.7.5.3	WEE Performance of DRL Based Power Allocation . . . . .	130
6.7.5.4	Time Cost . . . . .	131
6.7.5.5	Imapct of the weights on the EE . . . . .	132
6.8	Chapter Summary . . . . .	133

<b>7</b>	<b>Adaptive Vehicle Clustering and Data Traffic Explosion in SDN Enabled 5G-VANET</b>	<b>134</b>
7.1	Introduction . . . . .	135
7.2	SDN Enabled 5G-VANET Integrated Network Architecture . . . . .	137
7.3	Adaptive Clustering in SDN Enabled 5G-VANET . . . . .	138
7.4	NOMM System Model . . . . .	143
7.5	Energy Efficiency Analysis . . . . .	145
	7.5.1 EE for NOMM . . . . .	145
	7.5.2 EE for Traditional Orthogonal Transmission . . . . .	147
7.6	Simulations . . . . .	148
	7.6.1 NOMM Signature Design and Selection for Simulation . . . . .	148
	7.6.2 Simulation Results . . . . .	150
7.7	Chapter Summary . . . . .	152
<b>8</b>	<b>Conclusion and Future Work</b>	<b>153</b>
8.1	Conclusion . . . . .	153
8.2	Future Work . . . . .	156
	8.2.1 Cellular Network Assisted Flying Ad Hoc Network . . . . .	156
	8.2.2 Distributed AI Enabled Resource Management . . . . .	158
	<b>Bibliography</b>	<b>160</b>
	<b>Curriculum Vitae</b>	<b>171</b>

# List of Figures

1.1	Three dimensions for capacity enhancement for 5G networks. . . . .	2
1.2	Network architecture of 5G ultra-dense HetNet. . . . .	3
2.1	Illustration of NOMA via power domain multiplexing . . . . .	18
2.2	SCMA encoding and multiplexing. . . . .	19
2.3	Structure of MIMO-NOMA . . . . .	21
2.4	General structure of DRL based network control . . . . .	24
3.1	A two-tire network architecture consisting of one macro-cell and $S$ virtual small cells. . . . .	30
3.2	The implementation and information collection procedure for VSC formation. . . . .	32
3.3	Procedure of the protocol conversion and data packet re-capsulation at CH in VSC. . . . .	36
3.4	The data aggregation processing among UEs of VSCs, CHs and MBSs. . . . .	37
3.5	Structure of hybrid beamforming scheme for VSC. . . . .	39
3.6	Virtual small cell formation using K-MEANS clustering and far user removing. . . . .	47
3.7	Total power consumption against the number of MBS antennas for macro-only, traditional SCs and virtual SCs. . . . .	48
3.8	Total power consumption for different throughput rate constraints in three scenarios. . . . .	49
4.1	Network architecture of hotspot prediction based VSC. . . . .	55
4.2	UE location map in temporal and spatial domain. . . . .	57
4.3	Structure of LSTM memory cell. . . . .	58
4.4	Structure of one LSTM based UE distribution prediction method. . . . .	60
4.5	Grid map and the CDR heat map of Milan. . . . .	61
4.6	CDR distributions of Milan in the spatial domain and temporal domain. . . . .	62
4.7	Heatmap examples of real CDR data for Milan. . . . .	63
4.8	Structure of several LSTM based prediction method. . . . .	64
4.9	Evaluation of wavelet-based filter on 20th grid . . . . .	66
4.10	Histogram Comparison among one LSTM, several LSTM and ARIMA methods based user density prediction . . . . .	67
4.11	CDF Comparison among one LSTM, several LSTM and ARIMA methods based user density prediction . . . . .	68
4.12	Histogram Comparison among one LSTM, several LSTM and ARIMA methods based user density prediction . . . . .	69
4.13	CDF Comparison among one LSTM, several LSTM and ARIMA methods . . . . .	70

4.14	Heatmap comparison between ground truth and predicted values. . . . .	70
4.15	Power consumption comparison between K-means based VSC and hotspot prediction based VSC. . . . .	71
5.1	Intelligent and situation-aware resource allocation in MD-IMA system. . . . .	79
5.2	Block diagram of the proposed sub-optimal solution for resource allocation problem of MD-IMA network. . . . .	85
5.3	Deployment of MD-IMA for 12 UEs. . . . .	94
5.4	Convergence of Algorithm 5 with $K = 10$ , $M = 5$ and $[\alpha_1 = 0.5, \alpha_2 = 0.5]$ . . . . .	95
5.5	Convergence of Algorithm 6 with $K = 10$ , $M = 5$ and $[\alpha_1 = 0.5, \alpha_2 = 0.5]$ . . . . .	95
5.6	Convergence of Algorithm 7 with $K = 10$ , $M = 5$ and $[\alpha_1 = 0.5, \alpha_2 = 0.5]$ . . . . .	96
5.7	WEE of MD-IMA in respect of total transmit power by using different resource allocation algorithms with $K = 10$ , $M = 5$ and $[\alpha_1 = 0.5, \alpha_2 = 0.5]$ . . . . .	96
5.8	WEE of MD-IMA by using the Algorithm 7 in respect of transmit power for different weights of WEE with $K = 10$ , $M = 5$ . . . . .	97
5.9	Total spatial domain nonorthogonality with different cluster numbers. . . . .	98
5.10	WEE of different MA models in respect of transmit power with $K = 40$ , $M = 20$ and $[\alpha_1 = 0.5, \alpha_2 = 0.5]$ . . . . .	99
6.1	Deep learning based intelligent resource allocation of the MD-IMA Network . . . . .	104
6.2	Structure of one LSTM based sum-rate prediction method. . . . .	111
6.3	Grid map and the CDR heat map of Milan. . . . .	120
6.4	WEE comparison of DQN based method with different learning rate values during training period . . . . .	122
6.5	WEE comparison of DQN based method with different discount factor values during training period . . . . .	123
6.6	WEE performance of DQN based power allocation for training episodes with $\lambda = 0.1$ . . . . .	124
6.7	WEE comparison of DDPG based method with a different learning rate of the actor-network. . . . .	125
6.8	WEE comparison of DDPG based method with a different learning rate of the critic-network. . . . .	126
6.9	Histogram Comparison among one LSTM and three baselines based sum-rate prediction. . . . .	127
6.10	CDF Comparison among one LSTM and three baselines based sum-rate prediction. . . . .	128
6.11	Compare the predicted weight with real weight of sum-rate for the 12 <sup>th</sup> grid. . . . .	129
6.12	WEE comparison of DQN with different states in test episodes for $[\alpha_1 = 0.5, \alpha_2 = 0.5]$ . . . . .	130
6.13	WEE comparison between DQN and DDPG in training episodes for $[\alpha_1 = 0.5, \alpha_2 = 0.5]$ . . . . .	131
6.14	WEE comparison among DDPG, DQN, FP, WMMSE and exhaustive optimal solution in test episodes for $[\alpha_1 = 0.5, \alpha_2 = 0.5]$ . . . . .	132
6.15	WEE comparison of DDPG based power allocation for different weights . . . . .	133

7.1 SDN enabled 5G-VANET integrated network architecture. . . . . 138  
7.2 Baseband transmission using data aggregation for 5G-VANET. . . . . 139  
7.3 The dual cluster head selection scheme. . . . . 142  
7.4 Block diagram of a NOMM modulator. . . . . 144  
7.5 WER comparison among NOMM Example 2, 3 and 4. . . . . 150  
7.6 EE comparison among NOMM examples and orthogonal transmission. . . . . 151

# List of Tables

3.1	Parameters of hardware and channel model for small cell and macro-cell. . . . .	46
4.1	The parameters of the LSTM and ConvLSTM for user density prediction. . . . .	65
5.1	Simulation Parameters of MD-IMA networks . . . . .	93
6.1	Main Parameters of DRL enabled MD-IMA Network . . . . .	119
6.2	The parameters of the LSTM and ConvLSTM for sum-rate prediction. . . . .	121
6.3	The parameters of the DQN. . . . .	125
6.4	The parameters of the DDPG. . . . .	126
6.5	Average time cost per episode (sec) of DRL and optimization methods . . . . .	132

# List of Abbreviations

<b>5G</b>	5th Generation
<b>5G-VANET</b>	5G-Vehicular Ad Hoc Network
<b>A2G</b>	Air-to-Ground
<b>ACK/NACK</b>	Acknowledgment/Negative-Acknowledgment
<b>AI</b>	Artificial Intelligent
<b>AoA</b>	Angle of Arrival
<b>APs</b>	Access Points
<b>ARIMA</b>	Autoregressive Integrated Moving Average
<b>AWGN</b>	Additive White Gaussian Noise
<b>BS</b>	Base Stations
<b>CCT</b>	Charnes-Cooper Transformation
<b>CDF</b>	Cumulative Distribution Function
<b>CDR</b>	Call Detail Record
<b>CH</b>	Cluster Head
<b>ConvLSTM</b>	Convolutional LSTM
<b>CNA-FANET</b>	Cellular Network Assisted FANET
<b>CNN</b>	Convolutional Recurrent Unit
<b>CSI</b>	Channel State Information
<b>CSMA/ CA</b>	Carrier-sense Multiple Access
<b>C-RNTI</b>	Cell Audio Network Temporary Identifier
<b>D2D</b>	Device-to-Device
<b>DCI</b>	Downlink Control Information
<b>DDPG</b>	Deep Deterministic Policy Gradient
<b>DL</b>	Deep Learning

<b>DNN</b>	Deep Neural Network
<b>DQN</b>	Deep Q-Learning
<b>DRL</b>	Deep Reinforcement Learning
<b>EE</b>	Energy Efficiency
<b>EHF</b>	Extremely High Frequency
<b>FANET</b>	Flying ad Hoc Network
<b>FEC</b>	Forward Error Correction
<b>FIFO</b>	First-In-First-Out
<b>FP</b>	Fractional Programming
<b>GAN</b>	Generative Adversarial Network
<b>GP</b>	Gaussian Process
<b>GPU</b>	Graphic Processing Unit
<b>GPS</b>	Global Positioning System
<b>GRU</b>	Gate Recurrent Unit
<b>HetNets</b>	Heterogeneous Networks
<b>HBF</b>	Hybrid Beamforming
<b>I-QoSE</b>	Integrated Quality of System Experience
<b>IRC</b>	Interference Rejection Combing
<b>IOT</b>	Internet of Things
<b>IVD</b>	Inter-Vehicular Distance
<b>KKT</b>	Karush-Kuhn-Tucker
<b>LAA</b>	License Assisted Access
<b>LBT</b>	Listen Before Talk
<b>LoS</b>	Line of Sight
<b>LPWAN</b>	Low-Power Wide-Area Network
<b>LSA</b>	License Shared Access
<b>LSTM</b>	Long Short Term Memory



<b>LTE</b>	Long Term Evolution
<b>LTE-U</b>	Long Term Evolution in the Unlicensed Band
<b>MAC</b>	Media access control
<b>Max-SLNR</b>	Maximizing Signal-to-Leakage-and-Noise Ratio
<b>MBS</b>	Macro-cell Base Station
<b>MD-IMA</b>	Multi-dimensional Intelligent Multiple Access
<b>MDP</b>	Markov Decision Process
<b>MIMO</b>	Massive Multiple Input Multiple Output
<b>ML</b>	Maximum Likelihood
<b>mMTC</b>	Massive Machine Type Communications
<b>mmWave</b>	Millimeter Wave
<b>MOO</b>	Multi-Objective Optimization
<b>NLP</b>	Natural Language Processing
<b>NO</b>	Non-orthogonality
<b>NOMA</b>	Non-orthogonal Multiple Access
<b>NOMM</b>	Non-orthogonal Multiplexed Modulation
<b>OBF</b>	Opportunistic Beamforming
<b>OFDM</b>	Orthogonal Frequency Division Multiplexing
<b>OMA</b>	Orthogonal Multiple Access
<b>OT</b>	Orthogonal Transmission
<b>PCA</b>	Principle Component Analysis
<b>PDCP</b>	Packet Data Convergence Protocol
<b>PIT</b>	Predicted Inhabitant Time
<b>QoS</b>	Quality of Service
<b>QoSE</b>	Quality of System Experience
<b>RAT</b>	Radio Access Technology
<b>RBM</b>	Restricted Boltzmann Machine

<b>RC</b>	Receiver Complexity
<b>RF</b>	Radio Frequency
<b>RMSE</b>	Root Mean Square Error
<b>RNN</b>	Recurrent Neural Network
<b>RRHs</b>	Radio Remote Heads
<b>RSS</b>	Received Signal Strength
<b>RSUs</b>	Roadside Units
<b>SBS</b>	Small Base Station
<b>SCs</b>	Small Cells
<b>SCMA</b>	Sparse Code Multiple Access
<b>SDN</b>	Software Defined Networking
<b>SER</b>	Symbol Error Rate
<b>SIC</b>	Successive Interference Cancellation
<b>SGD</b>	Stochastic Gradient Descent
<b>SINR</b>	Signal-to-Interference-and-Noise ratio
<b>SOO</b>	Single-objective optimization
<b>SDN</b>	Software-Defined Networking
<b>SR</b>	Scheduling Request
<b>SU-MIMO</b>	Single-User MIMO
<b>SVM</b>	Support Vector Machine
<b>TBS</b>	Temporary Base Station
<b>TDD</b>	Time Division Duplex
<b>UDN</b>	Ultra-Dense Network
<b>UE</b>	User Equipment
<b>URLLC</b>	Ultra-Reliable and Low-Latency Communications
<b>V2I</b>	Vehicle-to-Infrastructure
<b>V2V</b>	Vehicle-to-Vehicle

<b>VANET</b>	Vehicular Ad Hoc Network
<b>VHF</b>	Very High Frequency
<b>VSC</b>	Virtual Small Cell
<b>WEE</b>	Weighted Energy Efficiency
<b>WER</b>	Word Error Rat
<b>WMMSE</b>	Weighted Minimum Mean Squared Error

# Chapter 1

## Introduction

### 1.1 Ultra-Dense Heterogeneous Networks in 5G

#### 1.1.1 5th Generation Mobile Networks (5G)

The prosperity of wireless mobile networks, including the popularization of various smart terminals and their emerging applications, leads to critical data storm challenge. The initial commercial deployment of 5G wireless networks has started in 2019 following the completion of the first full set of 5G standards. 5G wireless network marks the beginning of a truly digital society. It is going to achieve significant breakthroughs in terms of latency, data rates, mobility and number of connected devices in contrast to previous generations [1]. The global mobile data traffic is predicted to grow 1000 times from 4G to 5G [2].

Driven by the exponentially increased data traffic, 5G networks become ultra-densified and heterogeneous to improve the capacity [3]. By cooperating with other key technologies, the 5G ultra-dense heterogeneous network can further enhance the network capacity from three directions: spectral efficiency, area reuse and new spectrum exploring [4], as shown in Fig. 1.1. Massive multiple-input-multiple-output (MIMO) [5], high directional beamforming (BF) [6], and non-orthogonal multiple access (NOMA) [7] [8] have been applied to increase spectral efficiency. To improve area reuse factor, ultra-dense small cells [8], vehicular ad hoc network (VANET) [9] and device-to-device (D2D) communications [10] have been investigated. Meanwhile, technologies such as long term evolution (LTE) in the unlicensed band (LTE-U)

[11], millimeter wave (mmWave) [12], Wi-Fi offloading and license shared access (LSA) were developed to extend usable bandwidth.

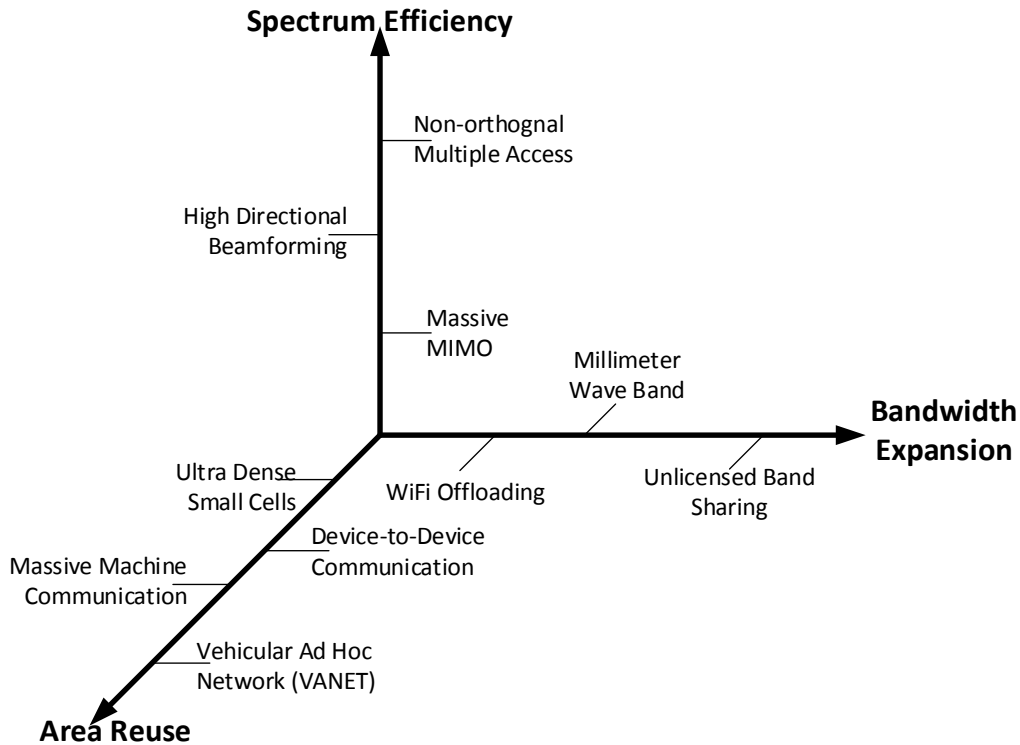


Figure 1.1: Three dimensions for capacity enhancement for 5G networks.

### 1.1.2 Ultra-Dense Heterogeneous Networks (HetNet)

With the widespread use of mobile and smart devices as well as the associated bandwidth-hungry applications, high data rate and low latency wireless services are in urgent need of the mobile network operators. Traditional solutions may not be able to meet the growing data traffic requirement as the spectral efficiency of present networks is approaching theoretical limits, particularly in a low signal-to-interference-plus-noise ratio (SINR) conditions like the indoor scenarios [13]. A promising solution is necessary to increase node deployment density to provide ubiquitous coverage and a larger data rate. Meanwhile, frequency bands between several hundred MHz and a few GHz, which are most suitable for wireless communication, have been almost entirely occupied by a variety of licensed or unlicensed networks [14]. New bandwidths

and idle spectra thus need to be explored. As an undeveloped band that can be used for high-speed wireless communications, millimeter-wave (mmWave) in the frequency range from 30 to 300 GHz can be exploited for the ultra-dense HetNets operation [15]. As a radio signal propagates in the extremely high frequency (EHF) or very high frequency (VHF) bands, mmWaves have high atmospheric attenuation. Hence, cell size in mmWave bands has to be small. These small-cell mmWave networks of high node deployment density are then going to configure a single holistic network of HetNet architecture [16]. High data rates can be supported by the small cells operating at high frequencies, due to their high spectral and energy efficiency. In

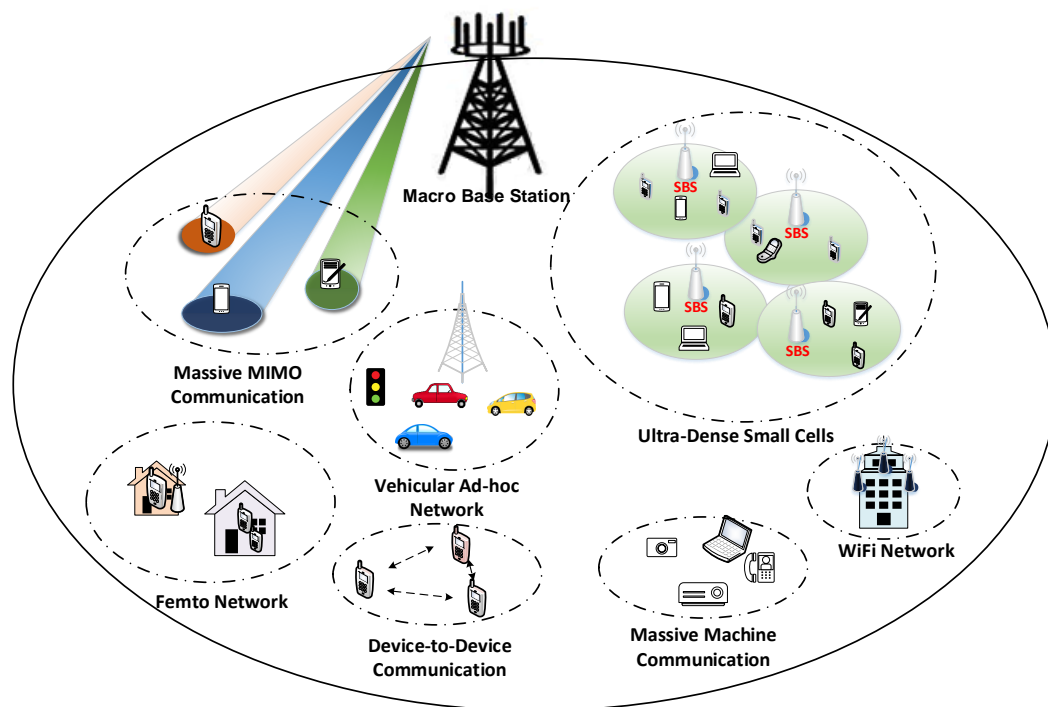


Figure 1.2: Network architecture of 5G ultra-dense HetNet.

ultra-dense HetNets, as shown in Fig.1.2 a wide range of access points (APs) including the traditional high-power macro cells, low-power small cells (i.e., pico, femto, and micro cells) and other non-cellular heterogeneous communication systems (i.e., VANET, D2D, Low-Power Wide-Area Network (LPWAN), etc.) are densified to meet the high capacity requirements in various environments [17]. Due to the dense deployment of heterogeneous nodes, ultra-dense HetNets would benefit from the increased spatial reuse of the scarce frequency resources and deployment flexibility to enhance coverage and capacity, especially in hotspot and blind wire-

less areas. Compared with traditional networks, prominent features of the ultra-dense HeteNet include:

- Significant enhancement of performance gains: network coverage and area spectral efficiency can be improved through network densification [18].
- Cell-less and user-centric: each user can be served by one or more APs flexibly through dynamic beamforming or cell cooperation [18].
- Rich types of APs: Several different APs, such as base stations (BSs), small cell BSs, relay nodes, radio remote heads (RRHs), D2D enabled users, roadside units (RSUs) in the vehicle networks and machine-type communication cooperation devices, etc., coexist in the wireless network [19].

## 1.2 Challenges of Ultra-dense Heterogeneous Networks

Ultra-dense HetNet is considered to be the main enabling technology for 5G and beyond 5G wireless networks. Along with the advantages, ultra-dense deployment of small cells and multi-tier architectures also arise new technical challenges, including complicated management, severe interference problem, high power consumption, diverse quality-of-service (QoS) requirements and spatio-temporal dynamics.

### 1.2.1 High Management Complexity

Network administration and service provisioning are challenging in this multi-tier model due to the huge number of base stations, the complexity of network architecture and equipment vendor-dependence. The resource allocation issues are always interpreted as highly complex large-scale optimization problems, for which finding the optimal decision is extremely challenging in terms of the computational complexity. This is partly due to the vast degrees of freedom and partly owing to that the allocation opportunities available exponentially increases with network density and the combination of multi-dimensional resources [20]. In addition, the information exchange among heterogeneous network infrastructures grows the complexity of network management, which is further compounded by the vendor-specific equipment

relying on different configuration interfaces [21]. It is also difficult to upgrade the information exchange protocol due to the ossification of the network infrastructure [16]. All the paths traversing the network have to be upgraded to make a new protocol available to applications. Therefore, we need to explore effective algorithms with low complexity to efficiently manage the resource in ultra-dense HetNet.

### **1.2.2 Severe Interference**

In the ultra-dense HetNet, the interference within the multi-tier architecture becomes rather serious and complicated as there are numerous heterogeneous interfering APs in the proximity. The ultra-dense deployment shortens the distances between the users and the interfering APs, which results in more and stronger interference sources when considering resource allocation problems [22]. Moreover, along with resource multiplexing for more access opportunities, resource allocation is coupled with multi-domain interference management performed in frequency, time, space, caching and computing resource domains simultaneously [23]. Therefore, how to balance interference with resource utilization is still an open issue for ultra-dense HetNets.

### **1.2.3 High Power Consumption**

As there are increasingly more small-cells deployed in the 5G cellular network, their power consumption needs to be addressed. It was reported in [24] that the typical power consumption is 10W for a small cell base station (SBS) and 930W for a macro-base station (MBS) in European countries. As a result, the power consumption of 100 SBSs could be larger than that of an MBS. Also, the MBS and the SBS are different in their power consumption rates with their traffic loads [25]. The MBS's power consumption increases exponentially with its traffic load in terms of the number of users served given each user has a constant rate requirement, while the SBS's power consumption is almost independent of its load and even flat for any load. The power consumption of macro-cells and small-cells thus needs to be jointly managed for more energy-efficient operation with traffic sharing. Data offloading from the MBS to the SBSs could save the MBS's power consumption but inevitably requires more SBSs to be turned



on, leading to high total power consumption [17]. The operator should be aware of the traffic sharing among the macro- and small-cells and simultaneously consider the heterogeneity of small-cells in location and user coverage. Therefore, it is a challenge for ultra-dense HetNet to reduce the total power consumption while meeting all users' service requirements.

#### **1.2.4 Diverse and New QoS Requirements**

Customers' requests for experiences should never be underestimated and are promoted by the merging of mobile networks and the Internet nowadays. Variety of emerging services like virtual reality, user-centric computing, and telemedicine place high QoS demands of tactile level latency, ultra-high reliability, security, and privacy, etc., which puts forward critical demands for both the physical transportation and resource scheduling technologies [26]. As such, QoS provisioning becomes essential in ultra-dense HetNet to allocate resources efficiently so as to improve the user experience. Different applications could have different operational constraints. Online gaming or multimedia are usually bandwidth aggressive, while real-time video calls are delay-sensitive [27]. In the case of enterprise-level communication, it could have extremely low-latency and high-security requirements. Cellular networks are thus expected to provide ubiquitous and global connectivity for everything (users, devices, sensors, machines) and also be competent for their applications of diverse demands. To this end, the next-generation network should be adaptable to the diverse QoS requirements, traffic load scenarios and varying channel conditions.

#### **1.2.5 Spatio-Temporal Dynamics**

As there are numerous APs and users, the level of interference in ultra-dense HetNet could be extraordinarily high but also present significant fluctuations. The spatial dynamics of interference is thus no longer negligible in ultra-dense HetNet. Meanwhile, temporal dynamics in the network such as traffic load and users' requests should also be taken into consideration [28]. The spatio-temporal dynamics, which is well known as an intricate issue in the traditional networks, are amplified in large-scale ultra-dense HetNets. In assisting the efficient operation of 5G networks, hidden patterns from the network traffic and user behavior have been proved to

be effective [29]. Therefore, intelligent real-time network traffic-awareness discovery is worthy of being investigated to treat the spatio-temporal dynamics in ultra-dense HetNet.

## 1.3 Research Objectives and Topics

In this thesis, we focus on solutions to these typical challenges in ultra-dense HetNets. The fundamental design objective is to improve the cost-effectiveness and operational efficiency of the service-oriented network operation, by learning the network situation through machine learning and then operating traffic-aware virtual small cells and intelligently utilizing the multi-dimensional resources.

In achieving this, we propose five novel technologies on the ultra-dense HetNet architecture: virtual small cells (VSCs) to reduce interference and power consumption, deep learning based network situation prediction, multi-dimensional intelligent multiple access techniques for highly efficient radio resource utilization, deep reinforcement learning-based resource allocation and non-orthogonal multiplexed modulation to improve the trunk-link capacity.

**Cost-Effective Virtual Small Cell:** The fixed deployment of a large number of small cells in 5G HetNet is neither cost-effective nor energy-efficient. To support such ultra-dense small cell networks, network architecture complexity, operational procedure and signaling overhead will all be increased dramatically [20]. In order to reduce interference and power consumption of ultra-dense HetNets, a dynamic small cell formation with adaptive operation could be investigated.

The purpose of the dynamic small cell formation is to develop an adaptive wireless infrastructure, which can have an extremely high spectrum and cost efficiency and at the same time support diverse service requirements from different UEs. The network real-time traffic load can be analyzed and utilized by MBS to adaptively form and operate temporary VSCs. Also, highly directional radio beams can be generated to effectively cover these VSCs. Instead of installing fixed SBS, the cell head (CH) in each VSC, which is going to collect the intra-cell traffic and relay to the MBS, can be adapted in real-time. In order to further reduce the co-channel interference, the collaboration between the unlicensed and licensed bands can be

developed. The intra-cell communication in each VSC and truck-link communication between the CH and MBS could be assigned to the unlicensed and licensed bands, respectively.

In order to achieve the overall goal, we divide the topic into three key sub-topics as follows. Firstly, we focus on the enabling techniques for the adaptive virtual small cell formation according to traffic conditions. Secondly, the protocol conversion for data transmission across the licensed and unlicensed band at CHs is studied. As a result, the CHs would be able to aggregate traffic from other devices in the unlicensed band and communicate with MBS in a licensed band. Thirdly, we design adaptive hybrid beamforming (HBF) algorithm based on the proposed VSCs system mode, which is going to guarantee that the virtual small cells with changing location and radius can always be effectively covered.

**Deep Learning based Network Situation Prediction:** With dramatically increased device density and network complexity, real-time operation of 5G HetNets becomes extremely challenging in meeting the stringent requirements of all devices with very limited radio resources and hardware constraints. Accurate prediction of cellular traffic and user distribution would facilitate carriers to schedule resources and cluster users, so as to ensure the overall quality of service and network performance and reduce unnecessary operation cost by allocating energy and bandwidth tightly based on the future traffic demand. Therefore, prediction of network situations such as spectrum availability, mobility and QoS are also explored to facilitate the real-time network operation of 5G HetNets.

Massive information collected from a large number of mobile devices, including user location, traffic requirement and service type, can be utilized to analyze and predict network dynamics. Deep neural network (DNN) that is able to capture temporal and spatial dependencies in sequential data due to its multiple hidden layers and hierarchical feature extraction [30], can be explored. Based on the analysis of the collected historical data, a machine-learning model could be utilized to achieve traffic and radio resource consumption prediction. In this theme, machine-learning models for network traffic/resource prediction are going to be developed. These predicted information of network situation can then be used to achieve situation-dependent network operation, such as the VSC formation, as well as the resource allocation.

**Multi-Dimensional Intelligent Multiple Access:** As addressed in the previous section, the emerging applications to be supported by ultra-dense HetNet typically require highly dynamic and have diverse requirements on various QoS like data rate, reliability, power consumption and latency. Meanwhile, the base station and different terminals could experience very different resource constraints in terms of power/battery supply and spectrum availability. In achieving diverse QoS with disparate resource constraints, intelligent and efficient multiple access techniques, which are able to flexibly provision and orchestrate multi-dimensional resources to continuously adapt to the current state and requirements of the wireless environment, need to be investigated.

In order to keep up with the varying requirements and available resources, the overall network experience requirements should be evaluated through real-time data analysis. A multi-dimensional intelligent multiple access technique could be developed based on the situation-aware discovery. It should be able to maximize the overall system requirements and minimize the non-orthogonality of the user devices in the multi-dimensional domains because that higher degree of non-orthogonality would directly incur higher signal processing burden to reconstruct signal orthogonality at receivers.

**Deep Reinforcement Learning-based Resource Allocation:** Resource allocation is a typical optimization problem in ultra-dense HetNets. Most existing research relied on traditional optimization methods, such as graph theory and optimization decomposition, to solve this optimization problem. However, the traditional optimization techniques highly depend on tractable mathematical models, which may not be able to capture the practical communication scenarios. Meanwhile, the resource allocation problem in ultra-dense HetNet is quite complex, and so the computational complexities of using traditional optimization algorithms would be extremely high.

As a model-free technology, deep reinforcement learning (DRL) has been a promising solution for optimizing the system performance of wireless communication networks. Also, reinforcement learning can interact with an unknown environment through exploration and exploitation [31]. Appropriate DRL models could thus be selected for the resource allocation in multi-dimensional multiple access operation, in order to further reduce the management com-

plexity and operation latency of ultra-dense networks. The target of the DRL based resource allocation scheme is to find the optimal resource allocation policy that can maximize long-term rewards.

**Capacity Enhancement of Trunk-Link:** The truck-link quality between SBSs (including both fixed SBSs and virtual SBS) and MBSs would impact the performance of the whole ultra-dense HetNet directly. When a large number of user devices request a high data rate simultaneously, there will be a high capacity demand, leading to a huge burden on the trunk-link. Therefore, an advanced transmission scheme for trunk-link should be designed to meet the data traffic explosion of trunk-link by fully utilizing the dynamic multi-dimensional resources.

In achieving these goals, advanced spatial transmission techniques, including massive MIMO can be explored in combination with NOMA. By using massive MIMO, a novel transmission scheme can be used for trunk-link to achieve an extremely high data rate. As a benefit, many users can share the same time-frequency radio resource by spatial separation, while the beam-formed transmission would also minimize the potential co-channel inferences. In addition, the principle of NOMA can be borrowed to aggregate the trunk-link traffic and further improve network capacity. The parallel data streams of one user can be modulated simultaneously and partially overlapped on a group of resource elements through a sparse spreading code.

## 1.4 Technical Contributions of the Thesis

The main contributions of this thesis are summarized below:

- To improve the spectrum and power efficiency of ultra-dense networks, a virtual small cell (VSC) design for 5G and beyond networks is proposed in Chapter 3. Different from the traditional small cell, there is no fixed small cell base station in VSC and the VSC are formed adaptively according to traffic conditions and service requirements. In order to reduce the signaling overhead, appropriate mobile devices in each cell are selected as cell head (CH) candidates and serve as the virtual SBS in turn. The CH aggregates intra-cell traffic in the unlicensed band and then relays the combined traffic to an MBS

in the cellular band. By offloading user devices to the unlicensed band, VSC can reduce the co-channel interference. Furthermore, a hybrid beamforming (HBF) scheme is designed to cover these VSCs based on massive MIMO technique with a large scale antenna array. Meanwhile, the total power consumption is minimized under constraints of maximum transmit power and the required throughput rate of each user. Both the mathematical analysis and simulation results demonstrate that VSCs can increase 50% power efficiency while providing flexibility and reduced cellular load, compared with macrocell only deployment and traditional fixed small cells scenario.

- To further improve cost efficiency and reduce the network latency, one LSTM based hotspot prediction method is proposed in Chapter 4. In the developed VSC, both cell formation and beamforming design cause increased operational complexity and latency. Therefore, we proposed one long short term memory (LSTM) based prediction method to predetermine the location of hotspots in advance, so as to reduce the latency from supporting cell formation and beamforming. More specifically, the historical location map of users is divided into several two-dimensional (2D) zones into the spatial and temporal domains. Different from several LSTM, in which every zone has its own LSTM, we used all of these 2D zones to train the one LSTM neural networks to enhance the training sample diversity and reduce the overfitting. The output is the UE numbers of all grids and so the hotspot can be determined by analyzing the predicted network-level UE density map. The simulation results demonstrate that the accuracy of one LSTM is similar to that of Convolutional LSTM with a simple structure.
- To realize efficient resource utilization, a novel multi-dimensional intelligent multiple access (MD-IMA) scheme is proposed in Chapter 5. The proposed MD-IMA is achieved by maximizing the separation distance among the multi-dimensional resource blocks allocated to co-existing devices, which could be in frequency, time, space, power and code domains. Different from the traditional orthogonal multiple access (OMA) and NOMA, the proposed MD-IMA is able to simultaneously share resources in as many domains as possible, while separate the co-existing devices with low interference cancellation. A new concept named integrated-quality-of-system-experience (I-QoSE) is also proposed

to integrate diverse QoS into one metric. It can be adaptively adjusted according to diverse and time-varying services and applications and then used to evaluate the overall performance of the MD-IMA. In light of the implementation constraint, the minimization of non-orthogonality transmission, which is ignored in the existing works, is also imposed in MD-IMA resource allocation. The objective of the resource allocation in MD-IMA is therefore to maximize the overall network performance but also minimize the non-orthogonality (NO) transmission under constraints of maximum power consumption and the QoS of each user. Simulation results demonstrate that the proposed achievable I-QoSE gain of MD-IMA over NOMA and OMA are approximate 15% and 18%, respectively.

- To further reduce the computational complexity in traditional optimization algorithms, a model-free deep reinforcement learning (DRL) enabled method is proposed in chapter 6 to solve the resource allocation problems for MD-IMA. A pre-trained DRL is proposed to orchestrate multi-dimensional resources to continuously adapt to the varying and diverse state and requirements of the wireless environment. In the proposed scheme, the I-QoSE that combining diverse QoS is going to be predicted through the LSTM neural network based on the historically collected information. On the basis of the predicted I-QoSE, the concrete DRL design is further introduced to solve resource allocation problems of the MD-IMA system. Value-based and actor-critic-based algorithms, namely deep Q-learning (DQL) and deep deterministic policy gradient (DDPG), respectively, are both implemented. The simulation results illustrate that the proposed DDPG based power allocation outperforms DQN and conventional model-based algorithms with lower time consumption, such as fractional programming method. Specifically, the DDPG based algorithm can improve around 17% and 35% WEE than that of WMMSE and FP, respectively. The time cost of DRL based method is 10 times and 100 times faster than that of FP and WMMSE.
- To improve energy efficiency and achieve green networking, a Software-Defined Networking (SDN) enabled 5G-Vehicular Ad Hoc Network (5G-VANET) is investigated in Chapter 7, which couples the high data rates of VANET with the wide coverage area of

5G. In this integrated architecture, SDN can provide a global view to adaptively cluster vehicles only when needed. In order to reduce the signaling overhead, one vehicle in each cluster is selected as a cell head to support aggregated traffic and another one vehicle is selected as a backup to guarantee seamless communication. To ensure the capacity of the trunk link between the gateway and base station, a novel transmission scheme, Non-orthogonal Multiplexed Modulation (NOMM), is also proposed. In this scheme, the aggregated data stream is divided into several multi-layers and use sparse spreading code to partially superpose these modulated symbols on several resource blocks. The simulation results show that the energy efficiency of the proposed NOMM is 1.3-2 times than that of the traditional orthogonal transmission scheme by carefully designing the sparse code of NOMM.

## 1.5 Thesis Outline

The rest of the thesis is organized as follows:

In Chapter 2, the research background, related to our topics, is briefly given, including the key technologies of 5G, the literature survey of deep learning in wireless networking.

In Chapter 3, the cellular network assisted virtual small cell (VSC) is investigated for cost-effective and reliable service provisioning in 5G ultra-dense networks. The overall system model of the dynamic VSC design in 5G ultra-dense networks is given first. Based on the network model, the K-means clustering based VSC forming algorithm is discussed and the protocol conversion for traffic aggregation at CHs is introduced. The details of optimal HBF design are also elaborated. Finally, link-level simulation is conducted in MATLAB to evaluate the performance of the proposed VSCs architecture, including both cell formation collection and beamforming design.

One LSTM based hotspot prediction method is studied in Chapter 4 to improve cost efficiency and reduce the operation latency of ultra-dense HetNet. Firstly, the system model of the hotspot prediction based VSCs is given. Afterward, the problem of hotspot prediction is formulated to predict the UE numbers of each grid and then three different LSTM based hotspot prediction methods are elaborated. A real dataset of telecommunication is used to evaluate the



proposed LSTM based prediction method. Simulation results regarding the root mean square error (RMSE) performance of one LSTM based network is compared with that of three benchmarks. Finally, the system performance of VSCs based hotspot prediction is compared with the traditional small cells and VSC with K-means scenarios.

The novel multi-dimensional intelligent multiple access (MD-IMA) scheme is presented in Chapter 5, which fully utilizes the available resources in multi-domains to ensure the diverse and varying QoS. The network architecture and system model of the proposed MD-IMA are described firstly. Then, the resource allocation problem for achieving the balance between overall network requirements and the receiver complexity is formulated as an optimization problem. To reduce the computational complexity, it is converted into three sub-optimization problems and jointly solved by using an alternative optimization algorithm. Finally, the I-QoSE and NO performance of the proposed MD-IMA are compared with that of the OMA and NOMA scenarios.

Based on the system architecture of MD-IMA proposed in Chapter 5, a DRL based power allocation is further developed in Chapter 6. By using deep learning, the overall network requirements can be predicted in advance and the complex resource allocation can be solved without mathematical models and so reduce the computational complexity. A DRL enabled resource allocation system architecture is firstly developed, where the base station is treated as the agent and the MD-IMA network is the environment. Then, the I-QoSE prediction is achieved by using one LSTM to learn the network requirements. Based on the predicted I-QoSE, the two different DRL based power allocation methods, DQN and DPPG, are elaborated. Finally, the performance of the DRL-based power allocation methods is evaluated by comparing it with that of traditional optimization-based algorithms.

In Chapter 7, SDN enabled 5G-VANET is studied to support the increasing vehicle traffic and improve management. The overall network architecture of 5G-VANET is given first, and then the adaptive vehicle clustering scheme and dual CH selection method are proposed to reduce the signaling overhead and guarantee seamless communication, respectively. To further improve the capacity of truck-link, non-orthogonal multiplexed modulation (NOMM) is proposed. The energy efficiency for the traditional orthogonal transmission scheme and the proposed NOMM are analyzed. Finally, the simulations are used to evaluate the proposed

NOMM in terms of energy efficiency.

Lastly, all the contributions presented in the previous chapters are concluded in Chapter 8. The plan for future research is discussed in this Chapter as well.

## Chapter 2

# Background on Enabling Technologies of Ultra-Dense HetNets

The ultra-dense HetNet is presented as a new network paradigm evolution to the 5G wireless networks to address the exponentially increasing traffic demands. However, the ultra-dense and heterogeneous deployment introduces new technical challenges such as severe interference, complicated radio resource allocation, significant signaling overhead, a significant increase in energy consumption, and degraded QoS. To overcome these challenges and achieve the performance requirements in future wireless networks, such as beyond 5G and 6G, there is a need to combine ultra-dense HetNets with other 5G enabling technologies and artificial intelligent (AI) technologies to design intelligent and efficient operation and management techniques for better performance of the overall networks. Hence, in this chapter, a fundamental introduction to 5G key technologies, including the Massive MIMO, NOMA, and MIMO-NOMA, are firstly elucidated. Then we present a comprehensive survey on deep learning (DL) enabled network prediction and resource allocation for wireless communication systems.

### 2.1 Key Technologies of 5G

To support the explosive proliferation of smart devices and drastically increased data traffic, 5G networks are expected to provide 1,000-fold capacity enhancement [32]. With constrained radio resources, increasing user density and network complexity, the success of 5G networks

relies on highly efficient technologies, including massive MIMO, highly directional beamforming, NOMA and unlicensed band operation.

### 2.1.1 Massive MIMO

Massive MIMO is a promising technology of 5G that upgrading from MIMO technology. The Massive MIMO is achieved by using a large scale antenna array with a few hundred antennas simultaneously at the macro base station to exploit the spatial domain multiplexing gain [5]. In this way, Massive MIMO can support tens of user terminals (UEs) at the same time without consuming extra scarce resource of frequency, time and power [6]. Several studies illustrate that the Massive MIMO can significantly improve spectrum efficiency, latency and reliability [33]. The specific advantages of Massive MIMO are listed below:

- **Improve Spectrum Efficiency:** The capacity of the Massive MIMO system is 10 or more times than the traditional MIMO system due to the spatial multiplexing gain. In fact, thanks to the large antenna array, highly direction beamforming can be formed to concentrate the energy into a small area to further improve the energy efficiency [34].
- **Reduce Latency:** Ultra-low latency is a critical requirement of the 5G networks. However the latency is inevitable if the received signal strength is not large enough. The received signal attenuation mainly caused by both large-scale and small-scale fading. If the receiver (UE) is caught in a fading dip, then it has to wait until the transmission channel changed to good enough that can successfully receive the data. By using a large number of antennas, Massive MIMO can form narrow beamforming for each UEs to avoid fading dips and so reduce the latency.

### 2.1.2 NOMA

Non-orthogonal multiple access (NOMA), which shifts the multiple access from orthogonal to non-orthogonal approaches, is one of the promising methodologies to support massive connectivity in 5G networks [35]. Comparing with the traditional orthogonal multiple access technologies, NOMA can support many more users via partially superimposed multiple users on

the same radio resource blocks, such as time slots, subcarriers or beams. Recently, several NOMA schemes have attracted lots of attention, and we can generally divide them into two categories: power domain multiplexing and code domain multiplexing.

- Power-domain NOMA

Power-domain NOMA was formally proposed by NTT DOCOMO in 2012 Aug. The principle behind the power-domain NOMA is adding power domain multiplexing on the transmitter side to multiple users and using successive interference cancellation on the receiver side to realize multi-user detection [36]. Although the receiver complexity will be increased by adopting successive interference cancellation successive interference cancellation (SIC), the non-orthogonal transmission can increase spectrum efficiency.

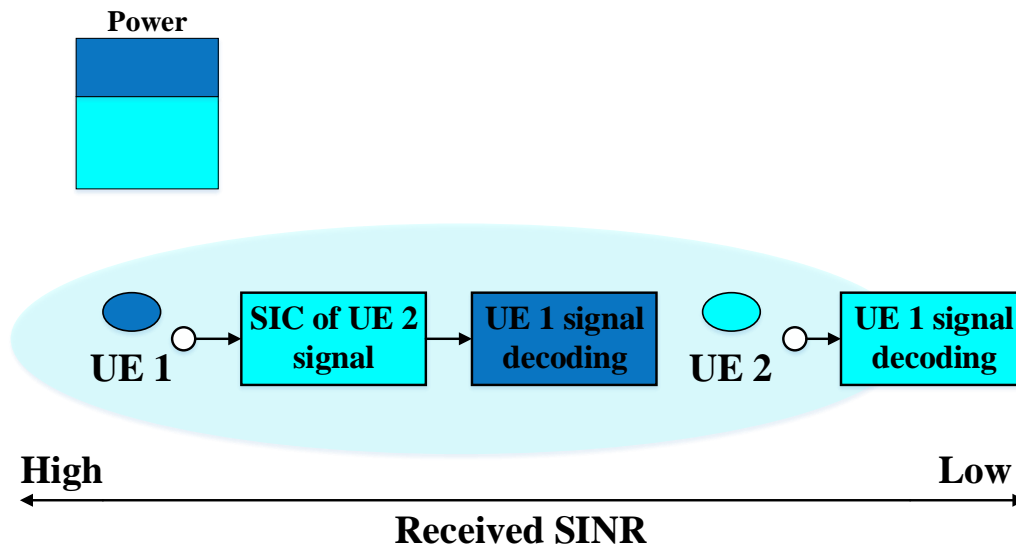


Figure 2.1: Illustration of NOMA via power domain multiplexing

In power-domain NOMA, sub-channels are orthogonal and there is no interference between them, because orthogonal frequency-division multiplexing (OFDM) is still used in sub-channels. However, each subchannel is no longer allocated by one user but shared by multiple users. In the same sub-channel, different transmission power level allocates to a different user. Therefore, inter-user interference is introduced and this is the reason why SIC should be used at the receiver side. Fig. 2.1 shows that the receiver subtracts the decoded stream from the received vector in every step of the decoding process. The de-

tection order detects the symbols in order of decreasing signal strength. The system-level simulation results show that both the capacity and cell-edge user throughput performance of power-domain NOMA is improved, compared to that of OMA [35].

- Code-domain NOMA

Sparse code multiple access (SCMA) is a famous kind of code-domain NOMA. SCMA directly maps different bit-streams to different sparse codewords, as illustrated in Fig. 2.2, where each user has a predefined codebook (there are 6 users and 4 orthogonal resources). All codewords in the same codebook contain zeros in the same two dimensions, and the positions of zeros in different codebooks are distinct to facilitate the collision avoidance of any two users [37]. For each user, two bits are mapped to a complex codeword. Codewords for all users are multiplexed over four shared orthogonal resources (e.g., OFDM subcarriers).

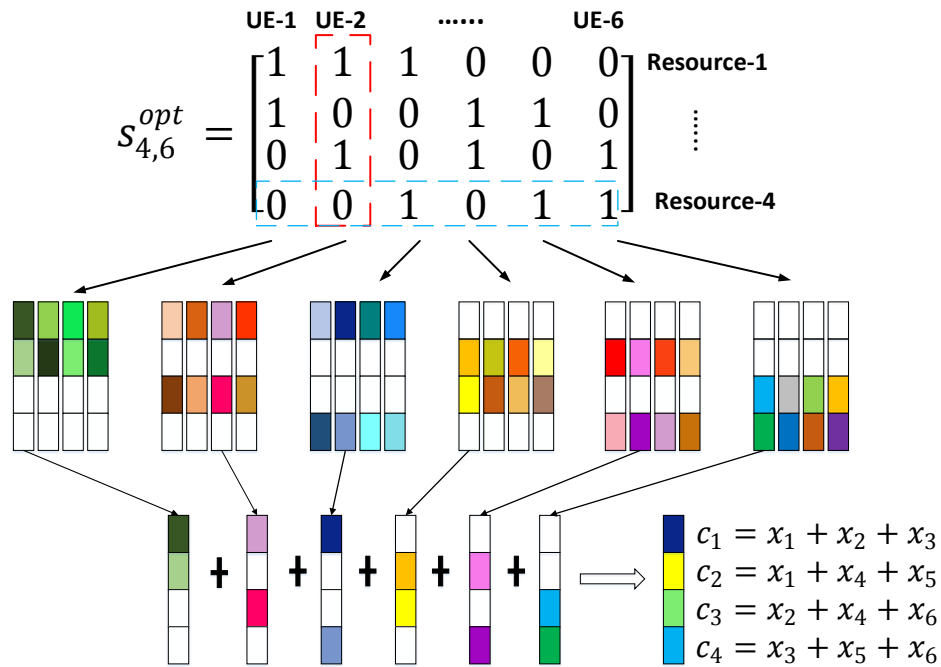


Figure 2.2: SCMA encoding and multiplexing.

SCMA is designed to generate codebooks, which brings the “shaping gain”. Here, “shaping gain” is the gain in the average symbol energy when the shape of a constellation is changed. In general, the shaping gain is higher when the shape of a constellation is

closer to a sphere, and the maximum achievable shaping gain by the optimization of a multi-dimensional constellation is 1.53 dB [38]. For the concatenated approach in high modulation order, the multi-dimensional constellation can be optimized to obtain shaping gain, and then codebooks are generated based on the multi-dimensional constellation. The SCMA codebook design is a complicated problem since different layers are multiplexed with different codebooks [39]. As the appropriate design criterion and specific solution to the multi-dimensional problem are still unknown, a multi-stage approach has been proposed to realize a suboptimal solution. Specifically, an  $N$ -dimensional complex constellation with  $M$  points (which is called the mother constellation) is first optimized to improve the shaping gain, and then some codebook-specific operations are performed to the mother constellation to generate the  $N$ -dimensional constellation for each codebook. Three typical operations are phase rotation, complex conjugate, and dimensional permutation of the constellation [36]. In the generated  $N$ -dimensional constellations after codebook-specific operations, each  $N$ -dimensional constellation point is multiplied with a projection matrix to generate a  $K$ -dimensional codeword ( $K \gg N$ ), which has  $N$  non-zero elements from the components of the  $N$ -dimensional constellation point. In this way, codebooks with  $M$  codewords can be obtained.

### 2.1.3 Massive MIMO-NOMA

In order to further improve the system capacity and spectrum efficiency, multiple-input multiple-output (MIMO) can be combined with NOMA. As illustrated in Fig. 2.3, multiple beams are formed in the spatial domain by using multiple antennas at the transmitter and each beam adopts basic NOMA. Receiver adopts two interference cancellation technologies to recover signals: SIC is used to suppress the intra-beam interference and interference rejection combining (IRC) is used to suppress the inter-beam interference. However, the performance of IRC is impacted by the spatial correlation between the own and interference users. Thus, in order to improve the spectrum efficiency, and appropriate user selection algorithm transmitter side is required. Random beamforming and opportunistic beamforming (OBF) are proposed as possible solutions in [40] and [39] respectively. In [39], the evaluation results show that NOMA

with OBF can improve system performance. Furthermore, the combination of NOMA with

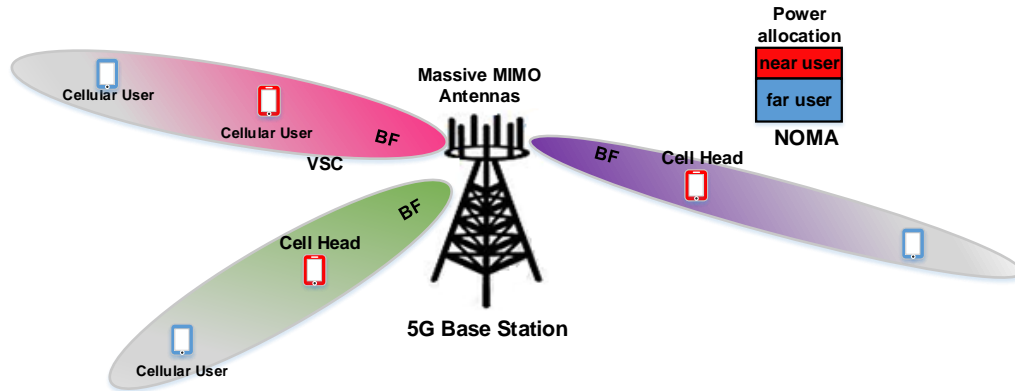


Figure 2.3: Structure of MIMO-NOMA

closed-loop (CL) single-user MIMO (SU-MIMO) is discussed in [37] and the combination of NOMA with open-loop SU-MIMO is discussed in [41]. In [37] the system-level simulation results show that both the average and cell-edge throughput performance of NOMA with CL SU-MIMO is better than that for OMA. The performance of the SIC-based receiver is impacted by error propagation. Therefore, how to model the error propagation for the SIC receiver is the key factor. Three available model method of error propagation is proposed in [37].

The combination of NOMA and Massive MIMO brings several major technical challenges for multi-dimensional resource allocation. Firstly, due to channel condition variation over time and frequency, scheduling users into appropriate channels in time and frequency domains highly improves the communication quality. Moreover, NOMA requires user pairing, where typically one near user and one far user are scheduled as a user pair to achieve multiplexing in power domain [42]. Another critical technique to operate the NOMA-enabled MIMO is to select the best subset of antennas due to the limited number of available RF chains. Hence, it is important to schedule users and select antennas jointly for multi-dimensional resource allocation in a Massive MIMO-NOMA system.

There are a few recent studies on user scheduling and antenna selection in NOMA and MIMO systems. In [43], user pairing algorithms are developed for two NOMA scenarios, with only one frequency band is considered. The technique proposed in [44] schedules two users with a large channel gain difference and high correlation as a user pair, with a focus on the



NOMA user pairing mechanism. In [45], a joint antenna selection and user scheduling (JASUS) algorithm is proposed. This algorithm finds the desired antenna and user subset by sequentially excluding the antennas and users which generate a minimum contribution to the system performance. A norm-based joint transmit and receive antenna selection (NBjTRAS) algorithm is developed in [46]. It searches all candidate transmit and receive antennas exhaustively for a subset with the largest channel norm. Nevertheless, these two joint antenna selection and user scheduling algorithms have very high complexity and can only be applied to scenarios with small numbers of candidate antennas and user sets. It is therefore difficult to apply the existing techniques to a Massive MIMO-NOMA system for allocating multi-dimensional resources.

## **2.2 Deep Learning enabled Network Prediction and Control**

The increasing diversity and complexity of mobile network architectures make it difficult to monitor and manage a large number of network elements. Therefore, machine intelligence is introduced into future mobile networks to predict the network situation and achieve intelligent network management. ML can systematically mine valuable information from traffic data and automatically discover correlations, otherwise the correlations may be too complicated to be extracted by human experts [47]. As the flagship of machine learning, deep learning has achieved excellent performance in areas such as computer vision and natural language processing (NLP) [48]. Network researchers have also begun to recognize the power and importance of deep learning and are exploring its potential to solve specific problems in the mobile network field [49].

### **2.2.1 Deep Learning based Network Prediction**

Recent years have witnessed a considerable amount of studies dedicated to mobility prediction schemes. In [50], according to the statistics of user occurrence frequency, the most distinctive sequential mobility pattern of users is extracted. However, this method fails to predict changing sequential mobility patterns when the users changed their mobility routines. Another popular method is using principal component analysis (PCA) and extracting eigenbehaviors [51] or eigenplaces [52], which features a two-layer shallow structure. The eigenbehavior

and eigenplaces of user's mobility and traffic are determined to extract a common underlying structure of users' daily mobility patterns. Nevertheless, the limited number of eigenbehavior and eigenplaces may not be sufficient to fully represent the mobility patterns of different users. Therefore, a 'deeper structure', such as the structure of deep neural network, should be used to address these challenges. By introducing multiple hidden layers between the input and output layers, deep neural network (DNN) is more powerful and flexible to predict complex mobility patterns due to the combined capability of multiple hidden layers [53]. In addition, by employing hierarchical feature extraction, deep learning can capture temporal and spatial dependencies in sequential data, while minimizing the data pre-processing effort [54]. Furthermore, it makes possible for deep learning to make inferences within milliseconds by using Graphic Processing Unit (GPU)-based parallel computing [55].

Therefore, the deep neural network is becoming a critical tool for user mobility analysis. In [56], deep learning was adopted first to recover the social network representations of users and then a basic recurrent neural network (RNN) and Gate Recurrent Unit (GRU) models were employed to discover mobility patterns of the individual user at different levels. In [57], an online learning scheme was proposed to train a hierarchical convolutional neural network (CNN), which can process data stream parallelly. However, most of the previous works are focused on predicting the individual trajectories instead of forecasting the network-level user distribution, which is more valuable for network operation. Since fluctuation of user density is influenced by short and long term behaviors, the long short term memory (LSTM) neural network, a kind of deep RNN, is adopted to predict the number of UEs in every small zone due to its excellent capability to memorize long-term dependencies. By using the LSTM neural network, the proposed method can also overcome the gradient problem that plagues conventional RNNs and captures long-short term temporal and spatial dependencies without suffering from the optimization hurdles [58].

### **2.2.2 Deep Learning based Network Control**

In recent years, deep learning has been a promising technology for optimizing the system performance of wireless communication networks, due to its model-free and the nature of the com-

plaint with optimizations in practical communication scenarios [59]. Furthermore, reinforcement learning has received wide attention because it can interact with an unknown environment by exploration and exploitation [47]. On the other hand, by introducing multiple hidden layers between the input and output layers, deep neural network (DNN) is more powerful and flexible to predict complex system performances, such as sum-rate and power consumption, due to the combined capability of multiple hidden layers [53]. The objective of the resource allo-

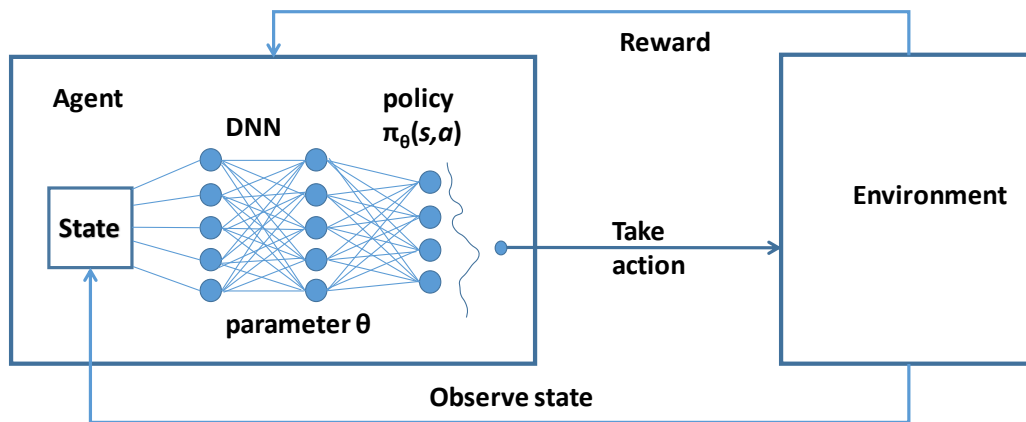


Figure 2.4: General structure of DRL based network control

cation optimization problem is to maximize the performance, including the sum-rate, energy efficiency and power consumption. The optimization of resource allocation, such as power allocation and subchannel assignment, is modeled as a deep reinforcement learning task, which consists of an agent and environment interacting with each other, as shown in Fig.2.4. The BS/AP can be regarded as the agent and the performance of the communication network is the environment. We define the state space is  $S$ , action space is  $A$  and the reward function is  $R$ . At time step  $t$ , based on the observed state  $s^t \in S$  of the environment, the agent takes an action  $a$  from the action space  $S$  to allocate resource according to the resource allocation policy  $\pi$ , where the policy is learned by an attention-based neural network. Then, the current reward  $r^t$  and the next state  $s^{t+1} \in S$  are obtained from environment. The target of the network is to take the optimal resource allocation and network control which can maximize the expected reward.

## **2.3 Chapter Summary**

In this chapter, the background concepts, key technologies and models used in the thesis are reviewed. At the beginning of this chapter, a brief introduction of 5G key technologies is given, emphasizing the Massive MIMO, NOMA and MIMO-NOMA. After that, the background and literature review of deep learning-based network prediction and control are also presented.

## Chapter 3

# Cost-Effective Virtual Small Cell for Ultra Dense HetNet

In order to exploit the potential capacity of 5G, the deployment of ultra-dense small cells is an approach that can dramatically increase the radio resource reuse factor and network capacity. However, network densification with a large number of small cells brings challenges due to increased network complexity, deployment cost and inter-cell interference. In this chapter, a new 5G architecture with virtual small cells (VSCs), which are dynamically formed by grouping a number of user devices in close proximity and adapted according to traffic condition, is proposed to improve the cost and energy efficiency compared with the traditional fixed deployment of small cells. In each virtual small cell, one mobile device is selected as a cell head (CH) to aggregate intra-cell traffic using unlicensed band transmissions and then communicates with its macro-cell base station in a licensed band through beamformed transmission, which reduces the inter-cell interference and improves spectrum efficiency. In this chapter, a highly directional hybrid beamforming technique is employed to enable a dedicated inband fronthaul link for VSC. Our work focuses on how to design adaptive beamforming to minimize the transmit power under throughput requirements and power constraints. Both the mathematical analysis and simulation results demonstrate that VSCs can increase power efficiency around 55% while providing flexibility and reduced cellular load, compared with the traditional fixed small cells scenario.

## 3.1 Introduction

With the explosive proliferation of smart devices, the dramatic increase of mobile data traffic and emerging applications particularly the Internet of things (IoT), the upgrading of cellular networks and deployment of new infrastructures to support the needed data increase is inevitable in 5G networks [60]. As a result, heterogeneous networks (HetNet) with overlaid densified small cells deployed on top of cellular networks are widely considered as a promising solution for 5G. In the meantime, the increasingly diversified network applications, such as online games, connected vehicles and intelligent machines, requires both massive capacity and diverse quality of service (QoS) provisioning [61].

Small cells (SCs) improve the overall network capacity by installing many small base stations with reduced cell sizes and transmission distance. However, fixed deployment of a large number of small cells in 5G HetNet is neither cost-effective nor energy-efficient. To support such ultra-dense small cell networks, direct connections between SCs and macro base stations (MBS) become more complicated due to the deployment of excessive optical fronthaul and backhaul links [11]. Maintaining a large number of small cells also requires tremendous computational resources and signaling overhead, which places a heavy burden on network management [62]. In addition, dense SCs could introduce severe inter-cell interference due to spectrum reuse, which is the key limiting factor of cellular network capacity [63]. Moreover, diverse services will be supported by 5G and beyond networks with the co-existence of heterogeneous user devices (UEs). The wide variety of service types also require different delay QoS provisioning[64].

Therefore, grouping multiple user devices to form flexible virtual small-cells within the integral cellular network infrastructure is envisioned as a cost-effective alternative. In [65] and [66], the authors proposed to use directive beams to support dense traffic areas adaptively. However, users in each beam still communicate with MBS in the cellular band, which introduces additional co-channel interference and signaling overhead. Therefore, we propose a cellular network assisted virtual small cell (VSC) as a solution for cost-effective and reliable service provisioning in 5G ultra-dense networks. Specifically, the VSCs are formed adaptively under the coordination of cellular MBS when needed. Within the VSCs, appropriate mobile

devices are selected as the cell head (CH) candidates and serve as virtual SBS such that the installation cost of fixed SBSs could be reduced[67]. These CHs aggregate the intra-cell traffic in the unlicensed band and then relay the combined traffic to the macro-cell base station (MBS) through cellular band [3]. By utilizing different frequency bands, the inter-cell interference is reduced dramatically with improved service quality at the same time.

Our overall objective of this topic is to develop an adaptive wireless infrastructure with the extremely high spectrum and cost efficiency, while the diverse service requirements from different UEs in terms of data rates and QoS can be met at the same time. In order to achieve the overall goal, we divide the topic into three key sub-topics as follows. Firstly, we focus on how to realize the adaptive virtual small cell formation according to traffic conditions and propose a K-means clustering based VSC formation scheme. Secondly, as the CHs aggregate traffic from other devices in the unlicensed band and communicate with MBS in a licensed band, the protocol conversion for data transmission across the licensed and unlicensed band at CHs is also studied for the realization of the VSC. Thirdly, we need to study how to realize the adaptive hybrid beamforming (HBF) based on the proposed VSCs system model so that the virtual small cells with changing location and radius are always effectively covered. Considering that the limited battery capacity is a bottleneck of UE and the power efficiency is essential for MBSs, the object of the beamforming design is to minimize the total power consumption under constraints of maximum transmit power and the required throughput rate of each user.

Specifically, the contributions of this work are summarized as follows:

1. We propose virtual small cell (VSC) design for 5G and beyond networks in this topic to reduce the co-channel interference by utilizing an unlicensed band within VSCs and beamformed trunk link transmission between MBS and VSCs. Specifically, VSC is formed adaptively according to traffic conditions and service requirements. A K-means clustering based VSC formation scheme is proposed in this work, and the corresponding protocol conversion for data transmission across unlicensed and licensed networks at cell head (CH) is developed. Then, by using massive MIMO techniques, the large scale antenna array is adaptively employed in this work for a highly directional beam to cover VSCs adaptively. In each VSC, appropriate mobile devices are selected as cell head (CH) candidates and serve as the CH in turn. The CH then aggregates intra-cell

- traffic in the unlicensed band and relays the combined traffic to an MBS in the cellular band.
2. We propose an optimization-based beamforming scheme to adaptively cover the virtual small cells with low latency. The key idea of the proposed solution is to minimize the total power consumption under constraints of maximum transmit power and the required throughput rate of each user. The problem above is further divided into two sub-optimal problems to reduce the computational complexity of the proposed optimal method with comparable performance.
  3. We use hybrid beamforming (HBF) scheme, combining the digital and analog beamforming, at the MBS to improve both cost and power efficiency of VSC. Based on the location information of the predicted hotspots, highly directional beamforming can be designed to cover these hotspots. Only digital beamforming scheme requires each antenna has its own Radio Frequency (RF) chain. However, the cost-prohibitive and power-hungry make it is not realistic for the massive MIMO system to implement full-digital beamforming. In a hybrid beamforming scheme, one RF chain can connect with several antennas, which will reduce the cost and circuit power consumption. The analog beamforming design can be achieved by adjusting the phase shifter to harvest the large array gain in massive MIMO systems.

The remainder of this chapter is organized as follows. Section 3.2 presents the system model of the dynamic VSC design in 5G ultra-dense networks. Based on the network model, the K-means clustering based VSC forming algorithm is then proposed and the protocol conversion for traffic aggregation at CHs is given in Section 3.3. The details of HBF design are elaborated in Section 3.4. Section 3.5 presents our main results regarding power consumption and system performance evaluation of the proposed VSCs architecture, including cell formation and beamforming design. Finally, the conclusion is drawn in Section 3.6.



## 3.2 System Model

### 3.2.1 Network Architecture

In order to support high system capacity with low deployment cost and signaling overhead, VSC design is proposed in this chapter to realize cost-effective 5G networks. Regarding the system model, we consider a heterogeneous network architecture consisting of one macro cell and  $S$  virtual small cells, where  $K$  users are distributed in the coverage of the macro cell, as shown in Fig. 3.1. The MBS decides to form VSCs when the target areas experience high load or heavy user density. The signaling of the macro-cell load can be exchanged periodically over the X2 interface between the MBSs. Moreover, the MBS is able to find remaining free sub-channels by monitoring ongoing transmissions or by collecting reports from users [68]. This way, the MBS could make the decision of VSC formation for a temporary high load area, and allocate available free sub-channels for intra-VSC transmission.

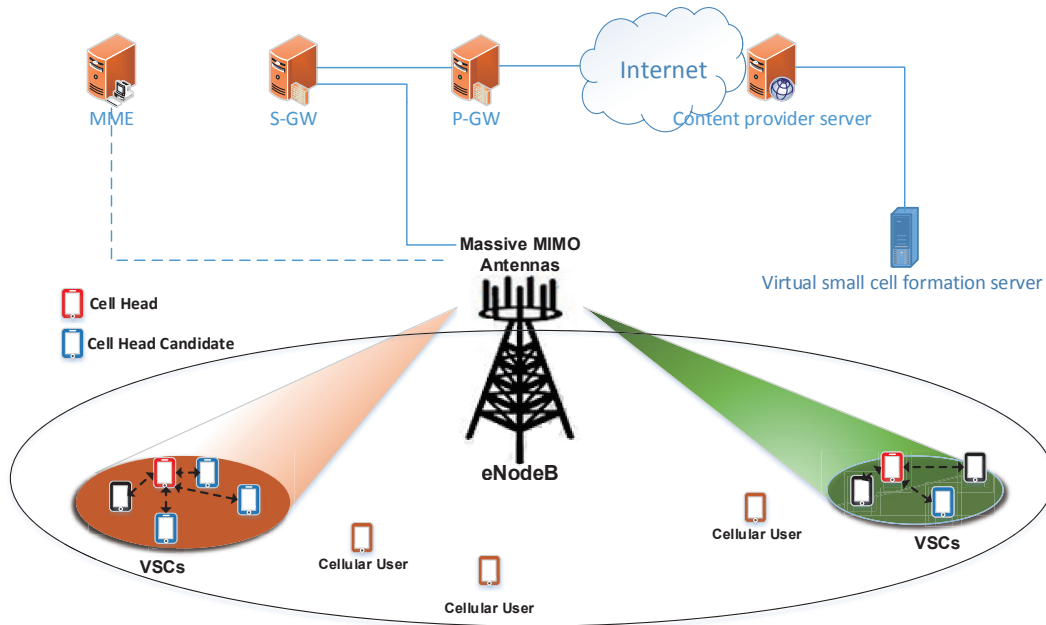


Figure 3.1: A two-tier network architecture consisting of one macro-cell and  $S$  virtual small cells.

Noted that compared with traditional small cells, there is not fixed access point in VSC. We assume that  $K$  users, equipped with  $N_K$  antennas, are randomly distributed in the macro-cell and one MBS, equipped with  $N_{BS}$  antenna and  $N_{RF}$  RF, is deployed at the center of the

macro-cell. The number of MBS antennas is large enough to achieve the Massive MIMO, which can be used to form a highly directional hybrid beamforming to cover the VSC. In each VSC, several UEs with high battery level and good channel quality is selected as CH candidates (colored in blue) and serve as the CH (colored in red) in turn. The CH should work as a flexible SBS. It aggregates the information from member UEs (colored in black) in VSC by using the unlicensed band and directly communicates with MBS through the beamformed fronthaul [67]. The UEs who have direct connection with MBS can be denoted by  $\mathcal{U} = \{1, \dots, L\}$ , while the others who communicate with CHs are described as  $\mathcal{U}^C$ , where  $\mathcal{U} \cup \mathcal{U}^C = \{1, \dots, K\}$ . There are  $L$  data streams from MBS to CHs. Because the number of data streams represents a lower bound on the number of RF chains, it is convenient to set  $N_{RF} \geq L$ .

### 3.2.2 Information Collection Procedure

The implementation and information collection procedure is described as a flowchart in Fig. 3.2. Note that in order to guarantee the quality of service (QoS) of user applications, the service provisioning of UEs with high latency requirements, such as those that are sensitive to delay, will be removed from VSCs and communicate with MBSs directly.

At the beginning of typical UE initiated HyperText Transfer Protocol (HTTP) data downloading, UEs send the requests to content provider servers through MBSs, and the HTTP requests include the information data  $z$  of the mobile devices, where  $z$  consists of user location information, which can be measured through available reference nodes [69], a charge per unit for distributing data (if serve as CH), and energy levels of the UEs [70]. Content provider server then collects the information of a set of mobile devices (preferably those requested similar content) and sends to the VSC formation server. The VSC formation server then executes K-means clustering-based algorithm to form the VSC using the location information and selects the CH using channel and energy information. The UEs that are not clustered into any virtual small cells will communicate with MBSs directly by themselves.

The content provider then sends requested contents to CHs directly and generates redirection meta-data packages to each intra-virtual small cell UEs. The meta-data package carries the information of unlicensed sub-channel selections, address of CH and the credentials, login

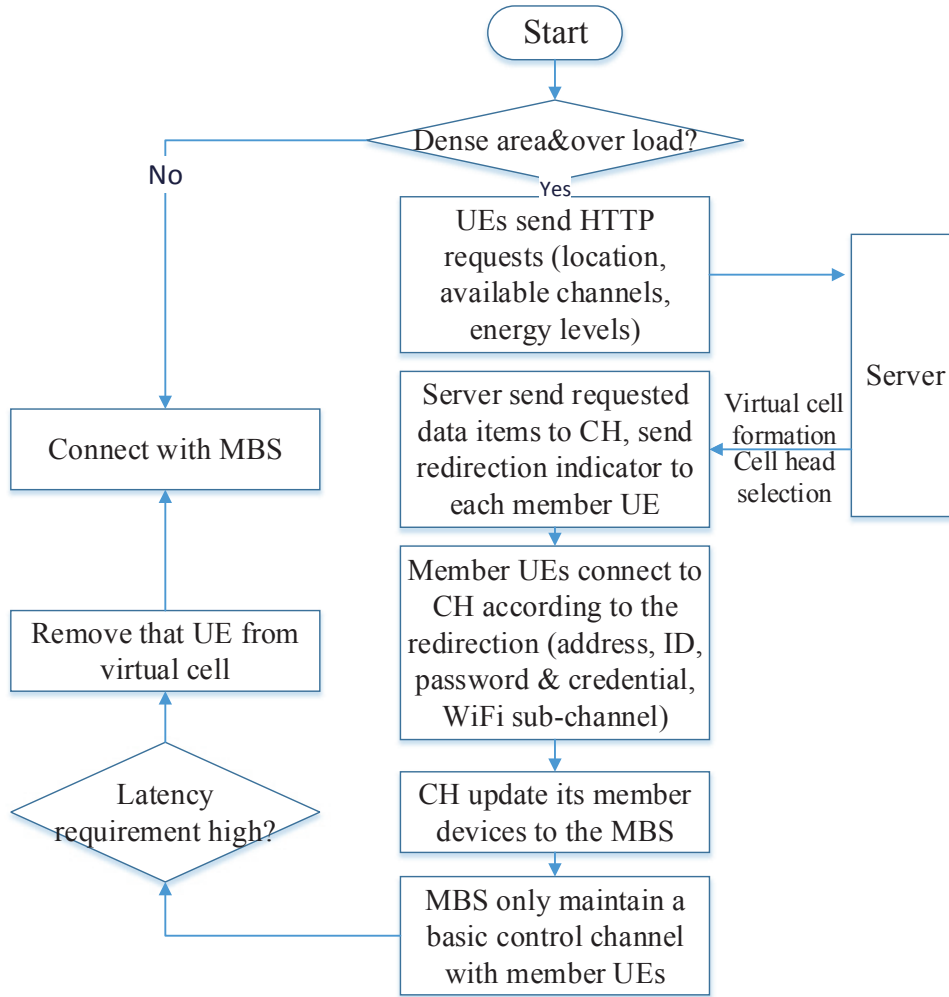


Figure 3.2: The implementation and information collection procedure for VSC formation.

ID/ password for other intra-virtual cell devices to access CH. Afterward, the CH updates its member devices to the MBS and the MBS would only maintain a basic control channel with the member devices to monitor the quality of service (QoS). Other mobile devices then request data from CH and the CH would work as a relay for the VSC. As the CH aggregates traffic in the unlicensed band and transmits high traffic volume with the MBS in a licensed band, both the traffic aggregation procedure across UDN and the resource allocation among different VSCs would be challenging. Therefore in the following sections, the protocol conversion at CHs and the resource allocation scheme for VSC are analyzed and developed.

### 3.2.3 Channel Model for Beamformed Fronthaul

To keep up with the changes in the coverage and location of VSCs, the antenna radiation pattern, including the beamwidth and steering of MBS, should be adjusted adaptively. This adjustment of the antenna radiation pattern will result in channel variation for the beamformed fronthaul link. Therefore, the analysis of the antenna radiation pattern is necessary before the discussion of the channel model for the beamformed fronthaul.

The VSC formation procedure defines the center and optimum radius of the virtual cells. The procedure details of cell formation are given in [66] and this chapter mainly focuses on adaptive beamforming design for VSC. Based on the location information of MBS and VSCs, the vertical steering and the beamwidth of the MBS beamforming can be obtained [65]

$$\begin{aligned}\theta_{ilt} &= -\tan^{-1}\left(\frac{h_{MBS}}{d}\right) \text{ (rad)}, \\ \theta_{3dB} &= 2\left[-\tan^{-1}\left(\frac{h_{MBS}}{d-r}\right) - \tan^{-1}\left(\frac{h_{MBS}}{d+r}\right)\right] \text{ (rad)},\end{aligned}\tag{3.1}$$

, where  $r$  represents the radius of VSC,  $d$ , denotes the distance from the MBS to the center of VSC and  $h_{MBS}$  is the antenna height of MBS. Similarly, the beam width and the steering of beamforming in the horizontal plane can be obtained [65]

$$\begin{aligned}\varphi_{ilt} &= -\tan^{-1}\left(\frac{y-y'}{x-x'}\right) \text{ (rad)}, \\ \varphi_{3dB} &= 2\left[\tan^{-1}\left(\frac{r}{d}\right)\right] \text{ (rad)},\end{aligned}\tag{3.2}$$

where  $(x, y)$  and  $(x', y')$  are coordinates of the center for MBS and VSC, respectively. By using massive MIMO, 5G base stations will be able to steer its radiation pattern with increased spatial selectivity both horizontally and vertically [71]:

$$\begin{aligned}
A_H(\varphi) &= -\min \left[ 12 \left( \frac{\varphi_{tilt}}{\varphi_{3dB}} \right)^2, 30 \right] \text{ dB}, \\
A_V(\theta) &= -\min \left[ 12 \left( \frac{\theta_{tilt} - \frac{\pi}{2}}{\theta_{3dB}} \right)^2, 30 \right] \text{ dB}.
\end{aligned} \tag{3.3}$$

Based on above analysis, the antenna radiation pattern of MBS is given by [71]

$$A(\varphi, \theta) = -\min \{ -(A_H(\varphi) + A_V(\theta)), 30 \} \text{ dB}. \tag{3.4}$$

The channel model  $\mathbf{h}_l \in \mathbb{C}^{1 \times N_{BS}}$  between UE  $l$  and MBS is given by [72]

$$\mathbf{h}_l = \mathbf{g}_l \mathbf{R}_l^R \underbrace{\sqrt{G \cdot A_l(\varphi, \theta) \cdot PL(d_l) \cdot Z_l \cdot \alpha_l}}_{P_G = \text{propagation gain}}, \tag{3.5}$$

where  $\mathbf{g}_l \sim \mathcal{CN}(0, \mathbf{I}_N)$  are independent fast fading channel vectors and  $P_G$  represents propagation gain consisting of the MBS antenna gain  $G$ , the antenna pattern  $A_l(\varphi, \theta)$ , path loss  $PL_l$ , the log-normal shadowing  $Z_l$  and the small-scale fading  $\alpha_l$ . Using the physical channel model in [73], channel covariance matrix  $\mathbf{R}_l^R = [\mathbf{A} \mathbf{0}_{N_{BS} \times N_{BS} - N_P}] \in \mathbb{C}^{N_{BS} \times N_{BS}}$  can be obtained, where  $N_P$  is the physical dimensions and the spatial correlation matrix  $\mathbf{A} \in \mathbb{C}^{N_{BS} \times N_P}$  is composed of the steering vectors  $\mathbf{a}(\varphi, \theta) \in \mathbb{C}^{N_{BS}}$ . Note that the channel model is related with antenna pattern and steering, which might be adapting to the changes of VSCs.

### 3.3 VSC Formation and Protocol Conversion

#### 3.3.1 K-means based VSC formation

K-means is one of the well-known learning algorithms for the clustering process [74]. As shown in the Algorithm 1, the number of UEs  $K$  in the high load area, the user's location matrix  $\mu$ , and the number of centers  $K_{max}$ , will be collected at the VSC formation server in advance. Then the iteration loops in the Algorithm 1 are adopted to determine the best clus-

ter for each data point by finding the minimum mean squared distance. Finally,  $K$  UEs are assigned to  $K_{max}$  centers ( $K \geq K_{max}$ ). From [74], the smoothed running time to the k-means method is polynomially bounded in  $K_{K_{max}}$  and hence the computational complexity of K-means increased with the number of users. The performance of K-means is impacted by the number of clustering. By observing the simulation results in Fig.5.9, the clustering number should be set as  $0.4K$  to minimize the non-orthogonality in the spatial domain.

---

**Algorithm 1** K-means clustering based VSC formation
 

---

```

1: Require:  $\mathbf{K}, \mu, K_{max}$ 
2: for  $K = 1, 2, \dots, K_{max}$  do
3:   Generate random center matrix  $m$ 
4:    $l = 0, m_q^l = m, m_q^{l-1} = 0$ 
5:   if  $m_q^l \neq m_q^{l-1}$  then
6:      $l = l + 1$ 
7:   Determine nearest cluster for each user  $K$ 
8:   for  $t = 1, 2, \dots, K$  do
9:     Determine distance between a user and a cluster
10:    for  $i = 1, 2, \dots, K_{max}$  do
11:       $d_i = \sqrt{(u_t y - m_i(y))^2 + (u_t x - m_i(x))^2}$ 
12:       $d_{min} = d_1$ 
13:      if  $d_i \leq d_{min}$  then
14:         $d_{min} = d_i, q = i$ 
15:      end if
16:    end for
17:  end for
18:  end if
19: end for
20: Calculate the center for cluster  $q$ :
21:  $m_q = \sum \mu_q / K^q: = 0$ 

```

---

### 3.3.2 Protocol Conversion for Traffic Aggregation

In the proposed dynamic VSC design, the CH first collects traffic from other member devices using an unlicensed band, such as Wi-Fi, and then transmits the aggregated data traffic to MBS in the licensed band. Due to the use of the unlicensed bands, such as Wi-Fi, within each VSC, the protocol converter is adopted to achieve traffic transmission. However, the protocols of the cellular network and Wi-Fi (e.g. 802.11) have fundamental differences at their media access control (MAC) layers: cellular network usually has a frame-based and centrally coordinated

MAC protocol, while 802.11 allows distributed control and a contention-based carrier-sense multiple access with collision avoidance (CSMA/ CA) medium-access [75]. Therefore, the protocol conversion and data packet re-capsulation across licensed and unlicensed bands are needed for the purpose of inter-networking.

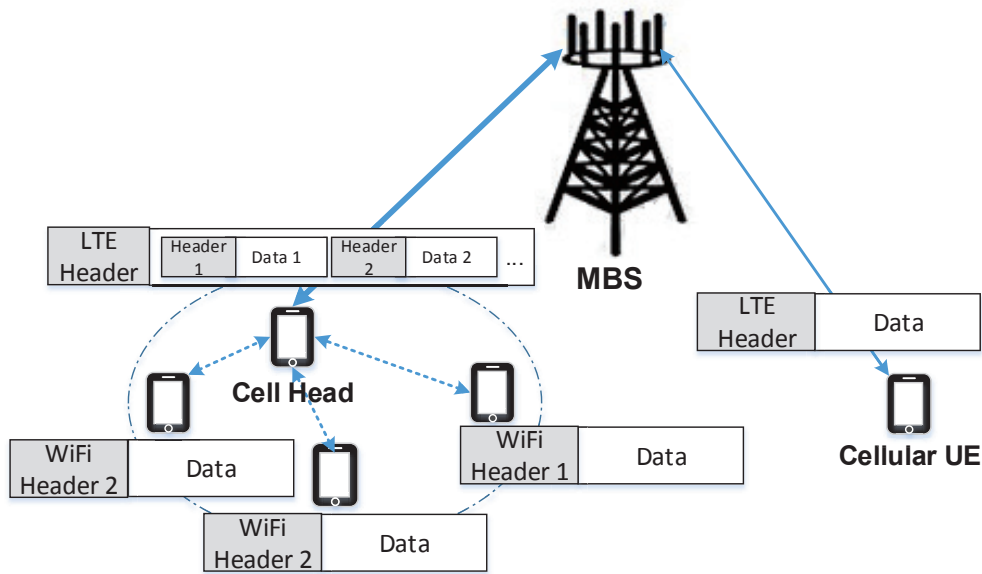


Figure 3.3: Procedure of the protocol conversion and data packet re-capsulation at CH in VSC.

In the proposed solution, it is assumed that CHs have both Wi-Fi and cellular radio interfaces. Take long term evolution (LTE) network as an example, the CH collects the traffic from member devices using the Wi-Fi interface, de-capsulate them at the MAC layer, and then re-pack them with LTE header and transmit to the MBS, as shown in Fig.3.3. From the view of the MBS, there is no big difference between CHs and normal LTE users, which reduces the complexity of VSC implementation.

The protocol conversion at the CH can be achieved at different layers of the protocol stack. The easiest way is to get this done at the upper layer, where all the implementation can be done in software. This will help to achieve flexibility and cost-effectiveness than hardware implementation. However, more delay and jitter will be introduced. On the other hand, faster protocol conversion is usually achieved at lower layers, which introduces more complexities. As a tradeoff, application or MAC layers are two popular choices. In this work, we use the

MAC layer for protocol conversion considering the stringent latency requirement of 5G applications.

Fig. 3.3 shows the protocol conversion and packet re-encapsulate procedure in the VSC. Use LTE network as an example, assume that the MBS uses OFDM in the physical layer and fixed TDMA techniques to provide time slot sharing between normal cellular UEs and CHs [10]. The CHs have two network interfaces, the LTE interface is to connect CHs with MBS while the Wi-Fi interface is used to communicate with the VSC member devices. Note that the resulting LTE and Wi-Fi data transfer operations are decoupled. For example, the legacy acknowledgment/negative-acknowledgment (ACK/ NACK) scheme is used to secure all the handled LTE traffic between CH and MBS, as if the exchanged LTE packets were all belonging to the CH.

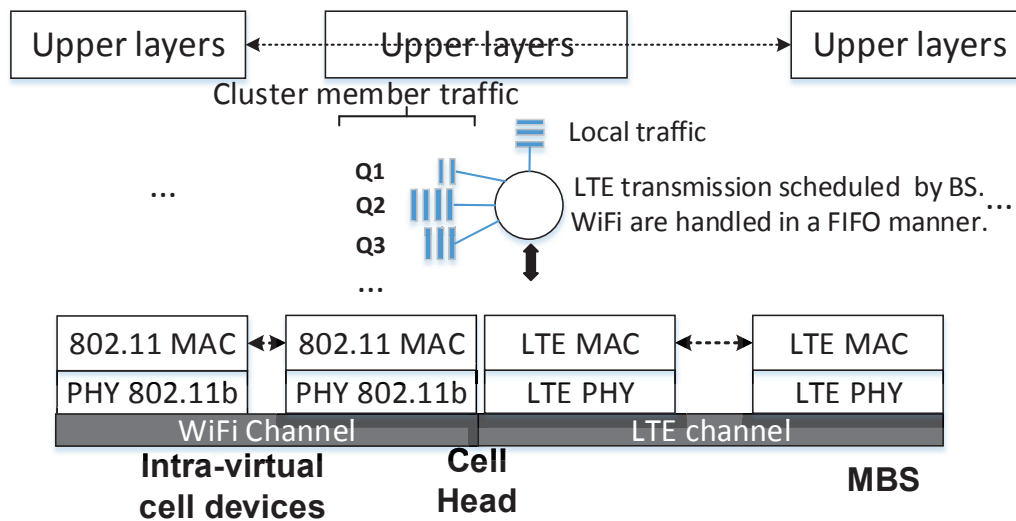


Figure 3.4: The data aggregation processing among UEs of VSCs, CHs and MBSs.

The CHs need a protocol converter to convey the data from the access network to backhaul. The protocol converter is designed to be comprised of traffic classifiers, scheduler and protocol encapsulation/de-encapsulation. As shown in Fig. 3.4, the incurred traffic is first classified, where local traffic is defined as the intra-VSC traffic, while other traffic goes from/to MBS. Secondly, the traffic is scheduled into queues based on the traffic types, for example, in the order of first-in-first-out (FIFO) or round-robin. Finally, the traffic that goes to/from MBS needs to be converted. WiFi packets are encapsulated in the LTE frame for the uplink and vice versa for the downlink traffic procedure.



Take the uplink procedure as an example, the member devices send their scheduling request (SR) to the CH to be forwarded to the MBS. The MBS then uses downlink control information (DCI) to inform the member devices regarding their downlink and uplink resource allocation. Since the CH might be the only member that is listening to the LTE channel, it receives the DCI and updates the scheduling decision to its own member devices, using an 802.11 management frame with the same subtype value used by the member devices to encapsulate SR messages in the Wi-Fi frame.

For data packets, the scheduled member devices encapsulate the LTE packet data convergence protocol (PDCP) PDUs in Wi-Fi frames and send them to the CH. The CH extracts the PDCP PDUs by dispatching the payload directly and forwards them to the MBS in the designated slot. During the transmission between CHs to the MBS, the CH includes the UE's cell radio network temporary identifier (C-RNTI) address with the data packets to simplify the identification of the source for returning packets.

Next, the CH encapsulates the LTE PDCP PDUs in regular Wi-Fi data frames and transmits to its member devices in the unlicensed band according to the C-RNTI identification information.

### 3.4 Adaptive Beamforming Design for VSC

In order to keep up with the changing location of the VSC, the hybrid beamforming at the MBS should be designed adaptively to fully cover the potential moving VSC. The hybrid beamforming design is achieved based on the channel information of trunk-link between the MBS and the CH, described in subsection II-C. The hybrid beamforming scheme is described in subsection IV-A and digital beamforming is formulated as an optimization problem in subsection IV-B. The optimal and sub-optimal solutions are given in subsection IV-C and IV-D, respectively.

#### 3.4.1 Hybrid Beamforming Scheme

The structure of the hybrid beamforming scheme is shown in Fig.3.5, which combines the digital baseband beamforming design  $\mathbf{W} \in \mathbb{C}^{N_{RF} \times N_{RF}}$  and the RF analog beamforming  $\mathbf{F} \in \mathbb{C}^{N_{BS} \times N_{RF}}$ . In terms of the analog beamforming design, in order to harvest the large array gain in massive

MIMO systems, the phase shifter can be adjusted to extract the phases of the conjugate transpose of the downlink channel [76].  $\mathbf{F}_{i,j}$  is denoted as the element of  $\mathbf{F}$  and the RF beamforming can be obtained by

$$\mathbf{F}_{i,j} = \frac{1}{\sqrt{N_{BS}}} e^{j\varphi_{i,j}}, \quad (3.6)$$

where  $\varphi_{i,j}$  is the phase of  $(i, j)$ th element the conjugate transpose of the downlink channel. Note that the RF beamforming only impacts the phase and so the equivalent channel  $\mathbf{H} = \mathbf{H}^o \mathbf{F}$ , which can be used to design the digital beamforming [77]. The design of digital BF is more complex than RF BF design because the digital BF controls both the amplitudes and phase of incoming complex symbols. We will discuss the digital BF design in the following subsections.

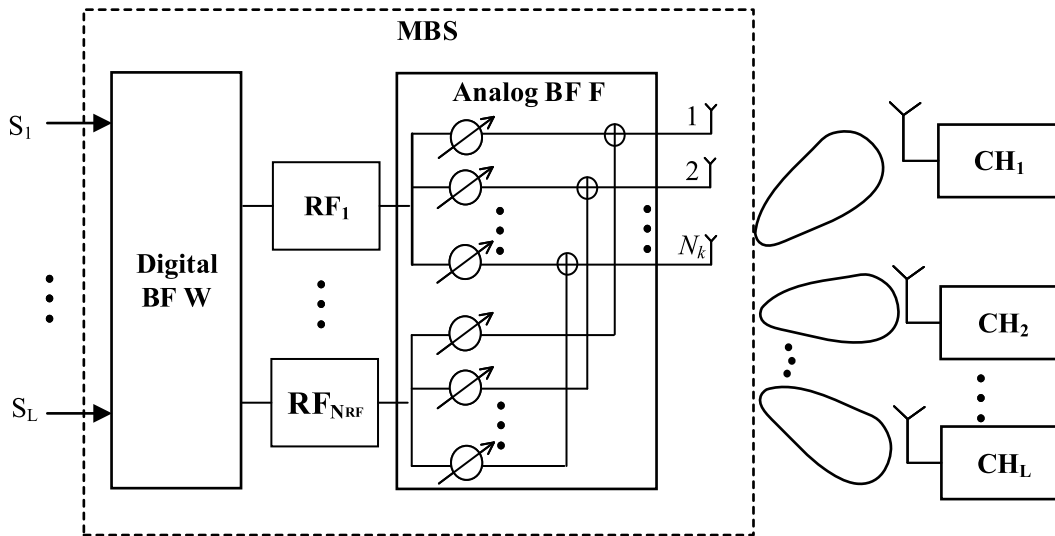


Figure 3.5: Structure of hybrid beamforming scheme for VSC.

### 3.4.2 Problem Formulation of Digital Beamforming

As the battery capacity is a bottleneck of the UE and power efficiency is essential for MBS, we should analyze the total power before the discussion of digital beamforming design. The total power consumption of per subcarrier is the sum of the power consumption,  $P_h$ , caused by hardware and the power consumption,  $P_b$ , related to the beamforming design [78], as shown in

(5.7)

$$\begin{aligned}
P_b &= \rho_0 \sum_{l=1}^L \|\mathbf{w}_l\|^2, \\
P_h &= \frac{\xi_0}{C} N_{BS} + \frac{\xi_{RF}}{C} N_{RF} + \sum_{j=1}^S \frac{\xi_j}{C} N_{CH}, \\
P_t &= P_b + P_h.
\end{aligned} \tag{3.7}$$

where  $1/\rho_0$  denotes the power efficiency of amplifiers,  $\xi_0$  is the circuit power consumption of each antenna at the MBS,  $\xi_{RF}$  is the circuit power consumption of each RF and  $\xi_j$  is the circuit power consumption of each antenna at the CH and  $C$  is the total number of subcarriers.

The downlink communication between the UEs and MBS is considered for the network architecture, shown in Fig.3.1. We assume that all UEs share the same time and frequency resource. The received signal  $y_l$  at the user  $l \in \{1, \dots, L\}$  is given by

$$y_l = \mathbf{h}_l^H \sum_{i=1}^L \mathbf{w}_i s_i + n_l, \tag{3.8}$$

where  $s_i \sim \mathcal{CN}(0, 1)$  are the information symbols generated from the MBS,  $\mathbf{w}_i \in \mathbb{C}^{N_{RF} \times 1}$  denotes the beamforming vectors and  $n_l$  is the white additive Gaussian noise with zero-mean and variance  $\sigma_l^2 \leq 0$ . Considering single-user detection at the receiver side, the signal-to-interference-and-noise ratio (SINR) of user  $l$  can be calculated by

$$SINR_l = \frac{|\mathbf{h}_l^H \mathbf{w}_l|^2}{\sum_{i=1, i \neq l}^L |\mathbf{h}_l^H \mathbf{w}_i|^2 + \sigma_l^2}. \tag{3.9}$$

The  $\sum_{i=1, i \neq l}^L |\mathbf{h}_l^H \mathbf{w}_i|^2$  represents the interference from other UEs who use the same channel with UE  $l$ . The near-far problem can be fully addressed in our proposed system by using beamforming for spatial separation of near-far users and control of transmission power at the base station, as well as the use of successive interference cancellation (SIC) at the related

mobile users for the complete removal of related interference. By using the unlicensed band for intra-cell communication, the number of directed links between MBS and UE in VSC is decreased dramatically. Therefore, the VSC has less co-channel interference than that of the traditional small cell.

Our objective of adaptive beamforming design is to minimize the total power consumption under the constraints of the transmitted power of the MBS and the rate requirement of each UE. Therefore, the adaptive beamforming design of the VSCs can be expressed as an optimization problem:

$$\begin{aligned}
 \min_{\mathbf{w}_l \forall l} \quad & \rho_0 \sum_{l=1}^L \|\mathbf{w}_l\|^2 + P_h, \\
 \text{subject to} \quad & \log_2\left(1 + \frac{|\mathbf{h}_l^H \mathbf{w}_l|^2}{\sum_{i=1, i \neq l}^L |\mathbf{h}_l^H \mathbf{w}_i|^2 + \sigma_l^2}\right) \geq \gamma_l \quad \forall l, \\
 & \sum_{l=1}^L \mathbf{w}_l^H \mathbf{w}_l \leq P_{max} \quad \forall l,
 \end{aligned} \tag{3.10}$$

where  $P_{max}$  is the maximum transmitted power of MBS. It is observed that the above problem contains the quadratic constraints and so it is not convex. In general, it is difficult to solve the non-convex optimization problems in polynomial time.

### 3.4.3 Semi-definite Relaxation

The non-convexity of the original problem is due to the quadratic form of  $\mathbf{w}_l$  in throughput rate constraints. By defining correlation matrix  $\mathbf{W}_l = \mathbf{w}_l \mathbf{w}_l^H$ , the original problem in Eq. (5.11) can be rewritten as

$$\begin{aligned}
\min_{\mathbf{W}_l \forall l} \quad & \rho_0 \sum_{l=1}^L \text{tr}(\mathbf{W}_l) + P_h, & (3.11) \\
\text{subject to} \quad & \mathbf{h}_l^H \left( \left( 1 + \frac{1}{\gamma_l} \mathbf{W}_l \right) - \sum_{i=1, i \neq l}^L \mathbf{W}_i \right) \mathbf{h}_l \geq \sigma_l^2 \quad \forall l, \\
& \sum_{n=1}^L \text{tr}(\mathbf{W}_l) \leq P_{max} \quad \forall l, \\
& \mathbf{W}_l \geq 0 \quad \forall l, \\
& \text{rank}(\mathbf{W}_l) = 1 \quad \forall l.
\end{aligned}$$

Due to rank-one constraint, optimization problem Eq. (5.13), which is equivalent to Eq. (5.11), is not a convex optimization problem. By removing rank constraint  $\text{rank}(\mathbf{W}_l) = 1$ , the relaxed version of the original problem in Eq. (5.13) is convex, which can be solved by using conventional alternative iteration method [79]. However, it is difficult to prove that there always exist an optimal solution that satisfies the rank-one constraint in theory. An optimizer of the relaxed version of Eq. (5.13),  $\mathbf{W}_l^*, l = 1, \dots, L$ , with  $\text{rank}(\mathbf{W}_l^*) > 1$ , for any  $l$ , only provides an upper bound on the optimal value of the optimization problem given by Eq. (5.11). To guarantee the rank constraint, a diagonal matrix  $\mathbf{B}_l \in \mathbb{C}^{N_{BS} \times N_{BS}}$  is introduced and the problem of Eq. (5.13) can be reformulated

$$\begin{aligned}
\min_{\mathbf{W}_l \forall l} \quad & \rho_0 \sum_{l=1}^L \text{tr}(\mathbf{B}_l \mathbf{W}_l) + P_h, & (3.12) \\
\text{subject to} \quad & \mathbf{h}_l^H \left( \left( 1 + \frac{1}{\gamma_l} \mathbf{W}_l \right) - \sum_{i=1, i \neq l}^L \mathbf{W}_i \right) \mathbf{h}_l \geq \sigma_l^2 \quad \forall l, \\
& \sum_{n=1}^L \text{tr}(\mathbf{W}_l) \leq P_{max} \quad \forall l, \\
& \mathbf{W}_l \geq 0 \quad \forall l.
\end{aligned}$$

where  $\mathbf{B}_l = b_l \mathbf{I}_{N_{RF}}$ . The basic idea of the proposed method is to adjust  $\mathbf{B}_l$  to make the solution of rank-one. The problem of Eq. (5.17) is equivalent to the problem of Eq. (5.13) by setting

$b_l = 1$  at the beginning. If any rank of  $\mathbf{W}_l$  is larger than one, the value of  $b_l$  is increased iteratively to reduce the entries of  $\mathbf{W}_l$ . Because of the same constraints, the optimal solution of  $\mathbf{W}_l$  in Eq. (5.17) is suitable for Eq. (5.13). The process of the modified semi-definite relaxation is provided in Algorithm 2.

---

**Algorithm 2** Modified Semi-definite Relaxation Algorithm
 

---

```

1: input:  $N_{RF}, T_b > 0, \beta > 1, \mathbf{h}_l$  and  $\gamma_l$  for all  $l \in L$ 
2: Initialize  $b_l = 1$  for all  $l \in L$ 
3: Set  $\mathbf{B}_l \leftarrow b_l \mathbf{I}_{N_{RF}}$ 
4: obtain the optimal  $\mathbf{W}$  based on the traditional alternative iteration solution.
5: if the rank of all  $\mathbf{W}_l$  is larger than one then
6:   while  $b_l < T_b$  do
7:     Set  $b_l \leftarrow \beta b_l$ 
8:   end while
9: else
10:  Exit
11: end if
12: output  $\mathbf{W} = 0$ 

```

---

In Algorithm 2,  $\beta > 1$  denotes the step size of iteration and  $T_b$  is the threshold. These values should be selected carefully to find a trade-off between the number of iteration and the effect of rank constraint.

### 3.4.4 Low Complexity Optimization Algorithm

It is noted that, the computational complexity of the optimization algorithm, semi-definite relaxation, of problem (5.11) is  $O(L^{4.5} \log(1/\varepsilon))$  [80] given a solution accuracy  $\varepsilon$ , which grows significantly with the number users  $L$ . To reduce the complexity, we should divide the original optimization problem into two parts and consider the constraint of throughput rate first. To extract the hidden convexity of throughput rate constraint, we assume that  $\sqrt{|\mathbf{h}_l^H \mathbf{w}_l|^2} = \mathbf{h}_l^H \mathbf{w}_l \geq 0$ . The constraint  $SINR_l \geq \tilde{\gamma}_l, \tilde{\gamma}_l = 2^{\gamma_l} - 1$  can be rewritten as [81]

$$\begin{aligned} \frac{1}{\tilde{\gamma}_l \sigma_l^2} |\mathbf{h}_l^H \mathbf{w}_l|^2 &\geq \sum_{i \neq l}^L \frac{1}{\sigma_i^2} |\mathbf{h}_i \mathbf{w}_i|^2 + 1, \\ \frac{1}{\sqrt{\tilde{\gamma}_l \sigma_l^2}} \Re(\mathbf{h}_l^H \mathbf{w}_l) &\geq \sqrt{\sum_{i \neq l}^L \frac{1}{\sigma_i^2} |\mathbf{h}_i \mathbf{w}_i|^2 + 1}. \end{aligned} \quad (3.13)$$

The SINR constraint in Eq. (3.13) can be reformulated as a second-order cone constraint and hence, strong duality and the Karush-Kuhn-Tucker (KKT) conditions can be used to solve the optimal problem. The Lagrangian function associated with Eq. (5.11), only considering the first constraint, is defined as

$$\begin{aligned} \mathcal{L}(\mathbf{w}_1, \dots, \mathbf{w}_L, \lambda_1, \dots, \lambda_L) &= \sum_{l=1}^L \|\mathbf{w}_l\|^2 + P_h, \\ &+ \sum_{l=1}^L \lambda_l \left( \sum_{i \neq l}^L \frac{1}{\sigma_i^2} |\mathbf{h}_i^H \mathbf{w}_i|^2 + 1 - \frac{1}{\tilde{\gamma}_l \sigma_l^2} |\mathbf{h}_l^H \mathbf{w}_l|^2 \right), \end{aligned} \quad (3.14)$$

where  $\lambda_l \geq 0$  is the Lagrange multiplier vector. For a given optimal  $\lambda$ , the KKT conditions are given by

$$\begin{aligned} \mathbf{w}_l + \sum_{i \neq l}^L \frac{\lambda_i}{\sigma_i^2} \mathbf{h}_i \mathbf{h}_i^H \mathbf{w}_i - \frac{\lambda_l}{\tilde{\gamma}_l \sigma_l^2} \mathbf{h}_l \mathbf{h}_l^H \mathbf{w}_l &= 0, \\ \Leftrightarrow \mathbf{w}_l &= \left( \mathbf{I} + \sum_{i \neq l}^L \frac{\lambda_i}{\sigma_i^2} \mathbf{h}_i \mathbf{h}_i^H \right)^{-1} \underbrace{\mathbf{h}_l \frac{\lambda_l}{\sigma_l^2} \left( 1 + \frac{1}{\tilde{\gamma}_l} \right) \mathbf{h}_l^H \mathbf{w}_l}_{\text{scalar}}, \\ \Leftrightarrow \mathbf{w}_l^* &= \underbrace{\sqrt{p_l}}_{=\text{beamforming power}} \frac{\left( \mathbf{I} + \sum_{i \neq l}^L \frac{\lambda_i}{\sigma_i^2} \mathbf{h}_i \mathbf{h}_i^H \right)^{-1} \mathbf{h}_l}{\underbrace{\left\| \left( \mathbf{I} + \sum_{i \neq l}^L \frac{\lambda_i}{\sigma_i^2} \mathbf{h}_i \mathbf{h}_i^H \right)^{-1} \mathbf{h}_l \right\|}_{=\tilde{\mathbf{w}}_l^*=\text{beamforming direction}}}}. \end{aligned} \quad (3.15)$$

Eq. (3.15) is the first-order optimality conditions of beamforming, consisting of beamforming power  $p_l$  and beamforming direction  $\tilde{\mathbf{w}}_l^*$ . To reduce complexity, an equal power allocation scheme can be used to find the beamforming direction first. Therefore, substituting  $\lambda_i = \frac{P_{max}}{L}$

into Eq. (3.15), the optimal beamforming direction can be obtained by

$$\tilde{\mathbf{w}}_l = \frac{\mathbf{h}_l \left( \sum_{i=1}^L \frac{1}{\sigma_i^2} \mathbf{h}_i \mathbf{h}_i^H + \frac{L}{P_{\max}} \mathbf{I} \right)^{-1}}{\left\| \mathbf{h}_l \left( \sum_{i=1}^L \frac{1}{\sigma_i^2} \mathbf{h}_i \mathbf{h}_i^H + \frac{L}{P_{\max}} \mathbf{I} \right)^{-1} \right\|}. \quad (3.16)$$

The Eq. (3.16) illustrates that the optimal beamforming directions can be found by maximizing the ratio of the desired signal power to the noise power and minimizing the interference caused by co-channel users. In fact, this is equal to the concept of maximizing signal-to-leakage-and-noise ratio (Max-SLNR) beamforming, which is a kind of heuristic beamforming method and is non-iterative [82]. Then, Eq. (5.11) can be rewritten as an optimization problem of power allocation

$$\begin{aligned} \min_{p_l \forall l} \quad & \rho_0 \sum_{l=1}^L p_l + P_h, \\ \text{subject to} \quad & \sum_{l=1}^L p_l \leq P_{\max} \quad \forall l, \\ & p_l |\mathbf{h}_l^H \tilde{\mathbf{w}}_l|^2 \left( 1 + \frac{1}{\tilde{\gamma}_l} \right) - \sum_{i=1}^L p_i |\mathbf{h}_l^H \tilde{\mathbf{w}}_l^*|^2 \geq \sigma_l^2 \quad \forall l. \end{aligned} \quad (3.17)$$

---

**Algorithm 3** Low-complexity Algorithm

---

- 1: **input:**  $N_{RF}$ ,  $\mathbf{h}_l$  and  $\tilde{\gamma}_l$  for all  $l \in L$
  - 2: **Initialize**  $\mathbf{w}_l$  for all  $l \in L$
  - 3: **Step 1:**
  - 4: **for** user form 1 to  $L$  **do**
  - 5:   *based on the equal power allocation scheme, the optimal beamforming direction of each user is calculated*  $\tilde{\mathbf{w}}_l = \frac{\mathbf{h}_l \left( \sum_{i=1}^L \frac{1}{\sigma_i^2} \mathbf{h}_i \mathbf{h}_i^H + \frac{L}{P_{\max}} \mathbf{I} \right)^{-1}}{\left\| \mathbf{h}_l \left( \sum_{i=1}^L \frac{1}{\sigma_i^2} \mathbf{h}_i \mathbf{h}_i^H + \frac{L}{P_{\max}} \mathbf{I} \right)^{-1} \right\|}$
  - 6: **end for**
  - 7: **Step 2:** Solve the convex optimization problem of (3.17) to obtain the optimal power allocation  $p_l^*$ .
  - 8: **Step 3:**  $\mathbf{w}_l = \sqrt{p_l^*} \tilde{\mathbf{w}}_l$  for all  $l \in L$
  - 9: **output:**  $\mathbf{w} = 0$
- 

The optimal power allocation  $p_l^*$  can be obtained by solving the above convex optimization



problem and should be sent to MBS to calculate the final optimal beamforming. The proposed low-complexity algorithm is summarized in Algorithm 3.

## 3.5 Performance Evaluation

### 3.5.1 Simulation Parameters

A heterogeneous network, where five VSCs deployed in one macro-cell, is considered. There are 30 users randomly distributed in the whole macro-cell. One CH, equipped with one antenna, is deployed in each VSC and one MBS, equipped with 128 antennas and 60 RF, is located at the center of macro-cell. Table 3.1 shows the main parameters, which are utilized to calculate the power consumption and model the channel [83] and [84].

Table 3.1: Parameters of hardware and channel model for small cell and macro-cell.

Parameters	Value
Carrier Frequency/No. of subcarriers	2GHz/600
Total bandwidth/Subcarrier bandwidth	10MHz/15kHz
Efficiency of power amplifier	0.38
Circuit power per antenna of MBS	160 mW
Circuit power per antenna of MBS	5.6 mW
Circuit power per RF	50 mW
Radius of small cell radius	50 m
Radius of macro cell radius	0.8 km
Standard deviation of log-normal shadowing	7 dB
Path and penetration loss for small cell	$127 + 30\log_{10}(d)$ dB
Path and penetration loss for macro-cell	$148.1 + 37.6\log_{10}(d)$ dB
Noise variance	-127 dBm
Noise figure	5 dB

### 3.5.2 K-means based VSC Formation

Fig. 3.6 shows the virtual small cell formation using the clustering algorithm and the define of the cell center/ radius. 100 users are generated randomly in an area, and the K-means clustering algorithm is executed as an example for the virtual small cell clustering procedure [66]. It can be seen in the figure that users are grouped as blue and red as the first step and the cell center

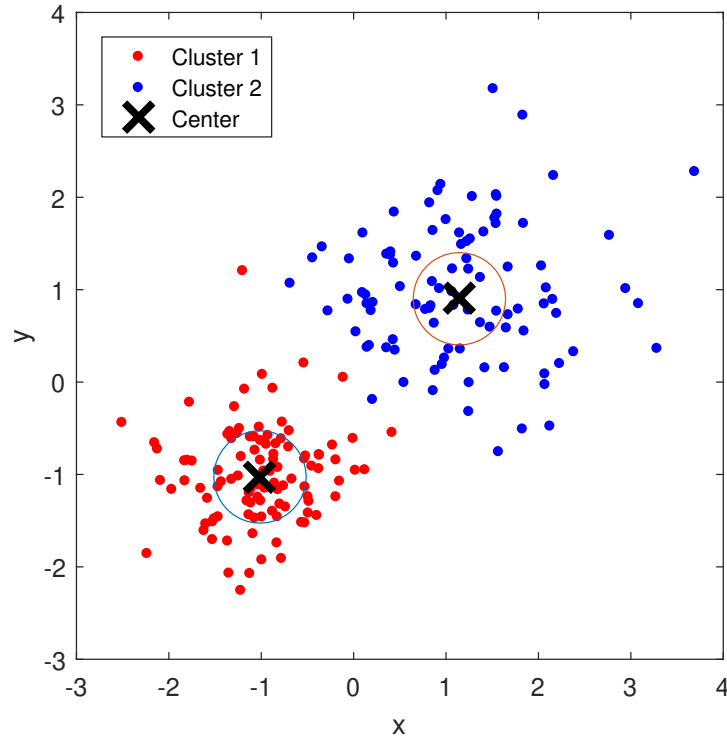


Figure 3.6: Virtual small cell formation using K-MEANS clustering and far user removing.

is decided. Afterward, far users are removed from the virtual cells using average distance plus standard deviation. In order to find the radius of virtual small cells, the transmission range of IEEE 802.11p protocol is applied, and the smaller value between the transmission range and average distance plus standard deviation would be the virtual small radius.

### 3.5.3 Power Consumption Performance of the Proposed VSC

Fig. 3.7 illustrates the total power consumption of three scenarios with the different numbers of antennas ( $N_{BS}$  and  $N_{CH}$ ), while the bit rates requirement of each user is 2 bits/s/Hz. The optimal beamforming algorithm has been elaborated in Section 3.4.3 and the solution of the convex optimization problem is obtained using the modeling language CVX in simulation[85]. In terms of traditional small cell scenario, soft cell [86] is applied, where each user communicates with any combination of transmitters (MBS and SCAs). As can be seen from Fig. 3.8, the average total power consumption decrease dramatically with the increase in antenna numbers at the MBS and CH. The reason is that the increase in the diversity gain outweighs the increase

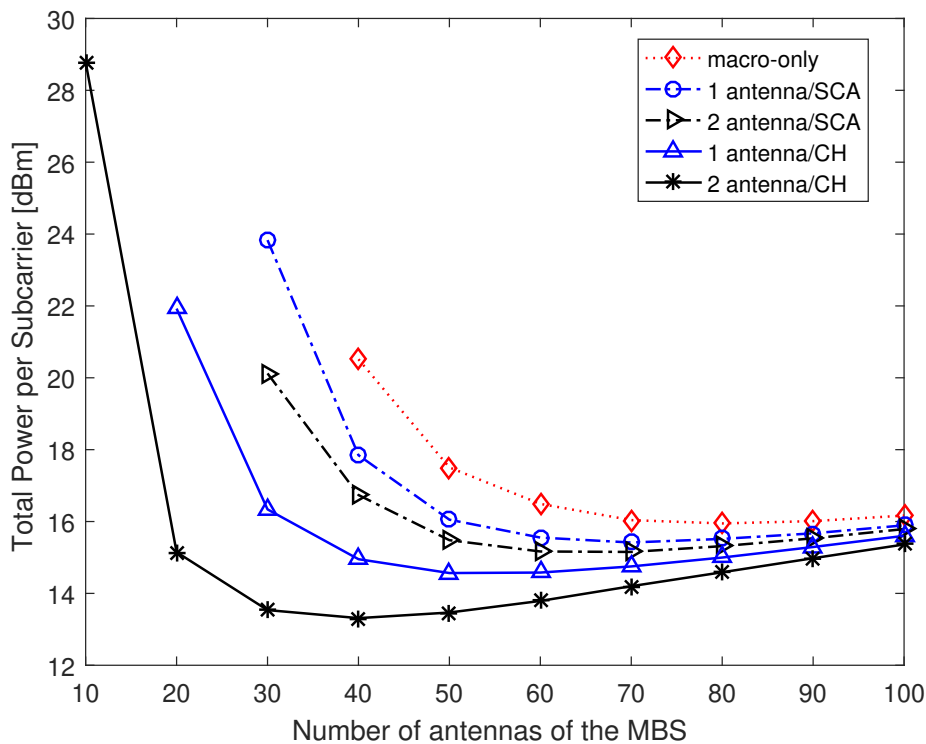


Figure 3.7: Total power consumption against the number of MBS antennas for macro-only, traditional SCs and virtual SCs.

in the hardware cost  $P_h$ . This situation bottomed out at  $N_{BS} = 40 - 60$  and the total power then starts to increase slowly. Furthermore, the lowest power consumption of VSC reduced from 16.8 dBm (47.8 mW) to 15.8 dBm (38 mW) by increasing the antenna number at CH from 1 to 2. Moreover, with the same antenna numbers at MBS, the VSC saved around 50% and 66% power consumption compared with that of macro-only and traditional small cell scenarios, respectively.

In Fig. 3.8, total power consumption under different throughput rate constraints are simulated using 60 antennas at MBSs and two antennas at CHs/APs. The energy efficiency of four scenarios are compared, including optimal beamforming without small cells discussed in [78], optimal soft cell proposed in [78], optimal VSCs (Algorithm 2) and sub-optimal VSCs (Algorithm 3). It can be seen that higher rate requirements cause higher power consumption. The total power consumption increased around 3 times when the QoS requirement rises from 2 bits/s/Hz to 4 bits/s/Hz. It is also clear that power consumption is saved by offloading users

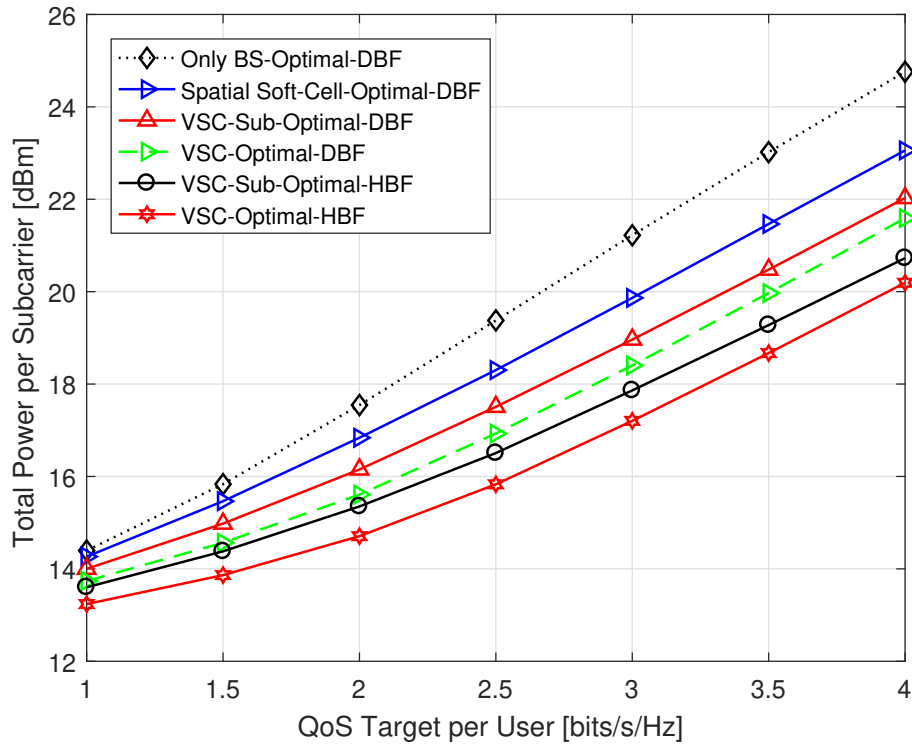


Figure 3.8: Total power consumption for different throughput rate constraints in three scenarios.

from the macro cell to small cells because SCs reduce the communication distance. Compared with soft small cells, with the same QoS requirement, the algorithms that utilize VSCs reduced 55% power consumption due to less inter-cell interference. Moreover, the proposed Max-SLNR beamforming scheme, discussed in Section 3.4.4, provides a similar performance of optimal beamforming algorithm with lower complexity with the use of Massive MIMO.

Furthermore, there are two different beamforming schemes, hybrid beamforming and digital-only beamforming, which are simulated in the situation of VSC. It can be seen that, to achieve 3 bps/s/Hz, the power consumption of digital beamforming in VSC is 18 dBm (63 mW), while the power consumption of hybrid beamforming scheme in VS is 17 dBm (50 mW). Therefore, the HBF can further save 16% power than that of DBF, because the hybrid beamforming can decrease the number of RF.

## 3.6 Chapter Summary

This section proposed virtual small cells as a flexible and cost-effective scheme to overcome the deployment challenges of traditional small cells. VSCs are formed adaptively according to dynamic traffic conditions, and one user device with better power and channel conditions is selected as the CH to aggregate the intra-cell traffic in the unlicensed band and communicate directly with the MBS in the cellular band. A K-means clustering based virtual small cell formation scheme is proposed, and the protocol conversion for data transmission across an unlicensed and licensed band at CHs is designed. Based on the proposed virtual small cell network architecture, adaptive hybrid beamforming is also designed to support the high traffic of the front-haul link. The objective of beamforming design is to minimize the total power while guaranteeing the throughput rate requirement of users and transmit power constraints at the MBS. This non-convex problem can be translated into a convex problem by using modified semi-definite relaxation. To reduce the optimization complexity, beamforming direction can be selected for equal power allocation first. After this step, the original optimization problem can be reformulated as a simple convex optimization problem of power allocation. The optimal and sub-optimal solutions of beamforming design are analyzed. Both mathematical and simulation results demonstrate that compared with soft small cells, the proposed VSCs with the adaptive HBF scheme can save 55% power consumption, due to better energy-focusing and less inter-cell interference.

# Chapter 4

## Deep Learning Based Hotspot Prediction for VSC in Ultra Dense HetNet

In this chapter, a hotspot prediction based virtual small cell (VSC) operation scheme is adopted to improve both the cost efficiency and operational efficiency of 5G networks. This study focuses on how to predict hotspots by using deep learning. We first leverage the feature extraction capabilities of deep learning and exploit the use of a long short term memory (LSTM) neural network to achieve hotspot prediction for the potential formation of the VSCs. Specifically, the location map of UEs is divided into several grids and the problem of hotspot prediction is formulated to predict the UE numbers of each grid. Our simulation results illustrate that the proposed LSTM based method can extract spatial and temporal traffic features of hotspot with higher accuracy, compared with some existing deep and non-deep learning approaches. Numerical results also show that VSCs with hotspot prediction and hybrid beamforming can improve the energy efficiency dramatically with flexible deployment and low latency, compared with the scenario of the convolutional fixed small cells.

### 4.1 Introduction

The proliferation of smart devices, forthcoming autonomous vehicles and dramatically growing Internet of Things (IoT) applications are expected to bring significantly increased data traffic to existing wireless infrastructures, which necessitates the research and development of 5th

generation (5G) networks. As a result, ultra-dense network (UDN) has been considered as a promising solution to cope with the explosive traffic growth and support high-speed services through the deployment of the ultra-dense small base station (SBS) with reduced transmission distance between users and access point [87]. However, the distribution of the 5G devices and traffic can vary unevenly. Small areas with a large number of user equipment (UE) transmitting within a short period, e.g. a crowded road intersection with vehicles, may introduce a heavy burden on cellular networks, producing hotspots of varying size and duration in the serving wireless networks [3]. Currently, the deployment of fixed wireless networks typically results in an architecture that lacks the capability and cost-efficiency to deal with scenarios having highly fluctuating network traffic variations due to user activity and mobility.

Unfortunately, the variation of user distribution in both temporal and spatial domains is very common in current and future cellular networks. For example, user distribution can be changed dramatically due to the different lifestyles and work habits of people[88]. Simply deploying a large number of fixed small cell base stations (SBS) will not only increase the infrastructure cost but also waste network resources when network traffic is low [29]. To address these challenges while fully utilizing the spatial and temporal patterns of user and traffic distributions, cost-effective network deployment and traffic-aware allocation of network resources are becoming essential. Hotspot location and prediction can provide very useful information concerning highly loaded areas both in the temporal and spatial domains, which can serve as the basis of traffic-aware network operation [89]. Achieving this requires understanding and forecasting the network-level mobility patterns and distribution of UEs with high accuracy and in a timely manner.

However, predicting large-scale and fine-grained user distribution can be extremely challenging because of the following three reasons: (i) due to the different lifestyle, mobility patterns and user behavior of an individual user could vary widely ; (ii) the user spatial distribution pattern within a region could be characterized and affected by both short and long term events [90]; and (iii) some additional factors, e.g. festival events and extreme weather conditions, may change the user distribution remarkably in temporal and spatial domain [28]. Therefore, extracting and predicting useful mobility patterns from multi-source and rapidly changing networks remains a challenge.

Recent years have witnessed a considerable amount of studies dedicated to mobility prediction schemes. In [50], according to the statistics of user occurrence frequency, the most distinctive sequential mobility pattern of users is extracted. However, this method fails to predict changing sequential mobility patterns when the users changed their mobility routines. Another popular method is using principal component analysis (PCA) and extracting eigenbehaviors [51] or eigenplaces [52], which features a two-layer shallow structure. The eigenbehavior and eigenplaces of user's mobility and traffic are determined to extract a common underlying structure of users' daily mobility patterns. Nevertheless, the limited number of eigenbehavior and eigenplaces may not be sufficient to fully represent the mobility patterns of different users. Therefore, a 'deeper structure', such as the structure of deep neural network, should be used to address these challenges. By introducing multiple hidden layers between the input and output layers, deep neural network (DNN) is more powerful and flexible to predict complex mobility patterns due to the combined capability of multiple hidden layers [53]. In addition, by employing hierarchical feature extraction, deep learning can capture temporal and spatial dependencies in sequential data, while minimizing the data pre-processing effort [54]. Furthermore, it makes possible for deep learning to make inferences within milliseconds by using Graphic Processing Unit (GPU)-based parallel computing [55].

Therefore, the deep neural network is becoming a critical tool for user mobility analysis. In [56], deep learning was adopted first to recover the social network representations of users and then a basic recurrent neural network (RNN) and Gate Recurrent Unit (GRU) models were employed to discover mobility patterns of the individual user at different levels. In [57], an online learning scheme was proposed to train a hierarchical convolutional neural network (CNN), which can process data stream parallelly. However, most of the previous works are focused on predicting the individual trajectories instead of forecasting the network-level user distribution, which is more valuable for network operation. Therefore, we directly predict the network-level user density in the temporal and spatial domain through deep learning methods in this chapter. Since fluctuation of user density is influenced by short and long term behaviors, the long short term memory (LSTM) neural network, a kind of deep RNN, is adopted to predict the number of UEs in every small zone due to its excellent capability to memorize long-term dependencies. By using the LSTM neural network, the proposed method can also overcome



the gradient problem that plagues conventional RNNs and captures long-short term temporal and spatial dependencies without suffering from the optimization hurdles [58].

By analyzing the network-level UE distribution, it is possible to automatically predict hotspots of the ultra-dense HeNet. Therefore, we proposed the machine learning based hotspot prediction and combined with the concept of virtual small cell (VSC) proposed in the previous topic as a flexible and cost-effective scheme to reduce co-channel interference and handle the latency requirement of cell formation. Specifically, We adopt the LSTM based hotspot prediction method in VSC to improve cost efficiency and handle the latency requirement. In our previous work [91], both the cell formation and beamforming design of VSC have to be collected and determined using real-time feedbacks from UEs, leading to increased real-time operational complexity and latency. In this chapter, the predicted location of hotspots can be determined in advance to reduce the latency from supporting cell formation and beamforming. In achieving the proposed one LSTM based prediction method, the historical location map of UEs is divided into several zones in the spatial domain and each zone consists of the neighboring grids. All of these two-dimensional zones are used to train one LSTM neural networks to explore both spatial and temporal features of UE distribution. By analyzing the predicted network-level UE density map, the hotspot can be detected.

The rest of this chapter is structured as follows. Section 4.2 introduces the system model of the hotspot prediction based VSCs. In Section 4.3, the problem of hotspot prediction is formulated to predict the UE numbers of each grid. The three different LSTM based hotspot prediction methods are elaborated in Section 4.4. In Section 4.5, a real dataset of telecommunication is used to evaluate the proposed one LSTM based prediction method. Further, performance evaluation is presented in Section 4.6. Simulation results regarding the root mean square error (RMSE) performance of one LSTM based network is compared with that of three benchmarks. The system performance of VSCs based hotspot prediction is compared with the traditional small cells and VSC with K-means scenarios. Finally, the conclusions are provided in Section 4.7.

## 4.2 Overall Network Architecture

The overall network architecture of the proposed hotspot prediction based VSC, which consists of a HetNet environment, as shown in Fig.4.1, is designed to reduce the deployment cost and operational complexity. As shown in Fig. 4.1, based on the received historical data of UE distribution, a deep learning model that may run on a cloud-based platform is utilized to achieve the user distribution prediction. The pre-trained module is trained in advance according to the long-term historical data of user distributions to determine the parameters of the LSTM network. The recent short-term available data (few hours) can be used to update the trained model online at each step. The predicted information of the hotspot is sent to the VSC server to form VSC and design the hybrid beamforming.

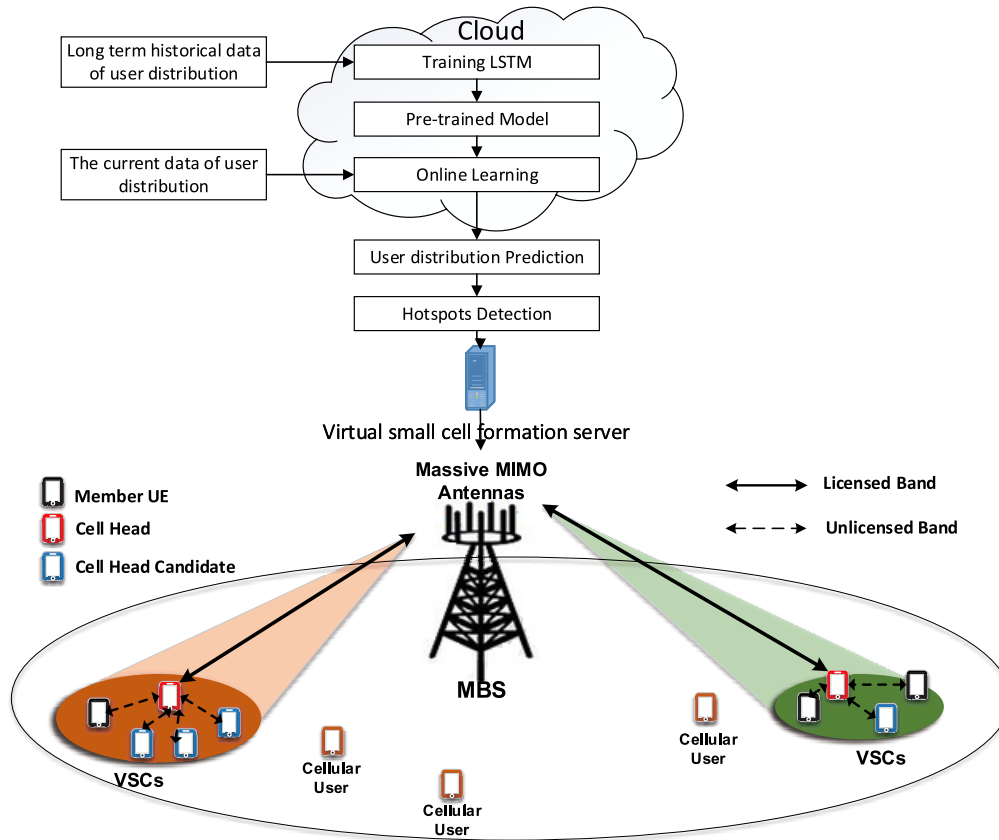


Figure 4.1: Network architecture of hotspot prediction based VSC.

Regarding the architecture of the whole network, we consider a two-tier heterogeneous network, where  $S$  VSCs are deployed in a macro-cell, as shown in Fig. 4.1. We assume that

$K$  users, equipped with  $N_K$  antennas, are randomly distributed in the macro-cell and one MBS, equipped with  $N_{BS}$  antenna and  $N_{RF}$  RF, is deployed at the center of the macro-cell. The number of MBS antennas is large enough to achieve the Massive MIMO, which can be used to form a highly directional hybrid beamforming to cover the VSC. In each VSC, several UEs with high battery level and good channel quality is selected as CH candidates (colored in blue) and serve as the CH (colored in red) in turn. The CH should work as a flexible SBS. It aggregates the information from member UEs (colored in black) in VSC by using the unlicensed band and directly communicates with MBS through the beamformed fronthaul [67]. The UEs who have direct connection with MBS can be denoted by  $\mathcal{U} = \{1, \dots, L\}$ , while the others who communicate with CHs are described as  $\mathcal{U}^C$ , where  $\mathcal{U} \cup \mathcal{U}^C = \{1, \dots, K\}$ . There are  $L$  data streams from MBS to CHs. Because the number of data streams represents a lower bound on the number of RF chains, it is convenient to set  $N_{RF} \geq L$ .

### 4.3 Problem Formulation of Hotspot Prediction

Advances in wireless communication and Global Positioning System (GPS) technologies allow timely collection of relevant information regarding the status and location of the active UEs. As a result, the location map of UEs can be developed. As shown in Fig. 4.2, the map can be divided into  $N_s \times N_s$  grids.

Specifically, the hotspot prediction problem can be formulated as follows. Let  $x_t^i$  denotes the number of UEs in the  $i^{th}$  grid at a given time  $t$ . Given a historical record of UE numbers  $\{\mathbf{x}_{t-1}, \dots, \mathbf{x}_{t-d}\}$ , where  $\mathbf{x}_{t-1} = \{x_{t-1}^1, \dots, x_{t-1}^{N_s^2}\}$ . The aim of this study is to predict hotspots by predicting the UE numbers of every grid  $\mathbf{x}_t$ . In general, the total number of UEs in the network is fairly constant, but the number of UEs in a given grid could vary dramatically over time. The number of UEs in a given grid is essentially a time series, where the historical events have an impact on the future evolution of the UE distribution in the time domain. Furthermore, the predicted UE numbers of each given grid are also impacted by the neighboring grids in the spatial domain.

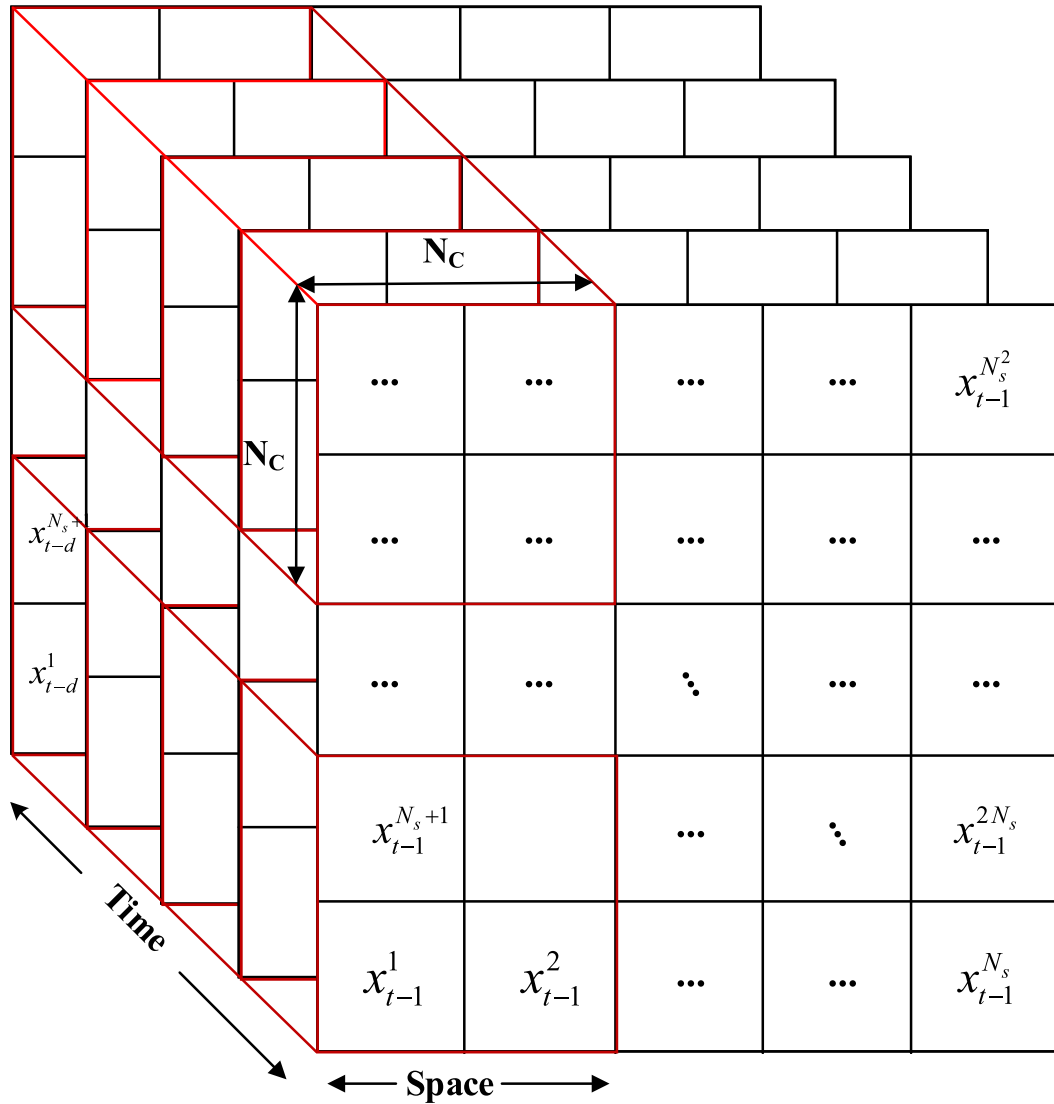


Figure 4.2: UE location map in temporal and spatial domain.

## 4.4 LSTM based User Distribution Prediction

The LSTM neural network is a special kind of deep RNNs that can capture the longer-term temporal dependencies than traditional RNNs [92]. Therefore, in this work, the LSTM neural network is adopted to predict the number of UEs in every grid, which is used to predict the final user distribution. Specifically, the memory cell structure of LSTM is introduced in subsection 4.4.1, and one LSTM based prediction method is presented in subsection 4.4.2.

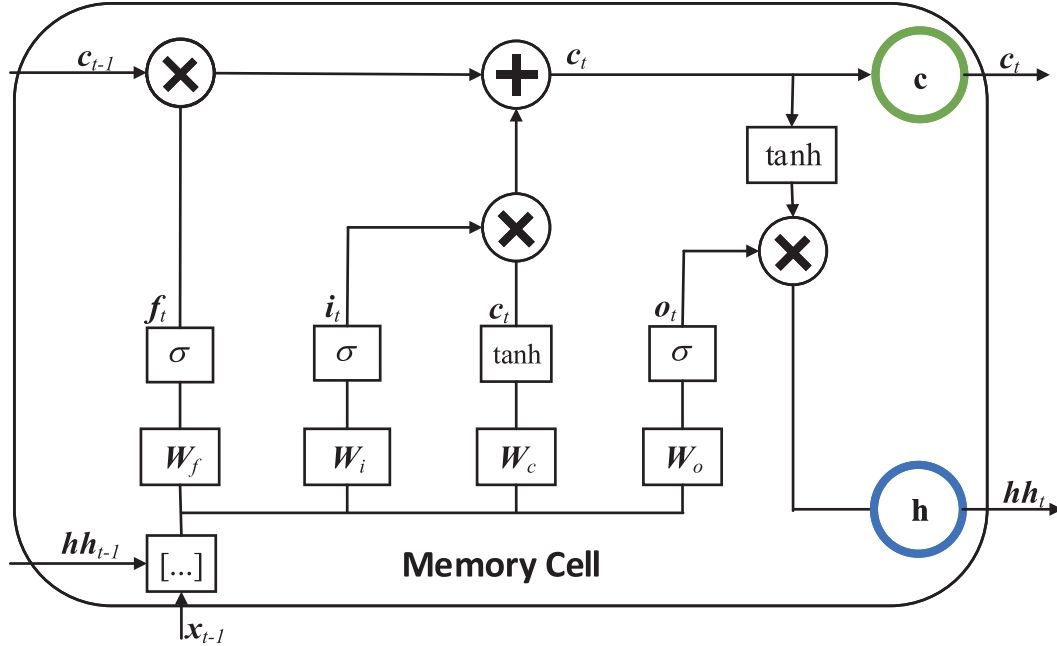


Figure 4.3: Structure of LSTM memory cell.

#### 4.4.1 Memory Cell Structure of LSTM

Each hidden node in LSTM network is regarded as a memory cell with three different gates, which regulating the information and thus allowing to keep the past information [93]. The structure of LSTM memory cell is shown in Fig. 4.3. At each time instant  $t$ , there are two inputs for the LSTM memory cell: the historical UE numbers  $\mathbf{x}_{t-1}$  and the previous state of hidden layer  $\mathbf{hh}_{t-1}$ . The output and update of the memory cell are determined by the cell state. The forget gate determines what kind of information should be eliminated away from cell state [94]. The output value of forget gate at  $t^{\text{th}}$  time is :

$$\mathbf{f}_t = \sigma(\mathbf{W}_f \cdot [\mathbf{hh}_{t-1}, \mathbf{x}_{t-1}] + \mathbf{b}_f), \quad (4.1)$$

where  $\mathbf{W}_f$  and  $\mathbf{b}_f$  are the weight matrix and the bias factors of the forget gate, respectively. The active function of forget gate is a sigmoid function  $\sigma \in [0, 1]$ , where the value of 1 represents passing information while a value 0 represents blocking information, respectively.

On the other hand, the input gate decides what kind of information should be stored in the

cell state [94]. The output value of the input gate at  $t^{\text{th}}$  time is:

$$\mathbf{i}_t = \sigma(\mathbf{W}_i \cdot [\mathbf{h}\mathbf{h}_{t-1}, \mathbf{x}_{t-1}] + \mathbf{b}_i), \quad (4.2)$$

where  $\mathbf{W}_i$  and  $\mathbf{b}_i$  are the weight matrix and the bias factors of the input gate, respectively. The active function is also a sigmoid function  $\sigma \in [0, 1]$ .

Then, a tanh function,  $\tanh \in [0, 1]$ , creates a vector of new candidate values of cell states:

$$\check{\mathbf{c}}_t = \tanh(\mathbf{W}_c \cdot [\mathbf{h}\mathbf{h}_{t-1}, \mathbf{x}_{t-1}] + \mathbf{b}_c). \quad (4.3)$$

Based on the output values of input gate and forget gate, the cell state of the current memory cell can be updated by the following formula:

$$\mathbf{c}_t = \mathbf{f}_t \circ \mathbf{c}_{t-1} + \mathbf{i}_t \circ \check{\mathbf{c}}_t, \quad (4.4)$$

where  $\circ$  denotes the Hadamard product. Finally, the current state of hidden layer  $\mathbf{h}\mathbf{h}_t$  is calculated based on the value of output gate and the cell states that are further filtered [92]:

$$\mathbf{h}\mathbf{h}_t = \mathbf{o}_t \circ \tanh(\mathbf{c}_t), \quad (4.5)$$

where  $\mathbf{o}_t$  is the value of output gate at  $t^{\text{th}}$  time, which is generated by a sigmoid function  $\sigma \in [0, 1]$ :

$$\mathbf{o}_t = \sigma(\mathbf{W}_o \cdot [\mathbf{h}\mathbf{h}_{t-1}, \mathbf{x}_{t-1}] + \mathbf{b}_o), \quad (4.6)$$

where  $\mathbf{W}_o$  and  $\mathbf{b}_o$  denote the weight matrix and the bias factors of the output gate, respectively.

#### 4.4.2 User Distribution Prediction based on One LSTM

The historical location map should be divided into  $\left(\frac{N_s}{N_c}\right)^2$  zones in spatial domain and each zone has  $N_c \times N_c$  grids at specific time  $t$ , as shown in the Fig.4.4. Note that the value of  $N_c$  should ensure the zone number,  $\left(\frac{N_s}{N_c}\right)^2$ , is an integer. The model of UE distribution prediction based on one LSTM network is shown in Fig. 4.4. There are three layers in the proposed LSTM model: the input layer, the hidden layer and the output layer.

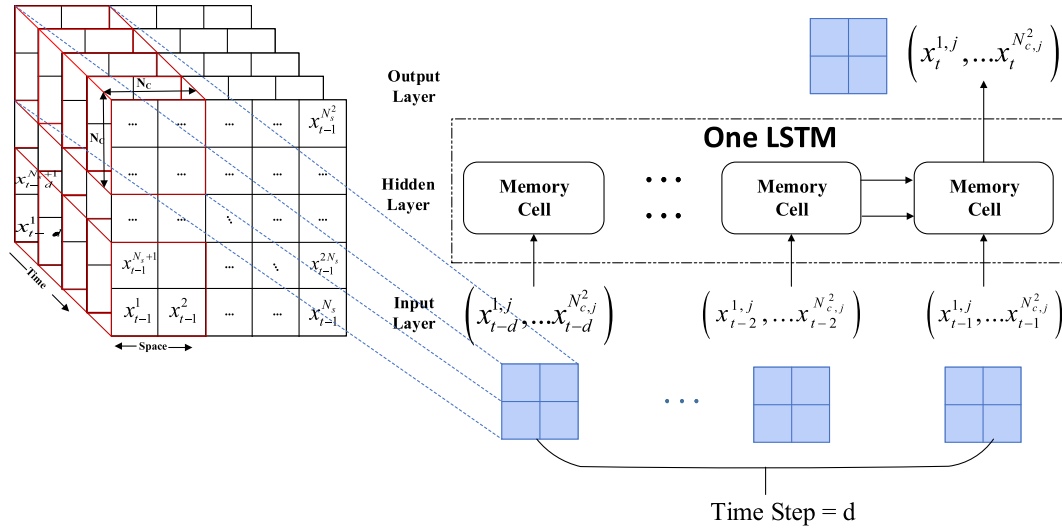


Figure 4.4: Structure of one LSTM based UE distribution prediction method.

The input to the LSTM model is the historical UE numbers of all grids in  $j^{th}$  zone:

$$\{\mathbf{x}_{t-1}^j, \mathbf{x}_{t-2}^j, \dots, \mathbf{x}_{t-d}^j\}, \quad (4.7)$$

where  $\mathbf{x}_{t-1}^j = \{x_{t-1}^{1,j}, \dots, x_{t-1}^{N_c,j}\}$ . The output is the predicted UE numbers of all grids in  $j^{th}$  zone at time  $t$ ,  $\mathbf{x}_t^j = \{x_t^{1,j}, \dots, x_t^{N_c,j}\}$ . The number of memory cells is determined by the time steps  $d$ . The hidden layer number in Fig. 4.4 is one, but it can be easily extended to several layers according to the situation. In this way, the input of the proposed one LSTM based method is the 2D (spatial and temporal domain) zones instead of the 1D (temporal domain) grid. Therefore, the proposed one LSTM network can exploit both spatial and temporal features of UE distribution. All of zones are should be used to train the same LSTM model to find the relationship function  $\mathbf{f}$  between the input and output:

$$\mathbf{x}_t^j = \mathbf{f}(\mathbf{x}_{t-1}^j, \mathbf{x}_{t-2}^j, \dots, \mathbf{x}_{t-d}^j) \quad \forall j = 1, \dots, \left(\frac{N_s}{N_c}\right)^2. \quad (4.8)$$

With this approach, the UE numbers of all small zones can be predicted and so the network-level user distribution in the temporal and spatial domain can be obtained.

## 4.5 Data Set

For data analysis with deep learning, it is essential to obtain a high-quality data set. In this work, a publicly available real-world multi-source dataset released through Telecom Italia in 2015 is adopted [95]. The dataset is composed of telecommunications, weather, social networks and electricity data from the city of Milan and the Province of Trentino, collected between 1 Nov 2013 and 1 Jan 2014. In this work, we focus on telecommunication records from Milan. These network activities are measured by using the terms of total call detail record (CDR) data, which is generated when a user receives or sends SMS, call and Internet over 10-minute intervals.

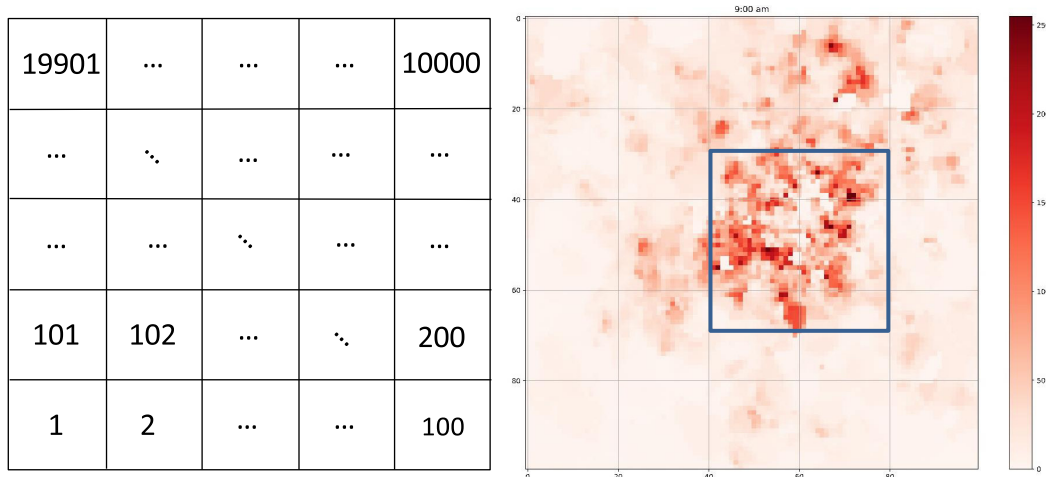


Figure 4.5: Grid map and the CDR heat map of Milan.

For the convenience of CDR recording, the city of Milan is divided into  $100 \times 100$  grids, marked by a unique ID, as shown in Fig. 4.5. The size of each grid is  $235 \times 235$  meters. The CDR numbers can reflect the UE density, and so we can predict the hotspot by predicting



the CDR numbers of every grid. By adding six-time intervals (10 minutes), the aggregated

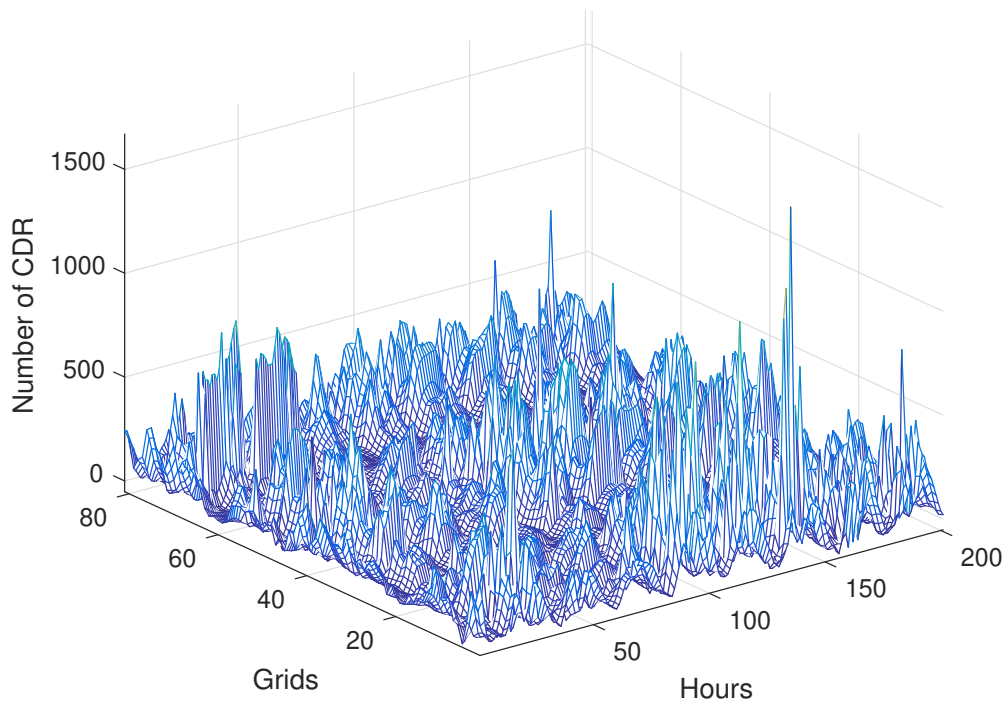


Figure 4.6: CDR distributions of Milan in the spatial domain and temporal domain.

CDR numbers of each grid in one hour are obtained. The CDR distributions of Milan in the spatial and temporal domains are shown in Fig. 4.6. From this figure, we can see that the CDR number is continuous both in the spatial and temporal domains. Some heatmaps examples at different times are given in Fig. 4.7. We noted that the active zones focus on the central 4040area (horizontal:40-80, vertical:30-70) with 1600 grids. Therefore, the data set of these grids is used to evaluate the performance of all prediction methods in the next section.

## 4.6 Performance Evaluation

To evaluate the effectiveness of LSTM based prediction method, the experiments are conducted on real-world data. The three baseline algorithms and simulation conditions are described in subsection 4.6.1 and 4.6.2, respectively. Then, the filter is adopted to preprocessing the raw data in subsection 4.6.3. In subsection 4.6.4, the proposed one LSTM based CDR numbers

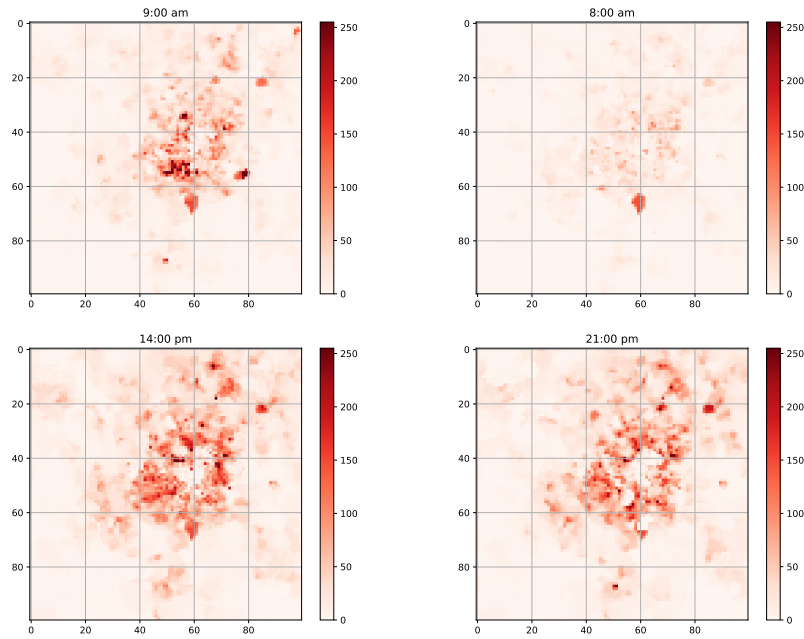


Figure 4.7: Heatmap examples of real CDR data for Milan.

forecasting is compared with three baseline methods. The accuracy evaluation of one LSTM based hotspot prediction is provided in subsection 4.6.5. Finally, the power consumption of VSCs with hotspot prediction is compared with the K-means in subsection 4.6.6.

#### 4.6.1 Baseline Algorithms of Hotspot Prediction

To verify the accuracy of the proposed one LSTM based algorithm, three models, including the autoregressive integrated moving average (ARIMA), several LSTM based algorithms and Convolutional LSTM (ConvLSTM), are employed as baselines.

- **ARIMA:** It is a kind of non-deep learning method that captures a suite of different standard temporal structures in time series data. ARIMA models are known to be robust in time series forecasting especially short-term prediction [96].
- **Several LSTM based algorithm:** Different with the proposed one LSTM method, every zone of several LSTM based method requires its own LSTM and so there are  $\left(\frac{N_s}{N_c}\right)^2$  LSTM

in this scheme, as shown in Fig. 4.8. The input of the several LSTM networks is still the 2 D (spatial and temporal domain) zones. Therefore, it can also exploit spatial and temporal features at the same time of distribution prediction.

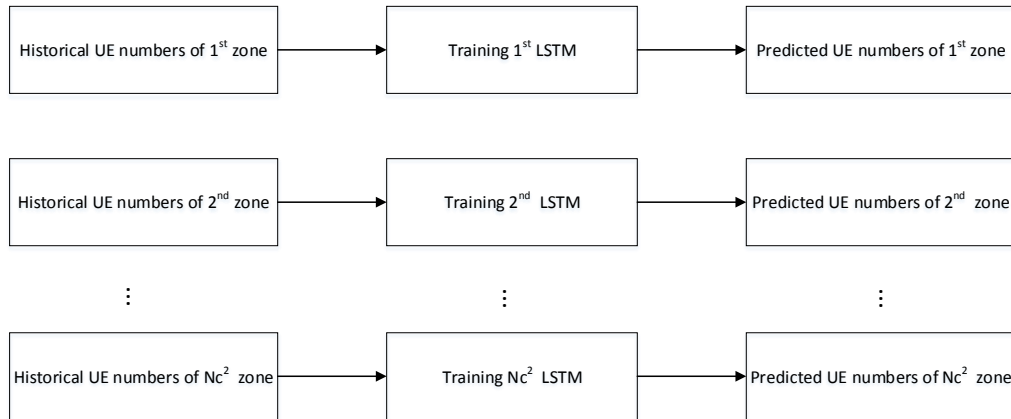


Figure 4.8: Structure of several LSTM based prediction method.

- **ConvLSTM:** By adding a convolutional layer to LSTMs, the ConvLSTM enables to capture spatio-temporal features of data for precipitation nowcasting [97]. The idea of convolutional LSTM models has been employed in many prediction studies. At the bottom of the model, the convolutional neural network (CNN) automatically extracts the spatial features which have embedded the information revealing the spatial correlations among the different sites. On top of the CNN, an LSTM is built to capture the temporal dependency among the spatial features, chronologically extracted by the CNN. The differences between ConvLSTM and LSTM are that ConvLSTM changes the feedforward method of LSTM from Hadamard product to convolution [98].

## 4.6.2 Simulation Conditions

LSTM models are trained on the first 1320 hours of data (first 55 days) and tested on the 24 hours (one day) of data. Their performances were evaluated by computing the RMSE (Root Mean Square Error) value of  $i^{th}$  grid [94]:

$$RMS E_i = \sqrt{\frac{1}{z} \sum_{t=1}^z (x_t^i - \hat{x}_t^i)^2}, \quad (4.9)$$

where  $\hat{x}_t^i$  and  $x_t^i$  are the predicted CDR numbers of  $i^{th}$  grid and the ground truth, respectively;  $z$  is the number of all predicted values.

Table 4.1: The parameters of the LSTM and ConvLSTM for user density prediction.

Parameters	LSTM	ConvLSTM
hidden layer numbers	2	1 and 2
hidden nodes of the first layer	50	50
hidden nodes of the second layer	25	25
Batch Size	64	64
Time Steps	24	24
Training Steps	150	150
Grid numbers for each time step	5*5 and 2*2	2*2, 5*5 and 10*10
Kernel size	N/A	2*2 and 5*5

ARIMA models are generally denoted ARIMA(p,d,q) where parameters p is the number of autoregressive terms, d is the degree of differencing and q is the size of the moving average window [96]. In our simulation, an ARIMA(2,2,0) is modeled by using the python statsmodels. The LSTM and ConvLSTM are built by using Keras of Tensorflow. We use Adam optimizer with learning rate=0.001, beta1=0.9, beta2=0.999 and epsilon=1e-08. In order to achieve the best results, the hyperparameters of LSTM should be adjusted and the main parameters of the LSTM and ConvLSTM neural network are shown in Table. 4.1 [96]. The time steps refer to the length of the input series and the batch size denotes the data number of each batch. The batch size should be selected carefully to find a tradeoff between the accuracy and the speed of the training. The kernel size of ConvLSTM means the size of a convolution filter. We assume that the CDR numbers of the given grid are impacted by the neighboring  $5 \times 5$  grids or  $2 \times 2$  grids. Therefore, the size of the 2D zones is (25,1320) or (4,1320).

### 4.6.3 Data Preprocessing

In order to reduce the impact of noise on time series, wavelet-based filtering is used to smooth the raw data. The performance of the wavelet filter on 20-th grid is shown in Fig. 4.9. Compared with the original data, the processed data reduced the high-frequency noise with the same shape.

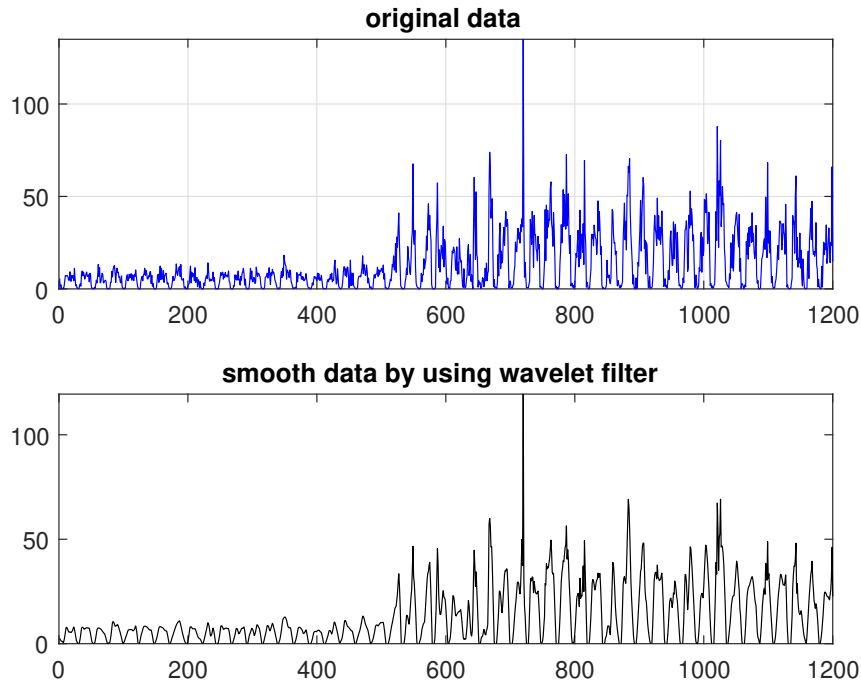


Figure 4.9: Evaluation of wavelet-based filter on 20th grid

### 4.6.4 CDR Numbers Forecasting Comparison

#### 4.6.4.1 Compare one LSTM with ARIMA and several LSTM

This section provides the comparison among one LSTM, several LSTM and ARIMA methods. The experiment is conducted on Milan downtown with about 1600 grids. Fig.4.10 and Fig. 4.11 demonstrate the distribution and cumulative distribution function (CDF) of forecasting RMSE of three methods, respectively.

Compared with the ARIMA, deep learning approaches based on LSTM have much better performance. The reason is that the LSTM can capture long-term dependencies due to its ro-

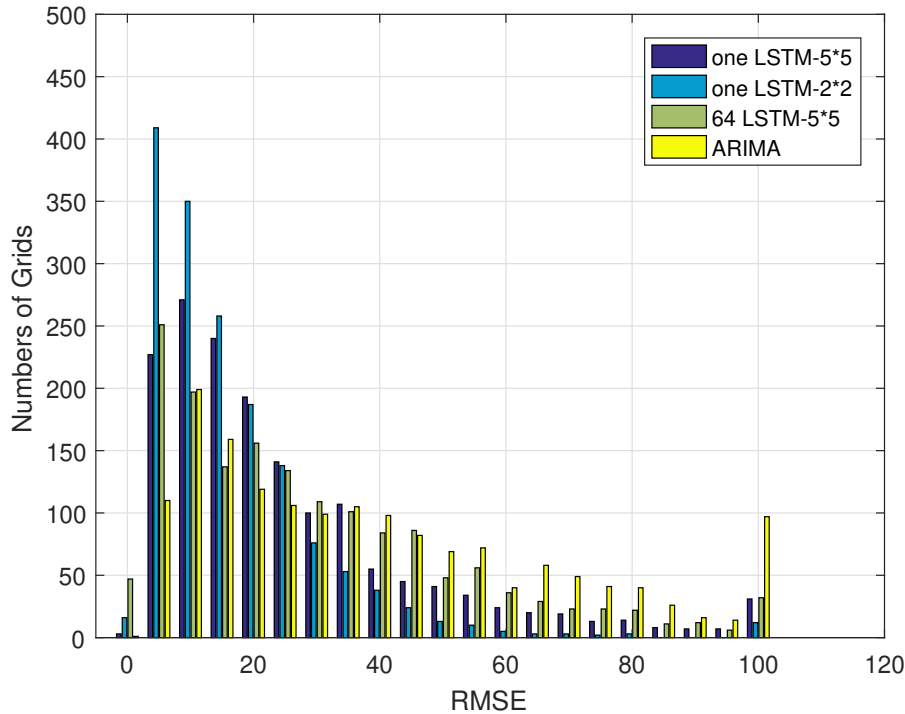


Figure 4.10: Histogram Comparison among one LSTM, several LSTM and ARIMA methods based user density prediction

bust nature and feedback connections. By comparing the two improved LSTM based scheme with  $5 \times 5$  zones, we can find that the 64 LSTM scheme has more grids whose  $RMSE < 10$  than that of one LSTM. There are 24 grids with several LSTM less than 5 RMSE and 2 grids less than 5 RMSE by using one LSTM. In several LSTM based scheme, every LSTM is training specifically for each grid and so it gets some higher accuracy results. However, due to overfitting and lower diversity of samples, the overall performance of several LSTM based scheme is worse than that of one LSTM based scheme. Specifically, there are 75% grids within 30 RMSE using one LSTM and 65% grids within 30 RMSE using several LSTM. Therefore, the one LSTM based method is the best choice with higher RMSE performance and lower complexity. What's more, we also noted that the performance of the one LSTM based scheme can be significantly improved around 12.5% by reducing the zone size from  $5 \times 5$  to with  $2 \times 2$ . There are two reasons. On the one hand, by adopting smaller zones, the number of samples, which can be used to train the LSTM, is increased. On the other hand, it also proves that the spatial correlation among neighboring 4 grids is larger than that of neighboring 25 grids. In

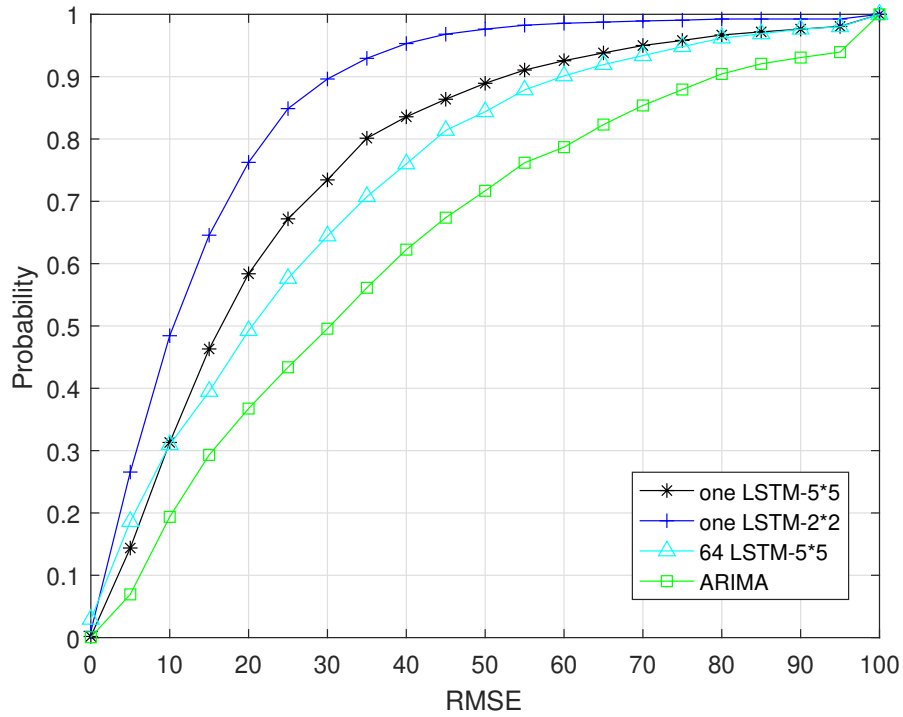


Figure 4.11: CDF Comparison among one LSTM, several LSTM and ARIMA methods based user density prediction

summary, the one LSTM whose input zone size is  $2 \times 2$  has the best performance with low complexity. Therefore, it can be selected as the candidate scheme to compare with the ConvLSTM in the following part.

#### 4.6.4.2 Compare one LSTM with ConvLSTM

This section provides the comparison between one LSTM and ConvLSTM methods. Fig.4.12 and Fig.4.13 demonstrate the distribution and cumulative distribution function (CDF) of forecasting RMSE of the two schemes for different conditions, respectively. As shown in Fig.4.12, comparing with one LSTM with  $2 \times 2$  zones, ConvLSTM with  $2 \times 2$  kernel size and  $2 \times 2$  zones has more grids whose  $RMSE < 10$ , because the convolution filter can further capture spatial-domain features. However, the ConvLSTM whose zone size and kernel size are  $2 \times 2$  has a similar CDF performance with that of one LSTM based method. It means that our proposed one LSTM based method enables to explore the temporal-spatial features for the small zone (4 grids) without the Convolutional layer. Furthermore, with the same kernel size, the RMSE

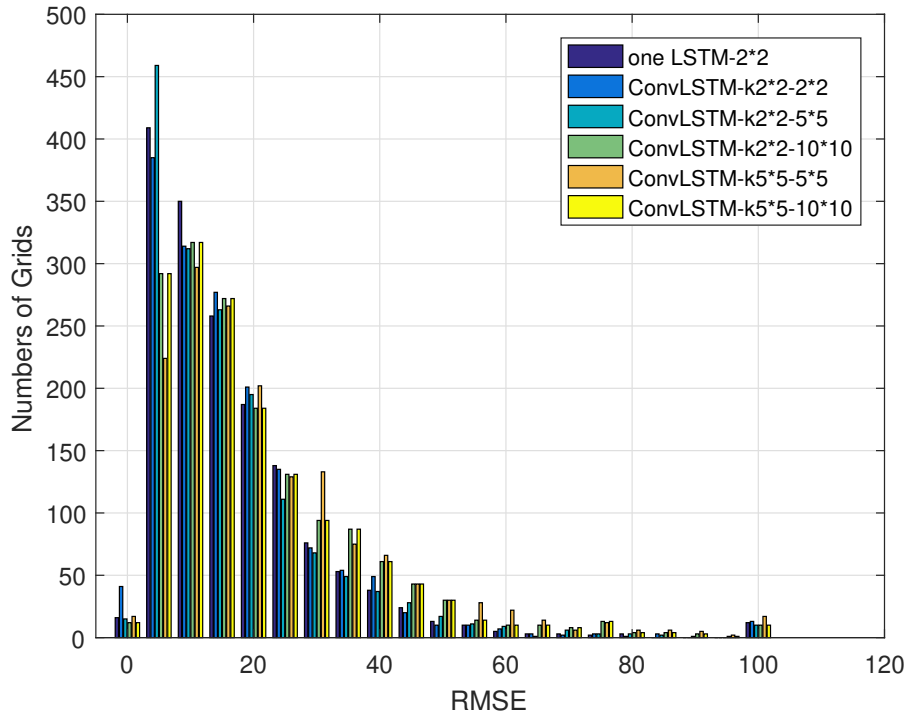


Figure 4.12: Histogram Comparison among one LSTM, several LSTM and ARIMA methods based user density prediction

performance decreased around 15% with the zone size increase from  $2 \times 2$  to  $10 \times 10$ . The reason is that the larger zone size causes less training sample diversity in the spatial domain and so reduce the prediction accuracy.

#### 4.6.5 Accuracy Evaluation of Hotspot Prediction

Based on the predicted CDR numbers of each grid, the predicted user distribution can be obtained to detect the hotspot. In Fig.4.14, by comparing the predicted heatmap using one LSTM ( $2 \times 2$ ) with the real heatmap for two typical cases (7:00 am and 3:00 pm), it can be seen that the predicted results have high reliability. For example, the hotspots of early morning 7:00 am are around the (20,20) and (36,35) grids. The highest density area of predicted distribution is also around these areas. Compared with the heatmap of ground truth at 3:00 pm, the predicted heatmap has a similar distribution.



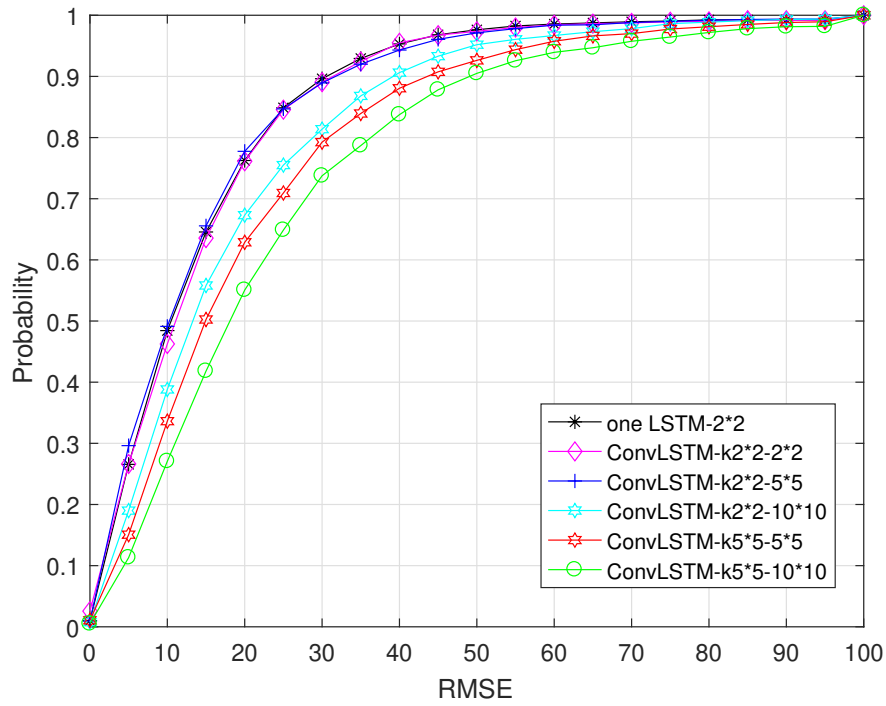


Figure 4.13: CDF Comparison among one LSTM, several LSTM and ARIMA methods

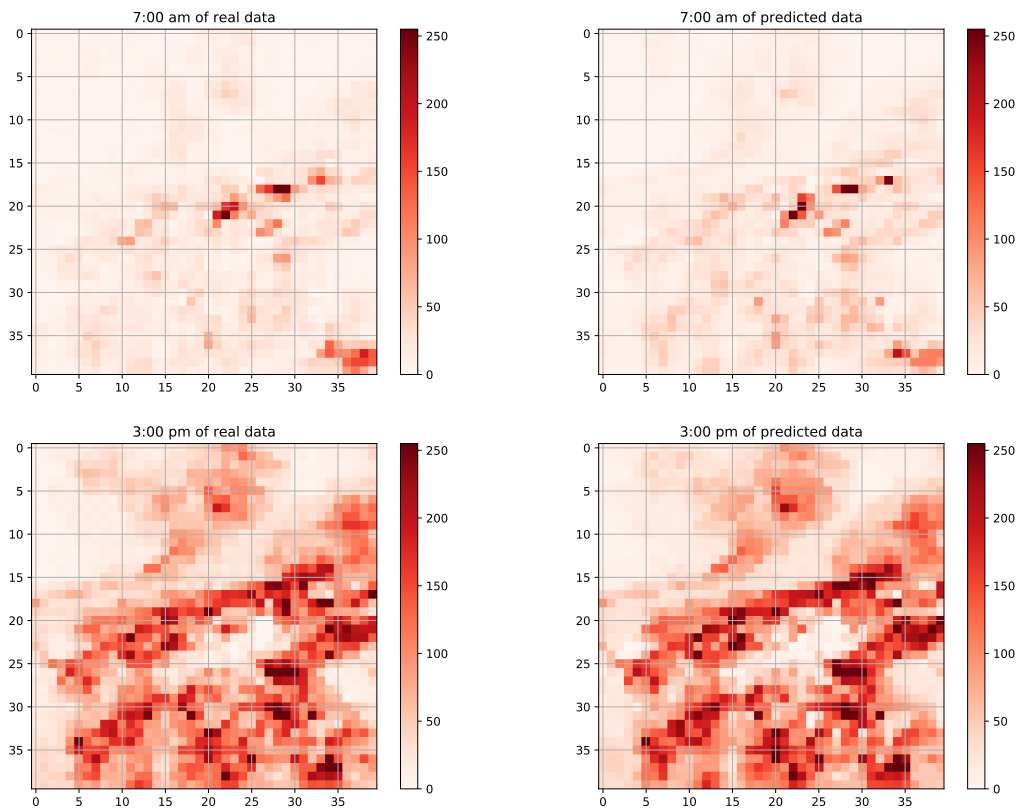


Figure 4.14: Heatmap comparison between ground truth and predicted values.

### 4.6.6 Performance of Hotspot Prediction based VSC

Based on the hotspot prediction, the center and radius of a VSC can be obtained to facilitate the beamforming design. In order to evaluate the performance of the hotspot prediction based VSC, a link-level simulation is built. Similar to Chapter 3, a heterogeneous network, where five VSCs deployed in one macro-cell, is considered. There are 30 users randomly distributed in the whole macro-cell. One CH, equipped with one antenna, is deployed in each VSC and one MBS, equipped with 128 antennas and 60 RF, is located at the center of macro-cell. The main parameters are given in Table 3.1.

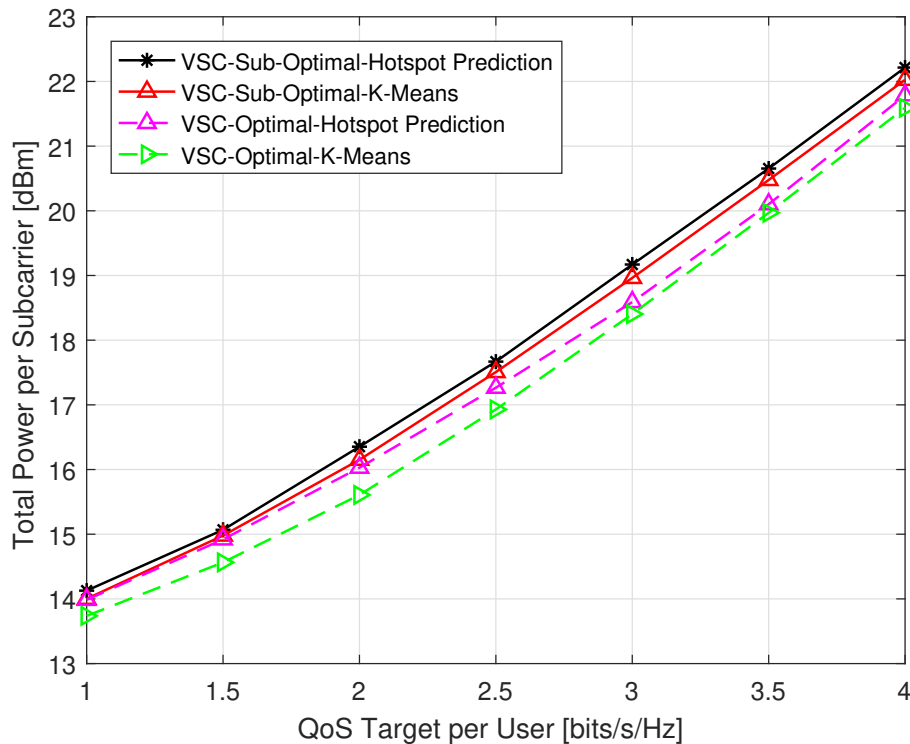


Figure 4.15: Power consumption comparison between K-means based VSC and hotspot prediction based VSC.

Fig. 4.15 compares the total power consumption of hotspot prediction based VSC and that of K-means based VSC. The VSC by using K-means clustering has a little (around 5%) better energy efficiency than that of VSC with hotspot prediction. The reason is that the radius of hotspots by using LSTM is fixed whereas the radius of hotspots by using K-means clustering is dynamic according to the perfect user distribution. However, the traditional clustering al-

gorithm, such as K-means, requires the accurate real-time location of each user whereas the proposed hotspot prediction only requires the historical records of UE numbers in each small zone. On the other hand, the complexity of plain k-means is  $O(nkdi)$ , where  $n$  is the number of samples,  $k$  is the number of clusters,  $d$  is the dimensionality of the data and  $i$  the number of iterations performed until convergence. It means that the total computational time increases with the increase in UE numbers, which will introduce latency. As mentioned before, we use off-line data to train the LSTM and hence the hotspots can be identified in advance to reduce the latency caused by the traditional clustering algorithm. In summary, the proposed VSC operation assisted with hotspot prediction can not only achieve comparable performance to that of VSC with traditional clustering methods but also obtain the additional benefit of reduced processing latency.

## 4.7 Chapter Summary

This chapter adopts a deep learning approach to forecast hotspot for supporting the operation of VSCs with high-cost efficiency and low latency. This topic focuses on 1) how to predict the hotspots by using deep learning, and then 2) demonstrates how the predictions can be leveraged to support adaptive beamforming and VSC operation. We first leverage the feature extraction capabilities of deep learning and exploit the use of a long short term memory (LSTM) neural network to achieve hotspot prediction for the potential formation of the VSCs. Specifically, the one LSTM neural network is unitized to predict the UE numbers of every grid due to its capability of learning long-term dependencies. By analyzing the predicted network-level user distribution, the hotspot can be detected to form the VSC in advance. By using a real data set of telecommunication, the simulation results show that, compared with several LSTM based method and ConvLSTM, one LSTM based method can predict the user distribution with high accuracy by using a simple network architecture. Our simulation results also demonstrate that compared with the scenario of VSC relying on traditional clustering, the proposed VSC operation assisted with the hotspot prediction can achieve higher power efficiency as well as lower processing latency.

## **Chapter 5**

# **Multi-Dimensional Intelligent Multiple Access for 5G Beyond Networks**

The ever-growing wireless applications and their diverse Quality of Service (QoS) requirements bring the challenge of tailored QoS provisioning with limited radio resources in future cellular networks. While resource constraint is ubiquitous, different communication equipment in cellular networks could experience very different constraints in a multi-dimensional resource domain. To achieve stringent yet diverse QoS with limited resources, a novel multi-dimensional intelligent multiple access (MD-IMA) scheme is proposed in this chapter to exploit disparate resource constraints among heterogeneous equipment for 5G beyond and 6G networks. With the assist of real-time data analysis, real-time QoS requirements and resource availability of the related equipment are first determined in the proposed MD-IMA. Based on this, multiple access (MA) scheme is then intelligently adapted accordingly for each equipment in multi-dimensional resource domain to maximize the system requirement as well as minimize the non-orthogonality with operation constraints. The resource allocation in the MD-IMA system is further formulated as an optimization problem. To solve this non-convexity optimization of high computational complexity, the overall optimization is divided into several sub-problems and a joint optimization algorithm is adopted. Simulation results demonstrate the achievable WEE gain of proposed MD-IMA over NOMA and OMA is approximately 15% and 18%, respectively.

## 5.1 Introduction

With the completion of 3GPP Release 15, 2019 has become the first year for the 5G commercialization[99]. While a number of new features have been included, the current 5G standard is still lack of critical solutions in supporting diverse Quality of Service (QoS) provisioning, particularly for massive machine-type communications (mMTC) and ultra-reliable low-latency communications (uRLLC). With ever-growing data traffic, increasing of total connected devices and ongoing convergence of wireless networks and vertical industry applications, critical design considerations for future wireless networks, e.g. 5G and beyond as well as 6G, are focused on diverse QoS provisioning techniques that can intelligently and efficiently utilize the constrained resources to achieve stringently and customized QoS [100]. The future 6G network is expected to be a multipurpose platform to enable a wide variety of applications and services, ranging from extended reality services to autonomous driving, smart city, telemedicine, and smart industry [101].

Emerging applications to be supported by 6G typically require a very different set of QoS parameters, including data rate, reliability, power consumption, latency, etc. For instance, augmented reality (AR) service requires high-reliability, low latency with super-high data rates [?], whereas smart wearable applications focus on low power consumption as well as potential high deployment density [26]. On the other hand, different devices and base stations could experience very different resource constraints in terms of power/battery supply and spectrum availability. Furthermore, the use of mmWave band and expanded bandwidth also dramatically increase resource heterogeneity in future wireless networks. In achieving diverse QoS with disparate resource constraints, new multiple access techniques in spatial/temporal/frequency domain should be proposed in the future wireless access networks. Consequently, more intelligent resource allocation and multiple access techniques play extremely important roles in fully utilizing situation-dependent multi-dimensional resources.

Under highly diverse and complex QoS requirements from the rich application domains, 6G will require an intelligent and efficient network fabric that flexibly utilizes and orchestrates multi-dimensional resources to continuously adapt to the current state and requirements of the wireless environment. In fact, several new radio access technologies, including massive

multiple-input multiple-output (MIMO) and non-orthogonal multiple access (NOMA), have been adopted in the 5G wireless network to improve the capacity and spectrum efficiency by exploiting extra resource dimension and introducing the non-orthogonality [102]. Specifically, NOMA can exploit the power and code domain resources to allow overlapped multiple user signals on the same resource block (RB) [35]. However, simply utilizing the NOMA to replace the conventional orthogonal multiple access (OMA) will not only increase the receiver complexity but also waste resources in most low traffic scenarios. With the evolution of 5G into 6G, there will be an urgent need for new intelligent multiple access (MA) techniques that can dynamically change the type of MA by unifying OMA, power-domain NOMA or spatial-domain NOMA according to the application requirements and the network situation.

Furthermore, new access techniques are needed to fully explore the disparate resource constraints among devices and networks in 6G. We first realize that radio resources for wireless communications can be divided into two categories: replenishable radio resource and non-replenishable radio resources. The replenishable resources, including the transmission time, frequency, code, and space, can be used over and over without any implication for future resource constraints, whereas the non-replenishable resources, such as transmission power, cannot be regenerated once utilized. Therefore, the power resources are very precious, especially for low-power devices. In addition, replenishable radio resources cannot be saved for future use as well. Opportunistic use of these properties of radio resources also requires more sophisticated multiple access and radio resource utilization schemes. However, from a signal processing point of view, NOMA techniques inevitably lead to extra power consumption at the device terminal because of the interference cancellation requirement [103], [104]. In order to reduce the power consumption caused by non-orthogonality, maximizing the separation distance among the resources allocated to the co-existing devices in the multi-dimension resource domain should be considered as one of the main design objectives for 6G networks.

To address the above issues, we propose a new multi-dimensional intelligent multiple access (MD-IMA) scheme that can adaptively multiplex co-existing devices in multi-dimensional resources to maximize the overall QoS as well as minimize their mutual non-orthogonality. To assist the operation of MD-IMA, the diverse set of QoS requirements will be determined by monitoring the requirements of the application. In order to evaluate the overall performance

of the MD-IMA, a new indicator of integrated-quality-of-system-experience (I-QoSE) is proposed for MD-IMA to integrate diverse QoS, such as rate, power consumption, and latency into one aggregated metric. Furthermore, the new I-QoSE metric could be adaptively adjusted to meet the diverse and varying 6G services and applications.

Specifically, the proposed MD-IMA consists of two phases- the definition of I-QoSE and multi-dimensional resource allocation for MD-IMA. In the first phase, a device-specific and situation-dependent I-QoSE is determined by combining all relevant metrics (e.g. power consumption, delay, and throughput) with different weights. The weight of each metric is determined by utilizing the closed-loop situation-awareness discovery through real-time data analytics [105], [106]. Then the following challenge of applying MD-IMA lies in resource allocation is how to fully and efficiently coordinate the use of available multi-dimensional resources.

There are many researchers have devoted efforts to studying the resource allocation in the NOMA, MIMO-NOMA, and hybrid NOMA systems. In [107], an optimal power allocation algorithm is proposed for the NOMA system to maximize the throughput rate considering individual QoS constraints. Wang et al. [108] developed a joint subchannel assignment and power allocation algorithm to maximize the energy efficiency under the constraints of transmit power and the required rate of each user. To further explore the spatial domain multiplexing, the resource allocation for 5G MIMO-NOMA is formulated in [109] as the max-sum-rate problem and solve by beamforming and user selection process. In [110], a dynamic user clustering algorithm is proposed firstly and then a joint channel assignment and power allocation optimization are designed for multi-cell MIMO-NOMA networks. Furthermore, by combining the NOMA with OMA, a novel concept of hybrid multiple access system was firstly introduced in [111] and the simulation results illustrated that, compared with the NOMA and OMA, the proposed hybrid NOMA has a better fairness performance. Energy-efficient power allocation for the hybrid multiple access systems is further developed in [112]. Authors in [113] proposed a joint resource allocation by using the heuristic optimization algorithm to achieve the trade-off between the spectrum and energy efficiency for hybrid multiple access systems. We noted that the objective of resource allocation in the NOMA related works almost utilized fixed single metrics, such as power consumption and sum rate, which cannot meet the demands of changing and diverse services in 6G networks. Most importantly, existing NOMA related works ignored

the extra computational complexity and power consumption at the user terminal caused by the interference cancellation due to the inherent non-orthogonality.

Motivated by the above observations, in the second stage of proposed MD-IMA, the goal of our resource allocation problem of the MD-IMA system is to maximize the real-time I-QoSE as well as minimize the non-orthogonality under constraints of power consumption and the QoS requirement of each user. Then a joint resource allocation of the user clustering, subchannel assignment and power allocation is proposed for the MD-IMA system.

The major contributions of this chapter are listed as follows:

1. A novel multi-dimensional intelligent multiple access (MD-IMA) scheme is proposed to exploit disparate resource constraints among heterogeneous equipment for 5G beyond and 6G networks. With the proposed MD-IMA, multi-dimensional resources can be fully utilized in achieving application-specific real-time QoS requirements.
2. A new concept named I-QoSE is developed to quantify the overall communication performance, which scales the different aspects of QoS with relevant weights. Moreover, the I-QoSE can be adjusted by tuning the weight of each metric to dynamically follow the changes in the service requirements.
3. In the resource allocation for MD-IMA, minimizing total non-orthogonality among concurrent users is imposed as one of the objectives, which is different from previous literature. The non-orthogonality in terms of spatial and power domain are modeled, respectively. The spatial-domain non-orthogonality heavily depends on how the devices are grouped. In this chapter, we adopt the K-means method to cluster users and choose the cluster numbers by minimizing the non-orthogonality in the spatial domain. Then a sub-optimal algorithm is proposed to jointly design subchannel and power allocation to find the trade-off between I-QoSE and non-orthogonality by using an alternative optimization algorithm.
4. While existing NOMA schemes use a single domain, the proposed MD-IMA can use as many domains as possible at the same time. Therefore, it is possible for the proposed MD-IMA to separate the co-existing devices by using low interference cancellation. The



proposed MD-IMA is achieved through maximizing the separation distance among the resource blocks allocated to co-existing devices in the multi-dimensional resources, including frequency, time, space, power and code domains.

The rest of this chapter is structured as follows. Section 5.2 introduces the network architecture of the proposed MD-IMA. In Section 5.3, the resource allocation problem for maximizing I-QoSE and minimizing NO is formulated as an optimization problem. Then sub-optimal solution is elaborated in Sections 5.4. Section 5.5 presents our simulation results regarding the I-QoSE and NO performance of the proposed MD-IMA compared with the OMA-MIMO and NOMA-MIMO scenarios. Finally, the conclusions are provided in Section 5.6.

## 5.2 System Model

The network architecture of the proposed intelligent and situation-awareness resource allocation for MD-IMA system is shown in Fig.5.1. The proposed MD-IMA can be achieved through two stages. In the first stage, the real-time system requirement and the non-orthogonality among UEs can be obtained by estimating the channel information and monitoring the network situations. Then the UEs are adaptively multiplexed to multi-dimensional resources to meet the diverse and varying requirements.

Specifically, the time division duplex (TDD) system is adopted in this work, and so we can obtain the downlink channel state information (CSI) by measuring the uplink CSI due to channel reciprocity [114]. According to the estimated downlink CSI, the non-orthogonality among UEs in spatial domain and power domain can be calculated. Furthermore, in order to jointly consider the diverse requirement, a new concept of I-QoSE is proposed in this chapter to combine all relevant performance metrics together with a weight-based approach. To further keep up with the changes of requirements and available resources, the weights of metrics are adjusted adaptively according to the real-time network traffic-awareness. As shown in Fig. 5.1, the local database collects massive information, including UE information, requirements and the available resources. Based on the collected real-time information, the kinds of metrics and the weights of every metric can be determined. If the sum-rate (SR), power consumption (PC) and delay (D) are considered as the three possible metrics, the mathematical expression

of I-QoSE is:

$$I - QoSE = \alpha_1 \times SR - \alpha_2 \times PC - \alpha_3 \times D, \alpha_1 + \alpha_2 + \alpha_3 = 1. \quad (5.1)$$

Where  $\alpha_1, \alpha_2$  and  $\alpha_3$  represent the weight value of the throughput rate, power consumption, and delay, respectively. These weight values are determined according to the real-time QoS requirements and available resources. The higher weight means the corresponding metric is more important. For example, if most devices are wearable sensors and the so minimizing power consumption is the most important objective of resource allocation and the weight of power consumption metric should be the highest. Then the UEs are allocated to multi-dimensional resources to maximize I-QoSE as well as minimize NO under several corresponding constraints. In terms of the whole network architecture, we assume that there is one BS,

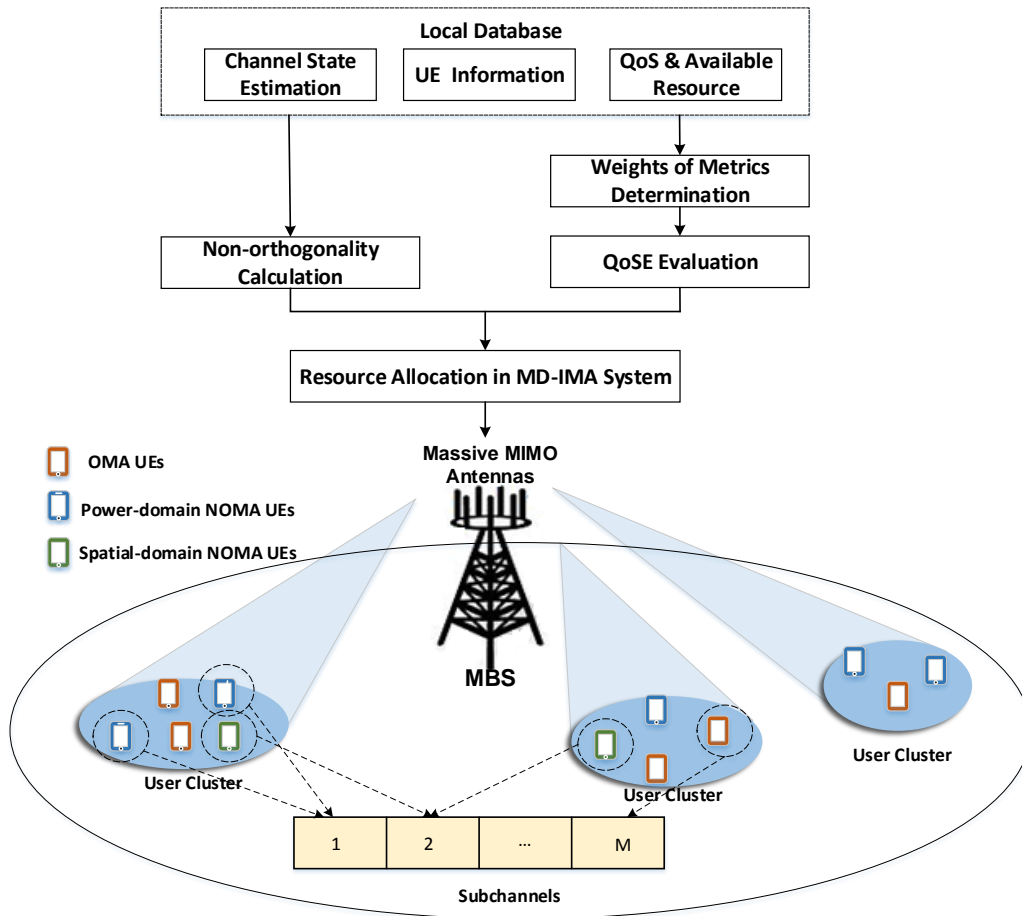


Figure 5.1: Intelligent and situation-aware resource allocation in MD-IMA system.

equipped with  $N_t$  transmit antennas at the center of the cell to serve  $K$  UEs, equipped with one antenna and denoted as  $\mathcal{K} = \{1, \dots, K\}$ . From Fig. 5.1, we can see that  $K$  UEs are divided into  $C$  clusters in spatial domain according to the geolocation information and the BS form beamforming to cover these clusters. The UEs in each cluster are represented by  $\{\mathcal{S}_1, \dots, \mathcal{S}_C\}$  and we have  $\bigcup_{c=1}^C \mathcal{S}_c = K$ . We divided the total bandwidth  $B$  into  $M$  orthogonal subchannels (SCs), which is defined as  $\mathcal{M} = \{1, \dots, M\}$ . In the same cluster, the UEs (colored blue) who have large channel gain differences can be assigned in the same SC by using power-domain NOMA and they can be distinguished at the receiver by adopting SIC. In different clusters, the UEs (colored green) who have large non-orthogonality in the spatial domain can be allocated in the same SC. The number of UEs which can be assigned on  $m$ -th SC is denoted by  $L_m, m \in \mathcal{M}$ . If  $L_m = 1$ , the  $m$ -th SC is regarded as a OMA-SC, whereas it is denoted as a NOMA-SC when  $L_m > 1$ . According to the non-orthogonality among UEs and the available resource,  $K$  UEs are adaptively assigned to  $M$  SCs in multi-dimension and each SC has different UE numbers. In order to simplify the problem, each UE is only allowed to be allocated to one SC and we assume  $K = \sum_{m=1}^M L_m$ . Motivated to meet vary diverse requirements, the power constraints of each SC, denoted by  $\{P_m, \forall m \in \mathcal{M}\}$ , can be different.

### 5.3 Problem Formulation

In many existing publications [115]-[116], the resource allocation for NOMA related systems is generally designed for maximizing the sum-rate, energy efficiency and spectral efficiency. However, the fixed performance metric cannot meet the diverse and varying QoS requirements of future networks. To solve this problem, a novel performance metric of I-QoSE, combing several QoS aspects with different weights, can be adaptively obtained according to the collected real-time information from UEs and the environment. Furthermore, most of the current works only use single-domain NOMA and also ignored the decoding complexity caused by non-orthogonality when using NOMA. In our proposed MD-IMA system, to fully utilize the available resources, all the degrees of freedom in resource allocation are jointly considered. The objective resource allocation of MD-IMA is to maximize the real-time overall system performance (I-QoSE) and minimize the receiver complexity at the same time. To simplify the

resource allocation problem, we only consider the sum-rate and power consumption firstly and so the I-QoSE can be regarded as weighted energy efficiency (WEE)  $\eta_{EE}^w$ . Therefore, the objective of resource allocation is equivalent to maximize the WEE as well as minimize NO. Before formulating the resource allocation problem, the achievable data rate, weighted energy efficiency, and non-orthogonality are analyzed below.

### 5.3.1 Achievable Rate

The  $c$ -th cluster and its corresponding UEs  $\mathcal{S}_c$  are adopted as an example to calculate the signal-to-interference-plus-noise rate (SINR) and the achievable rate. The interference for the received signals of the  $k$ -th UE on the  $n$ -th SC in cluster  $c$  consists of the intra-cluster interferences, the inter-cluster interferences, and the noise. The intra-cluster interferences are introduced by other UEs, whose channel gains are lower than that of  $k$ -th UE, in cluster  $c$  on the  $n$ -th SC, while the inter-cluster interferences come from the UEs in neighboring clusters on the  $n$ -th SC.

The principle behind the power-domain NOMA is adding power domain multiplexing on transmitter side to overlap users on the same subchannel and using SIC on receiver side to realize multi-user detection. Specifically, in the same subchannel, different transmitted power level is allocated to different UEs according to their channel gains. The received symbols should be detected in order of decreasing of channel gains. It means the UEs with poorer channel conditions are decoded firstly and are subtracted one by one [117]. The vector of the complex coefficients between the BS and UE  $k$  in  $c$ -th cluster on  $m$ -th SC is defined as  $\mathbf{h}_{k,m,c} = \mathbf{g}_{k,m,c} PL^{-1}(d) \in \mathbb{C}^{N_t \times 1}$ , where  $\mathbf{g}_{k,m,c}$  follows the Rayleigh fading and  $PL^{-1}(d)$  denotes the path loss from the BS to the UE  $k$  [37]. Let  $\mathbf{w}_c \in \mathbb{C}^{N_t \times N_t}$  be the beamforming matrix from BS to cluster  $c$ . We also define power allocation matrix  $\mathbf{P} \in \mathbb{C}^{K \times M \times C}$ , where  $[\mathbf{P}] = p_{k,m,c}$  denotes the downlink transmission power between BS and  $k$ -th UE on  $m$ -th subchannel in cluster  $c$ . The subchannel assignment scheme is reflected by matrix  $\mathbf{S} \in \mathbb{C}^{K \times M \times C}$ , where  $[\mathbf{S}] = s_{k,m,c}$  is the subchannel indicator. We set  $s_{k,m,c} = 1$  when the  $m$ -th subchannel is occupied by the UE  $k$  in cluster  $c$ , otherwise,  $s_{k,m,c} = 0$ . The intra-cluster interference of UE  $k$  in  $c$  th cluster on  $m$ -th subchannel can be given by:

$$I_{k,m,c}^{intra} = |\mathbf{h}_{k,m,c}^H \mathbf{w}_c|^2 \sum_{i \in \mathcal{S}_{c,k}} s_{i,m,c} p_{i,m,c}, \quad (5.2)$$

where  $\mathcal{S}_{c,k} = \{i | i \in \mathcal{S}_c, h_{k,m,c} > h_{i,m,c}\}$  denotes the set of UEs in  $\mathcal{S}_c$  on SC  $n$  who have worse channel than  $k$ -th UE. The inter-cluster interferences can be given by:

$$I_{k,m,c}^{inter} = |\mathbf{h}_{k,m,c}^H|^2 \sum_{i \neq c}^C \sum_{j=1}^K s_{j,m,i} p_{j,m,i} |\mathbf{w}_i|^2. \quad (5.3)$$

Therefore, the SINR of the received signal from UE  $k$  on  $m$ -th subchannel in cluster  $c$  is

$$\gamma_{k,m,c} = \frac{p_{k,m,c} |\mathbf{h}_{k,m,c}^H \mathbf{w}_c|^2}{I_{k,m,c}^{intra} + I_{k,m,c}^{inter} + \delta^2}, \quad (5.4)$$

where  $\delta^2$  represents the variance of additive Gaussian noise, and so the data rate of UE  $k$  on  $m$ -th subchannel in cluster  $c$  is

$$R_{k,m,c} = \frac{B}{M} \log_2 (1 + \gamma_{k,m,c}). \quad (5.5)$$

### 5.3.2 Weighted Energy Efficiency

In this chapter, we adopt the weighted energy efficiency as the I-QoSE to achieve MD-IMA system firstly and the weighted energy efficiency (WEE) is given by:

$$\eta_{EE}^w = \frac{\alpha_1 \sum_{k=1}^K \sum_{m=1}^M \sum_{c=1}^C s_{k,m,c} R_{k,m,c}}{\alpha_2 P_{total}}, \quad (5.6)$$

where  $\alpha_1$  and  $\alpha_2$  are the weight values for sum-rate and total power consumption, respectively. The varying WEE is achieved by dynamically tuning the weight values according to the requirement of the system. Furthermore,  $P_{total}$  denotes the total power consumption of BS, which is composed of the circuit power consumption,  $P_h$ , depending on the hardware design

of BS and the transmit power  $P_b$  which is related to the power allocation [78]:

$$P_b = \sum_{k=1}^K \sum_{m=1}^M \sum_{c=1}^C s_{k,m,c} P_{k,m,c}, \quad (5.7)$$

$$P_h = \xi_0 N_t,$$

where,  $\xi_0$  represents the circuits power consumption of each antenna.

### 5.3.3 Non-orthogonality Calculation

The total non-orthogonality  $T^{NO}$  is the summation of the total non-orthogonality in spatial domain, representing by  $T_s^{NO}$ , and the non-orthogonality in power domain, defining as  $T_p^{NO}$ :

$$T^{NO} = T_s^{NO} + T_p^{NO}. \quad (5.8)$$

#### 5.3.3.1 The Non-orthogonality in Space Domain

The non-orthogonality in the spatial domain is caused by UEs who are overlapped on the same SC but belong to different clusters, which is defined as

$$T_s^{NO} = \sum_{k=1}^K \sum_{m=1}^M \sum_{c=1}^C \left( \sum_{i=k+1}^K \sum_{j \neq c}^C \frac{\|s_{k,m,c} h_{k,m,c}\| \|s_{i,m,j} h_{i,m,j}\|}{\|s_{k,m,c} h_{k,m,c} \times s_{i,m,j} h_{i,m,j}^*\|} \right). \quad (5.9)$$

#### 5.3.3.2 The Non-orthogonality in Power Domain

The non-orthogonality in power domain is introduced by UEs who are assigned on the same SC and in the same cluster. The proposed SIC can successfully decoding the overlapped UEs when their channel gains difference are significantly high. Therefore, the non-orthogonality in power domain is depend on their channel gain difference, which is defined as:

$$T_p^{NO} = \sum_{k=1}^K \sum_{m=1}^M \sum_{c=1}^C \left( \frac{1}{1 - \frac{\min(|s_{k,m,c} h_{k,m,c}|, |\sum_{i \neq k}^K s_{i,m,c} h_{i,m,c}|)}{\max(|s_{k,m,c} h_{k,m,c}|, |\sum_{i \neq k}^K s_{i,m,c} h_{i,m,c}|)}} \right). \quad (5.10)$$

### 5.3.4 Problem Formulation

The objective of the resource allocation of MD-IMA system is to maximize the WEE as well as minimize the total NO, which can be formulated as an optimization problem (5.11). In this problem, the constraint C1 ensures the maximum transmitted power can no be larger than  $P$  and the constraint C2 is the minimum transmit power requirement which actually guarantees the QoS requirement for each user. The constraints C3 and C4 represent that each UE can be only allocated to one SC, while C5 denotes that maximum  $L_m$  UEs can be allowed to share one SC.

$$\begin{aligned}
 P1 : \{\mathcal{S}^*, \mathcal{P}^*\} &= \arg \max \{\eta_{EE}^w\} & (5.11) \\
 \{\mathcal{S}^*\} &= \arg \min \{T^{NO} = T_s^{NO} + T_p^{NO}\}, \\
 \text{subject to: } C_1 : & \sum_{k=1}^K \sum_{m=1}^M \sum_{c=1}^C s_{k,m,c} p_{k,m,c} \leq P, \\
 C_2 : & \sum_{m=1}^M \sum_{c=1}^C s_{k,m,c} p_{k,m,c} \geq P_k^{\min}, \forall k \in \mathcal{K} \\
 C_3 : & s_{k,m,c} \in \{0, 1\}, \forall m \in \mathcal{M}, \forall k \in \mathcal{K}, \forall c \in \mathcal{C}, \\
 C_4 : & \sum_{m \in \mathcal{M}} s_{k,m,c} = 1, \forall k \in \mathcal{K}, \forall c \in \mathcal{C}, \\
 C_5 : & \sum_{k=1}^K \sum_{c=1}^C s_{k,m,c} = L_m, \forall m \in \mathcal{M}.
 \end{aligned}$$

## 5.4 Sub-optimal Solution

Due to the non-concavity and nonlinearity in the objective function and constraints, Problem (P1) is a non-convex optimization problem, which is too complicated to solve. Therefore, in order to reduce the complexity, the original problem (5.11) is divided into several sub-optimization problems. Furthermore, we propose a sub-optimal resource allocation algorithm, which is shown in Fig. 5.2, to jointly solve the sub-problems of user clustering, subchannel assignment, and the power allocation. Firstly, the UEs are divided into  $M$  clusters in spatial domain according to their locations by using K-means. Then, we achieve optimal subchannel assignment with fixed power allocation through many to many matching algorithms to find

the balance between weighted energy efficiency and the total non-orthogonality. Based on the obtained subchannel allocation scheme, a dynamic power allocation algorithm is proposed to maximize WEE. Finally, joint resource allocation of MD-IMA can be obtained by using an alternative optimization algorithm.

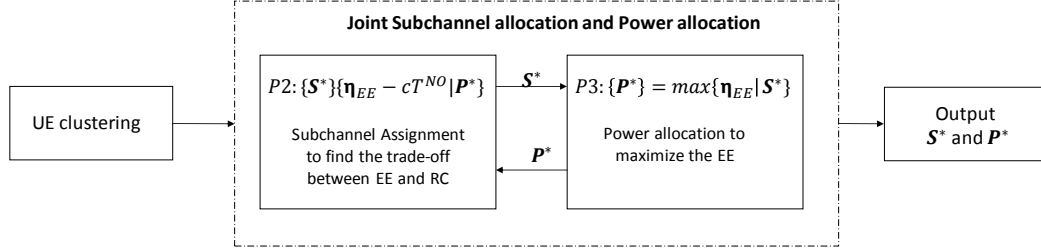


Figure 5.2: Block diagram of the proposed sub-optimal solution for resource allocation problem of MD-IMA network.

#### 5.4.1 User Clustering in Spatial Domain by Using K-means

In this section, the classic K-means [74] is adopted to divide  $K$  UEs to  $C$  clusters ( $K \geq C$ ) in spatial domain. As shown in Algorithm 4, each UE is allocated to the best cluster with the minimum mean squared distance through iteration loops.

---

##### Algorithm 4 K-Means User Clustering

---

- 1: **Input:** user location matrix  $\mathbf{X} = \{x^1, \dots, x^k\}$  and the number of clusters  $C$
  - 2: **initialization:**  $C$  cluster centroids  $\mu_1, \dots, \mu_C$  randomly selected from  $\mathbf{X}$
  - 3: **repeat**
  - 4:   Update cluster assignments
  - 5:   **for**  $i = 1, 2, \dots, K$  **do**
  - 6:      $cc^i = \arg \min_j |x^i - \mu^j|$
  - 7:   **end for**
  - 8:   Update cluster centroids
  - 9:   **for**  $j = 1, 2, \dots, C$  **do**
  - 10:     set  $Cluster_j = \{x^i | cc^i = j\}$
  - 11:     set  $\mu_j = \frac{\sum_{x^i \in Cluster_j} x^i}{|Cluster_j|}$
  - 12:   **end for**
  - 13: **until** center centroids convergency
  - 14: **Output:** cluster centroids  $\mu_{1, \dots, l}$  and cluster assignments  $cc = 0$
- 

Noted that the cluster numbers will impact the performance of the K-means clustering algo-



rithm and so the cluster number should be selected carefully to reduce the non-orthogonality in the spatial domain. After clustering  $K$  UEs into  $C$  clusters, we can set subchannel assignment indicators as:

$$s_{k,m,c} = 0, \forall k \notin \mathcal{S}_c. \quad (5.12)$$

### 5.4.2 Subchannel Assignment

In this section, we will study how to assign the set of UEs  $\mathcal{K} = \{1, 2, \dots, K\}$  to the set of subchannels  $\mathcal{M} = \{1, 2, \dots, M\}$ . Given the clustering in spatial domain, the subchannel assignment problem with fixed power allocation can be reduced from problem (5.11) to:

$$P2 : \{\mathcal{S}^*\} = \arg \max \{OE = \eta_{EE}^w - cT^{NO} | \mathcal{P}\} \quad (5.13)$$

$$\text{subject to: } C_3 - C_5.$$

Inspired by [41]-[36], the above subchannel assignment problem can be solved by using matching theory. As mentioned before, each UEs only can be assigned to one subchannel and at most  $L_m$  UEs can be multiplexed on the same subchannel. When the  $m$ -th subchannel ( $SC_m$ ) is occupied by the  $k$ -th UE ( $UE_k$ ), we say the  $UE_k$  and  $SC_m$  are matched with each other. Each UE and subchannel have their own preference lists, which can be denoted by

$$PF_{UE} = [PF_{UE}(1), \dots, PF_{UE}(k), \dots, PF_{UE}(K)], \quad (5.14)$$

$$PF_{SC} = [PF_{SC}(1), \dots, PF_{SC}(m), \dots, PF_{SC}(M)], \quad (5.15)$$

where  $PF_{UE}(k)$  denotes the preference lists of  $UE_k$  and the  $PF_{SC}(m)$  is the preference lists of  $SC_m$ . The  $k$ -th UE prefers to be assigned to subchannel  $i$  over  $j$  if  $UE_k$  with better channel condition on  $SC_i$  than that on  $SC_j$ , which is expressed as [36]:

$$SC_i(k) > SC_j(k). \quad (5.16)$$

The order of preference lists for SC is based on the weighted energy efficiency and the total non-orthogonality presented in the objective of P2. For example, we say  $SC_m$  prefers UE set  $q_i$  to  $q_j$ , where  $q_i$  and  $q_j$  are denoted as potential UE subsets of  $\mathcal{K}$  on  $m$ -th subchannel, because the former UE subset can provide higher WEE with lower NO. UE set  $\mathcal{K} = \{1, 2, \dots, K\}$  and subchannel set  $\mathcal{M} = \{1, 2, \dots, M\}$  are two disjoint sets.  $\mathcal{P}$  represents a two-sided matching map from all UE subsets  $\mathbf{K}$  into the set of subchannel  $\mathbf{M}$ , where  $UE_k \in \mathcal{K}$  and  $SC_m \in \mathcal{M}$ : (1)

$$\mathcal{P}(UE_k) \in \mathcal{M};$$

$$(2) \mathcal{P}^{-1}(SC_m) \subseteq \mathcal{K};$$

$$(3) |\mathcal{P}(UE_k)| = 1, |\mathcal{P}^{-1}(SC_m)| = L_m;$$

$$(4) SC_m \in \mathcal{P}(UE_k) \Leftrightarrow UE_k \in \mathcal{P}^{-1}(SC_m).$$

Condition 1) represents that each UE is matched with one subchannel and condition 2) implies each subchannel is matched with a subset of UEs. The third condition means that the largest size of  $\mathcal{P}(UE_k)$  and  $\mathcal{P}^{-1}(SC_m)$  is one and  $L_m$ , respectively. Last condition states  $UE_k$  and  $SC_m$  is the matched pair, which is defined as: We assumed that  $UE_k \notin \mathcal{P}^{-1}(SC_m)$  and  $SC_m \notin \mathcal{P}(UE_k)$ . The  $UE_k$  is a prefer to match with  $SC_m$ , if  $OE_m(S_{new}) > OE_m(\mathcal{P}^{-1}(SC_m))$  where  $S_{new} \subseteq UE_k \cup S$  and  $S = \mathcal{P}^{-1}(SC_m)$ .  $S$  represents the UE set which is already allocated to  $SC_m$  and  $S_{new}$  denote the new UE set combing  $UE_k$  and  $S$ . Based on the notation of preference lists, the two-sided matching between UEs and subchannels can be defined as

According to the above definitions, the matching process between the UEs and the subchannels is described in Algorithm 5. To elaborate, each UE firstly selects the most preferred subchannel  $\hat{m}$  based on its preference list. If the number of UEs assigned to the same subchannel is less than  $L_n$ , this request is accepted. Otherwise, selecting  $L_m$  UEs in  $\{S_{Match}(\hat{m}), k\}$ , which has the best OE. The rejected users on subchannel  $\hat{m}$  will be removed from their preference list. The matching process will be terminated until all UEs are allocated with subchannels.

---

**Algorithm 5** Subchannel Assignment Algorithm with Fixed Power Allocation

---

```

1: Initialization:
2: 1) UEs are randomly assigned to subchannels, subjected to the conditions in Definition 1.
3: 2) Record UEs who matched with  $m$ -th subchannel to the matched list  $S_{match}(m)$  for all the
   subchannels  $\forall m \in \{1, 2, \dots, M\}$  and the unmatched UEs to the unmatched list  $S_{unmatch}$ .
4: 3) Obtain the preference lists  $PF_{UE}(k)$ ,  $\forall k \in \{1, 2, \dots, K\}$  and  $PF_{SC}(m)$ ,  $\forall m \in$ 
    $\{1, 2, \dots, M\}$ .
5: while  $S_{unmatch}$  is not empty do
6:   for  $k = 1, 2, \dots, K$  do
7:      $UE_k$  selects its most preferred subchannel  $\hat{m}$  according to  $PF_{UE}(k)$ .
8:     if  $|S_{Match}(\hat{m})| < L_m$  then
9:       Add  $UE_k$  to  $S_{Match}(\hat{m})$ , and remove  $UE_k$  from  $S_{unmatch}$ .
10:    else if  $|S_{Match}(\hat{m})| = L_m$  then
11:      1)  $L_m$  UEs  $S_{q_i}$  who has better OE performance,  $OE_{\hat{m}}(q_i) > OE_{\hat{m}}(q_j)$ ,  $q_i, q_j \in$ 
         $\{S_{Match}(\hat{m}), k\}$  are selected to match the  $\hat{m}$ -th subchannel.
12:      2) The matched list of subchannel  $\hat{m}$  is set as  $S_{Match}(\hat{m}) = q_i$ . Allocated UEs are
        removed from  $S_{unmatch}$ , whereas the unallocated users are added to  $S_{unmatch}$ .
13:      3) Update the preference list of the rejected UEs by removing the subchannel  $\hat{m}$ .
14:    end if
15:  end for
16: end while
17: for  $k = 1, \dots, K$  do
18:   for  $m = 1, \dots, M$  do
19:    for  $c = 1, \dots, C$  do
20:     if  $k \in S_{Match}(m)$  and  $k \in S_c$  then
21:        $s_{k,m,c} = 1$ .
22:     else
23:        $s_{k,m,c} = 0$ .
24:     end if
25:   end for
26: end for
27: end for

```

---

### 5.4.3 Dynamic Power Allocation

Upon deriving the UE clustering and subchannel assignment results  $\mathcal{S}^*$ , the power allocation problem of MD-IMA is transformed to Problem (P3)

$$P3 : \{\mathcal{P}^*\} = \arg \max \{\eta_{EE}^w(P) | \mathcal{S}^*\} \quad (5.17)$$

$$\text{subject to: } C1 - C2. \quad (5.18)$$

As shown in Equation (4), we noted that the achievable rate of each user is a quasi-concave function due to the quadratic form of channel. Hence, the objective function of Problem (P3) is also non-concave, which includes the summation of the user's data rate. To exploit the hidden convexity of Problem (P3), the term of rate should be approximated by adopting an efficient approximation method [118] as follows:

$$\log_2(1 + \gamma_{k,m,c}) \geq a_{k,m,c} \log_2(\gamma_{k,m,c}) + b_{k,m,c} \begin{cases} a_{k,m,c} = \frac{\bar{\gamma}_{k,m,c}}{1 + \bar{\gamma}_{k,m,c}} \\ b_{k,m,c} = \log_2(1 + \bar{\gamma}_{k,m,c}) - \frac{\bar{\gamma}_{k,m,c}}{1 + \bar{\gamma}_{k,m,c}} \end{cases} \quad (5.19)$$

where  $\gamma_{k,m,c} = 1 + \frac{p_{k,m,c} |\mathbf{h}_{k,m,c}^H \mathbf{w}_c|^2}{I_{k,m,c}^{intra} + I_{k,m,c}^{inter} + \delta^2}$  is the SINR and the lower bound is tight at  $\gamma_{k,m,c} = \bar{\gamma}_{k,m,c}$  when the contents  $\{a_{k,m,c}, b_{k,m,c}\}$  are selected as above. Furthermore, a transformation  $q_{k,m,c} = \ln_{p_{k,m,c}}$  is introduced and so the power allocation Problem (5.17) can be converted into:

$$P4 : \{\mathcal{Q}^*\} = \arg \max \left\{ \tilde{\eta}_{EE}^w = \frac{\alpha_1 \sum_{k=1}^K \sum_{m=1}^M \sum_{c=1}^C s_{k,m,c} \tilde{R}_{k,m,c}}{\alpha_2 \sum_{k=1}^K \sum_{m=1}^M \sum_{c=1}^C s_{k,m,c} e^{q_{k,m,c}} + P_h} | \mathcal{S}^* \right\} \quad (5.20)$$

$$\text{subject to: } \sum_{k=1}^K \sum_{m=1}^M \sum_{c=1}^C s_{k,m,c} e^{q_{k,m,c}} \leq P,$$

$$\sum_{m=1}^M \sum_{c=1}^C s_{k,m,c} e^{q_{k,m,c}} \geq \hat{P}_k^{\min}, \forall k \in \mathcal{K}.$$

Where  $\mathcal{Q}$  is the sets of power allocation transformation  $q_{k,m,c}$  and  $\tilde{R}_{k,m,c}$  represents the lower

bound of the throughput rate of UE  $k$  on SC  $m$  in the  $c$ -th cluster, which is

$$\tilde{R}_{k,m,c} = a_{k,m,c} \frac{B}{M} \log_2 \left( 1 + \frac{e^{q_{k,m,c}} |\mathbf{h}_{k,m,c}^H \mathbf{w}_c|^2}{I_{k,m,c}^{intra} + I_{k,m,c}^{inter} + \delta^2} \right) + b_{k,m,c}. \quad (5.21)$$

We note that the sum rate in the objective function of Problem (5.20) is concave with the respect to  $\mathbf{q}$ , because the log-sum-exp is convex [119]. It also can be proved that the denominator of WEE in P4 is convex due to the constraints, and so the transformed P4 is a concave-convex fractional programming problem. As the numerator and denominator of WEE are differentiable, the Problem (5.20) can be further proved to be a pseudo-concave optimization problem, whose global optimal result is equal to the local optimization. This problem can be solved by using the iterative algorithms and the optimal solutions to meet the Karush-Kuhn-Tucker (KKT) condition.

To further decrease the computational complexity, Charnes-Cooper transformation (CCT) [120],  $\tilde{q}_{k,m,c} = \varnothing q_{k,m,c}$ , is adopted to convert the Problem 5.20 to the following equivalent problem:

$$\begin{aligned} P5 : \{ \tilde{\mathbf{Q}}^*, \varnothing^* \} = \arg \max_{\tilde{\mathbf{Q}}, \varnothing} & \left\{ \varnothing \left[ \alpha_1 \sum_{k=1}^K \sum_{m=1}^M \sum_{c=1}^C s_{k,m,c} \tilde{R}_{k,m,c}(\tilde{\mathbf{Q}}, \varnothing) \right] \right\} \\ \text{subject to:} & \varnothing \left( \alpha_2 \sum_{k=1}^K \sum_{m=1}^M \sum_{c=1}^C s_{k,m,c} e^{q_{k,m,c}/\varnothing} + P_h \right) \leq 1, \\ & \varnothing \left( \sum_{k=1}^K \sum_{m=1}^M \sum_{c=1}^C s_{k,m,c} e^{q_{k,m,c}/\varnothing} - P \right) \leq 0, \\ & \varnothing \left( \tilde{P}_k^{min} - \sum_{m=1}^M \sum_{c=1}^C e^{q_{k,m,c}/\varnothing} \right) \leq 0, \forall k \in \mathcal{K}, \end{aligned} \quad (5.22)$$

where

$$\tilde{R}_{k,m,c}(\tilde{\mathbf{Q}}, \varnothing) = a_{k,m,c} \frac{B}{M} \log_2 \left( 1 + \frac{e^{q_{k,m,c}/\varnothing} |\mathbf{h}_{k,m,c}^H \mathbf{w}_c|^2}{I_{k,m,c}^{intra} + I_{k,m,c}^{inter} + \delta^2} \right) + b_{k,m,c}. \quad (5.23)$$

The transformed Problem (5.22) is a concave optimization problem because the objective function of (5.22) is concave and the constraints of (5.22) is convex. Therefore, the optimal

solutions of Problem (5.22),  $\tilde{\mathcal{Q}}^*$  and  $\varnothing^*$ , can be efficiently solved by using iterative algorithms, and so the optimal solution of Problem (5.20) can be obtained through  $\mathcal{Q}^* = \tilde{\mathcal{Q}}^*/\varnothing^*$ .

According to the above analysis, the optimal solution of P3 can be obtained by iteratively solving the P5, and the optimal power allocation with fixed subchannel assignment algorithm is concluded in Algorithm 6.

---

**Algorithm 6** Optimal Power Allocation Algorithm with Fixed Subchannel Assignment

---

- 1: **Initialize parameters:**  
power allocation variables  $\mathcal{P}^0$ , iteration index  $i = 0$ , error tolerance  $\epsilon > 0$  and maximum iteration number  $I_6^{max}$ .
  - 2: **while**  $i < I_6^{max}$  and  $\tilde{\eta}^{(i)} - \tilde{\eta}^{(i-1)} > \epsilon$  **do**
  - 3:   Compute  $\tilde{\gamma}_{k,m,c}^{(i)} = \gamma_{k,m,c}(p_{k,m,c}^{(i-1)})$ ,  $\forall k, m, c$ ;
  - 4:   Compute  $\{a_{k,m,c}^i, b_{k,m,c}^i, \forall k, m, c\}$  according to Eq.(5.19);
  - 5:   Solve P5 and obtain the optimal variables:  
 $\tilde{\mathcal{Q}}^i = \{\tilde{q}_{k,m,c}^{(i)}, \forall k, m, c\}$  and  $\varnothing^{(i)}$ ;
  - 6:   Obtain the optimal solution of P4:  
 $\mathcal{Q}^i = \mathcal{Q}^i = \left\{ q_{k,m,c}^i = \frac{\tilde{q}_{k,m,c}^{(i)}}{\varnothing^{(i)}}, \forall k, m, c \right\}$
  - 7:   Solve P3 by updating  $\mathcal{P}^{*i}(q^{(i)})$ ;
  - 8:   Compute the  $\eta_{EE}^w$  with the  $\mathcal{P}^*$ ;
  - 9: **end while**
  - 10: **Output:** Optimal power allocation  $\mathcal{P}^* = 0$
- 

### 5.4.4 Joint Resource Allocation

The original resource allocation problem P1 has been divided into three sub-problems: user clustering, subchannel assignment and power allocation. The user clustering problem is solved by using Algorithm 4 (K-means) firstly to maximize the non-orthogonality in the spatial domain. Based on the optimal device grouping scheme, the subcarrier assignment for fixed power allocation is achieved by using Algorithm 5 (matching theory) to minimize the non-orthogonality in the power domain as well as maximize WEE. Then the optimization power allocation for fixed subchannel allocation is solved by Algorithm 6 to maximizing WEE.

However, these sub-problems only optimize one parameter and so the results are not optimal to P1. Therefore, to obtain more optimal results, an alternative optimization algorithm [48] is used to jointly optimize the clustering, subchannel assignment and power allocation, which is summarized in Algorithm 7.

---

**Algorithm 7** Joint Resource Allocation Algorithm

---

- 1: **Initialization:** (1) Set iteration index  $z = 1$ , (2) Initialize power allocation variables  $\mathbf{P}(1) = \frac{P}{K}$ .
  - 2: Cluster  $K$  UEs into  $C$  clusters in the spatial domain by using Algorithm 4.
  - 3: **repeat**
  - 4: For given  $\mathbf{P}(z)$ , solve the P2 through Algorithm 5 and obtain  $\mathbf{S}(z)$ .
  - 5: With  $\mathbf{S}(z)$ , solve the P3 through Algorithm 6 and obtain  $\mathbf{P}(z)$ .
  - 6: Update  $z = z + 1$
  - 7: **until**  $\mathbf{P}$  and  $\mathbf{S}$  converge
  - 8: **Output:** optimal power allocation  $\mathbf{P}^*$  and optimal subchannel allocation  $\mathbf{S}^* = 0$
- 

### 5.4.5 Complexity Analysis

In this section, we analyze the complexity of the proposed joint resource allocation of Algorithm 4 and the optimal exhaustive search method. The proposed Algorithm 4 needs to divide  $K$  UEs to  $C$  clusters by using Algorithm 4 firstly. The complexity of k-means based Algorithm 4 is  $O(KCI_4)$ , where  $K$  is the number of UEs,  $C$  is the number of clusters and  $I_4$  is the number of iterations performed until convergence. Then the  $K$  UEs should be assigned into  $M$  subchannels and each subchannel is allowed to share with at most  $L_m$  subchannels. Each iteration of Algorithm 5 requires at most  $\frac{1}{2}MKL_m$  swap matchings and so the complexity of Algorithm 5 can be presented by  $O(I_5MKL_m)$  [37]. In power allocation part, shown by Algorithm 6, the optimal power allocation scheme is achieved by using the interior point method, which requires the complexity of  $O(I_6K^4\delta)$  [121], where  $I_6$  is the iteration numbers of Algorithm 6,  $K$  is the number of UEs and  $\delta$  is the number of bits for representing the coefficients in the optimization problem. Therefore, the complexity upper bound of Algorithm 7 is  $O(KCI_4) + I_7(O(I_5MKL_m) + O(I_6K^4\delta))$ , where  $I_7$  is the iteration numbers of Algorithm 7 until convergence.

For the optimal exhaustive search scheme, all of the clustering and subchannel combinations should be considered. The complexity of exhaustive clustering method is  $\nabla_1 = C_K^C$ . For the exhaustive subchannel assignment, the matching times of user for each subchannel is  $\nabla_2 = C_M^1 + C_M^2 + \dots + C_M^{L_m}$  and so the total complexity is  $\nabla_2^K$ . Therefore, the overall complexity of exhaustive search based resource allocation is  $\nabla_1 + I_7(\nabla_2^K + O(I_6K^4\delta))$ . Compared with the proposed Algorithm 7, the exhaustive search-based method has higher complexity especially when the UE number  $K$  and the subchannel number  $M$  are large.

## 5.5 Simulation Results

In this section, a range of numerical results is provided for evaluating the performance of the MD-IMA system with the proposed resource allocation algorithms. In the simulations, we assume that one BS deployed in the cell center and all UEs are randomly distributed in the cell. The major parameters are given in Table 5.1:

Table 5.1: Simulation Parameters of MD-IMA networks

Parameters	Value
Circuit power consumption of each antenna at BS	190 mW
Maximumu transmit power of BS	43 dBm
Cell radius	500 m
System bandwidth	20 MHz
Standard deviation of log-normal shadowing	7 dB
Path Loss Model at 2.4 GHz	$17 + 37.6 \log_{10}(d)$ dB
Noise density	-137 dBm/Hz
Noise figure	6 dB

### 5.5.1 The Deployment of the MD-IMA

Fig.5.3 shows the deployment of the proposed scheme for 12 UEs, where the cross represents the OMA user and the circle means the NOMA user. Based on the K-means clustering method, 12 UEs are divided into three clusters in the spatial domain corresponding to red, green and blue circles. We assumed that each subchannel can be allocated at most 3 UEs and then the matching theory is used to assign the available subchannels to UEs. As shown in Fig. 5.3, in the same cluster UEs with large different channel gains can be selected as power-domain NOMA pairs (circle) and the UEs in the different clusters with large enough channel correlation coefficient can be chosen as code-domain NOMA pair (square).

### 5.5.2 Convergence and Optimality of the Proposed Algorithms

Fig. 5.4, Fig. 5.5 and Fig. 5.6 evaluate the convergence of the proposed subchannel assignment with fixed power allocation (Algorithm 5), power allocation with the fixed subchannel assignment (Algorithm 6) and the joint resource allocation (Algorithm 7) algorithms, respectively.



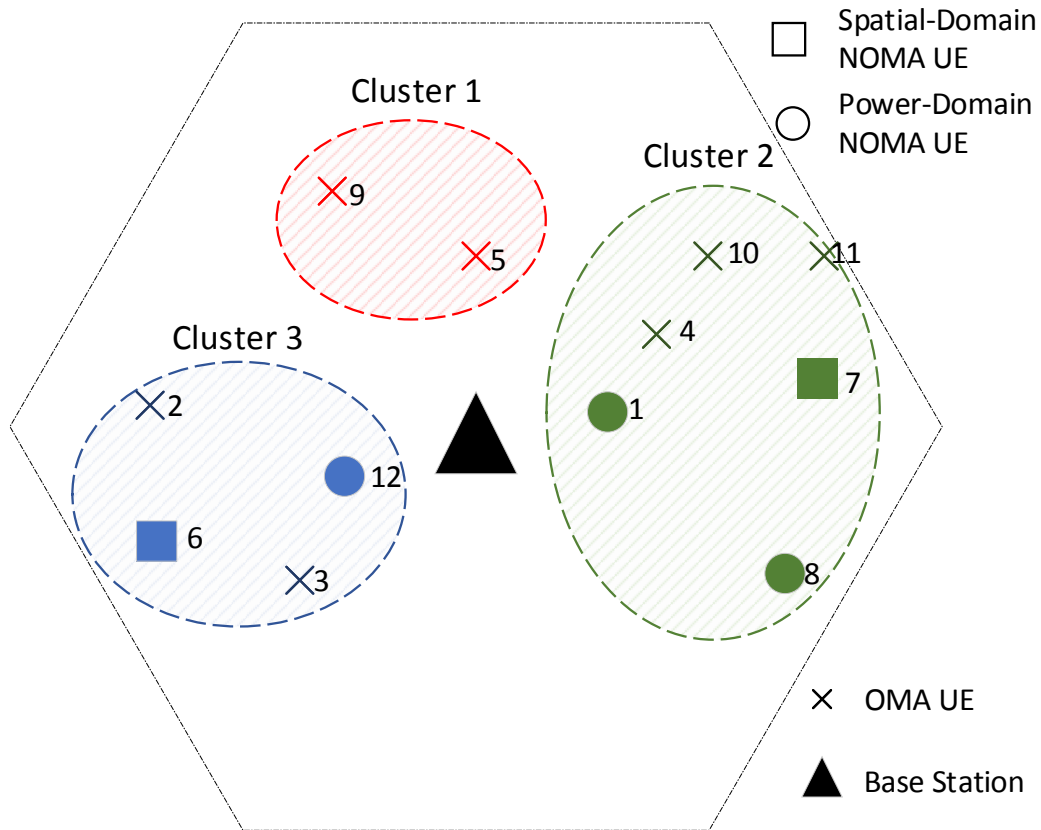


Figure 5.3: Deployment of MD-IMA for 12 UEs.

We assume that weights of sum-rate and power are equal to 0.5. It can be seen that all of the proposed algorithms have fast convergence speed. In order to evaluate the convergence of Algorithm 5 and Algorithm 7 in terms of non-orthogonality performance, the min-max normalized non-orthogonality is adopted. Therefore, the normalized total non-orthogonality of Algorithm 5 and Algorithm 7 for different UE numbers (from 10 to 50) are  $[0.006, 0.083, 0.267, 0.429, 1]$  and  $[0, 0.069, 0.229, 0.382, 0.883]$ , respectively. Specifically, Fig. 5.4 shows that the Algorithm 5 can achieve convergence within 20 iterations. The convergence speed of the Algorithm 5 decreases with the rise of UE numbers. Besides, Fig. 5.4 proves that the proposed Algorithm 6 is capable of converging within 10 steps and the convergence speed becomes slower as the maximum transmit power  $P_b$  increases. Moreover, Fig. 5.6 illustrates the joint resource allocation algorithm (Algorithm 7) is able to quickly convergent within 10 iterations and the convergence speed is impacted by the user number  $K$  and maximum transmit power  $P_b$ .

Fig. 5.7 compares the WEE of the proposed algorithms with that of the near-optimal al-

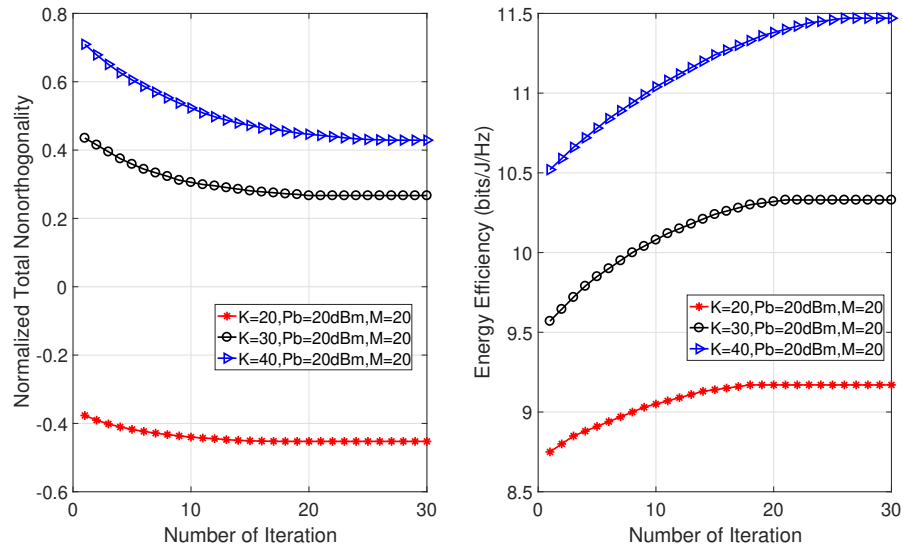


Figure 5.4: Convergence of Algorithm 5 with  $K = 10$ ,  $M = 5$  and  $[\alpha_1 = 0.5, \alpha_2 = 0.5]$ .

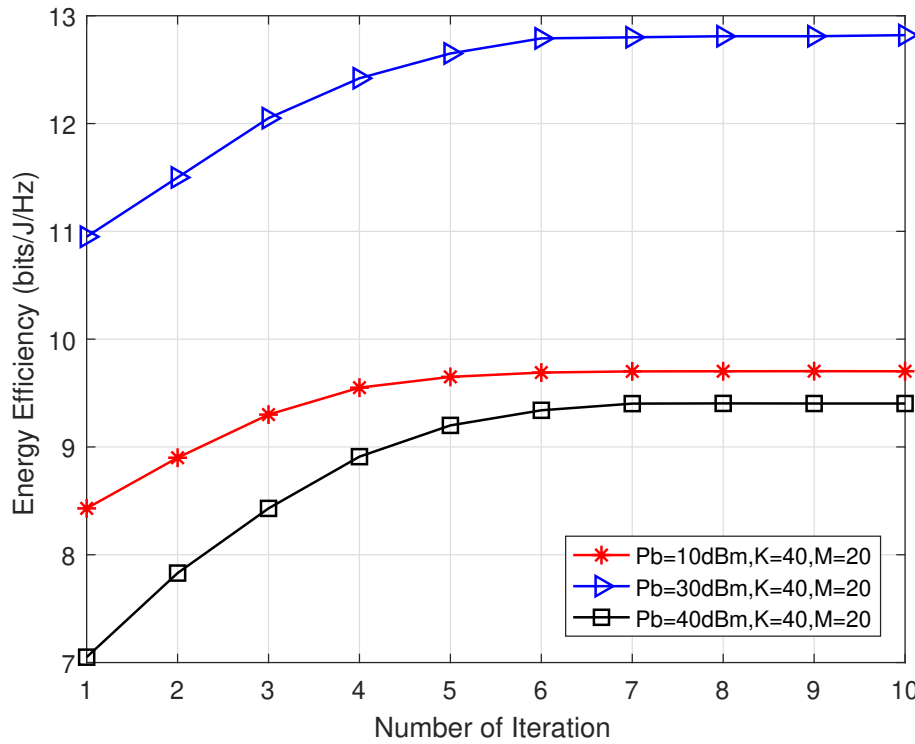


Figure 5.5: Convergence of Algorithm 6 with  $K = 10$ ,  $M = 5$  and  $[\alpha_1 = 0.5, \alpha_2 = 0.5]$ .

gorithm by using the exhaustive searching method. Considering the high computational complexity of the exhaustive searching method, we set UE number  $K = 10$ , subchannel number

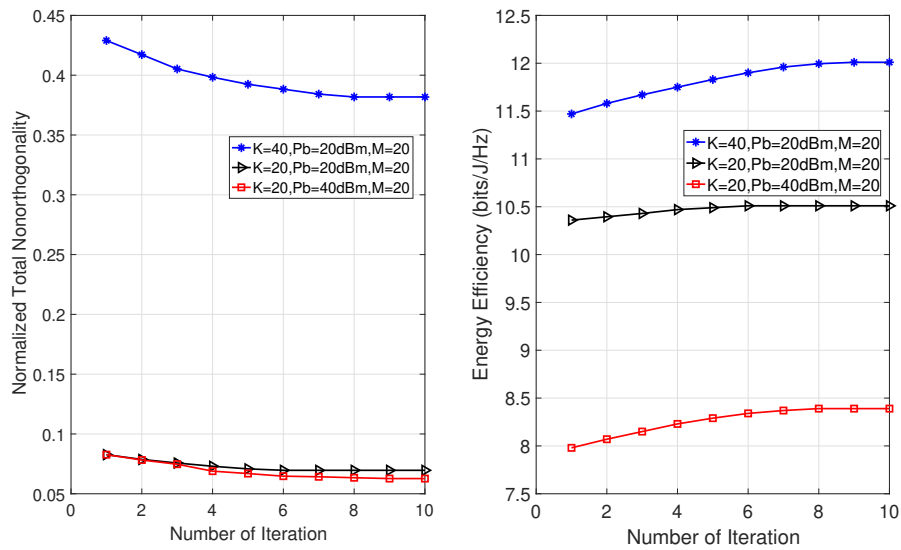


Figure 5.6: Convergence of Algorithm 7 with  $K = 10$ ,  $M = 5$  and  $[\alpha_1 = 0.5, \alpha_2 = 0.5]$ .

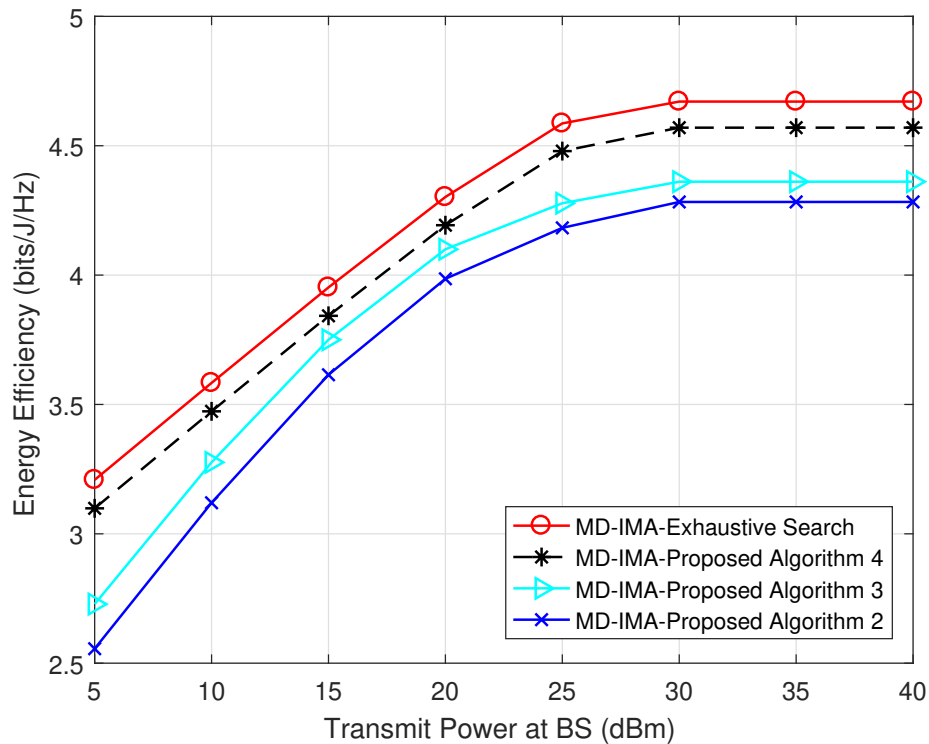


Figure 5.7: WEE of MD-IMA in respect of total transmit power by using different resource allocation algorithms with  $K = 10$ ,  $M = 5$  and  $[\alpha_1 = 0.5, \alpha_2 = 0.5]$ .

$M = 5$  and the weights of WEE  $[\alpha_1 = 0.5, \alpha_2 = 0.5]$ . First, Fig. 5.7 shows that the WEE firstly increased as the total transmit power grows and then remains at the maximum value. When the transmit power larger than a threshold (around 30 dBm), the sum rate can not be improved due to the fact that interference signals become the dominant factor of the SINR. Second, the Algorithm 7 can improve 12% and 8% WEE than that of Algorithm 5 and Algorithm 6, respectively. The reason is that Algorithm 7 can alternatively optimize the subchannel assignment and power allocation. Last, the exhaustive method only increases 2% WEE performance than that of Algorithm 7. It means that the proposed Algorithm 7 has acceptable optimal performance with lower computational complexity, as analysis in section IV-E.

### 5.5.3 Impact of the Weight Values on the WEE

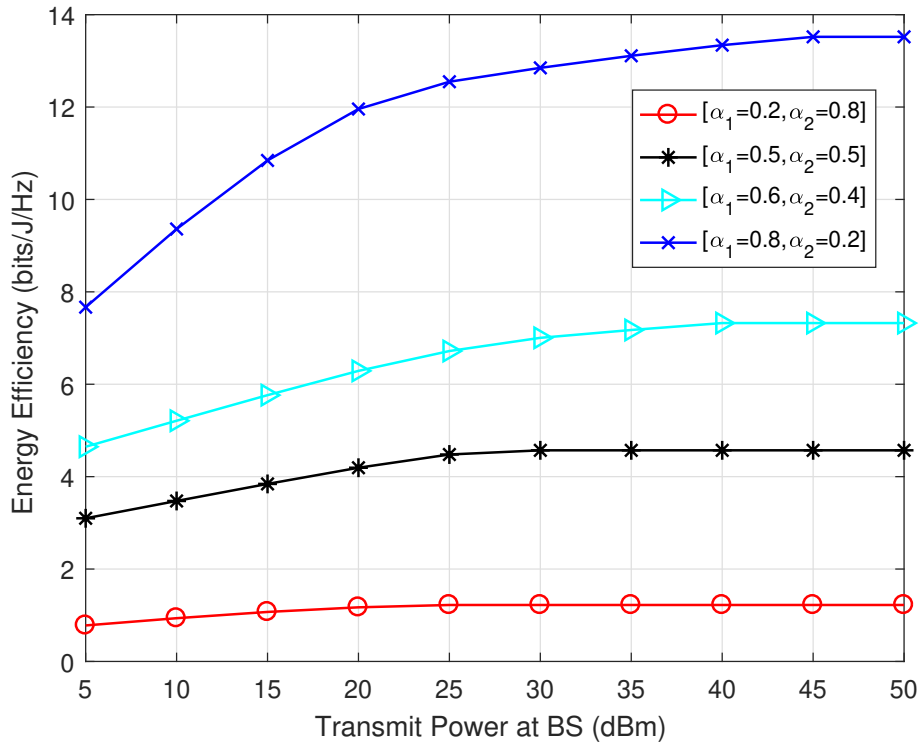


Figure 5.8: WEE of MD-IMA by using the Algorithm 7 in respect of transmit power for different weights of WEE with  $K = 10$ ,  $M = 5$ .

Fig.5.8 illustrates the WEE of Algorithm 7 in MD-IMA system for different weights with  $K = 10$ ,  $M = 5$  and  $[\alpha_1 = 0.5, \alpha_2 = 0.5]$ . In order to quantify the overall communication per-

formance, a new concept named I-QoSE is proposed in this chapter, which scales the different aspects of QoS with relevant weights. The new I-QoSE metric could be adaptively adjusted to meet the diverse and varying 6G services and applications by adjusting the weights. From Fig. 5.8, we can see that the WEE of Algorithm 7 increases with the weight of the sum-rate rise. The reason is that more power is allocated to meet the increased sum-rate requirements. However, the increased speed of weighted EE becomes slower with the increase of the weight value of the sum rate, due to the sum rate upper bound.

#### 5.5.4 Impact of the Cluster Number on the Total Non-orthogonality

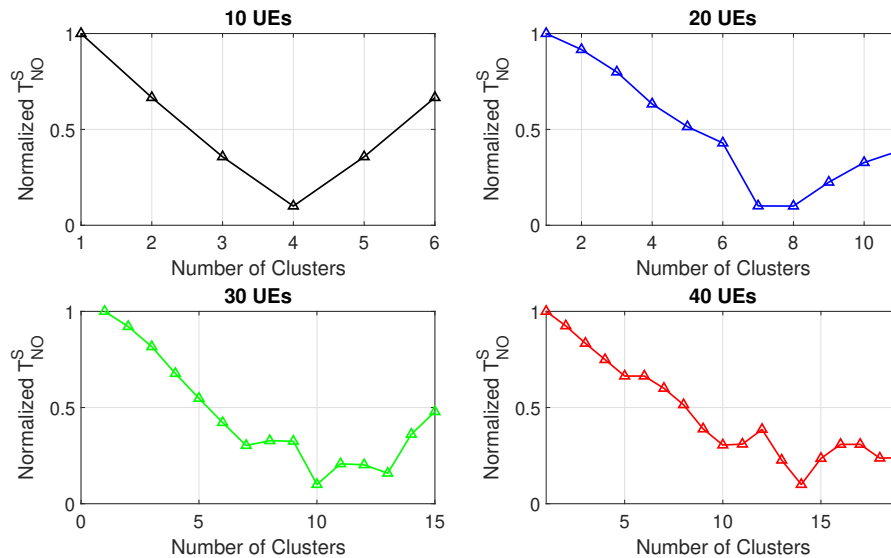


Figure 5.9: Total spatial domain nonorthogonality with different cluster numbers.

The performance of the K-means based clustering algorithm is affected by the choice of the number of the cluster. As shown in the Fig.5.9, an appropriate number of clusters should be selected first to minimize the spatial domain non-orthogonality. For example, when the best cluster number is 4 when there is 10 UEs. Furthermore, we can find a relationship between UE numbers  $K$  and best cluster numbers  $C$  is that  $C = 0.4 \times K$ .

### 5.5.5 Comparison of the WEE Performance for Different MA Modes

Fig.5.10 shows the WEE of proposed MD-IMA, OMA, NOMA systems when UE number is 40 and the subchannel number is 20 with  $[\alpha_1 = 0.5, \alpha_2 = 0.5]$ . As illustrated, the WEE performance of the proposed MD-IMA system is better than that of OMA and NOMA systems, because it is able to fully exploit the joint advantages of both OMA and NOMA. When the transmit power is lower than 20 dBm, the OMA has better performance than that of NOMA. The reason is that although NOMA enabling weak users and strong users simultaneously transmit on the same subcarrier, it will introduce more inter-user interference. For the same level of transmit power, the achievable WEE gain of MD-IMA over NOMA and OMA is approximate 15% and 18%, respectively. It implies that the proposed MD-IMA can combine the advantages of OMA and NOMA by fully utilizing multi-dimensional resources.

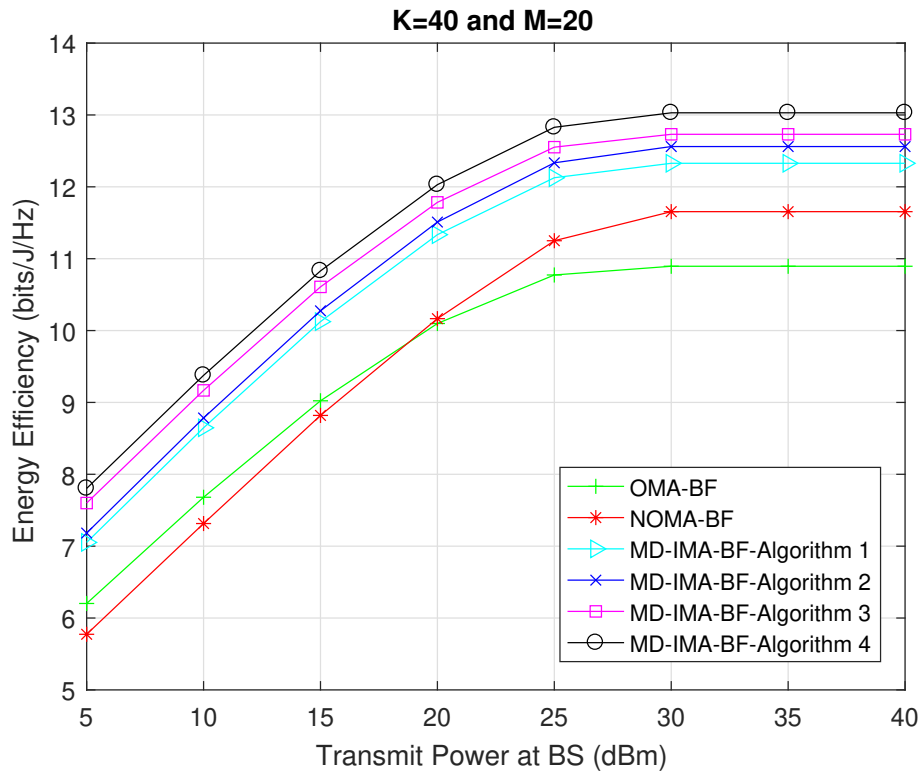


Figure 5.10: WEE of different MA models in respect of transmit power with  $K = 40$ ,  $M = 20$  and  $[\alpha_1 = 0.5, \alpha_2 = 0.5]$

## 5.6 Chapter Summary

In this chapter, an intelligent and efficient multiple access scheme, termed multi-dimensional intelligent multiple access (MD-IMA), is proposed to support the diverse QoS with limited radio resources in future wireless networks. A novel concept of I-QoSE is proposed to quantify the real-time overall system requirements. The I-QoSE combines the diverse QoS aspects with different weights and tunes the weights according to the changes of the network situation. In order to fully utilize the available resources, co-existing devices can be multiplexed in any combinations of multi-dimensional resources with any degree of non-orthogonality. The resource allocation problem of the MD-IMA system is formulated as a multi-objective optimization problem to maximize I-QoSE as well as minimize the non-orthogonality under constraints of maximum power consumption and the QoS requirement of each user. In order to reduce the computational complexity, the whole problem is divided into several sub-optimal problems and then an alternative optimization algorithm is adopted to jointly achieve resource allocation in the MD-IMA system. The simulation results illustrated that the proposed MD-IMA improve 15% - 18 % WEE than that of traditional MA schemes. Furthermore, compared with the exhaustive approach, the proposed joint resource allocation algorithm achieves considerable performance with lower computational complexity.

## Chapter 6

# Deep Reinforcement Learning Based Power Allocation for MD-IMA Networks

In this chapter, a multi-dimensional intelligent multiple access (MD-IMA) scheme is proposed for beyond 5G wireless network to support the ever-increasing communication devices and diverse requirements in real-time, by fully utilizing the available resources in multi-domains. Based on the user clustering, the power allocation problem of MD-IMA is formulated as a non-convex optimization problem. Nowadays, the data-driven model-free machine learning-based approaches are rapidly developing in this field, and among them, the deep reinforcement learning (DRL) is proved to be of great potential to solve such optimization problem. In this chapter, a value-based deep Q-learning neural (DQN) network and actor-critic deep deterministic policy gradient (DDPG) algorithms are adopted to do power allocation. In order to make sure of the maximum transmit power constraint, two possible methods are proposed. Furthermore, three different state types are described. Simulation results demonstrate that the proposed DDPG based power allocation outperforms DQN and conventional model-based algorithms with lower time consumption, such as fractional programming method. Specifically, the DDPG based algorithm can improve around 17% and 35% WEE than that of WMMSE and FP, respectively. The time cost of DRL based method is 10 times and 100 times faster than that of FP and WMMSE.



## 6.1 Introduction

In my previous work, a novel multi-dimensional intelligent multiple access (MD-IMA) is conceived to select multiple access (MA) in multi-dimension adaptively to accommodate the dynamic requirements by fully utilizing the closed-loop situation-awareness discovery through real-time data analytic. To fully utilize the benefit of the MD-IMA, the key issue is to optimally perform joint channel assignment and power allocation with limited resources. Such joint channel assignment and power allocation problem has been proven to be NP-hard in [48] and so we proposed a heuristic approach to solve this problem.

However, the traditional optimization techniques highly depend on tractable mathematical models, which may not be able to capture the real communication scenarios with specific user distribution, geographical environment and complicated channel characteristics [49]. Meanwhile, the optimization problem of resource allocation for MD-IMA system is very complex, nonlinear searching procedures are ineluctable and so the computational complexities of traditional optimization algorithms are high. In summary, conventional optimization approaches are not efficient enough to obtain good channel assignment and power allocation for MD-IMA system.

Furthermore, 5G and Beyond networks are foreseen to support diverse quality of service (QoS) requirements [101]. For example, super-high throughput is the most important requirement for high-definition videos, whereas strict power constraints should be considered for smart wearable devices [26]. Accordingly, the overall performance analysis of 5G and beyond communication systems should integrate diverse performance metrics into a whole. Furthermore, different working habits and lifestyles of users can also cause a significant fluctuation in QoS [55]. Simply utilizing the fixed and single system performance metric cannot meet diverse and varying service requirements of 5G and beyond wireless networks, which thereby stimulates the study of intelligent MA techniques.

In recent years, deep learning has been a promising technology for optimizing the system performance of wireless communication networks, due to its model-free and the nature of the complaint with optimizations in practical communication scenarios [59]. Furthermore, reinforcement learning has received wide attention because it can interact with an unknown

environment by exploration and exploitation [47]. On the other hand, by introducing multiple hidden layers between the input and output layers, deep neural network (DNN) is more powerful and flexible to predict complex system performances, such as sum-rate and power consumption, due to the combined capability of multiple hidden layers [53]. In addition, by employing hierarchical feature extraction, deep learning can capture temporal and spatial dependencies in sequential data, while minimizing the data pre-processing effort [54].

Therefore, we proposed a deep neural network-based intelligent resource allocation scheme for MD-IMA networks. In this scheme, a concept of integrated-quality-of-system-experience (I-QoSE), combining several metrics (e.g. power consumption, delay, and throughput) with different weights, is introduced. The proposed intelligent resource allocation method consists of two phases- the DNN based I-QoSE prediction and the deep reinforcement neural network-based resource allocation. In the first phase, since fluctuation of user density is influenced by short and long term behaviors, the long short term memory (LSTM) neural network, a kind of deep RNN, is adopted to predict the performance metrics due to its excellent capability to memorize long-term dependencies. According to these predicted results, the weight of each metric for I-QoSE is determined. In the second phase, the predicted I-QoSE is regarded as the rewards and the deep reinforcement learning (DRL) network is adopted to achieve optimal power allocation. The value-based DRL algorithm derives optimal action by the action-state value function, and deep Q learning (DQL), one of the most value-based DRL algorithms, is adopted in this chapter to achieve power allocation for MD-IMA networks. However, the main disadvantage of DQN is that the action space must be discrete. The discretized action space not only brings quantization error for tasks with continuous action space but also leads to an exponential increase in the number of action spaces. Therefore, to solve these problems, the actor-critic based deep deterministic policy gradient (DDPG) algorithm, as a hybrid of the value-based and policy-based methods, is further adopted in this topic to do power allocation, because it can perform the continuous spaces.

The rest of this chapter is structured as follows. Section 6.2 introduces the network architecture of DRL enabled resource allocation for MD-IMA. In Section 6.3, the communication model, including channel model, achievable rate and energy efficiency, are described. Then, the power allocation problem for MD-IMA is formulated in Section 6.4 as a non-convex opti-

mization problem to maximize the I-QoSE with several constraints. In Section 6.5, the I-QoSE prediction is achieved by using one LSTM to learn the network requirements, such as throughput rate and power consumption. Based on the predicted I-QoSE, the two different DRL based power allocation methods, DQN and DPPG, are elaborated in Section 6.6. Section 6.7 presents our simulation results regarding the I-QoSE performance of the proposed DRL based power allocation methods. Finally, the conclusions are provided in Section 6.8.

## 6.2 Network Architecture

As illustrated in our previous proposed MD-IMA network, we adopted the K-means method to cluster users and choose the cluster numbers by maximizing the total non-orthogonality. The network architecture of deep neural network-based intelligent resource allocation scheme for MD-IMA is illustrated in Fig. 6.1

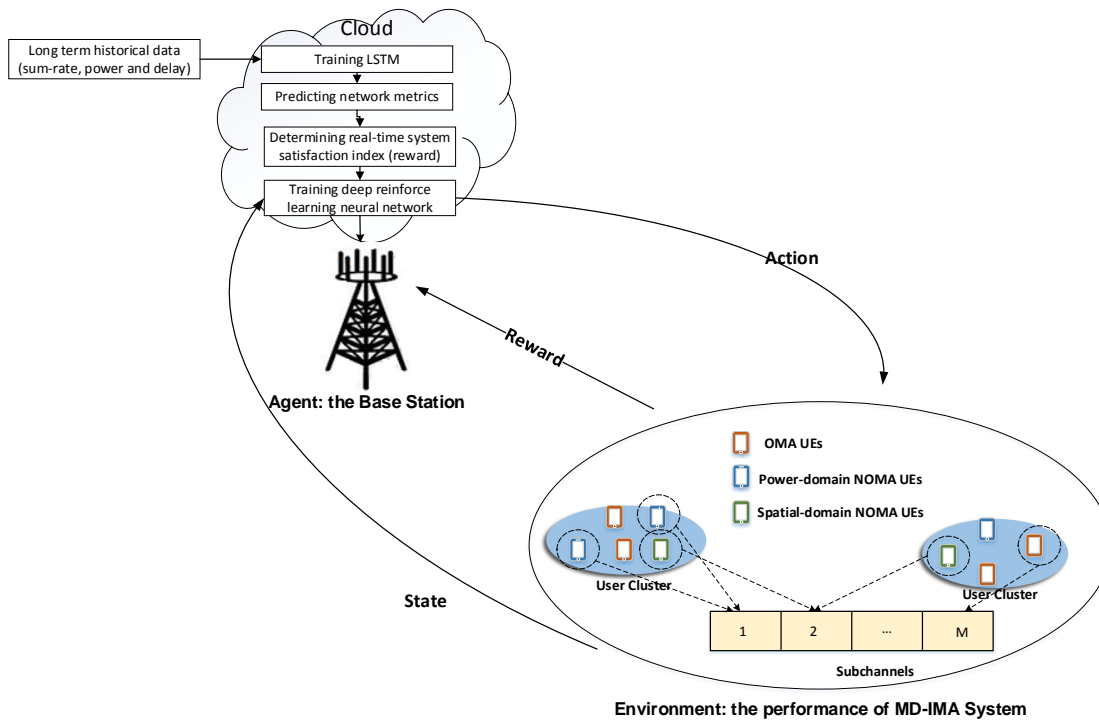


Figure 6.1: Deep learning based intelligent resource allocation of the MD-IMA Network

As shown in Fig. 6.1, based on the received historical data, including the sum-rate, power consumption and delay requirements, a deep learning model, such as the LSTM neural net-

work, that may run on a cloud-based platform is utilized to achieve the I-QoSE prediction. The I-QoSE is determined as the sum of all the important metrics by using a weight-based approach. If the sum-rate (SR), power consumption (PC) and delay (D) are considered as the three possible metrics, the mathematical expression of I-QoSE is:

$$I - QoSE = \alpha_1 \times SR - \alpha_2 \times PC - \alpha_3 \times D, \alpha_1 + \alpha_2 + \alpha_3 = 1, \quad (6.1)$$

where  $\alpha_1$ ,  $\alpha_2$  and  $\alpha_3$  represent the weight value of the throughput rate, power consumption, and delay, respectively. These weight values are determined according to the predicted results by using the LSTM. The higher weight means the corresponding metric is more important. For example, if the sum-rate requirement is very low and the so minimizing power consumption is the most important objective of resource allocation and the weight of power consumption metric should be the highest.

The objective of the resource allocation optimization problem is to maximize the real-time I-QoSE and so the I-QoSE is regarded as the reward of the MD-IMA network. The optimization of resource allocation, such as power allocation and subchannel assignment, is modeled as a deep reinforcement learning task, which consists of an agent and environment interacting with each other, as shown in Fig.6.1. The base station is treated as the agent and the performance of the MD-IMA network is the environment. We define the state space is  $S$ , action space is  $A$  and the reward function is  $R$ . At time step  $t$ , based on the observed state  $s^t \in S$  of the environment, the agent takes an action  $a$  from the action space  $S$  to allocate power to users according to the power allocation policy  $\pi$ , where the policy is learned by an attention-based neural network. Then, the current reward  $r^t$  and the next state  $s^{t+1} \in S$  are obtained from environment. The target of the network is to take the optimal power allocation which can maximize the expected reward.

### 6.3 Communication Model of MD-IMA Network

In terms of the MD-IMA network environment, we assume that BS, located at the center of a single cell and equipped with  $N_t$  transmit antennas, serves  $K$  UEs, equipped with one an-

tenna and denoted as  $\mathcal{K} = \{1, \dots, K\}$ . Based on the geolocation information,  $K$  UEs should be divided into  $C$  clusters, which are covered by using beamforming in the spatial domain. The UEs in each cluster are represented by  $\{\mathcal{X}_1, \dots, \mathcal{X}_C\}$  and we have  $\bigcup_{c=1}^C \mathcal{X}_c = K$ . We consider that the total bandwidth  $B$  is divided into  $M$  orthogonal subchannels (SCs), denoted by  $\mathcal{M} = \{1, \dots, M\}$ . In the same cluster, the UEs who have large channel gain differences can be assigned in the same SC by using power-domain NOMA and they can be distinguished at the receiver by adopting successive interference cancellation (SIC). In different clusters, the UEs who have large non-orthogonality in the spatial domain can be allocated in the same SC and they can be divided by using beamforming. The number of UEs which can be assigned on  $m$ -th SC is denoted by  $L_m, m \in \mathcal{M}$ . If  $L_m = 1$ , the  $m$ -th SC is regarded as a OMA-SC, whereas it is denoted as a NOMA-SC when  $L_m > 1$ . According to the non-orthogonality among UEs and the available resource,  $K$  UEs are adeptly assigned to  $M$  SCs in multi-dimension and each SC has different UE numbers. In order to simplify the problem, each UE is only allowed to be assigned to one SC and we assume  $K = \sum_{m=1}^M L_m$ . Motivated to meet vary diverse requirements of 5G and beyond wireless network, the power constraints of every UE, denoted by  $\{P_k, \forall k \in \mathcal{K}\}$ , can be different.

### 6.3.1 Channel Model

At time slot  $t$ , the vector of the complex coefficients between the BS and UE  $k$  in  $c$ -th cluster on  $m$ -th SC is defined as:

$$\mathbf{h}_{k,m,c}(t) = \mathbf{g}_{k,m,c}(t)PL^{-1}(d) \in \mathbb{C}^{N_r \times 1}, \quad (6.2)$$

where  $\mathbf{g}(t)_{k,m,c}$  is the Rayleigh fading channel gain and  $PL^{-1}(d)$  denotes the path loss function between the BS and the UE  $k$  at distance  $d$  [37]. In order to reflect the temporal-domain correlation of each channel gain  $\mathbf{g}(t)_{k,m,c}$ , the Gaussian Markov block fading autoregressive model [122] is adopted:

$$\mathbf{g}_{k,m,c}(t) = \rho_k \mathbf{g}_{k,m,c}(t-1) + \sqrt{1 - \rho_k^2} \mathbf{e}(t), \quad (6.3)$$

where  $\rho_k$  denotes the channel gain correlation coefficient of  $k$ -th user between time slot  $t$  and  $t - 1$  and the error vector  $\mathbf{e}(t)$  is the complex Gaussian. Specifically, the  $\rho_k$  is modeled by the first kind zero-order Bessel function [122]:

$$\rho_k = J_0(2\pi f_{d,k} T_s), \quad (6.4)$$

where  $f_{d,k}$  is the maximum Doppler frequency of user  $k$  and  $T_s$  is the length of time slot.

### 6.3.2 Achievable Rate

Let us take the  $c$ -th cluster and its corresponding UEs  $\mathcal{X}_c$  as an example to analyze the interference conditions and the achievable rate. Without loss of generality, we assume  $k \in \mathcal{X}_c$ . At each time slot  $t$ , for the received signals of the  $k$ -th UE on the  $n$ -th SC in cluster  $c$ , the main interference are composed of three parts: intra-cluster interference, inter-cluster interference and additive noise. The intra-cluster interference are introduced by other UEs, whose channel gains are lower than that of  $k$ -th UE, in cluster  $c$  on the  $n$ -th SC, while the inter-cluster interference come from the UEs in neighboring clusters on the  $n$ -th SC.

The principle behind the power-domain NOMA is adding power domain multiplexing on transmitter side to overlap users on the same subchannel and using SIC on receiver side to realize multi-user detection. Specifically, in the same subchannel, different transmitted power level is allocated to different UEs according to their channel gains. The received symbols should be detected in order of decreasing of channel gains. It means the UEs with poorer channel conditions are decoded firstly and are subtracted one by one. For UEs with better channel conditions are regarded as noise [117]. Let  $\mathbf{w}_c(t) \in \mathbb{C}^{N_t \times N_t}$  be the beamforming matrix from BS to cluster  $c$  at time slot  $t$ . We also define power allocation matrix  $\mathbf{P}(t) \in \mathbb{C}^{K \times M \times C}$ , where  $[\mathbf{P}] = p_{k,m,c}(t)$  denotes the downlink transmission power between BS and  $k$ -th UE on  $m$ -th subchannel in cluster  $c$  at time slot  $t$ . The subchannel assignment scheme at time slot  $t$  is reflected by matrix  $\mathbf{X}(t) \in \mathbb{C}^{K \times M \times C}$ , where  $[\mathbf{X}(t)] = x_{k,m,c}(t)$  is the subchannel indicator. We set  $x_{k,m,c}(t) = 1$  if the  $m$ -th subchannel is occupied by the UE  $k$  in cluster  $c$  at time slot  $t$ , otherwise,  $x_{k,m,c}(t) = 0$ . At each time slot  $t$ , the intra-cluster interference of UE  $k$  in  $c$  th cluster on  $m$ -th subchannel can be given by:

$$I_{k,m,c}^{intra}(t) = \left| \mathbf{h}_{k,m,c}(t)^H \mathbf{w}_c(t) \right|^2 \sum_{i \in \mathcal{X}_{c,k}(t)} x_{i,m,c}(t) p_{i,m,c}(t), \quad (6.5)$$

where  $\mathcal{X}_{c,k}(t) = \{i | i \in \mathcal{X}_c(t), h_{k,m,c}(t) > h_{i,m,c}(t)\}$  denotes the set of UEs in  $\mathcal{X}_c(t)$  on SC  $n$  whose channel conditions are worse than that of  $k$ -th UE. Then, the inter-cluster interference can be given by:

$$I_{k,m,c}^{inter}(t) = \left| \mathbf{h}_{k,m,c}(t)^H \right|^2 \sum_{i \neq c}^C \sum_{j=1}^K x_{j,m,i}(t) p_{j,m,i}(t) |\mathbf{w}_i(t)|^2. \quad (6.6)$$

Therefore, at time slot  $t$ , the signal-to-interference-plus-noise rate (SINR) of the received signal from UE  $k$  on  $m$ -th subchannel in cluster  $c$  is:

$$\gamma_{k,m,c}(t) = \frac{p_{k,m,c}(t) \left| \mathbf{h}_{k,m,c}(t)^H \mathbf{w}_c(t) \right|^2}{I_{k,m,c}^{intra}(t) + I_{k,m,c}^{inter}(t) + \delta(t)^2}, \quad (6.7)$$

where  $\delta(t)^2$  is the variance of additive Gaussian noise. Therefore, the data rates  $R_{k,m,c}$  and sum-rate  $R_{total}(t)$  is

$$R_{k,m,c}(t) = \frac{B}{M} \log_2 (1 + \gamma_{k,m,c}(t)), \quad (6.8)$$

$$R_{total}(t) = \sum_{k=1}^K \sum_{m=1}^M \sum_{c=1}^C x_{k,m,c}(t) R_{k,m,c}(t) \quad (6.9)$$

### 6.3.3 Weighted energy efficiency

The weighted energy efficiency (WEE) is defined as the ratio of the achievable sum rate to the total power consumption:

$$\eta_{EE}^w(t) = \frac{\alpha_1(t) R_{total}(t)}{\alpha_2(t) P_{total}(t)}, \quad (6.10)$$

where  $\alpha_1(t)$  and  $\alpha_2(t)$  are the weights of the required sum rate and the power consumption, respectively. The total power consumption  $P_{total}(t)$  of BS in Eq. (7.4) consists of two parts: the

circuit power consumption, depending on the hardware design of BS and the transmit power, which is related to the power allocation [78]:

$$P_{total}(t) = \sum_{k=1}^K \sum_{m=1}^M \sum_{c=1}^C x_{k,m,c}(t) p_{k,m,c}(t) + \xi_0 N_t, \quad (6.11)$$

where,  $\xi_0$  represents the circuits power consumption of each antenna of BS.

## 6.4 Problem Formulation

As illustrated in our previous topic, we have utilized the K-means based clustering and matching theory-based subchannel assignment algorithm with fixed power allocation to achieve the balance between receiver complexity and the I-QoSE. Therefore, in this chapter, we only focus on the power allocation problem of MD-IMA network.

Based on the optimal UE clustering, the objective of the power allocation problem for MD-IMA system is to maximizing I-QoSE under the constraints of maximum transmit power and minimum power requirements of each user. Based on the predicted system requirements of LSTM, the I-QoSE can be calculated by (6.1). To simplify the I-QoSE, we only consider the sum-rate and power consumption firstly and so the I-QoSE can be regarded as weighted energy efficiency. The power allocation of the MD-IMA can be formulated as an optimization problem to maximize the weighted energy efficiency with the constraints of maximum transmit power and minimum user's required QoS, which is defined as follows:

$$\begin{aligned} \{\mathcal{P}(t)^*\} &= \arg \max \left\{ I - QoS E(t) = \frac{\alpha_1(t) R_{total}(t)}{\alpha_2(t) P_{total}(t)} \mid \mathcal{X}(t)^* \right\} \quad (6.12) \\ \text{subject to: } C_1 &: \sum_{k=1}^K \sum_{m=1}^M \sum_{c=1}^C x_{k,m,c}(t) p_{k,m,c}(t) \leq P_{max}, \\ C_2 &: \sum_{m=1}^M \sum_{c=1}^C x_{k,m,c}(t) p_{k,m,c}(t) \geq P_k^{min}, \forall m \in \mathcal{M}, \forall c \in \mathcal{C}, \end{aligned}$$

where  $P_{max}$  is the maximum transmit power of the BS and  $P_k^{min}$  is the minimum required to transmit power of user  $k$ . The constraint C1 ensures the maximum transmitted power constraint and C2 guarantees the QoS requirement for each user. Because of the non-concavity



and nonlinearity in the objective function and constraints, problem (6.12) is a non-convex optimization problem, which is too complicated to solve. In our previous topic, the non-convex problem is transformed into a convex problem first and then an iteration optimization algorithm is used. However, the traditional optimization algorithm is based on the mathematical model, which is not available for some practical scenarios. Therefore, the model-free DRL neural network is adopted in this work to fit a more practical environment. Furthermore, in order to reduce the time delay caused by power allocation, the I-QoSE can be predicted by using LSTM in advance to train the DRL. The specific principle of LSTM based I-QoSE prediction and DRL based power allocation are given in the following sections.

## 6.5 I-QoSE Prediction based on One LSTM

We assumed that the I-QoSE consists of sum-rate and power allocation, and so the I-QoSE is determined by the weight of the sum-rate. The higher sum-rate requirement corresponds to higher weight value of sum-rate  $\alpha_1(t)$ . Therefore, the weight value can be determined by predicting the sum-rate requirement. The LSTM neural network is a special kind of deep RNNs that can capture the longer-term temporal dependencies than traditional RNNs [92]. Each hidden node in LSTM network is regarded as a memory cell with three different gates, which regulating the information and thus allowing to keep the past information [93]. Therefore, in this work, the LSTM neural network is adopted to predict the sum-rate in every grid, which is used to predict the final I-QoSE.

The historical location map should be divided into  $\left(\frac{N_s}{N_c}\right)^2$  zones in spatial domain and each zone has  $N_c \times N_c$  grids at specific time  $t$ , as shown in the Fig.6.2. Note that the value of  $N_c$  should ensure the zone number,  $\left(\frac{N_s}{N_c}\right)^2$ , is an integer. The model of sum rate requirement prediction based on one LSTM network is shown in Fig. 6.2. There are three layers in the proposed LSTM model: the input layer, the hidden layer and the output layer.

The input to the LSTM model is the historical sum-rate of all grids in  $j^{\text{th}}$  zone:

$$\{\mathbf{sr}_{t-1}^j, \mathbf{sr}_{t-2}^j, \dots, \mathbf{sr}_{t-d}^j\}, \quad (6.13)$$

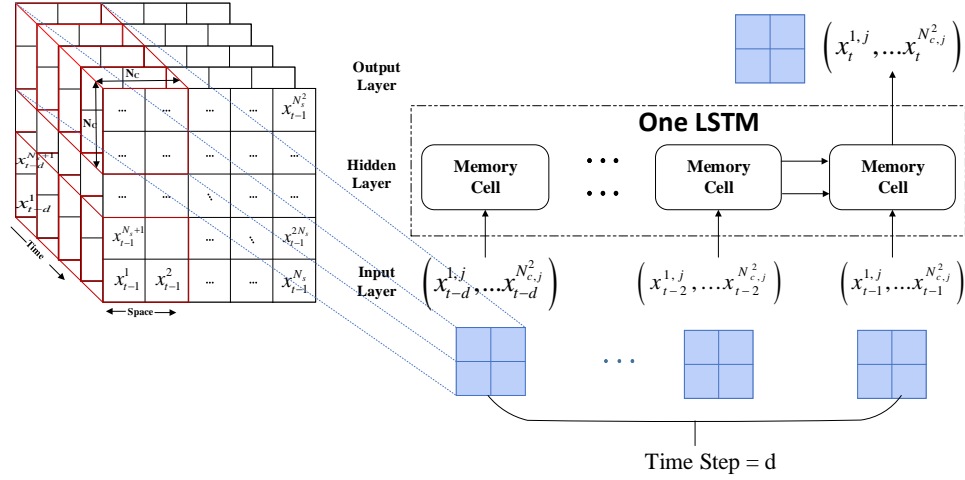


Figure 6.2: Structure of one LSTM based sum-rate prediction method.

where  $\mathbf{sr}_{t-1}^j = \{sr_{t-1}^{1,j}, \dots, sr_{t-1}^{N_c^2,j}\}$ . The output is the predicted sum-rate of all grids in  $j^{\text{th}}$  zone at time  $t$ ,  $\mathbf{sr}_t^j = \{sr_t^{1,j}, \dots, sr_t^{N_c^2,j}\}$ . The number of memory cells is determined by the time steps  $d$ . The hidden layer number in Fig. 6.2 is one, but it can be easily extended to several layers according to the situation. In this way, the input of the proposed one LSTM based method is the 2D (spatial and temporal domain) zones instead of the 1D (temporal domain) grid. Therefore, the proposed one LSTM network can exploit both spatial and temporal features of sum-rate. All of zones are should be used to train the same LSTM model to find the relationship function  $\mathbf{f}$  between the input and output:

$$\mathbf{sr}_t^j = \mathbf{f}(\mathbf{sr}_{t-1}^j, \mathbf{sr}_{t-2}^j, \dots, \mathbf{sr}_{t-d}^j) \quad \forall j = 1, \dots, \left(\frac{N_s}{N_c}\right)^2. \quad (6.14)$$

Bu using this method, sum-rate of  $i$ -th grid during  $T$  time steps can be obtained as  $\mathbf{sr}_T^i = \{sr_1^i, \dots, sr_T^i\}$ . Then the weights of sum-rate for the  $i$ -th grid can be calculated by using min-max normalized. Finally, the predicted WEE can be defined as:

$$EE^w(t) = \begin{cases} R_{total}(t) & \alpha_1 = 1 \\ \frac{\alpha_1 R_{total}(t)}{(1-\alpha_1)P_{total}(t)} & 0 < \alpha_1 < 1 \\ P_{total}(t) & \alpha_1 = 0 \end{cases} \quad (6.15)$$

## 6.6 Power Allocation based on DRL

A general reinforcement learning (RL) consists of three parts: the state space  $S$ , action space  $A$  and the reward function is  $R$ . At time step  $t$ , based on the observed state  $s^t \in S$  of the environment, the agent takes an action  $a$  from the action space  $S$ , which can maximize the expected reward. Integrating RL with DNN, which can be categorized into three classifications: value-based, policy-based and actor-critic methods.

- Value-based DRL:

The value-based DRL algorithm derives optimal action by the action-state value function, and the most widely-used algorithms include deep Q learning (DQL) and Sarsa. In this chapter, the DQN is adopted to achieve power allocation for MD-IMA networks. The main idea is using a DNN network to approximate the Q-value function  $Q^*(s_t, a_t; \theta)$ , where  $\theta$  is the parameter of DQN. The optimal parameter is updated to minimizing the difference between Q function value to the target value (expected reward). In this way, learned DQN can select an optimal action for a given state.

However, the main disadvantage of DQN is that the action space must be discrete. The discretized action space not only brings quantization error for tasks with continuous action space but also leads to an exponential increase in the number of action spaces. The reason is that the discretization of action-space may throw away some values which might be the optimal solution for solving problems.

- Actor-Critic based DRL: Fortunately, the actor-critic algorithm, as a hybrid of the value-based and policy-based methods, can perform the continuous spaces. A deep deterministic policy gradient (DDPG) is one of the famous actor-critic DRL algorithms. It consists of two components: an actor to generate policy and a critic to assess the policy. The

critic estimates the value of the current policy by Q-learning and actor updates policy in a direction that improves Q value. The specific DDPG algorithm will be described in the following part.

### 6.6.1 Basic Model of Reinforcement Learning

The above power allocation problem of MD-IMA can be regarded as a sequential decision-making process under a stochastic environment [47]. At each step, one power value is assigned to a corresponding user according to the decision-making process. The process will be terminated until all users are allocated with power. The objective is to find the optimal process that maximizes the weighted energy efficiency.

The specific definition of state, action and reward in this system are described as:

- **State:** The DRL works as an estimator to predict the current energy efficiency of corresponding current partial channel information  $\mathbf{H}(t)$  and so the channel information is the most critical feature. However, according to [123], the performance of such DRL is not good, since it is non-convex and the optimal point is hard to find. Therefore, more auxiliary features can be introduced to help the DQN get closer to the optimum.

As mentioned in section III-A, the channel is modeled as a Markov process and correlated in the time domain, and thus the last solutions can provide a better initialization for this moment's solve and interference information. Therefore, the last power allocation  $\mathbf{P}(t-1)$  and the last WEE  $\eta_{EE}^w(t-1)$  can be introduced as the assisted features. It means there are three possible states can be considered, and they are written as:

$$s_t^1 = \{\mathbf{H}(t)\} \quad (6.16)$$

$$s_t^2 = \{\mathbf{H}(t), \mathbf{P}(t-1)\} \quad (6.17)$$

$$s_t^3 = \{\mathbf{H}(t), \mathbf{P}(t-1), \eta_{EE}^w(t-1)\} \quad (6.18)$$

The performance of three states will be compared in the simulation section in terms of WEE to find the appropriate states.

- Action: The power allocation for each UE is a continuous variable and is constrained by maximum total transmitted power constraint  $P_{max}$  and minimum required power for each UE  $P_k^{min}$ . The actor of DDPG can directly output a deterministic action according to the trained policy. In order to enforce the total power constraint at the output layer of DDPG, the following normalized activation function for the output layer is used [124]:

$$P_k = \frac{P_k}{\sum_{k=1}^K P_k} P^{max} \quad (6.19)$$

The above equation guarantees that the total power constraint is satisfied.

However, the action space of DQN must be finite. The power allocation of each UE are quantized as  $N_p$  discretized power level from  $P_k^{min}$  and  $P_{max}$  and so there are maximum  $N_p^K$  power combinations for  $K$  UEs. We denote that an action corresponds to each combination. Noted that some of the combinations will be discarded due to the maximal total power constraint [125]. We assume that only  $C_p$  combinations meet the maximal power constraint and so the output layer size of DQN is  $C_p$ .

- Reward: In Section III, the objective of power allocation for MD-IMA is to maximize weighted energy efficiency. Therefore, the weighted energy efficiency represents the immediate reward  $r_t$  returned from environment after DRL selecting the action  $a_t$  based on the state  $s_t$

## 6.6.2 Q-Learning

Q-learning, as one of the most popular model-free reinforcement learning algorithms, can be used to deal with such Markov decision process (MDP) problems [126]. The Q function of the agent calculates the expected cumulative reward with an action  $a$  in state  $s$  under a certain policy  $\pi$ , which is given by [127]

$$Q^\pi(s, a) = \mathbb{E} \left[ \sum_{t=0}^{\infty} \lambda^t r(s_t, \pi(s_t)) \mid s_t = s, a_t = a \right], \quad (6.20)$$

where  $\lambda \in [0, 1)$  is a discount factor. It means that the immediate reward is the most important to Q function, and the importance of reward decreased over time. The aim of Q-learning is to find a policy that maximizes the Q-function. According to [126], the maximization Q-function is equivalent to the Bellman optimal equation:

$$Q^\pi(s_t, a_t) = r_{t+1} + \lambda \max_{a_{t+1}} Q(s_{t+1}, a_{t+1}), \forall s_t, a_t \quad (6.21)$$

As the agent explores the environment by applying actions and receiving rewards, it collects and stores transitions  $(s_t, a_t, r_{t+1}, s_{t+1})$  in a growing batch. From the batch of transitions, a training sequence of input-output pairs is formed and utilized to learn the Q-function. One of the popular method is called one-step Q-learning approach, which is defined as:

$$Q(s_t, a_t) \leftarrow Q(s_t, a_t) + \alpha \left( R_t + \lambda \max_a Q(s_{t+1}, a) - Q(s_t, a_t) \right), \quad (6.22)$$

where  $\alpha$  is the learning rate. The specific procedure of Q-learning is summarized in the Algorithm 8 [128].

---

**Algorithm 8** Q-learning
 

---

- 1: **Initialize:**  $Q(s_t, a_t)$  arbitrarily
  - 2: **for** all episodes **do**
  - 3:   Initialize  $s_t$
  - 4:   **for** all steps of episode **do**
  - 5:     Based on the policy, such as  $\xi$ -greedy algorithm, and the current state  $s_t$ , choose one action  $a_t$  from action sets
  - 6:     Take action  $a_t$ , observe the reward  $R_t$  and the next state  $s_{t+1}$
  - 7:     Update the Q:  $Q(s_t, a_t) \leftarrow Q(s_t, a_t) + \alpha (R_t + \lambda \max_a Q(s_{t+1}, a) - Q(s_t, a_t))$
  - 8:      $s_t \leftarrow s_{t+1}$
  - 9:   **end for**
  - 10: **end for**=0
- 

Noted that,  $\xi$ -greedy algorithm-based policy is generally adopted to balance the exploration of the environment and the exploitation of the accumulated knowledge. In  $\xi$ -greedy algorithm, the agent takes a random action with the probability  $\xi$  (exploration) and a policy action, such as  $\max_a Q(s_{t+1}, a)$ , with probability  $1 - \xi$  [127]. The value of  $\xi$  is gradually reduced over time from  $\xi_{max}$  to  $\xi_{min}$ .

### 6.6.3 Value-based DRL: DQN

However, since the dimensions of state and action are extremely high in our problem, it is difficult to use such iteration method to find the optimal Q-values. In order to settle infinite state and action space, deep Q-learning network (DQN), combining Q learning with a deep neural network, can be adopted [129]. In DQN, the Q function is represented by a deep neural network  $Q(s, a; \theta)$  instead of  $Q(s, a)$ . The parameter  $\theta$  stands for the weights of the neural network and the Q-network is trained by updating  $\theta$  at each iteration to toward the optimal Q values [130].

---

#### Algorithm 9 Deep Q-learning with Experience Replay

---

- 1: **Initialization:** Initialize replay memory  $\mathcal{D}$  to capacity  $D_N$
  - 2: **for** for all episode **do**
  - 3:   Initialize  $s_t$
  - 4:   **for** all steps of episode **do**
  - 5:     with probability  $\xi$  select random action  $a_t$
  - 6:     otherwise select  $a_t = \max_a Q^*(s_t, a; \theta)$
  - 7:     Take action  $a_t$ , observe the reward  $r_t$  and the next state  $s_{t+1}$
  - 8:     Store transition  $(s_t, a_t, r_t, s_{t+1})$  in  $\mathcal{D}$
  - 9:     Sample random mini-batch of transitions  $(s_j, a_j, r_j, s_{j+1})$  from  $\mathcal{D}$
  - 10:     Set  $y_j = r_j + \lambda \max_{a'} Q(s_{j+1}, a'; \theta)$  when  $s_{j+1}$  is non-terminal, otherwise  $y_j = r_j$
  - 11:     Perform a gradient descent step on  $(y_j - Q(s_j, a_j; \theta))^2$  according to Equation (8)
  - 12:   **end for**
  - 13: **end for**=0
- 

The deep Q-function is trained towards the target value by minimizing the loss function, which is defined as the mean-squared error in Q-values [78]:

$$L(\theta) = \mathbb{E} \left[ (y_t - Q(s_t, a_t; \theta))^2 \right], \quad (6.23)$$

where  $y_t = r_t + \lambda \max_a Q(s_{t+1}, a; \theta)$  is the Temporal Difference (TD) target. Then the gradient of the loss function can be expressed as:

$$\frac{\partial L(\theta)}{\partial \theta} = \mathbb{E} \left[ (y_t - Q(s_t, a_t; \theta)) \frac{\partial Q(s_t, a_t; \theta)}{\partial \theta} \right]. \quad (6.24)$$

Therefore, the parameter  $\theta$  of the deep neural network can be updated by using stochastic

gradient descent (SGD) [129];

$$\theta_{t+1} = \theta_t + \alpha (y_t - Q(s_t, a_t; \theta_t)) \nabla Q(s_t, a_t; \theta_t) \quad (6.25)$$

In order to make sure a stable solution of DQN, experience replay is used. At each time instant  $t$ , the agent stores its interaction experience tuple,  $e_t = (s_t, a_t, r_t)$ , into a replay memory,  $\mathcal{D}_t = \{e_1, \dots, e_t\}$ . Then the recorded batch data are randomly sampled from the replay memory to train the DQN. The basic deep Q-learning with experience replay is shown in Algorithm 10 [131]. Comparing the Algorithm 8, there are two main improvements in DQN Algorithm 10.

- Replacing Q function with multi-layer deep convolution networks. The hierarchical layers of tiled convolution filters can exploit the local spatial correlations, which makes it possible to extract high-level features from raw input data.
- Utilizing experience replay. This allows the network to learn from more various past experiences, and restrains the network from only focusing on what it is immediately doing.

#### 6.6.4 Actor-Critic based DRL: DDPG

As an actor-critic, model-free algorithm, the DDPG is achieved based on the deterministic policy gradient that can operate over continuous action spaces. As mentioned before, the DDPG consists of actor network and a critic network. With the input  $s_t$ , actor network  $\pi(s_t; \theta^a)$  generates deterministic action  $a_t = \pi(s_t; \theta^a)$ , where  $\theta^a$  is the actor parameter. One advantage of DDPG, off-policy, the exploration can be treated independently from the learning process. Similar with  $\xi$ -greedy algorithm, we add noise to the original output action to balance the exploration and the exploitation.

After generating action by actor network, the reward can be obtained from environment. Based on action-state pairs, we use the critic network with weight  $\theta^c$  to estimate the Q value  $Q(s_t, a_t; \theta^c)$  to evaluate the selected action  $a_t = \pi(s_t; \theta^a)$ . Similar to DQN, in order to get uncorrelated tuples, the experience replay. The optimal parameter is also updated to minimize the loss function, which is the mean square error between the estimated Q value and the target



value. [78]:

$$L(\theta) = \mathbb{E} \left[ (y_t - Q(s_t, a_t = \pi(s_t; \theta^a); \theta^c))^2 \right], \quad (6.26)$$

where  $y_t = r_t + \lambda \max_a \pi(s_t; \theta^a); \theta^c$  is the target Q value. Base on these Q values, the the actor network update its weights in the direction of getting larger Q value according to the deterministic policy gradient theorem, that is

$$\nabla_{\theta^a} J(\pi) = \mathbb{E} \left[ \nabla_a Q(s, a; \theta^c) \Big|_{a=\pi(s; \theta^a)} \nabla_{\theta^a} \pi(s; \theta^a) \right] \approx \frac{1}{N} \nabla_a Q(s, a; \theta^c) \Big|_{s=s_t, a=\pi(s_t; \theta^a)} \nabla_{\theta^a} \pi(s; \theta^a) \Big|_{s=s_t} \quad (6.27)$$

The DDPG algorithm is shown in below

---

#### Algorithm 10 DDGP

---

- 1: **Initialization:** Initialize critic network, actor network and replay memory  $\mathcal{D}$  to capacity  $D_N$
  - 2: **for** all episode **do**
  - 3:   Initialize a random process noise for action exploration
  - 4:   Receive initial observation state  $s_1$
  - 5:   **for** all steps of episode **do**
  - 6:     otherwise select  $a_t = \pi(s_t; \theta^a + \mathbb{N}_t)$  according to current policy and exploration noise
  - 7:     Take action  $a_t$ , observe the reward  $r_t$  and the next state  $s_{t+1}$
  - 8:     Store transition  $(s_t, a_t, r_t, s_{t+1})$  in  $\mathcal{D}$
  - 9:     Sample random mini-batch of transitions  $(s_j, a_j, r_j, s_{j+1})$  from  $\mathcal{D}$
  - 10:     Set  $y_j = r_j + \lambda \max_a \pi(s_{j+1}; \theta^a); \theta^c$  when  $s_{j+1}$  is non-terminal, otherwise  $y_j = r_j$
  - 11:     Update critic parameter by minimizing the loss function  $L(\theta) = \mathbb{E} \left[ (y_t - Q(s_t, a_t = \pi(s_t; \theta^a); \theta^c))^2 \right]$
  - 12:     Update actor policy by using the policy gradient in Eq.(25)
  - 13:   **end for**
  - 14: **end for**=0
- 

## 6.7 Simulation Results

### 6.7.1 Environment

We assumed that there are 50 UEs and the total bandwidth is 20 MHz. One BS, located at the center of the cell. These UEs are located uniformly and randomly within the cell rang

$r \in [0.01km, 1km]$ . The small-scale fading is assumed to be Rayleigh distribution and modelled by the Jakes model with Doppler frequency  $f_d = 10Hz$  and time slot  $T_s = 10ms$  [126] According to [132], the large scale is modeled as  $\beta = -120.9 - 37.6 \log_{10}(d) + 10 \log_{10}(z)$ , where  $d$  is the transmitter-to-receiver distance and  $z$  is a log-normal random variable with standard deviation being 8 dB. The AWGN power is  $-174dBm$  [47]. The power allocation objective of this network is to maximize the total throughput rate under the constraint emitting power.

Table 6.1: Main Parameters of DRL enabled MD-IMA Network

Parameters	Values
Macro cell radius	1 km
Total bandwidth	20 MHz
Maximum transmit power	40 W
Power level	10
Doppler frequency	10 Hz
Standard deviation of log-normal shadowing	8 dB
large scale fading	$\beta = -120.9 - 37.6 \log_{10}(d) + 10 \log_{10}(z)$ dB
AWGN power	-174 dBm

### 6.7.2 LSTM Parameters Setting

To evaluate the effectiveness of LSTM based prediction method, the experiments are conducted on real-world data. The data sets, simulation conditions and two baseline algorithms are described in this subsection.

- Data Set

For data analysis with deep learning, it is essential to obtain a high-quality data set. In this work, a publicly available real-world multi-source dataset released through Telecom Italia in 2015 is adopted [95]. The dataset is composed of telecommunications, weather, social networks and electricity data from the city of Milan and the Province of Trentino, collected between 1 Nov 2013 and 1 Jan 2014. In this work, we focus on telecommunication records from Milan. This traffic is measured by using the terms of total call detail record (CDR) data, which is generated when a user receives or sends SMS, call and Internet over 10-minute intervals.

For the convenience of CDR recording, the city of Milan is divided into  $100 \times 100$

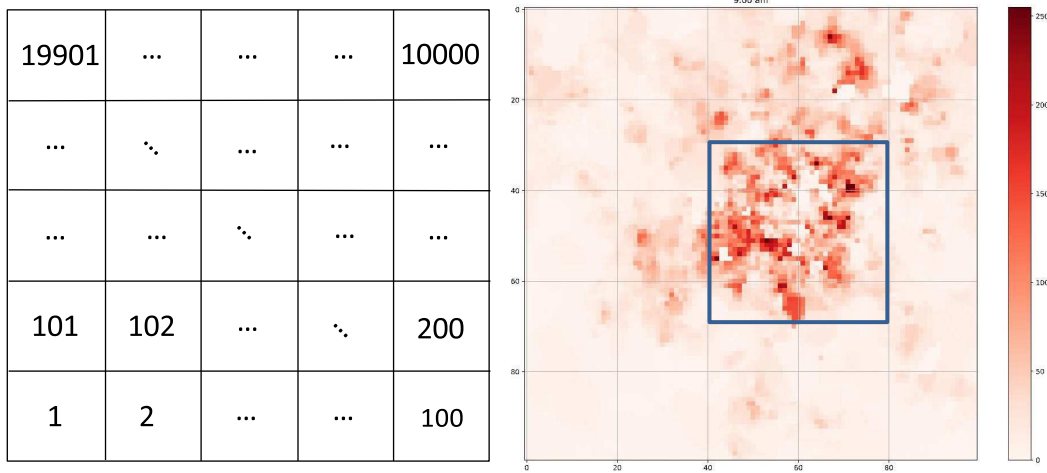


Figure 6.3: Grid map and the CDR heat map of Milan.

grids, marked by a unique ID, as shown in Fig. 6.3. The size of each grid is  $235 \times 235$  meters. The CDR numbers can reflect the UE density, and so we can predict the hotspot by predicting the CDR numbers of every grid. By adding six-time intervals (10 minutes), the aggregated CDR numbers of each grid in one hour are obtained.

- **Simulation Conditions**

From Fig. 6.3, we noted that the active zones focus on the central 40 grids (horizontal:40-80, vertical:30-70 ) with 1600 grids. Therefore, the data set of these grids is used to evaluate the performance of all prediction methods. In order to reduce the impact of noise on time series, wavelet-based filtering is used to smooth the raw data. All models are trained on the first 1320 hours of data (first 55 days) and tested on the 24 hours (one day) of data. Their performances were evaluated by computing the RMSE (Root Mean Square Error) value of  $i^{th}$  grid [94]:

$$RMSE_i = \sqrt{\frac{1}{z} \sum_{t=1}^z (x_t^i - \hat{x}_t^i)^2}, \quad (6.28)$$

where  $\hat{x}_t^i$  and  $x_t^i$  are the predicted CDR numbers of  $i^{th}$  grid and the ground truth, respectively;  $z$  is the number of all predicted values.

Table 6.2: The parameters of the LSTM and ConvLSTM for sum-rate prediction.

Parameters	LSTM	ConvLSTM
hidden layer numbers	2	1 and 2
hidden nodes of the first layer	50	50
hidden nodes of the second layer	25	25
Batch Size	64	64
Time Steps	24	24
Training Steps	150	150
Grid numbers for each time step	5*5 and 2*2	2*2, 5*5 and 10*10
Kernel size	N/A	2*2 and 5*5

To verify the accuracy of the proposed one LSTM based algorithm, three models, including the auto-regressive integrated moving average (ARIMA), several LSTM based algorithms and Convolutional LSTM (ConvLSTM), are employed as baselines. ARIMA models are generally denoted  $ARIMA(p,d,q)$  where parameters  $p$  is the number of auto-regressive terms,  $d$  is the degree of difference and  $q$  is the size of the moving average window [96]. In our simulation, an  $ARIMA(2,2,0)$  is modeled by using the python stats models. The LSTM and ConvLSTM are built by using Keras of Tensorflow. We use Adam optimizer with learning rate=0.001, beta1=0.9, beta2=0.999 and epsilon=1e-08. In order to achieve the best results, the hyperparameters of LSTM should be adjusted and the main parameters of the LSTM and ConvLSTM neural network are shown in Table. 6.2 [96].

### 6.7.3 DQN Parameters Setting

A four-layer feed-forward neural network is chosen as DQN. The rectified linear unit (ReLU) is adopted in the two hidden layers and the neuron numbers of two hidden layers are 128 and 64, respectively [47]. The input of the DQN is the state. The output is the power allocation. The power level is set as 10/5 and thus the output dimension is 10/5.

- **Learning Rate:** The Adam is adopted as the optimizer for DQN. The learning rate of optimizers should be selected carefully. Specifically, the learning rate is a configurable hyper-parameter used in the training of neural networks that has a small positive value, often in the range between 0.0 and 1.0. The learning rate hyperparameter controls the rate or speed at which the model learns. Fig. 6.4 compares the sum-rate performance for

three different learning rate values. In order to simplify the simulation, the discounted factor is set as 0 firstly. As shown in Fig. 6.4, the largest learning rate, allows the model to learn faster, at the cost of arriving on a sub-optimal final set of weights. A smaller learning rate allows the model to learn a more optimal set of weights but may take significantly longer to train. In order to balance the performance and the training cost, we set the learning rate as 0.01 in the following.

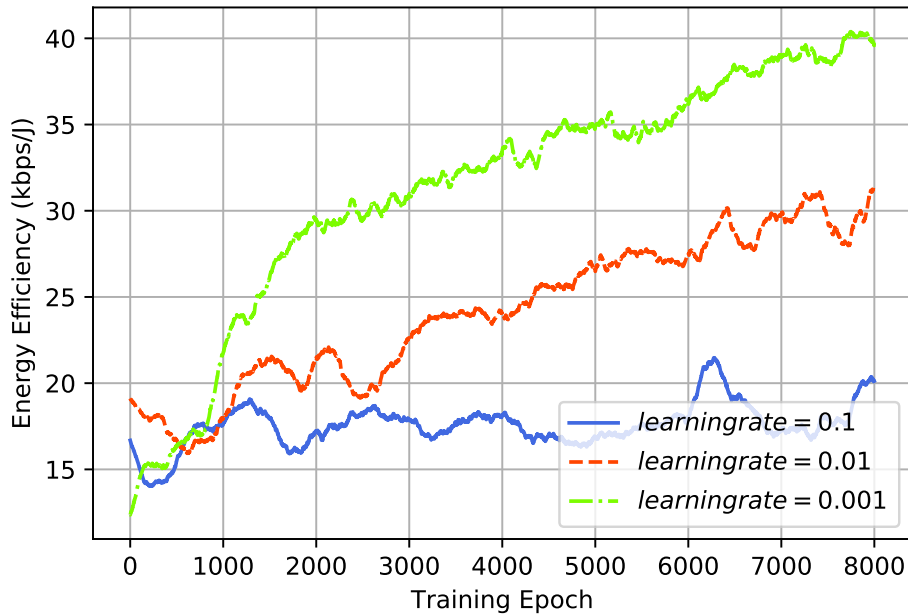


Figure 6.4: WEE comparison of DQN based method with different learning rate values during training period

- Discount Factor:** The discount factor,  $0 \geq \lambda \leq 1$ , essentially determines how much the reinforcement learning agents care about rewards in the distant future relative to those in the immediate future. If  $\lambda = 0$ , the agent will be completely myopic and only learn about actions that produce an immediate reward. If  $\lambda = 1$ , the agent will evaluate each of its actions based on the sum total of all of its future rewards. In this section, the EE performance of different discount factors is studied. We set  $\lambda \in \{0, 0.1, 0.3, 0.7, 0.9\}$ , and the EE over the 1200 training episodes is shown Fig.6.5. At the same time slot, the averaged EE performance with higher  $\lambda$  are worse than the rest with lower  $\lambda$  values.

According to the simulation results, the discount factor value is set as 0.1 to achieve the best WEE performance.

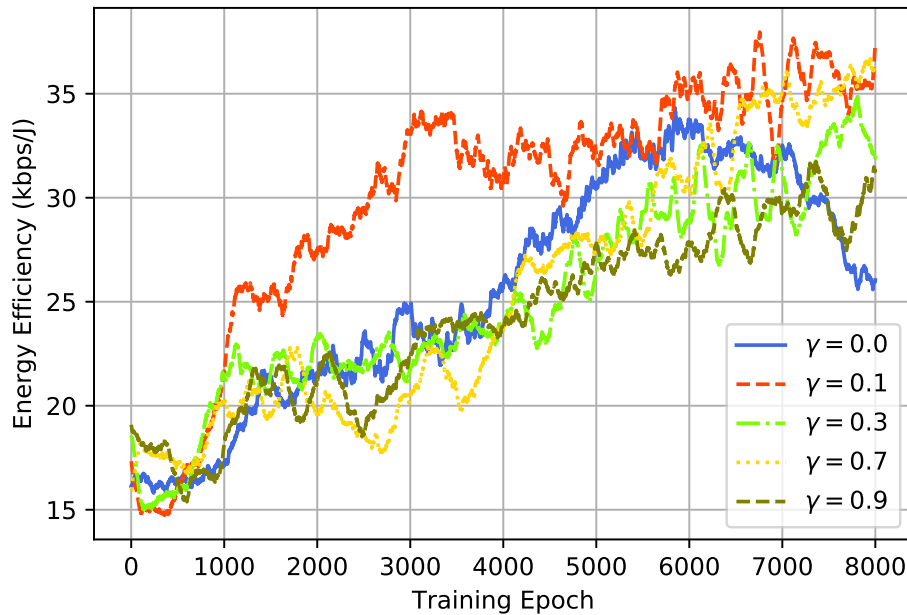


Figure 6.5: WEE comparison of DQN based method with different discount factor values during training period

- Training Episodes Number:** At the beginning, the DQN is initialized randomly and then trained epoch by epoch. In the exploration period, the  $\xi$ -greedy learning strategy is adopted. The value of  $\xi$  is gradually reduced over time from 0.9 to 0.1 [127]. In each episode, the large-scale fading is invariant and thus the total number of episodes should be set large enough to overcome the generalization problem. The time slot per episode could not be large to reduce over-fitting. In order to find the appreciate the number of training episode, the EE performance with  $\lambda = 0.1$  and 0.01 learning rate for 20000 training episode is shown in Fig. 6.6. We can see that the averaged EE becomes relatively stable after 6000 training episode. Therefore, the training episodes number is set as 8000 to ensure the performance of DQN.

In summary, we set training episodes number is 8000 and the time slots number is 50. Furthermore the batch size of reply memory is 256 and the training interval is 10. It means that

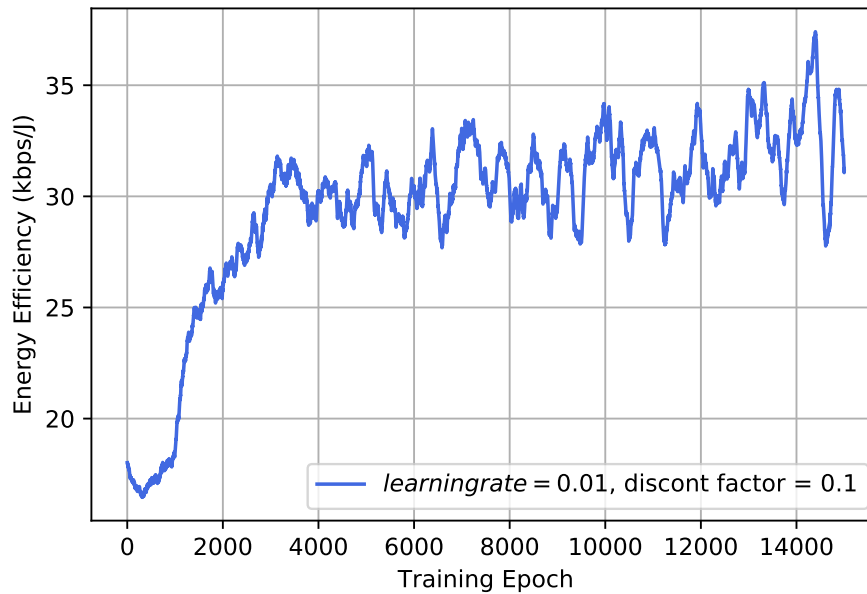


Figure 6.6: WEE performance of DQN based power allocation for training episodes with  $\lambda = 0.1$

the DQN is trained with 256 random samples in the experience replay memory every 10 time slots. The Adam is adopted as the optimizer for DQN with the learning rate of 0.01. All the parameters related with DQN is illustrated in the Table 6.3.

#### 6.7.4 DDPG Parameters Setting

The DDPG consists of two sub-networks: actor-network to select actions and critic network to estimate Q values of the selected actions. Most parameters of DDPG are similar as that of DQN. We mainly evaluate the choice of learning rate and the number of training episodes in this subsection.

- Learning Rate:** First, we evaluate the impact of the learning rate of DDPG on the WEE. Fig. 6.7 and Fig. 6.8 compares the WEE of DDPG with a different learning rate of actor and critic networks, respectively. It can be seen that the larger learning rate allows the model to learn faster at the cost performance, while a smaller learning rate allows the model to learn a more optimal performance but take longer to train. As a result, to offer faster converge speed with competitive performance, we set the learning rate of actor and

Table 6.3: The parameters of the DQN.

Parameters	Value
Learning Rate	$1e^{-2}$
Discount Factor	0.1
Exploration	$\xi_{max} = 0.9, \xi_{min} = 0.1$
Output layer of DQN	linear with 10 dimension
Input layer of DQN	linear with 51/34/17 dimension
1st hidden layer of DQN	ReLU,64
2nd hidden layer of DQN	ReLU,128
Batch Size of Relay memory	256
Training Episodes Number	8000
Test Episodes Number	100
Time slots per Episodes	50
Training interval of time slot	10

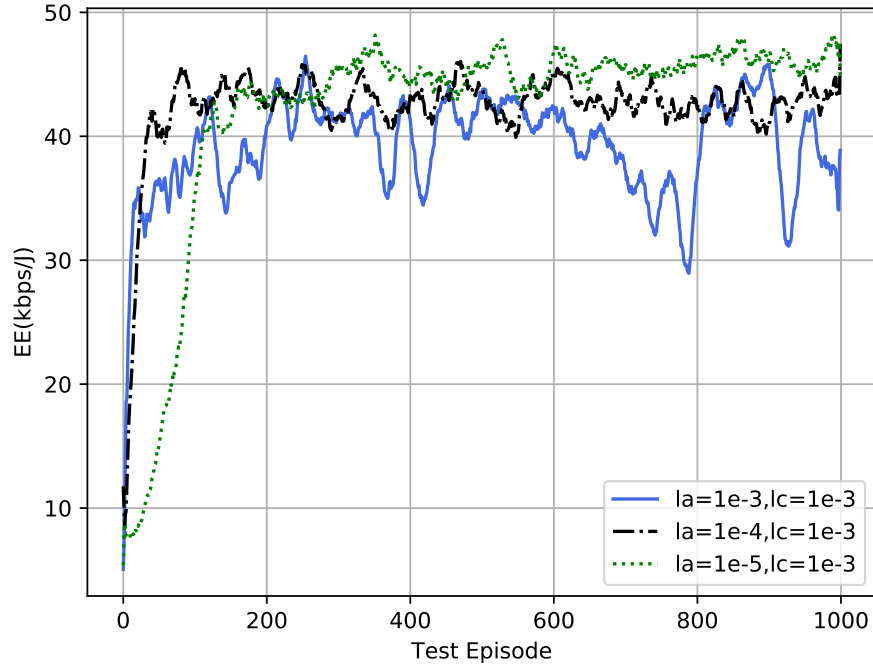


Figure 6.7: WEE comparison of DDPG based method with a different learning rate of the actor-network.

critic as  $1e - 4$  and  $1e - 3$ , respectively.

- **Training Episodes Number:** At the beginning, the DDPG is initialized randomly and then trained episode by episode. From Fig.6.7, we can see that the WEE becomes rela-



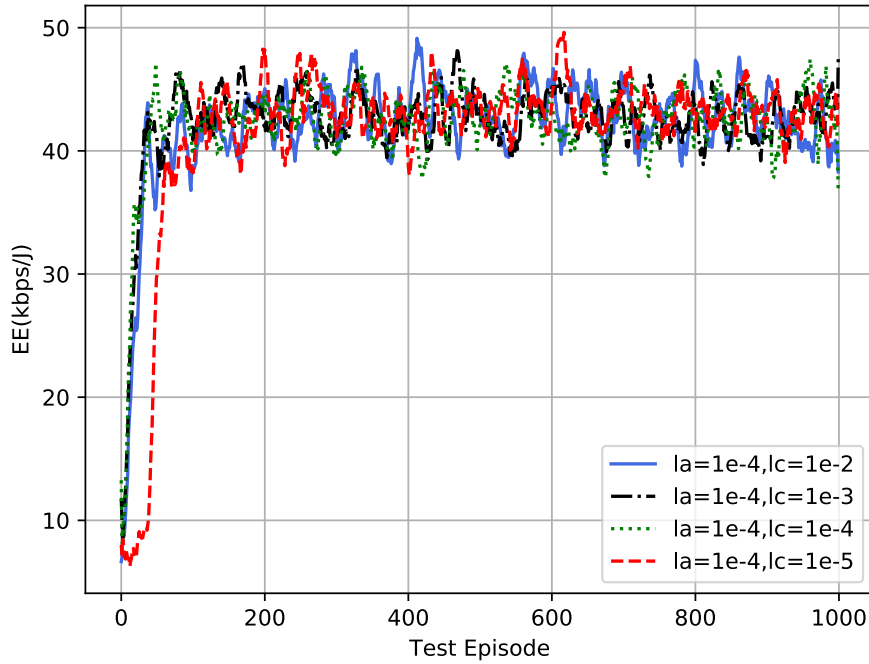


Figure 6.8: WEE comparison of DDPG based method with a different learning rate of the critic-network.

tively stable after 300 training episode when the  $la = 1e - 4$  and  $lc = 1e - 3$  and so the training episodes number is set as 400 to ensure the performance of DDPG. Compared with Fig.6.6, the DDPG can achieve convergence faster than that of DQN. In summary, the specific parameter of DDPG is shown in Table 6.4

Table 6.4: The parameters of the DDPG.

Parameters	Values of Actor	Values of Critic
Learning Rate	$1e^{-4}$	$1e^{-3}$
Discount Factor	NA	0.1
1st hidden layer	ReLU,64	ReLU,64
2nd hidden layer	ReLU,128	NA
Batch Size of Relay memory	256	256
Training Episodes Number	400	400
Test Episodes Number	100	100
Time slots per Episodes	50	50

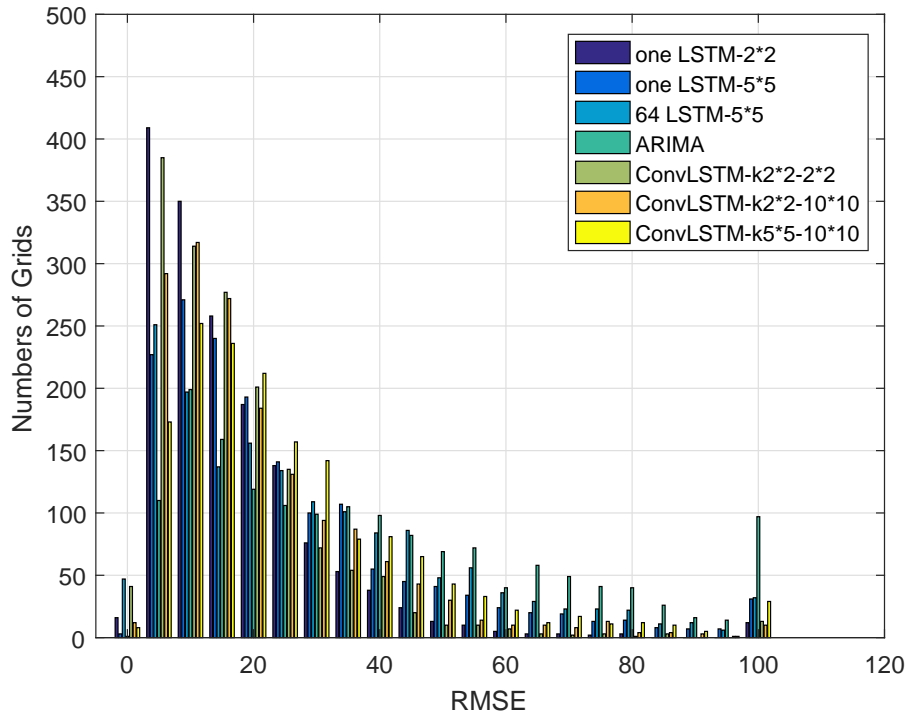


Figure 6.9: Histogram Comparison among one LSTM and three baselines based sum-rate prediction.

## 6.7.5 Simulation Results

### 6.7.5.1 Accuracy of LSTM based WEE Prediction

The prediction accuracy of the proposed one LSTM based forecasting method is compared with ARIMA, several LSTM and ConvLSTM methods. Fig. 6.9 and Fig. 6.10 demonstrate the distribution and cumulative distribution function (CDF) of forecasting RMSE of four methods, respectively.

Compared with the ARIMA, deep learning approaches based on LSTM have much better performance, due to the robust nature and feedback connections of LSTM. By comparing the two different LSTM based schemes with  $5 \times 5$  zones, it can be seen that the several LSTM based scheme has more grids whose  $RMSE < 10$  than that of one LSTM based method. In several LSTM based scheme, every LSTM is training specifically for each grid and so it has more high accuracy results ( $RMSE < 5$ ). However, due to overfitting and lower diversity of samples, the overall performance of several LSTM based scheme is worse than that of one

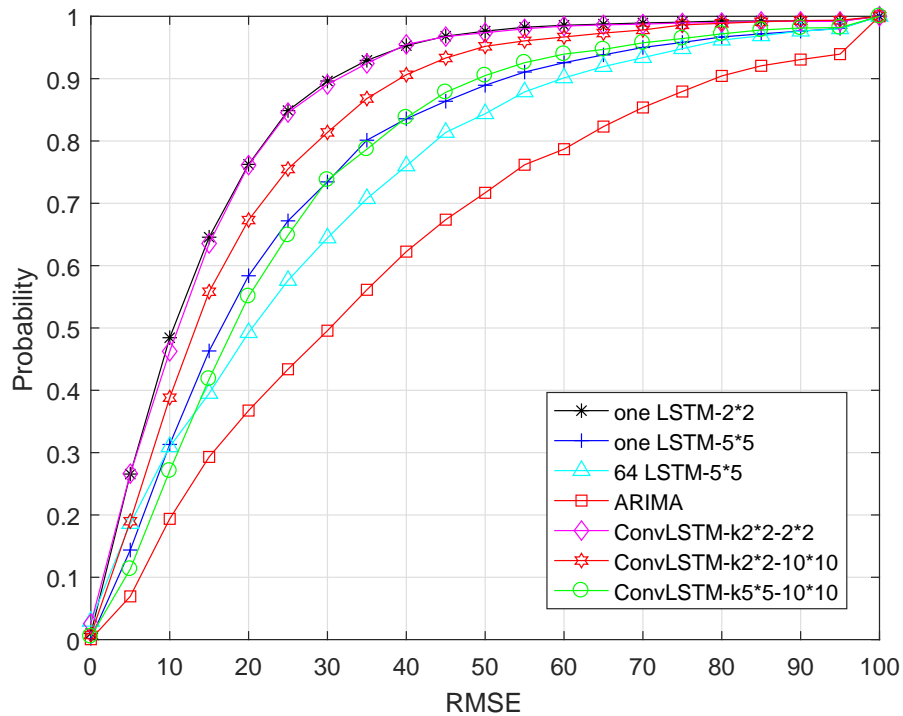


Figure 6.10: CDF Comparison among one LSTM and three baselines based sum-rate prediction.

LSTM based scheme. We also noted that the performance of the one based LSTM scheme is improved by reducing the zone size from  $5 \times 5$  to  $2 \times 2$ . There are two reasons. On the one hand, by adopting smaller zones, the number of training samples is increased. On the other hand, it also proves that the spatial correlation among neighboring 4 grids is larger than that of neighboring 25 grids.

The ConvLSTM, whose zone size and kernel size are  $2 \times 2$ , has a similar RMSE performance with that of one LSTM based method. If the input zone size of ConvLSTM is the same, the performance of ConvLSTM with  $2 \times 2$  kernel has better RMSE performance. It also illustrates that the neighboring 4 grids have a stronger spatial correlation. Furthermore, with the same kernel size, the RMSE performance decreased with the rise of zone size by introducing more redundant information. In summary, our proposed one LSTM based method enables to explore the temporal-spatial features for the small zone (4 grids) without the Convolutional layer. There are 90% grids whose RMSE is smaller than 30 by using one LSTM based sum-rate prediction.

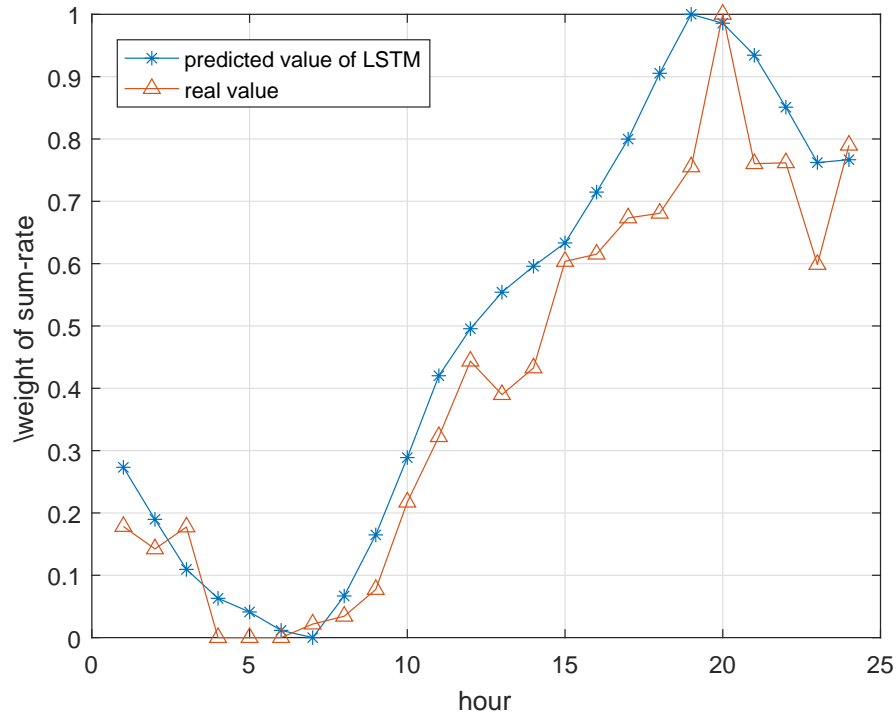


Figure 6.11: Compare the predicted weight with real weight of sum-rate for the 12<sup>th</sup> grid.

By using the proposed one LSTM, the sum-rate of all grids can be predicted and so the weight of the sum-rate can be determined by normalized the predicted results. In order to evaluate the predicted accuracy, we take  $\alpha_1$  of 12<sup>th</sup> grid as an example. As shown in Fig. 6.11, the predicted weight of the sum-rate can follow the real weight changes of the sum-rate.

### 6.7.5.2 WEE Performance of DQN with different States

As we described in VI-A, three states with different features are proposed. Specifically, state1  $s^1$  only considers the channel information, state 2  $s^2$  add last power allocation as the auxiliary features and state 3  $s^3$  includes channel information, last power allocation and last WEE. The WEE comparison of DQN with three states is shown in Fig.6.12. It can be seen that the DQN with  $s^3$  has the best WEE performance and the WEE of DQN with  $s^1$  is the worst. By introducing two more features, the EE performance can improve 17%. It means that the more auxiliary features can help the DQN to get closer to the optimum. Therefore, we use  $s^1$  to do the following simulations.

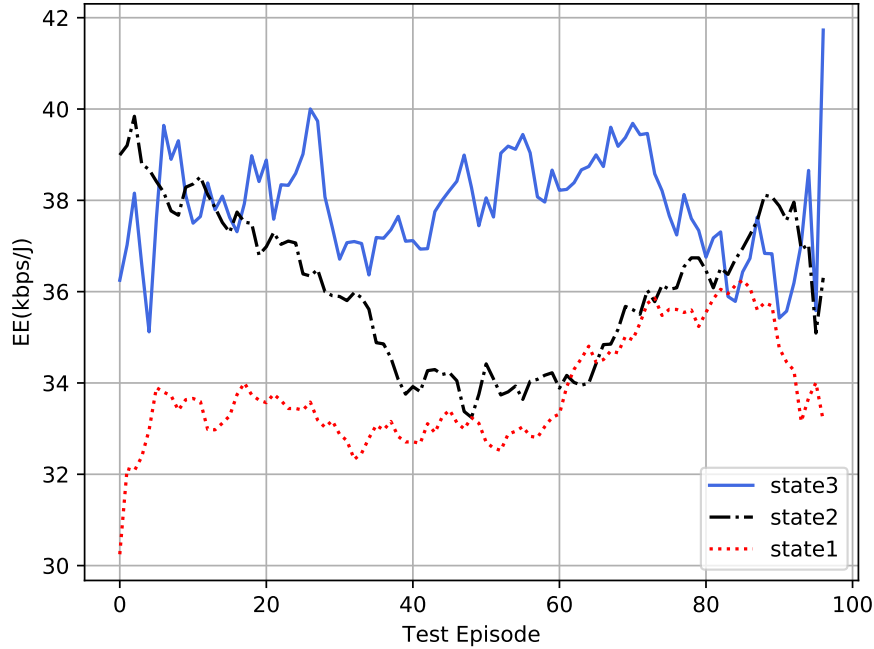


Figure 6.12: WEE comparison of DQN with different states in test episodes for  $[\alpha_1 = 0.5, \alpha_2 = 0.5]$

### 6.7.5.3 WEE Performance of DRL Based Power Allocation

In this section, the WEE comparison between DQN and DDPG based power allocation in training episodes is shown in Fig.6.13. As shown in Fig. 6.13, the DDPG based method outperforms than that of DQN based algorithm. Specifically, the EE gain of DDPG over DQN with 5 levels and DQN with 10 power levels are 15% and 20%, respectively. The reason is that the output decisions can only be discrete of DQN, which causes quantization error for continuous action tasks (e.g. power allocation). We also notice that the performance of DQN decline with the power level decrease from 10 to 5. Furthermore, the convergence of DDPG is extremely faster than that of DRL, because the action space dimension of DRL is exponentially increased with the power level.

Then, three advanced model-based optimization algorithms, namely fractional programming (FP), weighted minimum mean squared error (WMMSE) and near-optimal solution (Algorithm 6 in Chapter 5) are considered as benchmarks to evaluate our proposed DRL algorithms. The WEE comparison between DRL based algorithm with model-based methods for

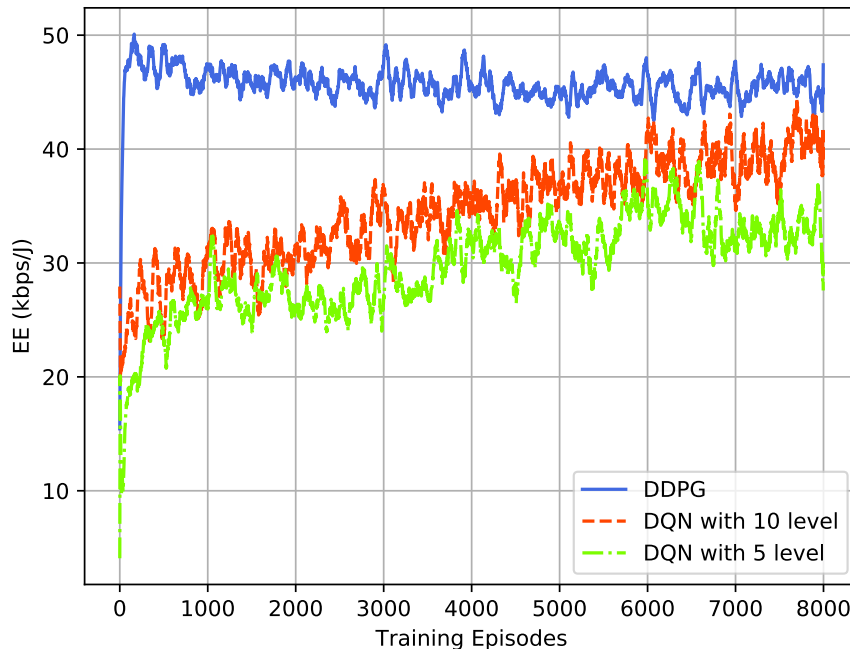


Figure 6.13: WEE comparison between DQN and DDPG in training episodes for  $[\alpha_1 = 0.5, \alpha_2 = 0.5]$

test episodes is shown in Fig. 6.14. We can see that the proposed DDPG achieves the highest WEE, which is similar to the near-optimal solution. The DDPG based method outperforms than that of the traditional optimization-based algorithms. Specifically, the DDPG based algorithm can improve around 17% and 35% WEE than that of WMMSE and FP, respectively.

#### 6.7.5.4 Time Cost

In terms of computation complexity, the time cost of DQN is in a linear relationship with layer numbers, with the utilization of GPU. Meanwhile, both FP, WMMSE and near-optimal algorithms are iterative algorithms, and thus the time cost is not constant, depending on the stopping criterion condition, initialization and CSI. The time cost per test episode of our proposed DRL based and model-based methods are listed in Table 6.5. It can be seen that the time cost of DQN and DDPG are similar due to similar DNN models, and they are about 10, 100 and 500 times faster than FP, WMMSE and near-optimal methods, respectively. In summary, the proposed DDPG can achieve the best WEE performance with the lowest computational time cost.

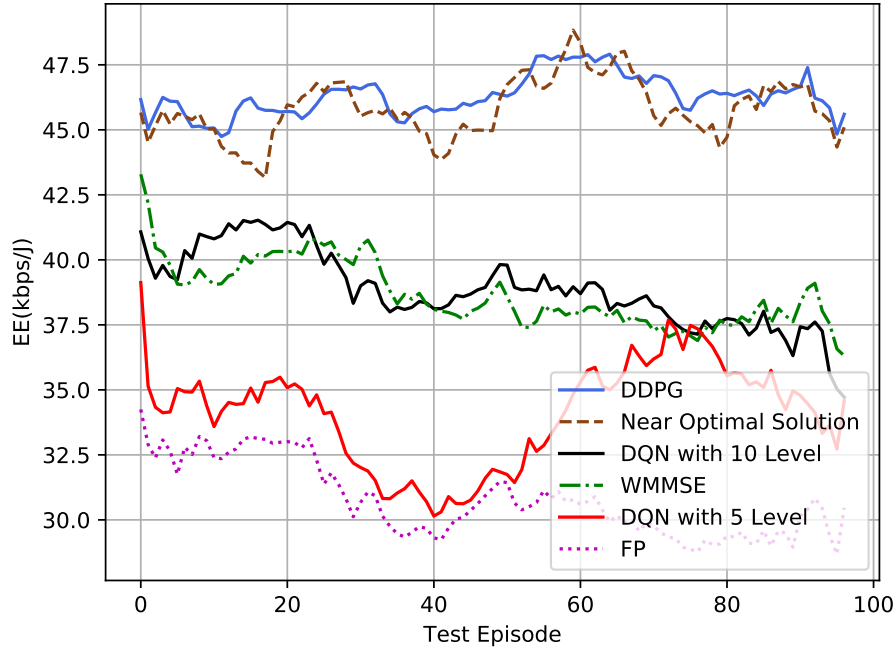


Figure 6.14: WEE comparison among DDPG, DQN, FP, WMMSE and exhaustive optimal solution in test episodes for  $[\alpha_1 = 0.5, \alpha_2 = 0.5]$

Table 6.5: Average time cost per episode (sec) of DRL and optimization methods

Methods	DDPG	DQN	FP	WMMSE	Near-Optimal
Time Cost	$3.83e^{-4}$	$3.28e^{-4}$	$5.2 e^{-3}$	$4.9 e^{-2}$	$2.2 e^{-2}$

### 6.7.5.5 Impact of the weights on the EE

The predicted weights of EE are varying and so the weighted EE of DDPG based power allocation algorithms for different weights are evaluated in Fig.6.15. we can see that the WEE is increased with the weight value of the sum rate. The reason is that more power is required to meet the increased sum-rate requirements. However, the increased speed of weighted EE becomes slower with the increase of the weight value of the sum rate. This is because when the total transmits power  $P$  used exceeds a relatively large value, the sum rate can not be improved due to the fact that interference signals become the dominant factor of the SINR.

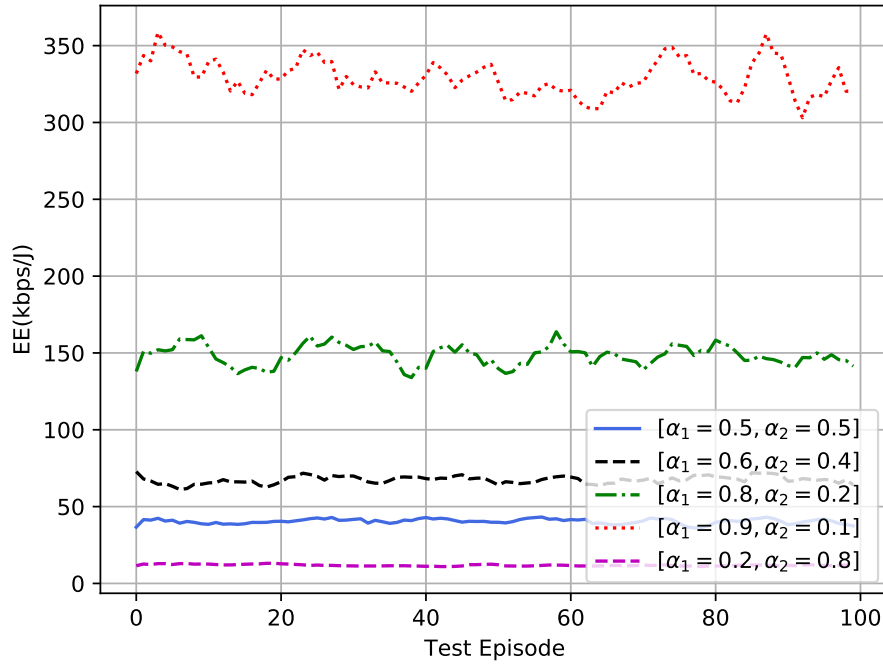


Figure 6.15: WEE comparison of DDPG based power allocation for different weights

## 6.8 Chapter Summary

In this chapter, we mainly study how to use DRL based methods to solve the optimization problem of resource allocation in the MD-IMA system. Compared with the traditional optimization algorithms, DRL based resource allocation methods are more compliant with optimizations in practical communication scenarios because of its model-free nature. In the proposed two-step scheme, the one-LSTM neural network is adopted to predict the overall network requirements (I-QoSE) and then DRL based power allocation algorithms are proposed to maximize the predicted I-QoSE under several practical constraints. Both value-based DRL algorithms, such as DQN, and the actor-critic based DDPG algorithm are adopted to do power allocation for the MD-IMA system. The simulation results illustrate that DDPG performs the best in terms of both I-QoSE performance convergence speed and time cost, compared with DQN based method and traditional optimization-based algorithm. Specifically, the EE gain of DDPG based method over DQN, FP and WMMSE are 15%, 17% and 35%, respectively. The time cost of DRL based method is 10 times and 100 times faster than that of FP and WMMSE.



## **Chapter 7**

# **Adaptive Vehicle Clustering and Data Traffic Explosion in SDN Enabled 5G-VANET**

With the anticipated arrival of autonomous vehicles, supporting vehicle generated data traffic due to the dramatically increased use of in-vehicle mobile Internet access will become extremely challenging in 5G based vehicular networks. This is mainly due to the high mobility of vehicles on the road and the high complexity of 5G heterogeneous networks (HetNet). In order to support the increasing traffic and improve the HetNet management, a Software-Defined Networking (SDN) enabled 5G-Vehicular Ad Hoc Network (5G-VANET) is proposed in this article. In this integrated architecture, vehicles are clustered under the condition of SDN, and one vehicle in each cluster is selected as a gateway to support aggregated traffic. To ensure the capacity of the trunk link between the gateway and base station, a Non-orthogonal Multiplexed Modulation (NOMM) scheme is proposed in this chapter to effectively aggregate the Vehicle-to-Infrastructure (V2I) traffic and further improve energy efficiency. NOMM splits the data stream of each user into multi-layers and modulates them simultaneously. Sparse spreading code is also applied in partially superposing the modulated symbols on several resource blocks. Furthermore, we analyzed the energy efficiency of the proposed NOMM scheme and the orthogonal transmission scheme theoretically. The simulation results show that the energy efficiency performance of proposed NOMM is 1.3-2 times than that of traditional orthogonal

transmission scheme, due to overlapping gain.

## 7.1 Introduction

With emerging of intelligent transportation applications, including traffic management and entertainment, Vehicular Ad Hoc Network (VANET) has been widely considered as a promising technology [133]. The VANETs not only provide Vehicle-to-vehicle (V2V) communication but also Vehicle-to-Infrastructure (V2I) communication [134]. Due to the increased in-car mobile data traffic and ubiquitous mobile access requirements of passengers, the large number of V2I communications become a challenge for future 5G cellular networks. For example, resource sharing between the potentially dense distributed vehicles from congested road dramatically increase the energy and resource consumption of V2I communication. Therefore, energy and resource efficiency would be the primary goal in the design of VANET-5G networks. Although there have been some candidate techniques in reducing the radiated power and base station energy consumption for 5G networks, such as mmWave and Massive MIMO, their applications to the high-density and fast-moving terminals of VANETs are constrained[135].

In order to improve the energy efficiency of vehicular communications, we propose a Software-Defined Networking (SDN) enabled 5G-VANET with the capability of adaptive vehicle clustering and beamformed transmission in supporting the aggregated traffic from the cluster head. Through the separation of data plane and control plane [136], SDN enables the 5G-VANET management and facilitates centralized control over HetNets by providing a global network view and a unified configuration interface despite of the underlying heterogeneous networks involved. With its open and reconfigurable interface, SDN provides an enabling platform to apply intelligence and consistent policy for 5G-VANET HetNets. In the proposed 5G-VANET, arriving road traffic will be predicted with the assist of SDN to achieve adaptive vehicle clustering. Within each vehicle cluster, a cluster head (CH) is selected to aggregate traffic from other vehicles and communicate with the cellular BS in order to reduce signaling overhead. A dual CH design is then proposed to guarantee the robustness and seamless trunk link communication.

The link quality between CHs and base stations would impact the performance of whole

V2I communications directly. When a large number of vehicles all request a high data rate at the same time, there will be high capacity demand and pose a huge burden on the trunk-link. Therefore, enhanced V2I data aggregation is needed to increase the trunk-link capacity or improve the energy and spectrum efficiency. Non-orthogonal multiple access (NOMA) [137] techniques have been considered as a promising solution for improving the 5G spectrum efficiency, capacity and network throughput. NOMA allows multiple users to share resources in a non-orthogonal way, while code domain or power domain multiplexing is applied to distinguish different users [138].

However, the fast variation of vehicle position and channel condition makes it difficult for NOMA to be deployed. Therefore in this chapter, we propose non-orthogonal multiplexed modulation (NOMM), which aims at increasing the trunk-link capacity of 5G-VANET and aggregated data traffic effectively. NOMM allows parallel data streams of one user to be modulated simultaneously and partially overlapped on a group of resource elements through sparse spreading code. Compared with NOMA, the advantage of NOMM is that multiple data streams belong to one user instead of multiple different users. This means that different data streams of NOMM come from the same channel, which would reduce the distortion complexity introduced by time-varying channels. Furthermore, NOMM is proved by theory and simulation that despite the aforementioned improvement in data aggregation, it is also highly energy efficient.

The remainder of this chapter is organized as follows. Section 7.2 outlines the architecture of the 5G-VANET integrated network. The system model for NOMM is presented in Section 7.3. Based on the network model, the proposed adaptive vehicle clustering and dual CH design enabled by SDN are then elaborated in Section 7.4. The energy efficiency for traditional orthogonal transmission and proposed NOMM are analyzed in Section 7.5 while the simulation results and conclusion are drawn in Section 7.6 and 7.7 respectively.

## 7.2 SDN Enabled 5G-VANET Integrated Network Architecture

As explained in the last section, energy efficiency is essential for vehicle communication networks. When all the vehicles communicate with cellular eNodeBs directly, massive number of radio link connections are required and eNodeBs have to allocate channel resources to each vehicle no matter how long they would be stay within the coverage of base station. Therefore, in order to reduce power consumption and save spectrum resources, a cluster-based VANET-5G heterogeneous network is introduced in this article. As shown in Fig. 7.1, the overall network architecture of the proposed SDN enabled 5G-VANET, which consists of a HetNet environment is designed to support adaptive vehicle clustering and trunk link traffic aggregation schemes. In our proposed SDN enabled 5G-VANET network, SDN is introduced in order to enable the coordination and information sharing between heterogeneous networks, i.e., base stations from different operators as shown in Fig. 1. SDN controller monitors and predicts the location of vehicles, and then prepare the relevant cellular base stations before the vehicles arrive to guarantee adaptive and efficient clustering. In Fig. 7.1, we can see that the vehicles in the cluster get services from eNBs through the cluster head (CH), which reduce signaling overhead during handover; moreover, communication between vehicles in clusters is through IEEE 802.11p connection, which also relieves the cellular burden and saves licensed spectrum resources. The back-up CH (i.e., yellow car in Fig. 7.1) records a copy of signaling message, i.e., floating car data (FCD) [139] from the existing CH, and prepared for emergencies. In the scenario that the existing CH leaves normally, back-up CH also works as CH immediately and a new back-up CH would be selected according to the pre-specified algorithm.

Due to the high data rate of 5G communication, higher channel capacity is required, especially for large VANET. Therefore in this work, we further propose non-orthogonal multiplexed modulation (NOMM) on top of the 5G-VANET structure in order to improve the trunk-link capacity and reduce the average transmit power. The data transmission processing of 5G-VANET is shown in Fig. 7.2. At the cluster head side, before OFDM signal generation, the aggregated data are divided into several layers, which are modulated and partially superposed. At the receiver side, after OFDM demodulation, channel information can be estimated to detect data.

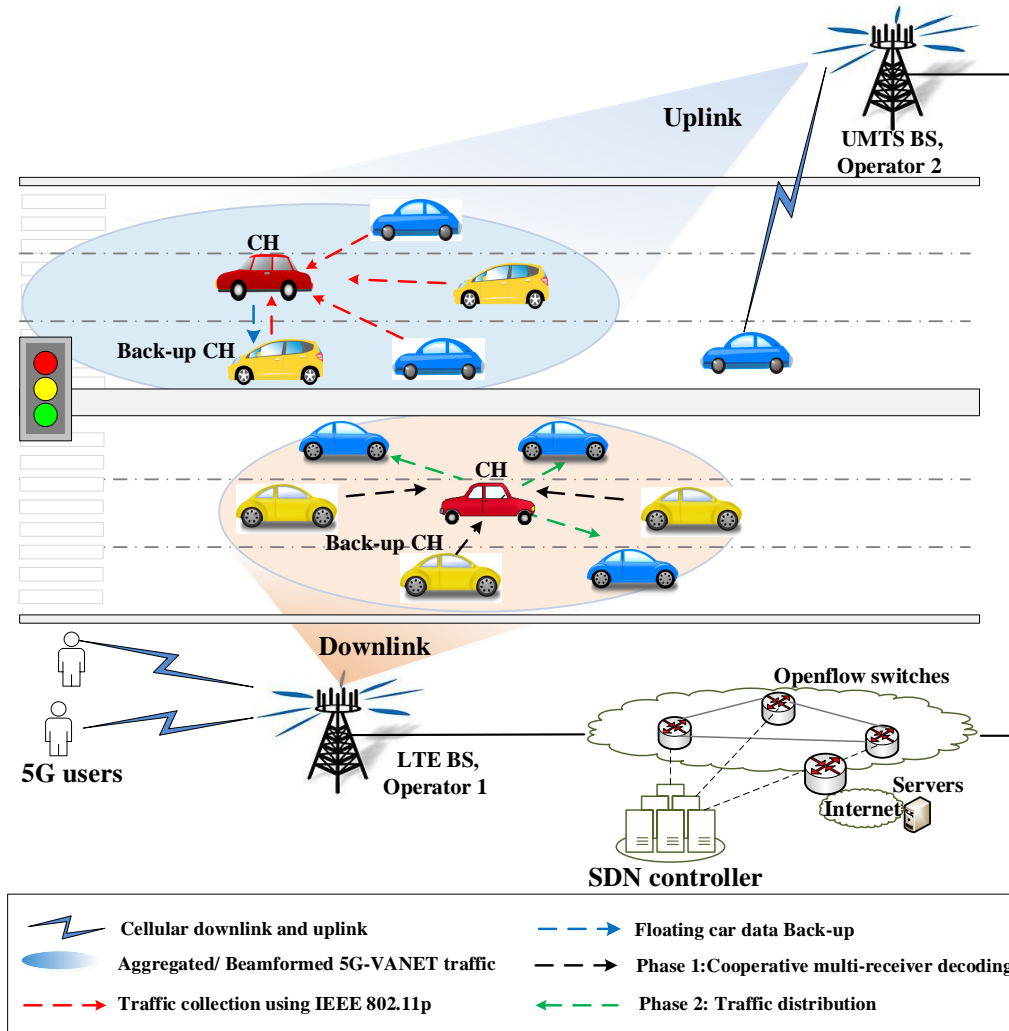


Figure 7.1: SDN enabled 5G-VANET integrated network architecture.

The specific system model of NOMM is presented in the next section.

### 7.3 Adaptive Clustering in SDN Enabled 5G-VANET

Due to the high mobility of vehicles and the restrictions in their range of motion, vehicle clustering is seen as a promising solution in reducing the overhead of cellular networks and providing better communication quality with a low relative speed among clustered vehicles. In related studies, authors in [11] provide a multi-layer Cloud-RAN architecture in order to cluster multi-domain resources for a group of vehicles as well as a single-vehicle. However, detailed

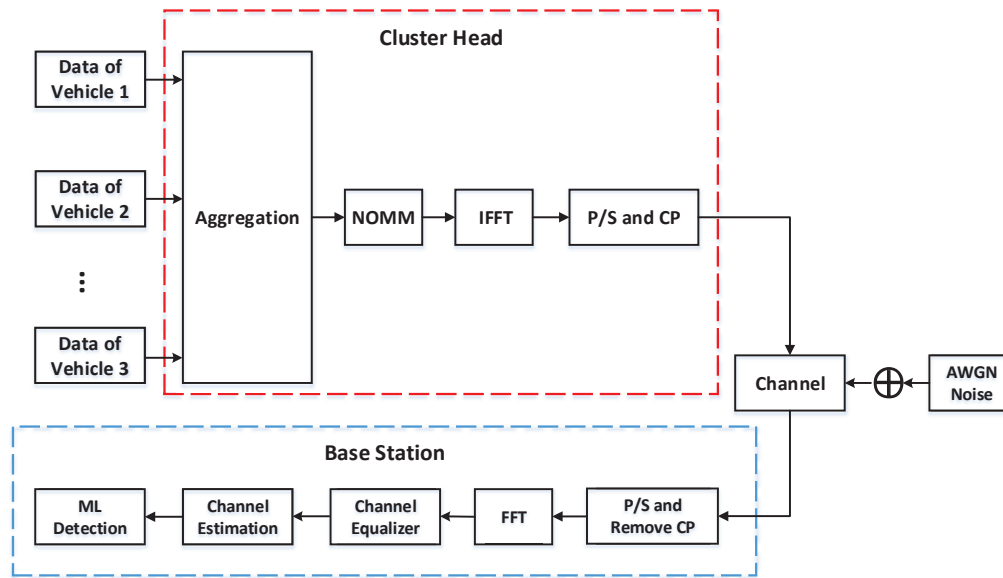


Figure 7.2: Baseband transmission using data aggregation for 5G-VANET.

algorithms are still yet to be designed under the soft-defined heterogeneous vehicular network architecture. In [140], a dynamic clustering-based mobile gateway management mechanism is proposed, which considers vehicle mobility and executes the clustering algorithm periodically. However, how to decide this period still remains as an open problem, and the cluster maintenance also dramatically increase the computing load of the cluster head. With a coexistence of multiple HetNet infrastructures in the future 5G networks, it is also difficult for a single base station to predict the arriving traffic and execute clustering algorithms adaptively due to the limited resources.

In the proposed SDN enabled 5G-VANET, the controller's global view over the HetNets and the timely updating of road traffic topology provides a viable solution in addressing the above challenges. As vehicles usually move fast and APs only have limited coverage, we consider that APs only provide updated information of related vehicles and the clustered vehicles would communicate with BSs through a selected vehicle, namely, cluster head (CH). Due to the consistency of moving speed and direction of traveling vehicles, SDN controller will be able to monitor and predict the location of arriving vehicles using different locations and data analytics techniques, and then inform the relevant cellular BSs in advance to guarantee adaptive and efficient clustering, as shown in Fig. 7.1. Based on the high level "road topology"

collected from heterogeneous BSs and APs of different infrastructures or operators, the proposed clustering algorithm would be executed only when needed instead of periodically. We can also define a traffic threshold and take the delay requirement and size of the upcoming in-vehicle data traffic into consideration when making vehicle clustering decisions.

In Fig. 7.1, vehicles that are moving in two directions are grouped into different clusters. The vehicles that have a cellular interface, i.e., yellow cars in Fig. 7.1, are defined as mobile gateway candidates as they are able to communicate with cellular networks. A CH is selected from the mobile gateway candidates and then all other vehicles in the same cluster communicate with BS through the CH. Moreover, communication between CH and other intra-cluster vehicles could be through different wireless protocols, e.g., IEEE 802.11p, to relieve the cellular burden and save licensed spectrum resources. In order to guarantee seamless communication, a back-up CH is also selected from the mobile gateway candidates to record a copy of the signaling message, namely, floating car data (FCD), from the existing CH and be prepared for emergencies. Note that in Fig. 7.1, the beamforming technique is applied to focus the cellular signal at areas with concentrated vehicles. The vehicle cluster colored blue illustrates the uplink traffic collection procedure, while the cluster colored orange shows the downlink traffic distribution.

Next, we will elaborate on the SDN enabled adaptive vehicle clustering mechanism in 5G-VANET. Specifically, SDN enabled adaptive clustering is realized under the collaboration of cellular BS and mobile gateway candidates. There are three parameters utilized during the clustering procedure: Angle of arrival (AoA) ( $\theta$ ), received signal strength (RSS), and inter-vehicular distance (IVD). Below, the adaptive clustering procedure is divided into four steps:

1) *Base station initialized grouping*: With the road traffic topology provided by the SDN controller, the BSs are aware of the arriving traffic and prepare themselves in advance. Once the cell is overload and clustering conditions are met, the vehicles are roughly classified into groups according to similar AoA and RSS, and the member information of each group is sent back to the mobile gateway candidates in the group.

Assume that at BS side, the received signals from vehicles are classified into  $N$  equally divided transmission angles of  $360/N$  degrees, and the speed limit of the road is around  $V_{MAX}$ . We can define different vehicle groups by the combination of different transmission angles and

$RSS$ . Each group is then characterized by  $\theta_x - \theta_y \leq \frac{360}{N}$  and  $RSS_x - RSS_y \leq 1 - e^{-\frac{\Delta V}{a}}$ , where  $x$  and  $y$  represents two vehicles,  $\Delta V$  is the speed difference of two vehicles, and  $a$  is a constant that defines the rate of variation of the 5G signal strength when the mobility speed increase or decrease by a unit [140].

2) *Vehicle clusters formation*: After receiving the vehicle grouping list from the base station, inter-vehicular distance (IVD) would be used by the mobile gateway candidates to refine the group and form the final cluster. As the vehicle position information measured or predicted by base stations might not be accurate, the mobile gateway candidates use broadcasting message (For example, IEEE 802.11p has a transmission range of around 250m) to verify the neighbor vehicles and update the group member list. The inter-vehicle distance of the final clusters is constrained by  $d \leq R_t \cdot (1 - \varepsilon)$ , where  $R_t$  denotes the maximum transmission range of IEEE 802.11p protocol and  $\varepsilon$  reflects the wireless channel fading conditions [141].

3) *Dual cluster head selection*: After the formation of the clusters, a CH would be selected in each cluster in order to effectively relay the vehicle-related traffic to cellular networks. Assume that there are  $K$  vehicles in a cluster, the CH selection could be defined by a linear optimization problem [141]. The objective of the CH selection is to maximize the throughput rate of the trunk link under the constraint of channel quality and moving speed of the vehicle. To be specific, the more closer the vehicle speed is to the average cluster speed, the longer this CH candidate would be staying in this cluster, and the better it can serve as a cluster head. Similarly, the better the channel quality between CH and BS, the more reliable the trunk link transmission would be.

Note that the selected CH collects the status (position, velocity and heading direction) of vehicles, i.e., floating car data (FCD) and reports to the BSs. This kind of data is characterized as high frequency and small data size, which occupies cellular network resources frequently and impair other applications. Through the clustering mechanism, FCD data is compressed and only transmits through the CH. However, this design increases the vulnerability of the system and poses a potential risk that the CH could be a single point of failure.

For this reason, we further propose a dual CH design in each cluster for SDN enabled 5G-VANET to improve network robustness and guarantee seamless communication during CH handover. In this dual CH scheme, a backup CH is also selected according to the CH



selection criteria. The existing CH always sends a copy of FCD data to the back-up CH, as shown in Fig. 7.3. Once there is something wrong with the CH, such as an accident or unpredictable emergencies, back-up CH could be prepared in advance and thus is able to take over the responsibility seamlessly. Moreover, the back-up CH also works as a smooth transition during a handover procedure to a new CH. As a result, under the scenario that the existing CH leaves cluster normally, the back-up CH becomes CH immediately and a new back-up CH would be selected, as we can see in Fig. 7.3. The dual CH design is especially beneficial for 5G latency-stringent applications with a reduced communication interruption probability.

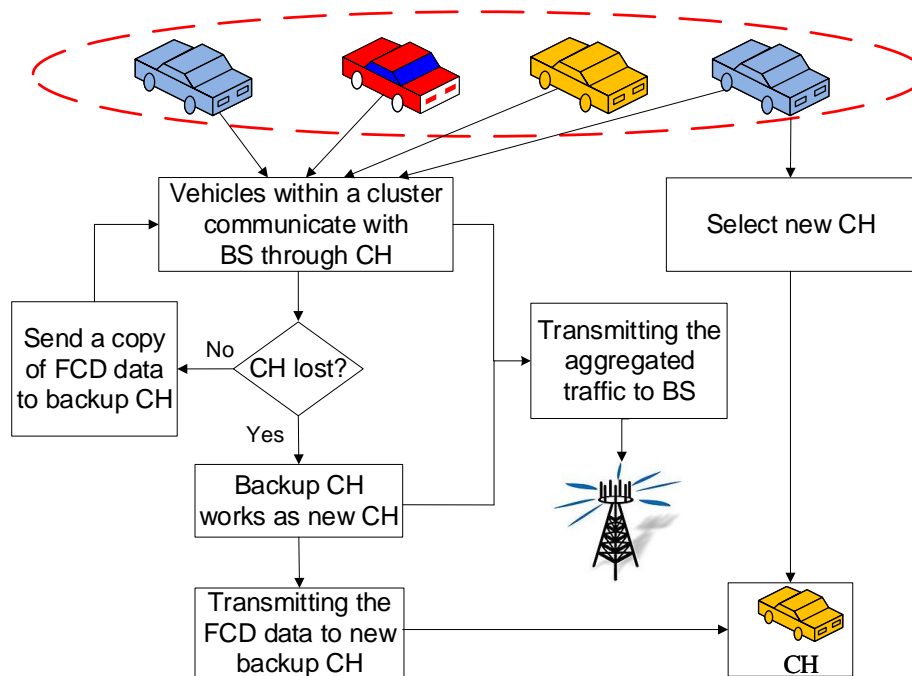


Figure 7.3: The dual cluster head selection scheme.

4) *Cluster maintenance and adaptation:* Last but not the least, the clusters should be maintained and updated due to frequent road traffic changes in VANET. In the proposed SDN enabled adaptive clustering scheme, the base station would only inform the corresponding CH if the new arriving vehicles will stay in the CH transmission area for a time period larger than a threshold  $T_p$ . The predicted inhabitant time (PIT) is calculated using the angle of the new arriving vehicle to the center of the cluster and the speed of the arriving vehicle [141]. Afterward, the CH would then be prepared for the new traffic and execute the clustering algorithm

only when needed.

On the other hand, if the aggregated amount of traffic exceeds the trunk-link capacity, the communication quality would deteriorate and outage probability will increase. Under this situation, some vehicles with high traffic requirements should be removed from the cluster to guarantee the communication Quality of Service (QoS). The cluster maintenance and adaptation should be monitored as an on-going procedure in terms of the communication quality index, e.g., outage probability.

## 7.4 NOMM System Model

NOMM is proposed as a novel transmission method in SDN enabled VANET to improve the capacity of trunk-link between CH and MBS. As shown in Fig. 7.4, an aggregated binary data stream is first split into  $K$  parallel binary data streams  $1 \sim K$ . After forward error correction (FEC) encoding, each layer  $k$  of the output is modulated into a set of QAM symbols  $x_k \in \mathcal{X} = \left\{ \frac{1}{\sqrt{2}} + \frac{i}{\sqrt{2}}, \frac{1}{\sqrt{2}} - \frac{i}{\sqrt{2}}, -\frac{1}{\sqrt{2}} + \frac{i}{\sqrt{2}}, -\frac{1}{\sqrt{2}} - \frac{i}{\sqrt{2}} \right\}$ . Next, the modulated symbols of each layer are spread on to  $N$  orthogonal resource blocks, i.e., time slot or frequency sub-band, through a sparse sequence  $(s_{1,k}, \dots, s_{N,k})$  with  $|s_{n,k}| \in \{0, 1\}$ . Notice that only part of the resource blocks carry information while the others don't [142]. Finally, spread data of  $K$  layers are partially overlapped on  $N$  resource blocks through a sparse signature matrix to obtain NOMM codewords  $c_n$ :

$$\begin{bmatrix} c_1 \\ c_2 \\ \vdots \\ c_3 \end{bmatrix} = \begin{bmatrix} s_{1,1} & s_{1,2} & \cdots & s_{1,K} \\ s_{2,1} & s_{2,2} & \cdots & s_{2,K} \\ \vdots & \vdots & \ddots & \vdots \\ s_{N,1} & s_{N,2} & \cdots & s_{N,K} \end{bmatrix} \begin{bmatrix} x_1 \\ x_2 \\ \vdots \\ x_K \end{bmatrix} \quad (7.1)$$

In this way, NOMM codewords are obtained. Each layer has its own pre-designed sparse codebook and the zeros in different codebooks reduce the collision between layers.

After the Additive White Gaussian Noise (AWGN) channel, the received signal at eNodeB can be derived as:

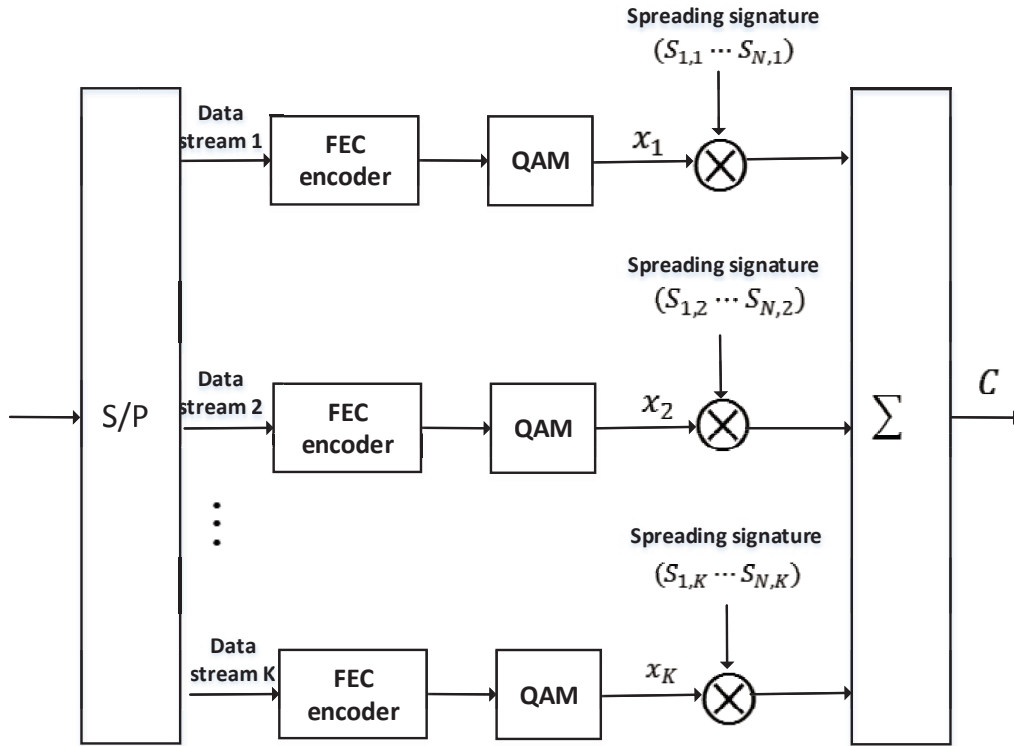


Figure 7.4: Block diagram of a NOMM modulator.

$$(y_1 \dots y_N)^T = h(c_1 \dots c_N)^T + (n_1 \dots n_N)^T, \quad (7.2)$$

where  $h$  denotes the channel fading coefficient between users and eNodeBs and  $n$  is a complex Gaussian noise vector with the normalized variance and zero mean. In order to recover the received signal, maximum likelihood (ML) detection is adopted:

$$\hat{c} = \underset{c}{\operatorname{argmax}} \Pr(y | c) = \underset{c}{\operatorname{argmin}} \|y - hc\| \quad (7.3)$$

Here  $y$  is the received signal,  $h$  is the estimated channel gain and  $c$  represents all possible NOMM codewords. There is  $4^k$  the number of different NOMM codewords and we assume that all codewords are selected with equal probability. The principle behind the ML detection is to find the codeword that has minimum distance to the received signal.

## 7.5 Energy Efficiency Analysis

In previous related works, energy efficiency (EE) is described as spectrum efficiency over the total power consumption, however, the transmission errors in the practical scenarios are ignored. Therefore in this chapter, we define EE as the successfully received bits over power consumption [137], which can be expressed as:

$$EE = \frac{bW(1 - \xi)}{P} \quad (7.4)$$

For traditional orthogonal transmission with M-QAM modulation,  $b = \log_2 M$  denotes the bits number of per symbol with M modulation order and  $\xi$  is the corresponding symbol error rate (SER). For NOMM modulation,  $b = K \log_2 M$  denotes the bits number per codeword with M modulation order and K layers.  $\xi$  is the corresponding word error rate(WER).

Here  $P$  denotes the total power consumption for whole transmission. However, it is difficult to estimate the practical power consumption due to different hardware design. Therefore, system power consumption is estimated by using a simplified model:

$$P = WP_{sta} + P_t + P_{BS}, \quad (7.5)$$

where  $W$  is the overall transmission bandwidth and  $P_{sta}$  represents the static power consumption. The  $P_{BS}$  and  $P_t$  are the power consumption at transmitter and receive side, respectively. In fact, how to get the  $\xi$  is the key problem for EE analysis, and we will discuss it under two scenarios: the proposed NOMM scheme and traditional orthogonal transmission (OT) scheme.

### 7.5.1 EE for NOMM

The WER upper bound of NOMM for ML detection can be obtained through distance enumerator function and the code distance. Therefore these two parameters need to be defined first.

*Definition 1:* Distance between two SCDMA code words  $c, c' \in C$  is

$$d(\mathbf{c}, \mathbf{c}') = \|\mathbf{c} - \mathbf{c}'\|, \quad (7.6)$$

where  $C$  is the NOMM code set.

*Definition 2:* Distance enumerator function for NOMM code with matrix  $S$  is used to calculate an average distance spectrum for all codewords in the code set, the mathematical expression is:

$$A(S, Z) = \frac{1}{|C|} \sum_{\mathbf{c}} \sum_{\mathbf{c}', \mathbf{c} \neq \mathbf{c}'} Z^{d(\mathbf{c}, \mathbf{c}')} \quad (7.7)$$

Here  $Z$  is a dummy variable and  $|C| = M^K$  is the number of all possible code set with  $K$  layers and  $M$  modulation order.

According to distance enumerator function and code distance, the WER  $\xi_{NOMM}$  of NOMM using ML Detection is upper bounded by

*Union Bound [142] :*

$$\xi_{NOMM} \leq A(0) + \sum_{d>0} A(d) Q\left(\frac{d}{\sqrt{2N_0}}\right), \quad (7.8)$$

where  $A(d)$  represents the average number of NOMM codeword pairs with distance  $d$ .

Therefore, re-investigating the EE of NOMM with the respect to the WER is :

$$EE_{NOMM} \geq \frac{W \frac{K}{N} \log_2 \left(1 - A(0) - \sum_{d>0} A(d) Q\left(\frac{d}{\sqrt{2N_0}}\right)\right)}{WP_{sta} + P_t + P_{BS}} \quad (7.9)$$

From the equation, it can be seen that the EE performance is directly influenced by two factors: the total layer numbers  $K$ , the total orthogonal RB  $N$  and the NOMM distance  $d$ . Indeed, the throughput is increased with higher layers but meanwhile, the WER is also increased due to the inter-layer interference. Therefore, layer selection is applied to find the trade-off

between throughput and WER. The code distance depends on the signature matrix design and so we need to design NOMM code carefully in order to improve the EE performance.

### 7.5.2 EE for Traditional Orthogonal Transmission

In the orthogonal transmission (OT) scheme, M-QAM modulation is adopted and the modulation symbols are allocated to orthogonal resource block without overlap. The SER of OT is equal to the SER of M-QAM. In [143], the SER  $\xi_{OT}$  of  $l_{th}$  user with M-QAM modulations:

$$\xi_{OT} = 2 \left( 1 - \frac{1}{\sqrt{2^b}} \right) Q \left( \sqrt{\frac{3}{2^b - 1}} \cdot \frac{\epsilon_{av}}{N_0} \right) \quad (7.10)$$

Here  $\epsilon_{av} = |h_k|^2 p_{tr}$  represents the transmitted power for per received symbol. Since,

$$Q(x) = \int_x^\infty \frac{1}{\sqrt{2\pi}} \exp\left(-\frac{y^2}{2}\right) dy \leq \frac{1}{2} \exp\left(-\frac{x^2}{2}\right) \quad (7.11)$$

The upper bound of SER is

$$\xi_{OT} \leq \left( 1 - \frac{1}{\sqrt{2^b}} \right) \exp\left(-\frac{3\epsilon_{av}}{2(2^b - 1)N_0}\right) \quad (7.12)$$

Finally, substituting (12) into (4), one can get the EE of traditional M-QAM:

$$EE_{OT} \geq \frac{W \log_2^M \left( 1 - \left( 1 - \frac{1}{\sqrt{2^b}} \right) \exp\left(-\frac{3\epsilon_{av}}{2(2^b - 1)N_0}\right) \right)}{WP_{sta} + P_t + P_{BS}} \quad (7.13)$$

Simply by comparing (13) and (9), it is hard to find out which modulation method provides better EE. Therefore simulation is also set up and the performance is given in Section V.

## 7.6 Simulations

### 7.6.1 NOMM Signature Design and Selection for Simulation

According to the analysis in section IV, the EE performance of NOMM is directly influenced by the code distance  $d$ . Therefore, NOMM signature design and selection plays an important role in EE performance simulation of NOMM. According to [142], there are two important factors for NOMM signature design: the minimum euclidean distance and the girth. The larger minimum euclidean distance, the better detection performance would be:

$$\Pr(\|\mathbf{y} - h_k \mathbf{c}'\| < \|\mathbf{y} - h_k \mathbf{c}\|) = Q\left(\frac{|h_k| \|\mathbf{c} - \mathbf{c}'\|}{2N_0}\right) \quad (7.14)$$

$$\|\mathbf{c} - \mathbf{c}'\| \uparrow \Rightarrow Pr(\mathbf{c} \rightarrow \mathbf{c}') \downarrow \quad (7.15)$$

On the other hand, girth is the minimum cycle length of the factor graph. The shorter the minimum cycle length, the better the detection performance. The principle of optimal signature design for a given factor graph is to find a trade-off between the minimum Euclidean distance and the minimum cycle length:

$$S^{opt} = \operatorname{argmax}_{d_{min}}(S) \quad (7.16)$$

According this principle, some optimal signature matrix examples are given below:

*Example 1 (An Optimal 8-Layers, 4 Resources NOMM Code):*

$$S_{4,8}^{opt} = \begin{bmatrix} 1 & 0 & e^{i\theta_2} & 0 & e^{i\theta_4} & 0 & 0 & 0 \\ 0 & e^{i\theta_1} & 0 & e^{i\theta_3} & 0 & e^{i\theta_5} & 0 & 0 \\ 0 & 0 & e^{i\theta_2} & 0 & 0 & e^{i\theta_{3,6}} & e^{i\theta_6} & 0 \\ 0 & 0 & 0 & e^{i\theta_3} & e^{i\theta_4} & 0 & 0 & e^{i\theta_7} \end{bmatrix} \quad (7.17)$$

Where  $(\theta_1, \dots, \theta_7) = (0.2618\pi, 0.1435\pi, 0.1279\pi, 0.2297\pi, 0.3505\pi, 0.3935\pi, 0.361\pi)$  and  $\theta_{3,6} = 0.2269\pi$ . Its the minimum code distance  $d$  is 0.83 and load ratio  $l$  is 2.

*Example 2 (An Optimal 6-Layers, 4 Resources NOMM Code):*

$$S_{4,6}^{opt} = \begin{bmatrix} 1 & e^{i\theta_2} & e^{i\theta_3} & 0 & 0 & 0 \\ 1 & 0 & 0 & e^{i\theta_4} & e^{i\theta_5} & 0 \\ 0 & e^{i\theta_2} & 0 & e^{i\theta_{3,4}} & & e^{i\theta_6} \\ 0 & 0 & e^{i\theta_3} & 0 & e^{i\theta_{4,5}} & e^{i\theta_{4,6}} \end{bmatrix} \quad (7.18)$$

Where  $(\theta_2, \dots, \theta_6) = (0.1431\pi, 0.2021\pi, 0.3127\pi, 0.3765\pi, 0.2667\pi)$ ,  $\theta_{3,4} = 0.5736\pi$ ,  $\theta_{4,5} = 0.3935\pi$  and  $\theta_{4,6} = 0.3078\pi$ . Its minimum code distance  $d$  is 1.1658 and load ratio  $l$  is 1.5.

*Example 3 (An Optimal 6-Layers, 4 Resources NOMM Code):*

$$S_{4,6}^{opt} = \begin{bmatrix} 1 & 0 & e^{\frac{i\pi}{6}} & 0 & 0 & e^{\frac{i\pi}{6}} \\ 0 & 1 & 0 & e^{\frac{i\pi}{6}} & e^{\frac{i\pi}{3}} & 0 \\ 0 & 0 & e^{\frac{i\pi}{6}} & 0 & e^{\frac{i\pi}{3}} & 0 \\ 0 & 0 & 0 & e^{\frac{i\pi}{6}} & 0 & -1 \end{bmatrix} \quad (7.19)$$

The minimum code distance  $d$  is 1.2679 and load ratio  $l$  is 1.5. Compared with example 2, its minimum code distance is larger and so the performance of ML detection is better.

*Example 4 (An Optimal 8-Layers, 6 Resources NOMM Code):*

$$S_{6,8}^{opt} = \begin{bmatrix} 1 & 0 & e^{\frac{i\pi}{6}} & 0 & 0 & 0 & 0 & e^{\frac{i\pi}{6}} \\ 0 & e^{\frac{i\pi}{3}} & 0 & e^{\frac{i\pi}{6}} & 0 & 0 & e^{\frac{i\pi}{6}} & 0 \\ 0 & 0 & e^{\frac{i\pi}{6}} & 0 & e^{\frac{i\pi}{3}} & 0 & 0 & 0 \\ 0 & 0 & 0 & e^{\frac{i\pi}{6}} & 0 & e^{\frac{i\pi}{3}} & 0 & 0 \\ 0 & 0 & 0 & 0 & e^{\frac{i\pi}{3}} & 0 & e^{\frac{i\pi}{6}} & 0 \\ 0 & 0 & 0 & 0 & 0 & e^{\frac{i\pi}{3}} & 0 & e^{\frac{i\pi}{6}} \end{bmatrix} \quad (7.20)$$

Its minimum code distance  $d$  is 1.412 and load ratio  $l$  is 1.33.



## 7.6.2 Simulation Results

In this part, the EE performance of the NOMM and 4-QAM based integrated 5G V2I communication are evaluated using MATLAB simulation. For NOMM scheme, QPSK modulation combined with sparse spreading was used for each layer and ML detection was applied at the receivers. Since 4-QAM and QPSK have the same modulation order, 4-QAM is selected in orthogonal transmission (OT) to compare with NOMM. It is assumed that there are 10 vehicles randomly distributed within a cluster and the traffic flow aggregated at the cluster head is 100 kbps. Link level simulation is implemented including channel coding, modulation and demodulation. Monte Carlo simulation is also given in order to verify the theoretical analysis.

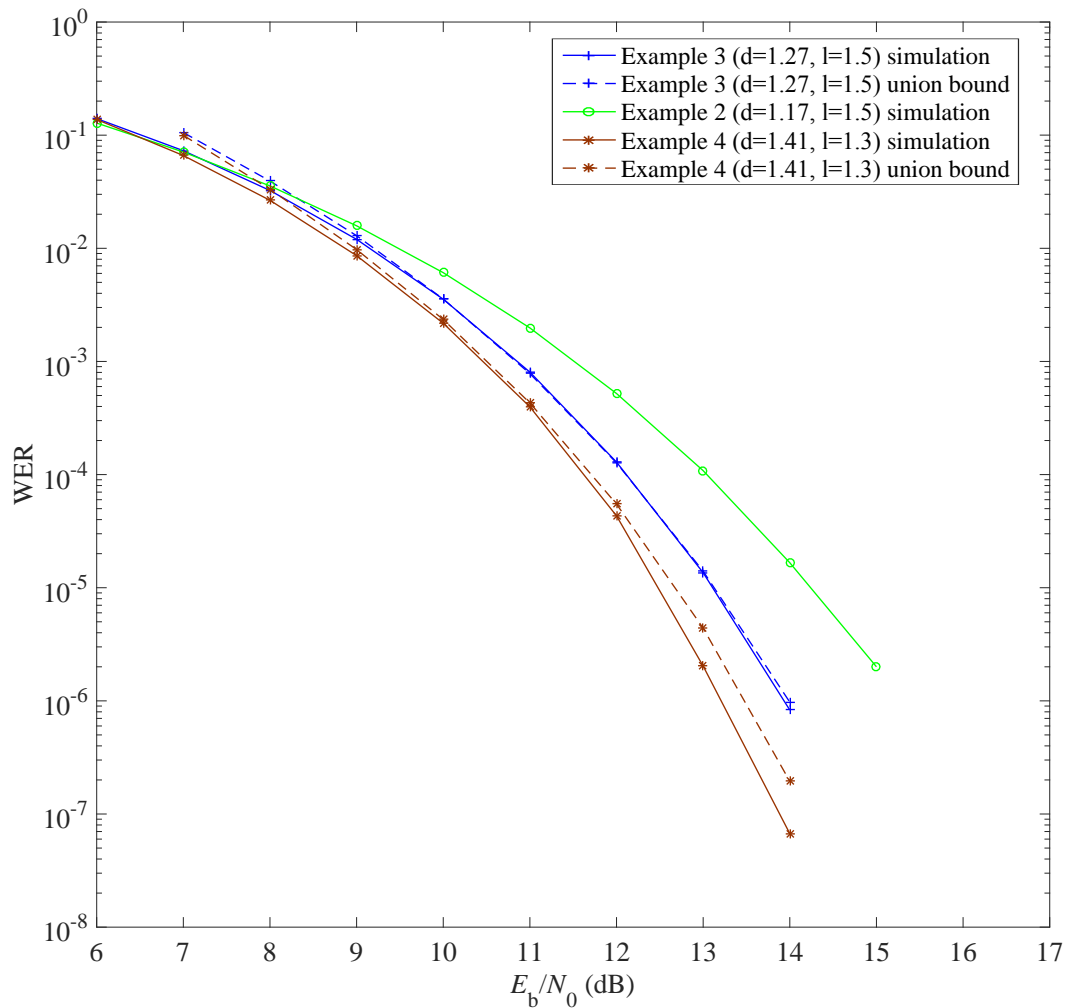


Figure 7.5: WER comparison among NOMM Example 2, 3 and 4.

Fig. 7.5 provides the WER performance comparison of the optimal 6-layers-4-resource

and 8-layers-6-resource NOMM codes, defined by Example 2, 3 and 4. The solid curves are simulation results and the dashed curves are the union bounds. It is also clear that the code design from Example 4 has the best WER performance since it has the largest code distance ( $d=1.41$ ). Although the Example 2 and Example 3 have the same overlap factor, the code obtained from Example 3 has more than 1 dB better performance gain over the optimal code obtained in Example 2, due to the larger minimum code distance. Specifically, when the  $\frac{E_b}{N_0}$ , the simulated WER of Example 4, 2 and 1 are  $5 \times 10^{-6}$ ,  $3 \times 10^{-5}$  and  $2 \times 10^{-4}$ , respectively. The simulation results illustrate that the WEE mainly impacted by the code distance, which is consistent with the theory analysis in Eq. (7.8).

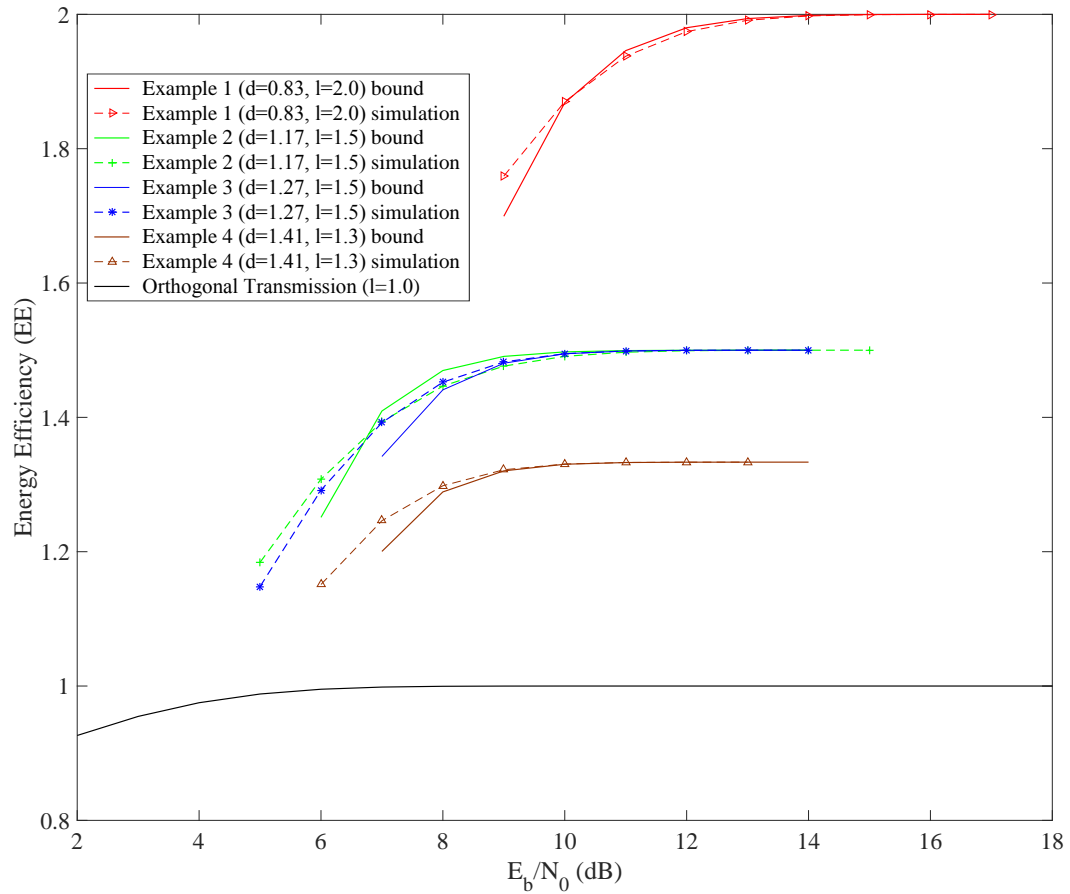


Figure 7.6: EE comparison among NOMM examples and orthogonal transmission.

Fig. 7.6 illustrates the EE curves (dashed lines) and the union bounds (solid lines) for  $K$ -Layers  $N$ -resources NOMM codes, obtained in Example 1,2,3,4, and orthogonal transmission with 4-QAM under ML detection. From the simulation results, we can see that: 1) The

EE performance of proposed NOMM increased around 1.3-2 times than that of orthogonal transmission, due to a higher load ratio. 2) All the simulations coincide well with their union bound most of the time, except a little mismatch at the low  $\frac{E_b}{N_0}$  caused by noise. 3) The EE performance is mainly influenced by the overlap ratio  $l$  and the NOMM distance  $d$ . Indeed, the throughput increased with a higher overlap rate but meanwhile, the WER is also increased due to the larger inter-layer interference. Therefore, overlap ratio selection should be careful to find the trade-off between throughput and WER.

## 7.7 Chapter Summary

In order to support the increasing vehicle traffic and improve the management, an SDN enabled 5G-VANET is proposed in this chapter. SDN can provide a global view to adaptively cluster vehicles only when needed. In order to reduce the signaling overhead, one vehicle in each cluster is selected as a cell head to support aggregated traffic and another one vehicle is selected as a backup to guarantee seamless communication. In order to meet the increased channel capacity demand, NOMM is further proposed for aggregated V2I data transmission in this integrated network. NOMM splits data into several layers, which are then multiplexed and overlapped on some orthogonal resources after modulation and sparse spreading. Simulation results show that the energy efficiency performance of proposed NOMM is 1.3-2 times than that of traditional orthogonal transmission scheme, due to overlapping gain. Therefore, it can be used as a promising energy-efficient approach for 5G-VANET network.

# Chapter 8

## Conclusion and Future Work

### 8.1 Conclusion

Densified multi-tier architectures bring new challenges, especially on resource management and security provisioning, due to the lack of common interface and consistent policy across HetNets. In this thesis, we aim to address the technical challenges through adaptively operating traffic-aware virtual small cells as well as intelligently utilizing the multi-dimensional radio resource to achieve massive capacity with extremely high energy efficiencies. The contributions that have been made in this thesis and the conclusions drawn from these contributions can be summarized as follows:

In Chapter 3, a novel virtual small cell operation is proposed as a flexible and cost-effective scheme to overcome the deployment challenges of traditional small cells. VSCs have formed adaptively according to dynamic traffic conditions, and one user device with better power and channel conditions is selected as the CH to aggregate the intra-cell traffic in the unlicensed band and communicate directly with the MBS in the cellular band. A K-means clustering based virtual small cell formation scheme is proposed, and the protocol conversion for data transmission across an unlicensed and licensed band at CHs is designed. Based on the proposed virtual small cell network architecture, adaptive hybrid beamforming is also designed to support the high traffic of the front-haul link. The objective of beamforming design is to minimize the total power while guaranteeing the throughput rate requirement of users and transmit power constraints at the MBS. This non-convex problem can be translated into a convex prob-

lem by using modified semi-definite relaxation. To reduce the optimization complexity, beamforming direction can be selected for equal power allocation first. After this step, the original optimization problem can be reformulated as a simple convex optimization problem of power allocation. The optimal and sub-optimal solutions of beamforming design are analyzed. Both mathematical and simulation results demonstrate that compared with traditional small cells, the proposed VSCs with the adaptive HBF scheme can improve 55% energy efficiency with better energy-focusing and less inter-cell interference.

To achieve an intelligent traffic-aware network with low latency, a long short term memory (LSTM) neural network-based hotspot prediction is proposed in VSC based ultra-dense HetNet for 5G and beyond. Specifically, the one LSTM neural network is unitized to predict the UE numbers of every grid due to its capability of learning long-term dependencies. By analyzing the predicted network-level user distribution, the hotspot can be detected to form the VSC in advance. By using a real data set of telecommunications, the simulation results show that, compared with several LSTM based methods and ConvLSTM, one LSTM based method can predict the user distribution with high accuracy by using a simple network architecture. Our simulation results also demonstrate that compared with the scenario of VSC relying on traditional clustering, the proposed VSC operation assisted with the hotspot prediction can achieve higher power efficiency as well as lower processing latency.

In Chapter 5, we proposed a multi-dimensional intelligent multiple access (MD-IMA) to optimize the network performance while minimizing receiver complexity (RC). By fully utilizing the closed-loop situation-awareness discovery through real-time data analytics, the proposed scheme will explore the dynamic and fast adaptation of multi-domain MA schemes. The MD-IMA design is formulated as a MOO problem to maximizing I-QoSE while minimizing the non-orthogonality (NO) under constraints of maximum power consumption and the QoS of each user. In order to reduce the computational complexity at devices, we have proposed an efficient method to jointly optimize the user clustering, channel assignment and power allocation in NOMA systems by exploiting the matching algorithm along with the optimal power allocation. The simulation results have shown that the proposed the achievable I-QoSE gain of MD-IMA over NOMA and OMA are approximate 15% and 18%, respectively.

In order to reduce the computational complexity caused by traditional optimization algo-

rithms, model-free deep reinforce learning (DRL) enabled resource allocation method is proposed in chapter 6. In the proposed two-step scheme, one-LSTM neural network is adopted to predict the overall network requirements (I-QoSE) and then DRL based power allocation algorithms are proposed to maximize the predicted I-QoSE under several practical constraints. Both valued-based DRL algorithm, such as DQN, and the actor-critic based DDPG algorithm are adopted to do power alloctaion for MD-IMA system. The simulation results illustrate that DDPG performs the best in terms of both I-QoSE performance and convergence because it can eliminate quantization error. Specifically, the DDPG based algorithm can improve around 17% and 35% WEE than that of WMMSE and FP, respectively. The time cost of DRL based method is 10 times and 100 times faster than that of FP and WMMSE.

To evaluate the resource management schemes in a particular network, the traffic offloading performance in 5G-VANET was studied in Chapter 7. In this chapter, we propose to integrate SDN into 5G-VANET and thus provide a programmable platform in addressing the challenges of dynamic vehicle communications. Through the proposed SDN-enabled adaptive vehicle clustering and dual cluster head scheme, signaling overhead of VANET is significantly reduced along with improved communication quality. To accommodate the varying traffic over the trunk link and reduce the latency during traffic distribution, adaptive trunk link transmission scheme and cooperative communication of mobile gateway candidates were proposed for the aggregated V2I traffic transmission in this integrated network. The simulation results show that the energy efficiency of proposed NOMM is 1.3-2 times than that of traditional orthogonal transmission scheme by carefully designing the sparse code of NOMM.

In summary, three new network architectures are proposed in this thesis to adaptively form virtual small cell, multiplex UEs and cluster vehicle networks based on the deep-learning enabled network awareness. Furthermore, both optimization and deep learning methods are used to do resource allocation in these networks. With more efforts on user QoS and application-specific performance enhancement, 5G and beyond networks are believed to be adaptable to user demand and thus improve everyday life.

## 8.2 Future Work

The contributions presented in this dissertation for 5G ultra-dense HetNets can be extended or used to explore new research topics. In the future, some aspects of the proposed algorithms are also worthwhile to be further investigated. Some potential research works are summarized as follows:

### 8.2.1 Cellular Network Assisted Flying Ad Hoc Network

One target of the next-generation network architecture is to expand the breadth and depth of communication coverage. Over the past decades, the unmanned aerial vehicle (UAV) has received unprecedented attention and huge worldwide interests. It exhibits outstanding performance and potential military and civilian applications, including surveillance, reconnaissance, source seeking, target detection and disaster sensing [144]. Therefore, a UAV-based wireless network is a potential integral component of the next-generation mobile communication system. Considering the limitations of a single UAV, multiple UAVs are grouped as the flying ad hoc network (FANET) to fulfill the tasks. The multiple UAVs relying on sophisticated sensors can be coordinated by the ground station (GS) [145]. Besides, a huge amount of research has been done in the communication of UAV networks. Although the extensive experimental studies confirm that Wi-Fi may indeed be used in communication between UAVs and GS, several of its features would be suboptimal in aerial communication scenarios. In fact, the features of Wi-Fi were designed for indoor wireless channels, which are characterized by rich multipath scattering, whereas the air-to-ground (A2G) wireless channel is characterized by sparse multipath scattering [146]. Furthermore, the A2G channel would have a strong line-of-sight (LoS) component, whereas the indoor channel will not have a LoS component in general [147]. Therefore, compared with the Wi-Fi, the cellular network is more suitable to support A2G communication since it has various outdoor wireless channel models. With respect to the communication needs, the request for services including video live streaming, geo-location or voice, issuing more and more stringent demands for communications resources. From this perspective, telecommunication, such as 5G, is also a good technology to support the communication between UAVs and GS, thanks to its capability of providing high data rates and coping

with a large number of users [148]. Furthermore, the key technologies of telecommunication, including Massive MIMO, beamforming and OFDM, can be adapted to further improve the quality of service (QoS) for the A2G communication.

However, if each UAV of the FANET is allowed to set up a direct communication link with the GS, they would lead to low spectral efficiency and severe interference. Therefore, similar to the basic idea of VSC, we can propose a cellular network assisted FANET (CNA-FANET). Specifically, the FANETs are formed adaptively under the coordination of cellular temporary base station (TBS) when needed. The TBS can be regarded as the GS. In each FANET, some of the superior drones, who experience good channels with the GS and have sufficient power, should be chosen as the head candidates and serve as the head in turn. The head then aggregates intra-FANET traffic in the unlicensed band, such as WiFi, and relays the combined traffic to a TBS in the cellular band. Using massive MIMO techniques, the large scale antenna array is adaptively employed to form a highly directional beam to cover FANET. With spatially confined transmission using cellular band radio resources, high throughput can be achieved on the trunk link between the TBS and the UAV head.

Despite the many promising benefits, cellular network assisted FANET is also faced with several new design challenges. First, as a new scenario for communication systems, UAV moves in the three-dimensional (3D) space. Different from the normal channel models in terrestrial systems, the flight parameters such as height and moving directions have important effects on the statistical characteristics of channel [149]. Therefore, we need to build a 3D geometry-based UAV-MIMO channel models for A2G communication environments, which is used to design the proposed CNA-FANET and evaluate the performance. Besides, the high mobility environment of UAVs generally results in highly dynamic network topologies [150]. It means the coverage and location of FANETs are not fixed. Therefore, we focus this study on how to realize the adaptive beamforming to keep up with the changes of the FANET. Another main challenge stems from the size, weight, and power (SWAP) constraints of UAVs, which could limit their communication, computation, and endurance capabilities [151]. To tackle such issues, energy-aware FANET deployment and operation mechanisms are needed for intelligent energy usage and replenishment. An optimal beamforming design scheme is proposed to minimize the total power consumption under constraints of maximum transmit power and



required throughput rate of each UAV. Furthermore, the capacity requirement for the data links critically depends on the applications, possibly ranging from several Kbps to dozens of Gbps [?]. Therefore, to ensure the capacity of the trunk link between the UAV head and BS, a Non-orthogonal Multiplexed Modulation (NOMM) scheme is proposed in this project to effectively aggregate the intra-FANET traffic and further improve energy efficiency.

The future long-term goal of this topic is to design an intelligent and energy-aware communication scheme and operation mechanisms for CNA-FANET. Based on the above discussions, the research directions that need to be seriously considered as follows:

- Modelling a 3D UAV-MIMO channel models for A2G communication environments to design proposed CNA-FANET and evaluate the performance;
- Designing optimal beamforming to minimize power consumption under throughput requirements;
- Developing beamforming tracking technique to deal with the rapid channel variation;
- Proposing a novel modulation scheme, named NOMM, to further improve the capacity of the trunk link between the UAV head and BS. The basic networking architecture of the proposed CNA-FANET, main channel characteristics and design considerations will be presented in the following sections.

### **8.2.2 Distributed AI Enabled Resource Management**

In our thesis, the DRL based resource allocation methods are proposed in Chapter 6. In this topic, only one macro cell is considered and machine learning is run on the cloud platform. Under this framework, the collected information, such as the channel state information, location and throughput rate, are send to the cloud and then DRL allocates the resource for the whole networks. However, several drawbacks are introduced by such centralized DRL enabled resource management framework, especially for the multi-cell situations:

- Space Explosion: The size of the DRL input and output is proportional to the number of pixels, and training such a DRL is very difficult because the state action space increases

exponentially with the input and output size. In addition, the search efficiency in high-dimensional space is low, so effective resource allocation may be impractical.

- **Latency Pressure:** The central agent needs all the information of the current time communication network to train the DRL. When the number of cells is large, the sending information to the central agent and the broadcast distribution scheme to each transmitter will introduce a large waiting time. However, the performance of autonomous applications (such as real-time navigation, collision avoidance and queuing) relies heavily on the ability to communicate with extremely low errors and delays. In this regard, for efficient radio resource management technologies, consideration should be given to achieving ultra-reliable low-latency communication (URLLC).

Therefore, in order to speed up the learning speed and reduce the delay, the resource management framework supported by distributed AI will be developed in the future network. The intelligent decision-making in this framework is made at the edge. For example, the power distribution scheme of MD-IMA is decentralized, the transmitter of each link is regarded as an edge device, and all AIs located at the edge of the communication network work in parallel and distributed. In addition, in order to obtain a global view, a model can be trained at the edge based on local sample patterns and sent to a centralized cloud for model averaging.

# Bibliography

- [1] M. Shafi, A.F. Molisch, P.J. Smith, T. Haustein, P. Zhu, and P. D. Silva. 5g: A tutorial overview of standards, trials, challenges, deployment, and practice. *IEEE Transactions on Selected Areas in Communications*, 35(6):1201–1221, June 2017.
- [2] Cisco Visual Networking Index : Global Mobile Data Traffic Forecast Update, 2016-2021. [www.cisco.com/c/en/us/solutions/collateral/service-provider/visual-networking-index-vni/mobile-white-paper-c11-520862.html](http://www.cisco.com/c/en/us/solutions/collateral/service-provider/visual-networking-index-vni/mobile-white-paper-c11-520862.html), 2017.
- [3] X.Duan, Y.Liu, and X.Wang. Sdn enabled 5g-vanet: Adaptive vehicle clustering and beamformed transmission for aggregated traffic. *IEEE Communications Magazine*, 55(7):120–127, July 2017.
- [4] T. X. Tran, A. Hajisami, P. Pandey, and D. Pompili. Collaborative mobile edge computing in 5g networks: New paradigms, scenarios, and challenges. *IEEE Transactions on Communications Magazine*, 55(4):54–61, April 2017.
- [5] B. Wang, F. Gao, S. Jin, H. Lin, and G. Y. Li. Spatial- and frequency-wideband effects in millimeter-wave massive mimo systems. *IEEE Transactions on Signal Processing*, 66(13):3393–3406, July 2018.
- [6] B. Yang, Z. Yu, J. Lan, R. Zhang, J. Zhou, and W. Hong. Digital beamforming-based massive mimo transceiver for 5g millimeter-wave communications. *IEEE Transactions on Microwave Theory and Techniques*, 66(7):3403–3418, July 2018.
- [7] Y. Zhang, H. Wang, T. Zheng, and Q. Yang. Energy-efficient transmission design in non-orthogonal multiple access. *IEEE Transactions on Vehicular Technology*, 66(3):2852–2857, March 2017.
- [8] Y. Cai, Z. Qin, F. Cui, G. Y. Li, and J. A. McCann. Modulation and multiple access for 5g networks. *IEEE Transactions on Communications Surveys Tutorials*, 20(1):629–646, Firstquarter 2018.
- [9] M. Lauridsen, L. C. Gimenez, I. Rodriguez, T. B. Sorensen, and P. Mogensen. From lte to 5g for connected mobility. *IEEE Communications Magazine*, 55(3):156–162, March 2017.

- [10] A.Asadi and V.Mancuso. *IEEE Transactions on Mobile Computing*, title=*Network-assisted Outband D2D-clustering in 5G Cellular Networks: Theory and Practice*, year=2016, volume=16, number=8, pages=2246-2259, month=August.
- [11] H.Zhang, Y.Dong, J.Cheng, M.J.Hossain, and V.C.MLeung. Fronthauling for 5g lte-u ultra dense cloud small cell networks. *IEEE Transactions on Wireless Communications*, 23(6):48–53, January 2017.
- [12] J. G. Andrews, T. Bai, M. N. Kulkarni, A. Alkhateeb, A. K. Gupta, and R. W. Heath. Modeling and analyzing millimeter wave cellular systems. *IEEE Transactions on Communications*, 65(1):403–430, January 2017.
- [13] Q.Cui, Y.Gu, W.Ni, X. Zhang, X.Tao, P.Zhang, and R.Liu. Preserving reliability of heterogeneous ultra-dense distributed networks in unlicensed spectrum. *IEEE Transactions on Communications Magazine*, 56(6):72–78, June 2018.
- [14] J. Zeng, J. Peng, R. P. Liu, and X. Su. Comments on “cross-tier cooperation for optimal resource utilization in ultra-dense heterogeneous networks. *IEEE Transactions on Vehicular Technology*, 67(11):11307–11308, November 2018.
- [15] S. Andreev, V. Petrov, M. Dohler, and H. Yanikomeroğlu. Future of ultra-dense networks beyond 5g: Harnessing heterogeneous moving cells. *IEEE Transactions on Communications Magazine*, 57(6):86–92, October 2019.
- [16] B. Yang, G. Mao, X. Ge, M. Ding, and X. Yang. On the energy-efficient deployment for ultra-dense heterogeneous networks with nlos and los transmissions. *IEEE Transactions on Green Communications and Networking*, 2(2):369–384, October 2018.
- [17] L. Wang, C. Yang, and R. Q. Hu. Autonomous traffic offloading in heterogeneous ultra-dense networks using machine learning. *IEEE Transactions on Wireless Communications*, 26(4):102–109, October 2019.
- [18] M. M. Hasan and S. Kwon. Cluster-based load balancing algorithm for ultra-dense heterogeneous networks. *IEEE Access*, 8:2153–2162, 2020.
- [19] M. Gao, J. Li, D. N. K. Jayakody, H. Chen, Y. Li, and J. Shi. A super base station architecture for future ultra-dense cellular networks: Toward low latency and high energy efficiency. *IEEE Transactions on Communications Magazine*, 56(6):35–41, June 2018.
- [20] C. Pan, M. ElKashlan, J. Wang, J. Yuan, and L. Hanzo. User-centric c-ran architecture for ultra-dense 5g networks: Challenges and methodologies. *IEEE Transactions on Communications Magazine*, 56(6):14–20, June 2018.
- [21] Y. Li, Y. Zhang, K. Luo, T. Jiang, Z. Li, and W. Peng. Ultra-dense hetnets meet big data: Green frameworks, techniques, and approaches. *IEEE Transactions on Communications Magazine*, 56(6):56–63, June 2018.

- [22] M. M. Hasan, S. Kwon, and S. Oh. Frequent-handover mitigation in ultra-dense heterogeneous networks. *IEEE Transactions on Vehicular Technology*, 68(1):1035–1040, January 2019.
- [23] Q. Zhu, X. Wang, and Z. Qian. Energy-efficient small cell cooperation in ultra-dense heterogeneous networks. *IEEE Transactions on Communications Letters*, 23(9):1648–1651, September 2019.
- [24] A. M. Hatami, M. Mirmohseni, and F. Ashtiani. A new data offloading algorithm by considering interactive preferences. In *2016 IEEE 27th Annual International Symposium on Personal, Indoor, and Mobile Radio Communications (PIMRC)*, pages 1–6, Sept 2016.
- [25] C. She, C. Yang, and T. Q. S. Quek. Radio resource management for ultra-reliable and low-latency communications. *IEEE Transactions on Communications Magazine*, 55(6):72–78, June 2017.
- [26] L.Zhu, Z.Xiao, X.Xia, D.Q.Wu, H.Yao, and Y.Liu. Millimeter-wave communications with non-orthogonal multiple access for b5g/6g. *IEEE Access*, 57:116123 – 116132, August 2019.
- [27] Z. Zhang, Y.Xiao, Z.Ma, M.Xiao, Z.Ding, X.Lei, G.K.Karagiannidis, and P.Fan. 6g wireless networks: Vision, requirements, architecture, and key technologies. *IEEE Veh Technol Mag*, 14(3):28–41, July 2019.
- [28] X.Wang, Z.Zhou, F.Xiao, K.Xing, Z.Yang, Y.Liu, and C.Peng. Spatio-temporal analysis and prediction of cellular traffic in metropolis. *IEEE Transactions on Mobile Computing*, 18(9):2190–2202, September 2019.
- [29] X.Zhang, F.Zhou, J.Ning, P.Yu, and W. Li. Hotspot localization and prediction in wireless cellular networks via spatial traffic fitting. *IEEE/IFIP Network Operations and Management Symposium*, pages 1–6, July 2017.
- [30] F. Tang, Z. M. Fadlullah, B. Mao, and N. Kato. An intelligent traffic load prediction-based adaptive channel assignment algorithm in sdn-iot: A deep learning approach. *IEEE Transactions on Internet of Things*, 5(6):5141–5154, December 2018.
- [31] M. G. Kibria, K. Nguyen, G. P. Villardi, O. Zhao, K. Ishizu, and F. Kojima. Big data analytics, machine learning, and artificial intelligence in next-generation wireless networks. *IEEE Access*, 6:32328–32338, May 2018.
- [32] G. Akpakwu, B. Silva, G. Hancke, and A. Abu-Mahfouz. A survey on 5g networks for the internet of things: Communication technologies and challenges. *IEEE Access*, 6:3619–3647, December 2018.
- [33] S. A. Busari, K. M. S. Huq, S. Mumtaz, L. Dai, and J. Rodriguez. Millimeter-wave massive mimo communication for future wireless systems: A survey. *IEEE Transactions on Signal Process*, 20(2):836–869, Secondquarter 2018.

- [34] Z. Dawy, W. Saad, A. Ghosh, J. G. Andrews, and E. Yaacoub. Toward massive machine type cellular communications. *IEEE Transactions on Wireless Communications*, 24(1):120–128, February 2017.
- [35] Y. Yuan, Y. Xu, Z. Yang, P. Xu, and Z. Ding. Energy efficiency optimization in full-duplex user-aided cooperative swipt noma systems. *Wireless Communications*, 67(8):5735–5767, August 2019.
- [36] H. Zhang, B. Wang, C. Jiang, K. Long, A. Nallanathan, V. C. M. Leung, and H. V. Poor. Energy efficient dynamic resource optimization in noma systems. *IEEE Transactions on Wireless Communications*, 17(9):5671–5682, September 2018.
- [37] B. Di, L. Song, and Y. Li. Sub-channel assignment, power allocation, and user scheduling for non-orthogonal multiple access networks. *IEEE Transactions on Wireless Communications*, 65(11):7686–7698, November 2016.
- [38] J. Shi, W. Yu, Q. Ni, W. Liang, Z. Li, and P. Xiao. Energy efficient resource allocation in hybrid non-orthogonal multiple access systems. *IEEE Transactions on Communications*, 67(5):3496–3511, May 2019.
- [39] Y. Sun, D. W. K. Ng, Z. Ding, and R. Schober. Optimal joint power and subcarrier allocation for full-duplex multicarrier non-orthogonal multiple access systems. *IEEE Transactions on Communications*, 65(3):1077–1091, March 2017.
- [40] D. He, C. Chen, J. Bu, S. Chan, and Y. Zhang. Security and efficiency in roaming services for wireless networks: Challenges, approaches, and prospects. *IEEE communication magazine*, 51(2):142–150, February 2013.
- [41] F. Fang, H. Zhang, J. Cheng, S. Roy, and V. C. M. Leung. Joint user scheduling and power allocation optimization for energy-efficient noma systems with imperfect csi. *IEEE Journal on Selected Areas in Communications*, 35(12):2874–2885, December 2017.
- [42] J. Choi. Minimum power multicast beamforming with superposition coding for multiresolution broadcast and application to noma systems. *IEEE Transaction on Communications*, 63(3):791–800, January 2015.
- [43] Z. Ding, Y. Liu, J. Choi, Q. Sun, M. ElKashlan, C. Lin, and H. V. Poor. Application of non-orthogonal multiple access in lte and 5g networks. *IEEE Communications Magazine*, 55(2):185–191, December 2017.
- [44]
- [45] M. Benmimoune, E. Driouch, W. Ajib, and D. Massicotte. Joint transmit antenna selection and user scheduling for massive mimo systems. *IEEE Wireless Communications and Networking Conference*, pages 381–386, March 2015.
- [46] P. Zhang, S. Chen, and L. Hanzo. Two-tier channel estimation aided near-capacity mimo transceivers relying on norm-based joint transmit and receive antenna selection. *IEEE Transaction on Wireless Communications*, 14:122–137, July 2014.

- [47] G.Sun, Z.T.Gebrekidan, G.O.Boateng, D.A.Mensah, and W.Jiang. Dynamic reservation and deep reinforcement learning based autonomous resource slicing for virtualized radio access networks. *IEEE Access*, 7(6):45758–45772, April 2019.
- [48] F.Fang, J.Cheng, and Z.Ding. Joint energy efficient subchannel and power optimization for a downlink noma heterogeneous network. *IEEE Transactions on Vehicular Technology*, 68(2):1351–1364, February 2019.
- [49] H.Sun, X.Chen, Q.Shi, M.Hong, X.Fu, and N.D.Sidiropoulos. Learning to optimize: Training deep neural networks for interference management. *IEEE Transactions on Signal Process*, 66(20):5438–5453, October 2019.
- [50] Y.Lee and H.Ko. Efficient stmpm (spatio-temporal moving pattern mining) using moving sequence tree. *International Conference on Networked Computing and Advanced Information Management*, pages 432–437, September 2008.
- [51] N.Eagle and A.S.Pentland. Eigenbehaviors: identifying structure in routine. *Behavioral Ecology and Sociobiology*, 63(11):1057–1066, July 2009.
- [52] F.Calabrese, J.Reades, and C.Ratti. Eigenplaces: segmenting space through digital signatures. *IEEE Pervasive Computing*, 9(1):78–84, March 2010.
- [53] N.Shone, T.N.Ngoc, V.D.Phai, and Q.Shi. A deep learning approach to network intrusion detection. *IEEE Transactions on Emerging Topics in Computational Intelligence*, 2(1):41–50, January 2018.
- [54] J. Ngiam, A.Khosla, M.Kim, J.Nam, H.Lee, and A.Y Ng. Multimodal deep learning. *28th International Conference on Machine Learning*, pages 689–696, July 2011.
- [55] D.Naboulsi, M.Fiore, S.Ribot, and R.Stanica. Large-scale mobile traffic analysis: a survey. *IEEE Commun Surveys and Tutorials*, 18(1):124–161, Firstquarter 2016.
- [56] X. Ouyang, C. Zhanf, P.Zhou, and H.Jiang. Deepspace: An online deep learning framework for mobile big data to understand human mobility patterns. pages 1–11, September 2016.
- [57] C.Yang, M.Sun, W.Zhao, and E.Y.Chang. A neural network approach to jointly modeling social networks and mobile trajectories. *ACM Transactions on Information Systems*, 35(4):1–28, October 2017.
- [58] X.Shi, Z.Chen, H.Wang, D.Yeung, and W.Woo. Convolutional lstm network: a machine learning approach for precipitation nowcasting. *28th Advances in Neural Information Processing Systems*, pages 1–9, November 2015.
- [59] F.D.Calabrese, L.Wang, E.Ghadimi, G.Peters, L.Hanzo, and P. Soldati. Learning radio resource management in rans: Framework, opportunities, and challenges. *IEEE Transactions on Communications Magazine*, 56(9):138–145, September 2018.

- [60] Y. S.Soh, T.S.Quek, M.Koutouris, and H.Shin. Energy efficient heterogeneous cellular networks. *IEEE Journal on Selected Areas in Communications*, 31(5):840–850, May 2013.
- [61] Y.Park, J.Heo, and D.Hong. Spectral efficiency analysis of ultra-dense small cell networks with heterogeneous channel estimation capabilities. *IEEE Communication Letters*, 21(8):1839–1842, August 2017.
- [62] S.Maghsudiand and E. Hossain. Distributed user association in energy harvesting dense small cell networks: A mean-field multi-armed bandit approach. *IEEE Access*, 5:3513–3523, March 2017.
- [63] A.Abdelnasser, E.Hossain, M.J.Hossain D.I.Kim, and V.C.MLeung. Distributed user association in energy harvesting dense small cell networks: A mean-field multi-armed bandit approach. *IEEE Transactions on Wireless Communications*, 13(3):1628–1641, March 2014.
- [64] Z.Chang, K.Zhu, Z. Zhou, and T. Ristaniemi. Service provisioning with multiple service providers in 5g ultra-dense small cell networks. *IEEE International Symposium on Personal Indoor and Mobile Radio Communications*, pages 1895–1900, October 2016.
- [65] A.Galindo-Serrano, S.M.Lopez, A.De Ronzi, and A.Gati. *IEEE Vehicular Technology Conference Spring, title=Virtual Small Cells Using Large Antenna Arrays as an Alternative to Classical HetNets, year=2015, pages=1-6, month=May.*
- [66] T. V.Santana, A.Galindo-Serrano, B.Sayrac, and S.M.Lopez. Dynamic network configuration: Hotspot identification for virtual small cells. *International Symposium on Wireless Communication Systems (ISWCS)*, pages 49–53, September 2016.
- [67] X.Duan, X.Wang, Y. Liu, and K. Zheng. Sdn enabled dual cluster head selection and adaptive clustering in 5g-vanet. *IEEE Vehicular Technology Conference Fall*, pages 1–6, September 2016.
- [68] C.Cano and D. J.Leith. Coexistence of wifi and lte in unlicensed bands: A proportional fair allocation scheme. *IEEE International Conference on Communication Workshop (ICCW)*, pages 2288–2293, June 2015.
- [69] Y.He, A.Behnad, and X.Wang. Accuracy analysis of the two-reference-node angle-of-arrival localization system. *IEEE Communication Letters*, 4(3):329–332, May 2015.
- [70] S.Andreev, A.Pyattaev, K.Johnsson, O.Galinina, and Y.Koucheryavy. Cellular traffic offloading onto network-assisted device-to-device connections. *IEEE Communication Magazine*, 52(4):20–31, April 2014.
- [71] Q.Nadeem, A.Kammoun, M.Debbah, and M.Alouini. Spatial correlation characterization of a full dimension massive mimo system. *IEEE Global Communications Conference*, pages 1–6, December 2016.



- [72] B.Yu, L.Yang, and H.Ishii. Load balancing with 3-d beamforming in macro-assisted small cell architecture. *IEEE Transactions on Wireless Communications*, 15(8):5626–5636, August 2016.
- [73] X.Zhang, S.Sun, F. Qi, R. Bo, R.Q. Hu, and Y.Qian. Massive mimo based hybrid unicast/multicast services for 5g. *IEEE Global Communications Conference*, pages 160–171, December 2016.
- [74] A.Razavi, M.Valkama, and E.S.Lohan. K-means fingerprint clustering for low-complexity floor estimation in indoor mobile localization. *IEEE Global Communications Conference*, pages 1–5, December 2015.
- [75] 3rd generation partnership project; technical specification group services and system aspects; policy and charging control architecture. TS 23.2 Release 13, 3GPP, April 2016.
- [76] L. Liang, W. Xu, and X. Dong. Low-complexity hybrid precoding in massive multiuser mimo systems. *IEEE Wireless Communication Letter*, 3(6):653–657, December 2014.
- [77] I.Ahmed, H.Khammari, and A.Shahid. Low-complexity hybrid precoding in massive multiuser mimo systems. *IEEE Access*, 5:170–182, December 2016.
- [78] E.Bjornson, M.Debbah, and M.Kountouris. Massive MIMO and Small Cells: Improving Energy Efficiency by Optimal Soft-Cell Coordination, year=2015, pages=1-5, month=May. *International Conference on Telecommunication*.
- [79] K.Xiong, C.Chen, G. Qu, P. Fan, and K.Letaief. Group cooperation with optimal resource allocation in wireless powered communication networks. *IEEE Transactions on Wireless Communications*, 16(6):3840–3853, June 2017.
- [80] I.Ahmed, H.Khammari, and A.Shahid. Semidefinite relaxation of quadratic optimization problems. *IEEE Signal Processing Magazine*, 27(3):20–34, May 2010.
- [81] E.Bjornson, M.Bengsson, and B. Ottersten. Optimal multiuser transmit beamforming: A difficult problem with a simple solution structure. *IEEE Signal Processing Magazine*, 59(12):142–148, July 2014.
- [82] F.Shu, Y.Zhou, R.Chen, J.Wang, J.Li, and B.Vucetic. High-performance beamformer and low-complexity detector for df-based full-duplex mimo relaying networks. *China Communications*, 14(2):173–182, February 2017.
- [83] Further advancements for e-utra physical layer aspects. TS 36.814 Release 9, 3GPP, March 2010.
- [84] A.Gupta and R.K.Jha. Power optimization using massive mimo and small cells approach in different deployment scenarios. *Wireless Networks*, 23(3):959–973, April 2017.
- [85] Cvx: Matlab software for disciplined convex programming 2.0. <http://cvxr.com/cvx/>, 2013.

- [86] Heterogeneous network deployments in lte – the soft-cell approach. aa, February 2011.
- [87] S.Andreev M.Dohler O.Galinina, A.Pyattaev and Y.Koucheryavy. A5g multi-rat lte-wifi ultra-dense small cells: Performance dynamics, architecture, and trends. *IEEE Journal on Selected Areas in Communications*, 33(6):1224–1240, June 2015.
- [88] Y.Xiao, J.Lai, and Y. Liu. A user participation behaviour prediction model of social hotspots based on influence and markov random field. *China Communications*, 14(5):145–159, May 2017.
- [89] M.Chen, U.Challita, W.Saad, C.Yin, and M.Debbah. Echo state networks for proactive caching in cloud-based radio access networks with mobile users. *IEEE Transactions on Wireless Communications*, 16(6):3520–3535, September 2017.
- [90] J.Zhang, Y.Zheng, and D.Qi. Deep spatio-temporal residual networks for citywide crowd flows prediction. *The 31th AAAI Conference on Artificial Intelligence*, pages 1–7, January 2017.
- [91] D.Boudreau A.B.Sediq Y.Liu, X.Duan and X.Wang. Adaptive beamforming based in-band fronthaul for cost-effective virtual small cell in 5g networks. *IEEE Global Communications Conference*, pages 1–6, December 2017.
- [92] C.Zhang, P.Patras, and H.Haddadi. Deep learning in mobile and wireless networking: a survey. *IEEE Commun Surveys and Tutorials*, 21(3):2224–2287, March 2019.
- [93] Y.Wang, J.Zhou, K.Chen, Y.Wang, and L.Liu. 12th international conference on intelligent systems and knowledge engineering. *IEEE Global Communications Conference*, pages 1–6, November 2017.
- [94] Q.Zhang, H.Wang, J.Dong, G.Zhong, and X. Sun. Prediction of sea surface temperature using long short-term memory. *IEEE Geoscience and Remote Sensing Letters*, 14(10):1745–1749, October 2017.
- [95] A multi-source dataset of urban life in the city of milan and the province of trentino v1. <https://doi.org/10.7910/DVN/EGZHFV>, 2015.
- [96] D.Janardhanan and E.Barret. Cpu workload forecasting of machines in data centers using lstm recurrent neural networks and arima models. *Internet Technology and Secured Transactions*, pages 1–5, December 2018.
- [97] Q.Zhu, J.Chen, D.Shi, L.Zhu, X.Bai, X.Duan, and Y.Liu. Learning temporal and spatial correlations jointly: a unified framework for wind speed prediction. *IEEE Transactions on Sustainable Energy*, 2019.
- [98] K.Niu, C.Cheng, J.Chang, H.Zhang, and T. Zhou. Real-time taxi-passenger prediction with L-CNN, year=2018, volume=68, number=5, pages=4122-4129, month=November. *IEEE Transactions on Vehicular Technology*.

- [99] B. Qi. Ten trends in the cellular industry and an outlook on 6g. *IEEE Communication Magazine*, 57(12):31–36, December 2019.
- [100] W.Saad, M.Bennis, and M.Chen. A vision of 6g wireless systems: applications, trends, technologies, and open research problems. *IEEE Network*, 14(3):18–27, July 2019.
- [101] C.Fang, S.Guo, Z.Wang, H.Huang, H.Yao, and Y.Liu. Data-driven intelligent future network: architecture, use cases, and challenges. *IEEE Communications Magazine*, 57(7):34–40, July 2019.
- [102] X.Hou G. Liu, Y.Huang, H.Shao, Y.Zheng, F.Wang, and Q.Wang. Coverage enhancement and fundamental performance of 5g: analysis and field trial. *IEEE Communication Magazine*, 57(6):126–131, June 2019.
- [103] Y. Qiu, H.Zhang, K.Long, Y.Huang, X.Song, and V.C.M.Leung. Energy-efficient power allocation with interference mitigation in mmwave-based fog radio access networks. *IEEE Wireless Communications*, 25(4):25–31, September 2018.
- [104] L. Xiao, P.Xiao, Y.Xiao, H.Haas, A.Mohamed, and L.Hanzo. Compressive sensing assisted generalized quadrature spatial modulation for massive mimo systems. *IEEE IEEE Transactions on Wireless Communications*, 67(7):4795–4810, August 2019.
- [105] Q.Y.Liau and C. Y.Leow. Successive user relaying in cooperative noma system. *IEEE Wireless Communications Letters*, 8(3):921–924, February 2019.
- [106] W.A. AI-Hussaibi and F.H.Ali. Efficient user clustering, receive antenna selection, and power allocation algorithms for massive mimo-noma systems. *IEEE Access*, 7:31865–31882, February 2017.
- [107] Z.Yang, W.Xu, C.Pan, Y.Pan, and M.Chen. On the optimality of power allocation for noma downlinks with individual qos constraints. *IEEE Commun. Letters*, 21(7):1649–1652, July 2017.
- [108] J.Wang, H.Xu, L.Fan, B.Zhu, and A.Zhou. Energy-efficient joint power and bandwidth allocation for noma systems. *IEEE Commun. Letters*, 22(4):780–783, April 2018.
- [109] C.Chen, W.Cai, X.Cheng, L.Yang, and Y.Jin. Low complexity beamforming and user selection schemes for 5g mimo-noma systems. *IEEE J. Sel. Areas Commun.*, 35(12):2708–2722, December 2017.
- [110] X.Zhang, X.Zhu, and H.Zhu. Joint user clustering and multi-dimensional resource allocation in downlink mimo–noma networks. *IEEE Access*, 7:81783 – 81793, June 2019.
- [111] Z.Yang, Z.Ding, P.Fan, and Z. Ma. Outage performance for dynamic power allocation in hybrid non-orthogonal multiple access systems. *IEEE Communications Letters*, 20(8):1695–1698, August 2016.
- [112] K.Wang, Z.Ding, and W. Liang. A game theory approach for user grouping in hybrid non-orthogonal multiple access systems. *International Symposium on Wireless Communication Systems (ISWCS)*, pages 643–647, September 2016.

- [113] Z.Song, Q.Ni, and X.Sun. Spectrum and energy efficient resource allocation with qos requirements for hybrid mc-noma 5g systems. *IEEE Access*, 6:37055–37069, July 2018.
- [114] C.Pan, H.Mehrpouyan, Y.Liu, M.Elkachlan, and N.Arumugam. Joint pilot allocation and robust transmission design for ultra-dense user-centric tdd c-ran with imperfect csi. *IEEE Transactions on Wireless Communications*, 17(3):2038–2053, March 2018.
- [115] Y.Pan C.Pan Z.Yang, W.Xu and M.Chen. Energy efficient resource allocation in machine-to-machine communications with multiple access and energy harvesting for iot. *IEEE Internet of Things*, 5(1):229–245, February 2018.
- [116] N. P. Le, F. Safaei, and L. C. Tran. Antenna selection strategies for mimo-ofdm wireless systems: an energy efficiency perspective. *IEEE Transactions on Vehicular Technology*, 65(4):2048–2062, April 2016.
- [117] W.Liang, Z. Ding, Y.Li, and L.Song. User pairing for downlink non-orthogonal multiple access networks using matching algorithm. *IEEE Transactions on Communications*, 65(12):5319–5332, December 2017.
- [118] J.Papandriopoulos and J.S.Evans. Low-complexity distributed algorithms for spectrum balancing in multi-user dsl networks. *IEEE International Conference on Communication*, pages 3270–3275, June 2006.
- [119] S.Boyd and L.Vandenberghe. Convex optimization. *Cambridge Univ. Press*, 2004.
- [120] F.Tan, T.Lv, and S.Yang. Power allocation optimization for energy-efficient massive mimo aided multi-pair decode-and-forward relay systems. *IEEE Transactions on Communications*, 65(6):2368–2381, June 2017.
- [121] I. J.Lustig, R. E.Marsten, and D. F.Shanno. Feature article-interior point methods for linear programming: computational state of the art. *ORSA Journal on Computing*, 6(1):1–14, February 1994.
- [122] Z.Chen and X.Wang. Decentralized computation offloading for multi-user mobile edge computing: a deep reinforcement learning approach. pages 1–11, December 2018.
- [123] F.Meng, P. Chen, and L.Wu.
- [124] C.Ye, M.C.Gursoy, and S.Velipasalar. Deep learning based power control for quality-driven wireless video transmissions. *IEEE Global Conference on Signal and Information Processing (GlobalSIP)*, pages 1–6, November 2019.
- [125] K.Ahmed and E.Hossain. A deep q-learning method for downlink power allocation in multi-cell networks. pages 1–8, April 2019.
- [126] Y.Zhang, C.Kang, T.Ma, Y. Teng, and D.Guo. Power allocation in multi-cell networks using deep reinforcement learning. *IEEE Vehicular Technology Conference Fall*, pages 1–5, August 2018.

- [127] E.Ghadimi, F.D.Calabrese, G.Peters, and P.Soldati. A reinforcement learning approach to power control and rate adaptation in cellular networks. *IEEE International Conference on Communications (ICC)*, pages 1–5, May 2017.
- [128] R.Amiri, H.Mehrpouyan, L.Fridman, R.K.Mallik, A. Nallanathan, and D.M.Matolak. A machine learning approach for power allocation in hetnets considering qos. *IEEE International Conference on Communications (ICC)*, pages 1–5, July 2018.
- [129] Y.Weii, F.R.Yu, M.Song, and Z.Han. Joint optimization of caching, computing, and radio resources for fog-enabled iot using natural actor–critic deep reinforcement learning. *IEEE Internet of Things Journal*, 6(2):2016–2073, April 2019.
- [130] Y.He, N.Zhao, and H.Yin. Integrated networking, caching, and computing for connected vehicles: A deep reinforcement learning approach. *IEEE Transactions on Vehicular Technology*, 67(1):44–55, January 2018.
- [131] V.Mnih, K.Kavukcuoglu, D. Silver, A. Graves, I. Antonoglou, D. Wierstra, and M.Riedmiller. Playing atari with deep reinforcement learning. *IEEE Vehicular Technology Conference Fall*, pages 1–7, December 2013.
- [132] Study of heterogeneous networks management. TS 32.835 Release 12, 3GPP, March 2013.
- [133] M.Wang, H. Shan, T.H. Tom, N. Lu, X.Shen, and F. Bai. Asymptotic throughput capacity analysis of vanets exploiting mobility diversity. *IEEE Transactions on Vehicular Technology*, 64(9):4187–4202, September 2015.
- [134] Liu K., J.K.Yin Ng, J. Wang, V.C. Lee, W. Wu, and S.H.Son. Network-coding-assisted data dissemination via cooperative vehicle-to-vehicle/-infrastructure communications. *IEEE Transactions on Intelligent Transportation Systems*, PP(99):1–12, September 2015.
- [135] D.T. Phan-Huy, M. Sternad, and T. Svensson. Making 5g adaptive antennas work for very fast moving vehicles. *IEEE Intelligent Transportation Systems Magazine*, 7(2):71–84, April 2015.
- [136] H. Li, M. Dong, and K. Ota. Control Plane Optimization in Software-Defined Vehicular Ad Hoc Networks. *IEEE Trans. on Vehicular Technology*, 65(10):7895–7904, October 2016.
- [137] S. Zhang, X. Xu, L. Lu, and Y. Wu. Sparse code multiple access: An energy efficient uplink approach for 5g wireless systems. *IEEE International Conference on Global Communications Conference (GLOBECOM)*, pages 4782–4787, 2014.
- [138] L. Dai, B. Wang, Y. Yuan, and S. Han. Non-orthogonal multiple access for 5g: solutions, challenges, opportunities, and future research trends. *IEEE Communications Magazine*, 53(9):74–81, September 2015.

- [139] X. Duan and X. Wang. Authentication handover and privacy protection in 5g hetnets using software-defined networking. *IEEE Communications Magazine*, 53(4):28–35, April 2015.
- [140] B. Abderrahim, T. Tarik, and S. Rajarajan. Dynamic clustering-based adaptive mobile gateway management in integrated VANET-3G Heterogeneous Wireless Networks. *IEEE Journal on Selected Areas in Communications*, 29(3):559–570, March 2011.
- [141] X.Duan, X.Wang, and Y. Liu. SDN Enabled Dual Cluster Head Selection and Adaptive Clustering in 5G-VANET. *IEEE VTC Fall*, 2016.
- [142] G. Song and J. Cheng. Distance enumerator analysis for multi-user codes. *IEEE International Conference on Information Theory (ISIT)*, pages 3137–3141, 2014.
- [143] S. Zhang, J. Cheng, and S. Xu. Improving energy efficiency through bandwidth, power, and adaptive modulation. *IEEE International Conference on Vehicular Technology Conference Fall (VTC 2010-Fall)*, pages 1–5, 2010.
- [144] M.Aljehani and M.Inoue. A swarm of computational clouds as multiple ground control stations of multi-uav. *IEEE 6th Global Conference on Consumer Electronics*, pages 1–5, October 2017.
- [145] X.Li, T.Zhang, and J.Li. A particle swarm mobility model for flying ad hoc networks. *2017 IEEE Global Communications Conference*, pages 1–5, December 2017.
- [146] R. Jia, Y. Li, X. Cheng, and B. Ai. 3d geometry-based uav-mimo channel modeling and simulation. *IEEE Transactions on China Communications*, 15:64–74, December 2018.
- [147] M. Rajashekar, R. Renzo, M. Di, H. K.V.S., and H. Lajos. A beamforming aided full-diversity scheme for low-altitude air-to-ground communication systems operating with limited feedback. *IEEE Transactions on Communications*, 66:6602–6613, December 2018.
- [148] S. Yeh, J.F. Chamberland, and G. H. Huff. An investigation of geolocation-aware beamforming algorithms for swarming uavs. *2017 IEEE International Symposium on Antennas and Propagation USNC/URSI National Radio Science Meeting*, July 2017.
- [149] S.J. Maeng, H. Park, and Y.S. Cho. Beam tracking technique for multiple unmanned aerial vehicles. *2017 IEEE 85th Vehicular Technology Conference*, June 2017.
- [150] J. Chen, Q. Wu and Y. Xu, Y. Zhang, and Y Yang. Distributed demand-aware channel-slot selection for multi-uav networks: A game-theoretic learning approach. *IEEE Access*, 6:14799–14811, March 2018.
- [151] P. Si, R. Yang, and Y. Zhang. Dynamic spectrum management for heterogeneous uav networks with navigation data assistance. *2015 IEEE Wireless Communications and Networking Conference*, March 2015.

# Curriculum Vitae

**Name:** Yanan Liu

**Post-Secondary Education and Degrees:** 2015 - present, PhD  
Electrical and Computer Engineering  
The University of Western Ontario  
London, Ontario, Canada

2011 - 2012, M.E.Sc  
Communication Engineering  
The University of Manchester  
Manchester, UK

2007 - 2011, B.Eng  
Communication Engineering  
Dalian Maritime University  
Dalian, China

**Related Working Experience** System Engineer  
DaTang Mobile Communication Equipment Co.  
Beijing, China  
2012 - 2015

Research Assistant  
The University of Western Ontario  
London, Ontario, Canada  
2015-2020

Teaching Assistant  
The University of Western Ontario  
London, Ontario, Canada  
2015-2019

**Publications:****Journal:**

- [1] X. Liu, X. Wang, Y. Liu and H. Lin, "Power Allocation and Performance Analysis of the Collaborative NOMA Assisted Relaying Systems in 5G," in *China Communication*, vol. 14, no. 1, pp.50-60, February, 2017.
- [2] X. Duan, Y. Liu and X. Wang, "SDN Enabled 5G-VANET: Adaptive Vehicle Clustering and Beamformed Transmission for Aggregated Traffic," in *IEEE Communications Magazine*, vol.55, no.7, pp.120-127, July 2017.
- [3] X. Liu, Y. Liu, X. Wang and H. Li, "Highly Efficient 3D Resource Allocation Techniques in 5G for NOMA Enabled Massive MIMO and Relaying Systems", in *IEEE Journal on Selected Areas*, vol. 35, no. 12, pp.2785-2797, December, 2017.
- [4] Y. Zhao, Y. Liu, G. Boudreau, A. B. Sediq and X. Wang, "Angle-based Beamforming in mmWave Massive MIMO Systems with Low Feedback Overhead using Multi-pattern Codebooks," in *China Communication*, vol. 16, no.9, pp.18-30, September 2019.
- [5] Y. Liu, X. Wang, G. Boudreau, A. B. Sediq and H. Abou-zeid "Deep Learning Based Hotspot Prediction and Beam Management for Adaptive Virtual Small Cell in 5G Networks," in *IEEE Transactions on Emerging Topics in Computational Intelligence*, vol. 4, no.1, pp.83-94, January 2020.
- [6] Y. Liu, X. Wang, G. Boudreau, A. B. Sediq, and H. Abou-zeid , " A Multi-Dimensional Intelligent Multiple Access Technique for 5G Beyond and 6G Wireless Networks," in *IEEE Transaction on Wireless Communications*, submitted, 2020.
- [7] Y. Liu, X. Wang, G. Boudreau, A. B. Sediq, and H. Abou-zeid , " Deep Reinforcement Learning Based Power Allocation for Multi-dimensional Intelligent Multiple Access Networks," will be submitted, 2020.

**Conference:**

- [1] Y. Liu, X. Wang, X. Duan and H. Lin, "Aggregated V2I Communications for Improved Energy Efficiency using Non-Orthogonal Multiplexed Modulation," in *IEEE Vehicular Technology Conference (VTC) Fall*, pp.1-5, 2016
- [2] X. Duan, X. Wang, Y. Liu and H. Lin, "SDN Enabled Dual Cluster Head Selection and Adaptive Clustering in 5G-VANET," in *IEEE Vehicular Technology Conference (VTC) Fall*, 2016.
- [3] Y. Liu, X. Duan, G. Boudreau, A. B. Sediq and X. Wang, "Adaptive Beamforming based Inband Fronthaul for Cost-Effective Virtual Small Cell in 5G Networks", in *IEEE Global Communications Conference (GLOBECOM)*, pp.1-6, 2017.
- [4] X. Duan, Y. Liu, A. B. Sediq, G. Boudreau and X. Wang, "Protocol Conversion and Weighted Resource Allocation in Virtual Small Cells of 5G Ultra Dense Networks for Cost-Effective Service Provisioning", in *IEEE International Symposium on Personal, Indoor and Mobile Radio Communications (PIMRC)*, pp.1-6, 2017.
- [5] Y. Liu, X. Wang, G. Boudreau, A. B. Sediq and H. Li, "An Adaptive Two-Dimensional Non-orthogonal Multiple Access Technique Using Multi-level Modulation and Interleaving", in *IEEE International Conference on Computer and Communications (ICCC)*, pp.1-6, 2017.
- [6] Y. Zhao, Y. Liu, G. Boudreau, A. B. Sediq, H. Abou-zeid and X. Wang, "A Two-Step Neural Network Based Beamforming in MIMO Without Reference Signal," in *IEEE Global Communications Conference (GLOBECOM)*, accepted, 2019.